Aerospace and Mechanical Engineering Department
Space Structures and Systems Laboratory

# Performance and Robustness of Nonlinear Systems Using Bifurcation Analysis

Thesis submitted in fulfilment of the requirements for the degree of
Doctor in Engineering Sciences

by

**Thibaut Detroux, Ir.**

March 2016

**Author's contact details**

Thibaut DETROUX

Space Structures and Systems Laboratory
Aerospace and Mechanical Engineering Department
University of Liège

Quartier Polytech 1 (B52/3)
Allée de la découverte 9
4000 Liège, Belgium

Email: tdetroux@ulg.ac.be
Phone: +32 4 3669098

## Members of the Examination Committee

Prof. Olivier BRULS (President of the Committee)
University of Liège (Liège, Belgium)
Email: o.bruls@ulg.ac.be

Prof. Gaëtan KERSCHEN (Advisor)
University of Liège (Liège, Belgium)
Email: g.kerschen@ulg.ac.be

Prof. Jakob S. JENSEN
Danmarks Tekniske Universitet (Copenhagen, Denmark)

Prof. Sébastien BAGUET
Université de Lyon (Lyon, France)

Prof. Claude-Henri LAMARQUE
Université de Lyon (Lyon, France)

Prof. Dirk ROOSE
Katholieke Universiteit Leuven (Leuven, Belgium)

Prof. Tristan GILET
University of Liège (Liège, Belgium)

Prof. Ludovic NOELS
University of Liège (Liège, Belgium)

# Abstract

Nonlinear vibrations can be frequently encountered in engineering applications, and take their origin from different sources including contact, friction or large displacements. Other manifestations of nonlinearities are peculiar phenomena such as amplitude jumps, quasi-periodic oscillations and isolated response curves. These phenomena are closely related to the presence of bifurcations in the frequency response, which dictate the system's dynamics. While recent progress has been achieved to develop tools for nonlinear modal analysis of industrial applications, bifurcation analysis was still limited to reduced models and academic case studies. Along with the lack of an efficient algorithm to detect and study bifurcations, bifurcation analysis for design purposes also remained unexplored.

The fundamental contribution of this doctoral thesis is the development of a new methodology for the detection, characterization and tracking of bifurcations of large-scale mechanical systems. To this end, an extension of the harmonic balance (HB) method is proposed. Taking advantage of the efficiency of the HB method for the continuation of nonlinear normal modes and frequency responses, this extension allows for robust computation of bifurcation curves in the system's parameter space. A validation of the methodology is performed on the strongly nonlinear model of an Airbus Defence & Space spacecraft, which possesses an impact-type nonlinear device consisting of multiple mechanical stops limiting the motion of an inertia wheel mounted on an elastomeric interface.

The second main contribution is the development of a new vibration absorber, the nonlinear tuned vibration absorber (NLTVA), which generalizes Den Hartog's equal-peak method to nonlinear systems. The absorber is demonstrated to exhibit unprecedented performance for the mitigation of nonlinear resonances. In a second step, the HB-based bifurcation methodology is utilized to characterize the performance regions of the NLTVA, and to ensure its robustness with respect to parameter uncertainties.

# Acknowledgements

*This doctoral dissertation is the result of several years of research at the University of Liège, and would have been unachievable without the involvement of a number of people.*

*First, I am very pleased to acknowledge my advisor, Prof. Gaëtan Kerschen, for his guidance and inspiring ideas. It is thanks to his encouragement and constant enthusiasm that I could bring this thesis to fruition.*

*I am also thankful to my colleagues at the Space Structures and Systems Laboratory for our scientific and friendly discussions. In particular, I am grateful to Giuseppe, Jean-Philippe, Lamberto, Luc and Ludovic, for their helpful advice. I would like to thank Edouard, Emeline, Marco Lucio, Samir, Vincent and other colleagues from the Aerospace and Mechanical Engineering Department, who created a friendly working atmosphere.*

*I would like to acknowledge Prof. Lawrence Virgin for his warm hospitality during my stay at Duke University, and for the opportunity that I had to work in his laboratory.*

*I express my gratitude to Profs. Olivier Brüls, Tristan Gilet, Ludovic Noels, Sébastien Baguet, Jakob Jensen, Claude-Henri Lamarque and Dirk Roose, for accepting to participate in the examination committee of this doctoral thesis.*

*I would like to thank all my friends, especially Mehmet and Sébastien, for their encouragement during these four years.*

*Enfin, j'aimerais du fond du coeur remercier ma famille, et mes parents en particulier, d'avoir toujours cru en moi et de m'avoir tant aidé. Lauriane, merci pour ton amour et ton soutien, particulièrement durant ces derniers mois.*

# Contents

# Introduction

In mechanical engineering, the performance envelope of new prototypes is continuously being expanded. This is especially verified in aeronautics, where market needs and environmental legislations demand constant efforts to lower fuel consumption and to reduce noise and gas emissions [35]. In this context, specific attention is devoted to each structural component, from wing spars to engine blades. Taking advantage of increasing computational power, parametric and topological optimizations now represent standard tools to design lighter elements. Advanced materials, such as carbon composites for fuselage panels or elastomeric mounts for engine pylons, are also widely utilized. With the introduction of these light, flexible elements, with possibly involved constitutive laws and complicated dynamics at the interconnections, modern structures are prone to operate beyond linear regimes of motion.

Occurrences of nonlinearity have been reported in the literature for several industrial applications. During the modal survey of the Cassini spacecraft, the softening of a resonance was related to the presence of gaps in the attachments of the Huygens probe [28]. The ground vibration test campaign of the Airbus A400M revealed that the elastomeric mounts supporting the engines were affecting the modal shapes and frequencies of the aircraft [3]. Because nonlinearities are rarely well-understood, however, common practice in industry is to ignore them. In this case, applying classical linear design methodologies results, at best, in suboptimal performance.

Besides performance deterioration, a peculiar feature of nonlinear systems is that, for the slight variation of a parameter, undesired phenomena can be suddenly triggered. These phenomena, including limit cycle oscillations, modal interactions, isolated response curves, quasiperiodic oscillations, and even chaos, are directly related to the presence of bifurcations in the response [185]. As they lead to unexpected vibrations of possibly high amplitude, bifurcations can jeopardize some components, or even undermine the structure's integrity. Limit cycle oscillations, for instance, emanate from a Hopf bifurcation, and represent a major concern for aeroelastic systems [45]. In [179], modal interactions were shown to cause unacceptable disturbances during the mission of the Hubble Space Telescope. It is therefore clear that, in the design cycle of a structure, robustness against adverse dynamics must also be verified. As they directly affect the system's response, bifurcations, in this circumstance, deserve particular attention.

# Contributions of the Thesis

Several software packages allowing the investigation of bifurcations have been developed over the last decades. They have been applied to numerous studies, but their use usually remains limited to low-order models, while bifurcations-related phenomena can also be observed at large scale. It is only recently that bifurcation analysis was performed on larger systems, such as aircraft components [140, 172]. The method employed, however, built on a formalism that is not optimized to study nonlinear mechanical vibrations. An attempt to target bifurcation analysis of large systems was also carried out with the LOCA package [167], but this software requires expert programming skills.

In this context, the first objective of this doctoral thesis is to introduce numerical techniques to perform advanced nonlinear vibration analysis on large-scale systems. These methods, based on the harmonic balance formalism, are not only utilized to calculate nonlinear frequency responses and nonlinear normal modes, but also to determine the effect of system's parameters on the response bifurcations. Techniques to uncover nonlinear adverse phenomena are described, which serves to characterize the robustness of the structure. Further efforts are devoted to understand the mechanisms that generate these phenomena, and to propose updated designs that lead to their suppression.

The second objective of this work is to improve the performance of nonlinear structures by means of a nonlinear tuned vibration absorber. Our approach consists in exploiting the additional flexibility that nonlinear absorbers offer with respect to their linear counterpart. To this end, a procedure to synthesize the absorber's load-deflection characteristic for optimal vibration mitigation is presented.

The overall purpose of this doctoral thesis is thus to provide tools to guarantee the performance and robustness of real-life nonlinear mechanical structures, that can be integrated in a design cycle. This motivates the division of the present manuscript into 5 chapters as follows.

Chapter 1 introduces the harmonic balance formalism for the computation of nonlinear frequency response curves, and extend the method to bifurcation analysis in codimension-2 parameter space. Because this manuscript targets large-scale mechanical systems with localized nonlinearities, an algorithm that efficiently combines the calculation of the Floquet exponents and bordering techniques is developed. Nonlinear modal analysis is also performed, through the computation of nonlinear normal modes.

Chapter 2 demonstrates the capabilities of the proposed algorithm on the SmallSat spacecraft. In particular, the integration of the harmonic balance methodology in the design cycle of the structure is presented. Unexpected behaviors, observed in experimental data and numerical simulations, motivate bifurcation and modal analyses, which reveal the presence of modal interactions, isolated response curves and quasiperiodic oscillations.

In Chapter 3, the relations between nonlinear resonances and nonlinear normal modes are studied. To this end, two criteria, namely the nonlinear phase lag quadrature and energy balance criteria, are developed in the harmonic balance formalism. The former is employed to detect resonances along frequency responses, and the latter serves to derive the force necessary to excite normal modes. Another use of the energy balance criterion is enlightened, with the possibility to predict the creation of isolated response curves and their merging with the main response in the vicinity of modal interactions.

The experimental demonstration of the connections between isolated response curves and modal interactions is carried out in Chapter 4. A two-degree-of-freedom nonlinear set-up is constructed, and tuned to feature a modal interaction. A measurement campaign is then performed to characterize the isolated response curve in both detached and merged configurations, and the main observations are validated with a numerical model.

Chapter 5 investigates a nonlinear tuned vibration absorber to mitigate vibrations of nonlinear systems. The linear components of the absorber are selected to ensure performance at low energy as good as that of linear absorbers. The generalization of Den Hartog's equal-peak method is presented, which provides a procedure to select the nonlinear component of the absorber. In order to assess the performance and robustness of the absorber with respect to parameter uncertainties, the combined use of global analysis and bifurcation tracking is proposed.

Conclusions are finally drawn, and the contributions of this doctoral thesis are discussed. Three main directions for future research are also presented, and illustrated with preliminary results.

# Chapter 1

# Harmonic Balance Method for Advanced Nonlinear Vibration Analysis

### Abstract

The present chapter addresses the vibration analysis of nonlinear mechanical systems based on the harmonic balance (HB) method. The HB formalism, commonly used to study periodic solutions, is first employed to compute nonlinear frequency response curves (NFRCs). The Floquet exponents, which provide information regarding the stability of the solutions, are exploited for the detection of bifurcations along the NFRCs. A procedure for tracking the bifurcations in a codimension-2 parameter space is then proposed. In the last part of the chapter, the HB method is adapted to perform modal analysis through the computation of nonlinear normal modes.

## 1.1 Introduction

The computation of periodic solutions represents a fundamental step for the vibration analysis of nonlinear structures [129, 171]. For this purpose, different algorithms and numerical methods can be found in the literature. Time-domain methods, which deal with the resolution of a boundary value problem (BVP), have proven efficient for low-dimensional problems. The shooting technique, for example, optimizes the initial state of periodic solutions through time integration to solve the BVP [94]. When applied to larger systems, however, its computational burden can become substantial due to the numerous simulations it requires. Efforts have therefore been undertaken to make shooting less computationally intensive by using parallelization [183] and sensitivity analysis [144]. Another approach, the so-called orthogonal collocation, builds on the discretization of the BVP and its approximation with orthogonal polynomials. Methods based on orthogonal collocation are utilized in several software packages, *e.g.*, AUTO [41], COLSYS [9], CONTENT [108], DDE-BIFTOOL [52], MATCONT [38] and, more recently, COCO [36]. In spite of its high accuracy and ability to address stiff problems, orthogonal collocation is rarely employed for large mechanical systems, to which it is less adapted.

In the frequency domain, harmonic balance (HB) is certainly the most widely used method. It is also known as the Fourier–Galerkin method, since it consists in the application of the Galerkin method with Fourier basis and test functions. The periodic signals are approximated with their Fourier coefficients, which become the new unknowns of the problem. The term *harmonic balance* was first introduced by Krylov and Bogoliubov [102] who performed linearization of nonlinear dynamical equations with single-harmonic approximations. In the 1960s a demonstration of the convergence of the method for Fourier approximations truncated to several harmonics was offered by Urabe [193]. The main advantage of HB is when low orders of approximation are sufficient to obtain an accurate solution, which usually holds for smooth nonlinearities. In this case, the method involves algebraic equations with less unknowns than for orthogonal collocation. The reader can refer to [93] for a comparison between HB and orthogonal collocation applied to smooth and nonsmooth nonlinearities.

In the field of mechanical engineering, Cardona *et al.* developed a multi-harmonic resolution scheme for vibration analysis with nonsmooth nonlinear functions [26]. The HB method was applied to realistic examples including bladed disks [153], bolted joints [89, 187], rotor/stator contacts [200], vibro-impact systems [149, 201], geometrically nonlinear beams [117] and plates [164]. Following a pioneer work on wing-control surface flutter [176], the HB method was successfully adapted to aeroelastic systems, *e.g.*, to airfoils with freeplay [120] and cubic stiffness [114]. A comparative review of HB applied to limit cycle oscillations can be found in [39]. The dynamics of complete vehicles [15] and full-scale aircraft [170] were also examined with HB, which demonstrates its effectiveness when applied to reduced finite element models. Comparisons between experiments and the results of HB simulations gave further evidence of the accuracy of the method [31, 32].

HB has enjoyed numerous applications in the literature, not restricted to the vibrations of elastic structures. In electrical engineering, for instance, Kundert *et al.* reported its superiority over time-domain techniques for the simulation of nonlinear circuits [105]. Using a well-known variant of the method based on single-harmonic approximations, the so-called describing function (DF) method, Genesio *et al.* [59] provided analytical expressions for regions of chaotic behavior of Lur'e systems. Other studies were carried out, *e.g.*, for piezoelectric inertial generators [180] or DC-DC converters [54]. More recently, fluid dynamics problems where unsteady flows are periodic in time were also tackled. In [79], Hall *et al.* formulated the HB method for the Navier-Stokes equations, and applications can be found for flows in multi-stage turbomachinery [33, 62] and helicopter blades [50].

The purpose of this chapter is to introduce a framework based on the harmonic balance approximation to carry out advanced vibration analysis. Section 1.2 reviews the HB formulation for the computation of periodic solutions, and for the analysis of their stability. In order to extend the analysis to a range of forcing frequencies, nonlinear frequency response curves are introduced in Section 1.3. Because they are responsible for dramatic changes in the system's dynamics, a particular attention is devoted to the detection of bifurcations in the frequency response. An efficient procedure for the tracking of bifurcation in codimension-2 parameter space is then proposed in Section 1.4. Building on the HB and continuation methodologies, Section 1.5 adapts the outlined techniques for performing nonlinear modal analysis, through the computation of nonlinear normal modes. Finally, the conclusions of the present chapter are drawn in Section 1.6.

## 1.2 Computation of Periodic Solutions

The equations of motion governing the dynamics of a nonautonomous nonlinear dynamical systems with $n$ degrees of freedom (DOFs) are

$$\mathbf{M}\ddot{\mathbf{x}} + \mathbf{C}\dot{\mathbf{x}} + \mathbf{K}\mathbf{x} + \mathbf{f}_{nl}(\mathbf{x}, \dot{\mathbf{x}}) = \mathbf{f}_{ext}(\omega, t) \tag{1.1}$$

where $\mathbf{M}$, $\mathbf{C}$ and $\mathbf{K}$ are the mass, damping and stiffness matrices, respectively. Vectors $\mathbf{x}$, $\mathbf{f}_{nl}$ and $\mathbf{f}_{ext}$ represent the displacements, the nonlinear forces and the external forces that are supposed periodic with frequency $\omega$ herein. The dots refer to the derivatives with respect to time $t$.

In this chapter, the computation of the periodic solutions $\mathbf{x}(t)$ of Eq. (1.1) are sought by using the HB method. The different developments are illustrated using a 2-DOF system pictured in Fig. 1.1, referred to as the coupled Duffing system throughout this thesis, and whose parameters are listed in Table 1.1. Table 1.2 gives the natural frequencies and damping ratios for the two modes of the system.

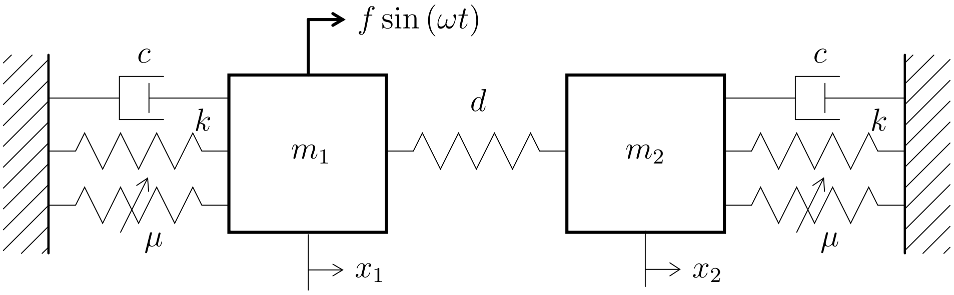

Figure 1.1: Schematic representation of the coupled Duffing system.

| $m_1$ (kg) | $m_2$ (kg) | $k$ (N/m) | $d$ (N/m) | $c$ (N/ms) | $\mu$ (N/m$^3$) |
|---|---|---|---|---|---|
| 1 | 1 | 1 | 5 | 0.1 | 1 |

Table 1.1: Linear and nonlinear parameters of the coupled Duffing system.

| Mode | Frequency (rad/s) | Damping ratio (%) |
|---|---|---|
| 1 | 1.00 | 5.00 |
| 2 | 3.32 | 1.51 |

Table 1.2: Linear natural frequencies and damping ratios of the coupled Duffing system.

### 1.2.1 Formulation of the Dynamics in the Frequency Domain

As they are assumed periodic, the signals $\mathbf{x}(t)$ and $\mathbf{f}(\mathbf{x}, \dot{\mathbf{x}}, \omega, t) = \mathbf{f}_{ext}(\omega, t) - \mathbf{f}_{nl}(\mathbf{x}, \dot{\mathbf{x}})$ are approximated by Fourier series truncated to the $N_H$-th harmonic:

$$\mathbf{x}(t) = \frac{\mathbf{c}_0^x}{\sqrt{2}} + \sum_{k=1}^{N_H} \left(\mathbf{s}_k^x \sin(k\omega t) + \mathbf{c}_k^x \cos(k\omega t)\right) \tag{1.2}$$

$$\mathbf{f}(t) = \frac{\mathbf{c}_0^f}{\sqrt{2}} + \sum_{k=1}^{N_H} \left(\mathbf{s}_k^f \sin(k\omega t) + \mathbf{c}_k^f \cos(k\omega t)\right) \tag{1.3}$$

where $\mathbf{s}_k$ and $\mathbf{c}_k$ represent the vectors of the Fourier coefficients related to the sine and cosine terms, respectively. In order to account for subharmonics of the forcing frequency, $\omega$ can also be replaced by $\omega/\nu$, where $\nu$ is an integer [200]. The Fourier coefficients of $\mathbf{f}(t)$, $\mathbf{c}_k^f$ and $\mathbf{s}_k^f$, depend on the Fourier coefficients of the displacements $\mathbf{x}(t)$, $\mathbf{c}_k^x$ and $\mathbf{s}_k^x$, which represent the new unknowns of the problem. These coefficients are gathered into the $(2N_H + 1)\, n \times 1$ vectors

$$\mathbf{z} = \begin{bmatrix} (\mathbf{c}_0^x)^{\mathrm{T}} & (\mathbf{s}_1^x)^{\mathrm{T}} & (\mathbf{c}_1^x)^{\mathrm{T}} & \ldots & (\mathbf{s}_{N_H}^x)^{\mathrm{T}} & (\mathbf{c}_{N_H}^x)^{\mathrm{T}} \end{bmatrix}^{\mathrm{T}} \tag{1.4}$$

$$\mathbf{b} = \left[ \begin{array}{cccccc} \left(\mathbf{c}_0^f\right)^{\mathrm{T}} & \left(\mathbf{s}_1^f\right)^{\mathrm{T}} & \left(\mathbf{c}_1^f\right)^{\mathrm{T}} & \dots & \left(\mathbf{s}_{N_H}^f\right)^{\mathrm{T}} & \left(\mathbf{c}_{N_H}^f\right)^{\mathrm{T}} \end{array} \right]^{\mathrm{T}} \tag{1.5}$$

where the operator $(\cdot)^{\mathrm{T}}$ denotes the transpose. The displacements and forces are recast into a more compact form [89]

$$\mathbf{x}(t) = \left(\mathbf{Q}(t) \otimes \mathbb{I}_n\right) \mathbf{z} \tag{1.6}$$

$$\mathbf{f}(t) = \left(\mathbf{Q}(t) \otimes \mathbb{I}_n\right) \mathbf{b} \tag{1.7}$$

where $\otimes$ and $\mathbb{I}_n$ stand for the Kronecker tensor product and the identity matrix of size $n$, respectively, and $\mathbf{Q}(t)$ is a vector containing the sine and cosine series

$$\mathbf{Q}(t) = \left[ \begin{array}{cccccc} \frac{1}{\sqrt{2}} & \sin(\omega t) & \cos(\omega t) & \dots & \sin(N_H \omega t) & \cos(N_H \omega t) \end{array} \right] \tag{1.8}$$

Velocities and accelerations can also be defined using the Fourier series, with

$$\dot{\mathbf{x}}(t) = \left(\dot{\mathbf{Q}}(t) \otimes \mathbb{I}_n\right) \mathbf{z} = \left(\left(\mathbf{Q}(t)\boldsymbol{\nabla}\right) \otimes \mathbb{I}_n\right) \mathbf{z} \tag{1.9}$$

$$\ddot{\mathbf{x}}(t) = \left(\ddot{\mathbf{Q}}(t) \otimes \mathbb{I}_n\right) \mathbf{z} = \left(\left(\mathbf{Q}(t)\boldsymbol{\nabla}^2\right) \otimes \mathbb{I}_n\right) \mathbf{z} \tag{1.10}$$

where

$$\boldsymbol{\nabla} = \begin{bmatrix} 0 & & & & \\ & \ddots & & & \\ & & \boldsymbol{\nabla}_k & & \\ & & & \ddots & \\ & & & & \boldsymbol{\nabla}_{N_H} \end{bmatrix}, \quad \boldsymbol{\nabla}\boldsymbol{\nabla} = \boldsymbol{\nabla}^2 = \begin{bmatrix} 0 & & & & \\ & \ddots & & & \\ & & \boldsymbol{\nabla}_k^2 & & \\ & & & \ddots & \\ & & & & \boldsymbol{\nabla}_{N_H}^2 \end{bmatrix} \tag{1.11}$$

with

$$\boldsymbol{\nabla}_k = \begin{bmatrix} 0 & -k\omega \\ k\omega & 0 \end{bmatrix}, \quad \boldsymbol{\nabla}_k^2 = \begin{bmatrix} -(k\omega)^2 & 0 \\ 0 & -(k\omega)^2 \end{bmatrix} \tag{1.12}$$

Substituting Eqs. (1.6)-(1.7) and (1.9)-(1.10) in the equations of motion (1.1) yields

$$\mathbf{M}\left(\left(\mathbf{Q}(t)\boldsymbol{\nabla}^2\right) \otimes \mathbb{I}_n\right)\mathbf{z} + \mathbf{C}\left(\left(\mathbf{Q}(t)\boldsymbol{\nabla}\right) \otimes \mathbb{I}_n\right)\mathbf{z} + \mathbf{K}\left(\mathbf{Q}(t) \otimes \mathbb{I}_n\right)\mathbf{z} = \left(\mathbf{Q}(t) \otimes \mathbb{I}_n\right)\mathbf{b} \tag{1.13}$$

Considering the mixed-product property of the Kronecker tensor product $(\mathbf{A} \otimes \mathbf{B})(\mathbf{C} \otimes \mathbf{D}) = (\mathbf{AC}) \otimes (\mathbf{BD})$ yields

$$\mathbf{M}\left(\left(\mathbf{Q}(t)\boldsymbol{\nabla}^2\right) \otimes \mathbb{I}_n\right) = (1 \otimes \mathbf{M})\left(\left(\mathbf{Q}(t)\boldsymbol{\nabla}^2\right) \otimes \mathbb{I}_n\right) = \left(\mathbf{Q}(t)\boldsymbol{\nabla}^2\right) \otimes \mathbf{M} \tag{1.14}$$

$$\mathbf{C}\left(\left(\mathbf{Q}(t)\boldsymbol{\nabla}\right) \otimes \mathbb{I}_n\right) = (1 \otimes \mathbf{C})\left(\left(\mathbf{Q}(t)\boldsymbol{\nabla}\right) \otimes \mathbb{I}_n\right) = \left(\mathbf{Q}(t)\boldsymbol{\nabla}\right) \otimes \mathbf{C} \tag{1.15}$$

$$\mathbf{K}\left(\mathbf{Q}(t) \otimes \mathbb{I}_n\right) = (1 \otimes \mathbf{K})\left(\mathbf{Q}(t) \otimes \mathbb{I}_n\right) = \mathbf{Q}(t) \otimes \mathbf{K} \tag{1.16}$$

These expressions are plugged into Eq. (1.13), which gives

$$\left(\left(\mathbf{Q}(t)\boldsymbol{\nabla}^2\right) \otimes \mathbf{M}\right)\mathbf{z} + \left(\left(\mathbf{Q}(t)\boldsymbol{\nabla}\right) \otimes \mathbf{C}\right)\mathbf{z} + \left(\mathbf{Q}(t) \otimes \mathbf{K}\right)\mathbf{z} = \left(\mathbf{Q}(t) \otimes \mathbb{I}_n\right)\mathbf{b} \tag{1.17}$$

In order to remove the time dependency and to obtain an expression relating the different Fourier coefficients, a Galerkin procedure projects Eq. (1.17) on the orthogonal trigonometric basis $\mathbf{Q}(t)$

$$\left(\left(\frac{2}{T}\int_0^T \mathbf{Q}^{\mathrm{T}}(t)\mathbf{Q}(t)\,dt\,\boldsymbol{\nabla}^2\right)\otimes\mathbf{M}\right)\mathbf{z}+\left(\left(\frac{2}{T}\int_0^T \mathbf{Q}^{\mathrm{T}}(t)\mathbf{Q}(t)\,dt\,\boldsymbol{\nabla}\right)\otimes\mathbf{C}\right)\mathbf{z}+\dots$$
$$\left(\left(\frac{2}{T}\int_0^T \mathbf{Q}^{\mathrm{T}}(t)\mathbf{Q}(t)\,dt\right)\otimes\mathbf{K}\right)\mathbf{z}=\left(\left(\frac{2}{T}\int_0^T \mathbf{Q}^{\mathrm{T}}(t)\mathbf{Q}(t)\,dt\right)\otimes\mathbb{I}_n\right)\mathbf{b} \quad (1.18)$$

where $T = 2\pi/\omega$ is the period of the external force. Considering that

$$\frac{2}{T}\int_0^T \mathbf{Q}^{\mathrm{T}}(t)\mathbf{Q}(t)dt=\mathbb{I}_{2N_H+1} \quad (1.19)$$

the equations of motion expressed in the frequency domain are eventually obtained

$$\left(\boldsymbol{\nabla}^2\otimes\mathbf{M}\right)\mathbf{z}+\left(\boldsymbol{\nabla}\otimes\mathbf{C}\right)\mathbf{z}+\left(\mathbb{I}_{2N_H+1}\otimes\mathbf{K}\right)\mathbf{z}=\left(\mathbb{I}_{2N_H+1}\otimes\mathbb{I}_n\right)\mathbf{b} \quad (1.20)$$

or, in a more compact form,

$$\mathbf{h}(\mathbf{z},\omega)=\mathbf{A}(\omega)\mathbf{z}-\mathbf{b}(\mathbf{z})=\mathbf{0} \quad (1.21)$$

where $\mathbf{A}$ is the $(2N_H+1)\,n\times(2N_H+1)\,n$ matrix describing the linear dynamics

$$\begin{aligned}\mathbf{A} &= \boldsymbol{\nabla}^2\otimes\mathbf{M}+\boldsymbol{\nabla}\otimes\mathbf{C}+\mathbb{I}_{2N_H+1}\otimes\mathbf{K}\\ &= \begin{bmatrix}\mathbf{K} & & & & & \\ & \mathbf{K}-\omega^2\mathbf{M} & -\omega\mathbf{C} & & & \\ & \omega\mathbf{C} & \mathbf{K}-\omega^2\mathbf{M} & & & \\ & & & \ddots & & \\ & & & & \mathbf{K}-\left(N_H\omega\right)^2\mathbf{M} & -N_H\omega\mathbf{C}\\ & & & & N_H\omega\mathbf{C} & \mathbf{K}-\left(N_H\omega\right)^2\mathbf{M}\end{bmatrix}\end{aligned} \quad (1.22)$$

Eq. (1.21) can be seen as the equations of amplitude of Eq. (1.1), *i.e.*, if $\mathbf{z}^*$ is a solution of Eq. (1.21), then the time signal $\mathbf{x}^*$ constructed from $\mathbf{z}^*$ is periodic and verifies Eq. (1.1).

Eq. (1.21) is nonlinear and can be solved iteratively, *e.g.*, with a Newton-Raphson procedure, or with the hybrid Powell nonlinear solver [127, 159]. In the former case, the incremental procedure to find a periodic solution at a given frequency $\omega$ reads

1. Use an initial guess for the first iteration $\mathbf{z}^{(0)}$;
2. Update the current iteration with

$$\mathbf{z}^{(j+1)}=\mathbf{z}^{(j)}-\frac{\mathbf{h}\left(\mathbf{z},\omega\right)}{\mathbf{h}_{\mathbf{z}}\left(\mathbf{z},\omega\right)} \quad (1.23)$$

   where $\mathbf{h}_{\mathbf{z}}=\partial\mathbf{h}/\partial\mathbf{z}$ is the Jacobian matrix, until Eq. (1.21) is satisfied up to a given tolerance.

At this point, it is important to mention that, for the same forcing parameters, a nonlinear system may possess several solutions corresponding to, *e.g.*, low- and large-amplitude vibrations. Depending on the initial guess, the Newton-Raphson procedure in Eq. (1.23) will converge toward only one of them. In order to reveal additional solutions for a given forcing, methods relying on the homotopy method [118] or Groebner bases [73] can be employed.

### 1.2.2 Expression of the Nonlinear Terms and Jacobian Matrix

Eq. (1.23) requires the evaluation of $\mathbf{h}$ and of the Jacobian matrix $\mathbf{h_z}$ at each iteration, which in turn involves the computation of the components of $\mathbf{b}$ and of their derivatives. When $\mathbf{f}$ can be accurately approximated with few harmonics and when its analytical sinusoidal expansion is known [114], or for some types of restoring forces [153], analytical expressions relating the Fourier coefficients of the forces $\mathbf{b}$ and of the displacements $\mathbf{z}$ can be obtained together with the expression of $\mathbf{h_z}$.

Taking advantage of the fast Fourier transform, Cameron *et al.* proposed a more general technique to compute $\mathbf{b}$, the so-called alternating frequency-time domain (AFT) method, that evaluates the nonlinear terms of the equations in the time domain where their analytical expression is known [24]:

$$\mathbf{z} \xrightarrow{\text{FFT}^{-1}} \mathbf{x}(t) \rightarrow \mathbf{f}\left(\mathbf{x}, \dot{\mathbf{x}}, \omega, t\right) \xrightarrow{\text{FFT}} \mathbf{b}(\mathbf{z}) \tag{1.24}$$

Since then, many studies have utilized the AFT method [27, 89, 178]. Similar developments led to the hybrid frequency-time domain method, with applications to systems with dry friction [75, 158].

The Jacobian matrix $\mathbf{h_z}$ can be computed through finite differences, but this approach is computationally demanding. An efficient alternative consists in rewriting the inverse Fourier transform as a linear operator $\mathbf{\Gamma}(\omega)$. Inspired by the *trigonometric collocation* [88], this method has been widely used in combination with the AFT technique (see, *e.g.*, [22, 46, 99, 128]). This approach first requires to discretize the period of oscillation $T$ into $N$ partitions of length $\Delta T$, denoted as $t_1 = 0, t_2 = \Delta t, \ldots, t_N = T - \Delta T$. One then defines vectors $\tilde{\mathbf{x}}$ and $\tilde{\mathbf{f}}$ containing the concatenated $nN$ time samples of the displacements and the forces, respectively, for all DOFs:

$$\begin{aligned} \tilde{\mathbf{x}} &= \begin{bmatrix} x_1(t_1) & \ldots & x_1(t_N) & \ldots & x_n(t_1) & \ldots & x_n(t_N) \end{bmatrix}^{\mathrm{T}} & (1.25) \\ \tilde{\mathbf{f}} &= \begin{bmatrix} f_1(t_1) & \ldots & f_1(t_N) & \ldots & f_n(t_1) & \ldots & f_n(t_N) \end{bmatrix}^{\mathrm{T}} & (1.26) \end{aligned}$$

The inverse Fourier transform can then be written as a linear operation:

$$\tilde{\mathbf{x}} = \mathbf{\Gamma}(\omega)\, \mathbf{z} \tag{1.27}$$

with the $nN \times (2N_H+1)\,n$ sparse operator

$$\mathbf{\Gamma}(\omega) = \left[\begin{array}{ccccc} \mathbb{I}_n \otimes \begin{bmatrix} 1/\sqrt{2} \\ 1/\sqrt{2} \\ \vdots \\ 1/\sqrt{2} \end{bmatrix} & \mathbb{I}_n \otimes \begin{bmatrix} \sin(\omega t_1) \\ \sin(\omega t_2) \\ \vdots \\ \sin(\omega t_N) \end{bmatrix} & \mathbb{I}_n \otimes \begin{bmatrix} \cos(\omega t_1) \\ \cos(\omega t_2) \\ \vdots \\ \cos(\omega t_N) \end{bmatrix} & \dots & \\ & & & \mathbb{I}_n \otimes \begin{bmatrix} \sin(N_H\omega t_1) \\ \sin(N_H\omega t_2) \\ \vdots \\ \sin(N_H\omega t_N) \end{bmatrix} & \mathbb{I}_n \otimes \begin{bmatrix} \cos(N_H\omega t_1) \\ \cos(N_H\omega t_2) \\ \vdots \\ \cos(N_H\omega t_N) \end{bmatrix} \end{array}\right] \tag{1.28}$$

Fig. 1.2 illustrates the inverse transformation matrix for the case $n = 2$, $N = 64$, and $N_H = 5$.

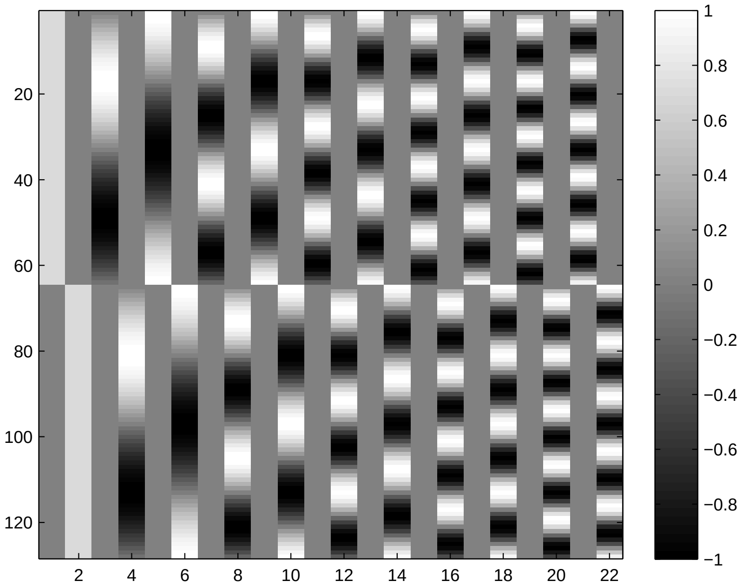

Figure 1.2: Inverse Fourier transformation matrix $\mathbf{\Gamma}(\omega)$ for $n = 2$, $N = 64$, and $N_H = 5$.

The direct Fourier transformation is written as

$$\mathbf{z} = (\mathbf{\Gamma}(\omega))^{+}\,\tilde{\mathbf{x}} \tag{1.29}$$

where $^{+}$ stands for the Moore-Penrose pseudoinverse $\mathbf{\Gamma}^{+} = \mathbf{\Gamma}^{\mathrm{T}}\left(\mathbf{\Gamma}\mathbf{\Gamma}^{\mathrm{T}}\right)^{-1}$. The Fourier coefficients of the external and nonlinear forces are simply obtained by transforming the signals in the time domain back to the frequency domain:

$$\mathbf{b}(\mathbf{z}) = (\mathbf{\Gamma}(\omega))^{+}\,\tilde{\mathbf{f}} \tag{1.30}$$

Considering elastic nonlinear forces, *i.e.*, $\mathbf{f}_{nl} = \mathbf{f}_{nl}(\mathbf{x})$, the Jacobian matrix is then computed as

$$\mathbf{h}_{\mathbf{z}} = \frac{\partial \mathbf{h}}{\partial \mathbf{z}} = \mathbf{A} - \frac{\partial \mathbf{b}}{\partial \mathbf{z}} = \mathbf{A} - \frac{\partial \mathbf{b}}{\partial \tilde{\mathbf{f}}} \frac{\partial \tilde{\mathbf{f}}}{\partial \tilde{\mathbf{x}}} \frac{\partial \tilde{\mathbf{x}}}{\partial \mathbf{z}} = \mathbf{A} - \boldsymbol{\Gamma}^{+} \frac{\partial \tilde{\mathbf{f}}}{\partial \tilde{\mathbf{x}}} \boldsymbol{\Gamma} \tag{1.31}$$

A similar expression can also be obtained for nonlinear damping [202]. In general, the derivatives of the forces with respect to the displacements in the time domain can be expressed analytically, which leads to a very efficient computation of the Jacobian matrix. These derivatives have to be evaluated only for the nonlinear DOFs.

For illustration, Fig. 1.3(a) shows a periodic solution of the coupled Duffing system computed for $f = 2\,\mathrm{N}$, $\omega = 1.2\,\mathrm{rad/s}$, and $N_H = 5$. Although the excitation is a pure sine, the response is distorted because of the nonlinearities in the system. The corresponding normalized harmonic coefficients

$$\sigma_i = \frac{\phi_i}{\sum_{k=0}^{N_H} \phi_i} \quad (i = 0, \ldots, N_H) \tag{1.32}$$

with

$$\phi_0 = \frac{c_0^x}{\sqrt{2}}, \quad \phi_i = \sqrt{(s_i^x)^2 + (c_i^x)^2} \quad (i = 1, \ldots, N_H) \tag{1.33}$$

are represented in Fig. 1.3(b). This figure confirms that the contribution of higher harmonics is not negligible.

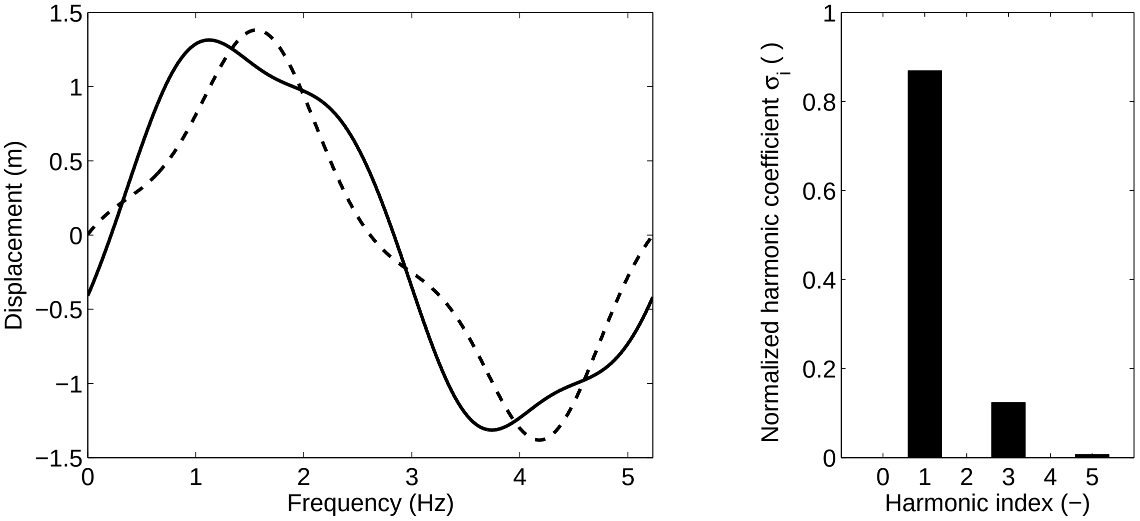

(a) (b)

Figure 1.3: Periodic solution of the coupled Duffing system for $f = 2\,\mathrm{N}$, $\omega = 1.2\,\mathrm{rad/s}$, and $N_H = 5$. (a) Time series of $x_1$ (solid line) and $x_2$ (dashed line); (b) normalized harmonic coefficients of $x_1$.

There exist alternatives to the computation of $\mathbf{b}$ and its derivatives described in this section. A first solution consists in applying the HB approximation on increments of the linearized version of Eq. (1.1); this approach, referred to as the *incremental harmonic balance method*, was presented by Lau and Cheung [111] and has been used in several other studies since then (see, *e.g.*, [12, 30, 156, 188]). A second solution, proposed by Cochelin and Vergez [34], is to recast Eq. (1.1) into a new system where the nonlinearities are at most quadratic polynomials, to which the HB approximation can be efficiently applied [92, 141].

### 1.2.3 Stability Analysis

In order to assess the stability of a computed periodic solution, its $2n$ *Floquet multipliers* $\tilde{\boldsymbol{\sigma}}$ are determined. Equivalently, its $2n$ *Floquet exponents* $\tilde{\boldsymbol{\lambda}}$ can be considered; they are related to the Floquet multipliers through the exponential function

$$\tilde{\sigma}_i = e^{\tilde{\lambda}_i T}, \qquad i = 1, \dots, 2n \tag{1.34}$$

A periodic solution is unstable if there exists at least one Floquet multiplier with a magnitude higher than 1 or, equivalently, if there exists at least one Floquet exponent with a real part higher than 0; otherwise, the solution is stable. The Floquet multipliers and exponents are usually depicted in the complex plane and compared to the unit circle or to the imaginary axis, respectively [171].

When relying on time-domain methods such as the shooting technique, the Floquet multipliers can be conveniently computed as the eigenvalues of the monodromy matrix of the system obtained from time integrations [144]. For frequency-domain techniques such as the HB method, alternative approaches can be found in the literature. In [110], Lanza *et al.* provided an analytical approximation of Floquet exponents using the DF method. A semi-analytical version was also developed for an arbitrary number of harmonics [22]. However, these developments are limited to systems expressed in Lur'e form. For this reason, we prefer to use a variant of Floquet theory, the so-called *Hill's method* [81], to provide approximations of the Floquet exponents within the HB formalism.

Following the procedure described in [200], a periodic solution $\mathbf{x}^*(t)$ satisfying Eq. (1.1) is perturbed with a periodic solution $\mathbf{s}(t)$ modulated by an exponential decay:

$$\mathbf{p}(t) = \mathbf{x}^*(t) + e^{\lambda t}\mathbf{s}(t) \tag{1.35}$$

Introducing this perturbation into Eq. (1.1) yields

$$\mathbf{M}\ddot{\mathbf{x}}^* + \mathbf{C}\dot{\mathbf{x}}^* + \mathbf{K}\mathbf{x}^* + \left(\lambda^2\mathbf{M}\mathbf{s} + \lambda\left(2\mathbf{M}\dot{\mathbf{s}} + \mathbf{C}\mathbf{s}\right) + \mathbf{M}\ddot{\mathbf{s}} + \mathbf{C}\dot{\mathbf{s}} + \mathbf{K}\mathbf{s}\right)e^{\lambda t} = \mathbf{f}\left(\mathbf{p}, \dot{\mathbf{p}}, \omega, t\right) \tag{1.36}$$

The solution and the perturbation are then approximated by Fourier series truncated to the $N_H$-th order, *i.e.*, $\mathbf{x}^*(t) = \left(\mathbf{Q}(t) \otimes \mathbb{I}_n\right)\mathbf{z}^*$ and $\mathbf{s}(t) = \left(\mathbf{Q}(t) \otimes \mathbb{I}_n\right)\mathbf{u}$, where $\mathbf{z}^*$ and $\mathbf{u}$ contain the Fourier coefficients of $\mathbf{x}^*$ and $\mathbf{s}$, respectively. By applying a Galerkin procedure to Eq. (1.36) as in Section 1.2.1, one obtains

$$\mathbf{A}\mathbf{z}^* + \left(\boldsymbol{\Delta}_2\lambda^2 + \boldsymbol{\Delta}_1\lambda + \mathbf{A}\right)e^{\lambda t}\mathbf{u} = \mathbf{b}\left(\mathbf{z}^* + e^{\lambda t}\mathbf{u}\right) \tag{1.37}$$

with

$$\begin{aligned}\boldsymbol{\Delta}_1 &= \boldsymbol{\nabla} \otimes 2\mathbf{M} + \mathbb{I}_{2N_H+1} \otimes \mathbf{C} \\ &= \begin{bmatrix} \mathbf{C} & & & & & \\ & \mathbf{C} & -2\omega\mathbf{M} & & & \\ & 2\omega\mathbf{M} & \mathbf{C} & & & \\ & & & \ddots & & \\ & & & & \mathbf{C} & -2N_H\omega\mathbf{M} \\ & & & & 2N_H\omega\mathbf{M} & \mathbf{C} \end{bmatrix} \qquad (1.38) \\ \boldsymbol{\Delta}_2 &= \mathbb{I}_{2N_H+1} \otimes \mathbf{M} \qquad (1.39)\end{aligned}$$

The right-hand side of Eq. (1.37) is evaluated through a Taylor series expansion around the solution $\mathbf{z}^*$

$$\mathbf{b}\left(\mathbf{z}^* + e^{\lambda t}\mathbf{u}\right) = \mathbf{b}\left(\mathbf{z}^*\right) + \left.\frac{\partial \mathbf{b}}{\partial \mathbf{z}}\right|_{\mathbf{z}=\mathbf{z}^*} \left(e^{\lambda t}\mathbf{u}\right) \qquad (1.40)$$

Since $\mathbf{A}\mathbf{z}^* - \mathbf{b}\left(\mathbf{z}^*\right)$ is equal to zero by definition, and given that

$$\mathbf{A} - \left.\frac{\partial \mathbf{b}}{\partial \mathbf{z}}\right|_{\mathbf{z}=\mathbf{z}^*} = \mathbf{h}_{\mathbf{z}} \qquad (1.41)$$

replacing Eq. (1.40) in Eq. (1.37) yields

$$\left(\boldsymbol{\Delta}_2\lambda^2 + \boldsymbol{\Delta}_1\lambda + \mathbf{h}_{\mathbf{z}}\right) e^{\lambda t}\mathbf{u} = \mathbf{0} \qquad (1.42)$$

Hill's coefficients $\boldsymbol{\lambda}$ are thus the solutions of the quadratic eigenvalue problem

$$\left(\boldsymbol{\Delta}_2\lambda^2 + \boldsymbol{\Delta}_1\lambda + \mathbf{h}_{\mathbf{z}}\right) \mathbf{u} = \mathbf{0} \qquad (1.43)$$

When embedded in a Newton-Raphson procedure, $\mathbf{h}_{\mathbf{z}}$ is already obtained from the resolution of Eq. (1.21). Since $\boldsymbol{\Delta}_1$ and $\boldsymbol{\Delta}_2$ can be easily computed, the main computational effort amounts to solving a quadratic eigenvalue problem, which can be rewritten as a linear eigenvalue problem of double size

$$\left(\mathbf{B}_1 - \gamma\mathbf{B}_2\right) \mathbf{r} = \mathbf{0} \qquad (1.44)$$

with

$$\mathbf{B}_1 = \begin{bmatrix} \boldsymbol{\Delta}_1 & \mathbf{h}_{\mathbf{z}} \\ -\mathbb{I} & \mathbf{0} \end{bmatrix}, \qquad \mathbf{B}_2 = -\begin{bmatrix} \boldsymbol{\Delta}_2 & \mathbf{0} \\ \mathbf{0} & \mathbb{I} \end{bmatrix} \qquad (1.45)$$

The coefficients $\boldsymbol{\lambda}$ are found as the eigenvalues of the $\left(2N_H+1\right)2n \times \left(2N_H+1\right)2n$ matrix

$$\begin{aligned}\mathbf{B} &= \mathbf{B}_2^{-1}\mathbf{B}_1 \\ &= \begin{bmatrix} -\boldsymbol{\Delta}_2^{-1}\boldsymbol{\Delta}_1 & -\boldsymbol{\Delta}_2^{-1}\mathbf{h}_{\mathbf{z}} \\ \mathbb{I} & \mathbf{0} \end{bmatrix} \qquad (1.46)\end{aligned}$$

Only $2n$ eigenvalues among the complete set $\boldsymbol{\lambda}$ approximate the Floquet exponents $\tilde{\boldsymbol{\lambda}}$ of the solution $\mathbf{x}^*$ [113]. Moore [123] showed that the Floquet exponents $\tilde{\boldsymbol{\lambda}}$ are the $2n$

eigenvalues with the smallest imaginary part in modulus. The other eigenvalues are spurious and do not have any physical meaning; their number also increases with the size of the eigenvalue problem in Eq. (1.44), *i.e.*, with the number of harmonics $N_H$. On the other hand, the approximation of the Floquet exponents improves with $N_H$, as Hill's method also depends on the truncation of the Fourier series.

The diagonal matrix

$$\tilde{\mathbf{B}} = \begin{bmatrix} \tilde{\lambda}_1 & & & \\ & \tilde{\lambda}_2 & & \\ & & \ddots & \\ & & & \tilde{\lambda}_{2n} \end{bmatrix} \tag{1.47}$$

gathers the Floquet exponents identified from the $(2N_H + 1)\,2n$ Hill's coefficients. It plays a key role for the detection and tracking of bifurcations in Sections 1.3.2 and 1.4.

The stability analysis of the periodic solution depicted in Fig. 1.3 is carried out in Fig. 1.4. The Floquet multipliers computed from the monodromy matrix through time integration, herein assumed as the reference solution, are given in Fig. 1.4(a). Their projection as Floquet exponents are compared in Figs. 1.4(b), (c) and (d) to Hill's coefficients $\boldsymbol{\lambda}$ computed for $N_H = 1$, 3 and 5. These figures confirm that the $2n$ Hill's coefficients with the smallest imaginary part in modulus provide the best approximation to the Floquet exponents, with an accuracy increasing with $N_H$. We refer the interested reader to [145] for a more in-depth comparison of the performance between the monodromy matrix and Hill's method.

## 1.3 Computation of Nonlinear Forced Response Curves

As the response of a nonlinear system is usually to be computed for a range of frequencies, this section addresses the computation of branches of forced periodic solutions, termed *nonlinear forced response curves* (NFRCs). Most methods for obtaining the NFRCs build on a continuation procedure [139], *e.g.*, with arc-length continuation [200] or the so-called asymptotic numerical method [6, 13] utilized in the MANLAB package. In this work, a Moore-Penrose scheme is adapted to the HB formalism, inspired by the continuation toolbox MATCONT [38, 67]. A methodology for detecting bifurcations using the HB formalism is also proposed.

### 1.3.1 Continuation Procedure

A continuation scheme is an iterative procedure that constructs the branch of solutions of a function $\mathbf{p} : \mathbb{R}^{m+1} \to \mathbb{R}^m$ [171]. The computation of periodic solutions with the HB method possesses a similar structure, with $\mathbf{h} \in \mathbb{R}^{(2N_H+1)n}$ in Eq. (1.21) which depends on $\mathbf{z} \in \mathbb{R}^{(2N_H+1)n}$ and $\omega \in \mathbb{R}^1$.

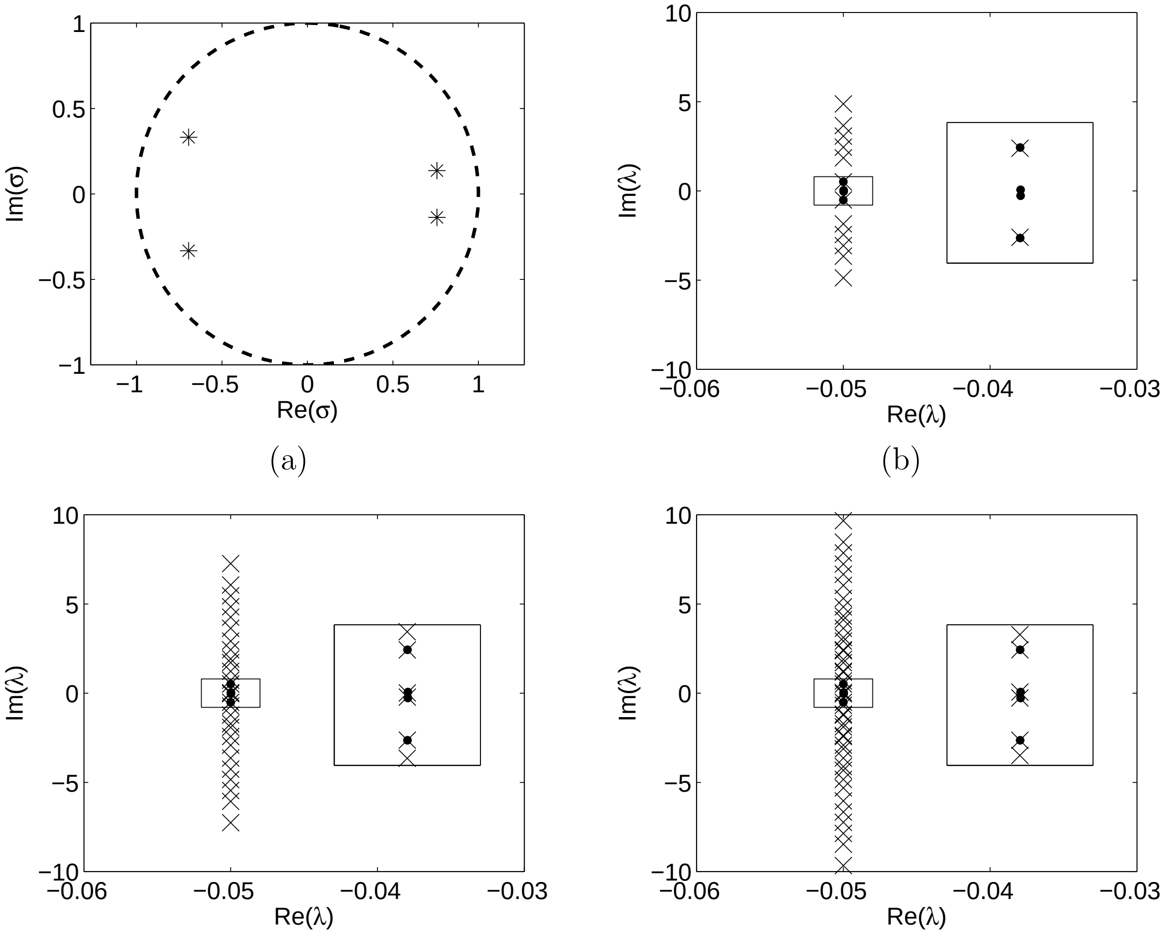

(a) (b)

(c) (d)

Figure 1.4: Stability of the periodic solution of the coupled Duffing system for $f = 2\,\mathrm{N}$ and $\omega = 1.2\,\mathrm{rad/s}$. (a) Floquet multipliers computed from the monodromy matrix; Hill's coefficients (cross markers) computed for (b) $N_H = 1$, (c) $N_H = 3$ and (d) $N_H = 5$. In (b-d), the dot markers represent the projection of the Floquet multipliers computed in (a).

The approach adopted herein is based on tangent predictions followed by corrections. The search for a tangent vector $\mathbf{t}_{(i)}$ at a solution $\mathbf{y}_{(i)} = \left[\mathbf{z}_{(i)}^{\mathrm{T}}\ \omega_{(i)}\right]^{\mathrm{T}}$ reads

$$\begin{bmatrix} \mathbf{J}\left(\mathbf{y}_{(i)}\right) \\ \mathbf{t}_{(i-1)}^{\mathrm{T}} \end{bmatrix} \mathbf{t}_{(i)} = \begin{bmatrix} \mathbf{0} \\ 1 \end{bmatrix} \tag{1.48}$$

with

$$\mathbf{J}\left(\mathbf{y}_{(i)}\right) = \left[\mathbf{h}_{\mathbf{z}}\left(\mathbf{y}_{(i)}\right)\ \mathbf{h}_{\omega}\left(\mathbf{y}_{(i)}\right)\right] \tag{1.49}$$

where $\mathbf{h}_{\omega}$ stands for the derivative of $\mathbf{h}$ with respect to $\omega$, *i.e.*,

$$\mathbf{h}_{\omega} = \frac{\partial \mathbf{h}}{\partial \omega} = \frac{\partial \mathbf{A}}{\partial \omega}\mathbf{z} \tag{1.50}$$

The last row in Eq. (1.48) prevents the continuation procedure from turning back. For the first iteration of the procedure, it is replaced by a line of 1 so that the sum of the components of the tangent vector is imposed to be equal to 1. The prediction $\mathbf{y}_{(i+1)}^{(1)}$ is then constructed from the previous iteration as follows:

$$\mathbf{y}_{(i+1)}^{(1)} = \mathbf{y}_{(i)} + s_{(i)}\mathbf{t}_{(i)} \tag{1.51}$$

where $s_{(i)}$ is the predictor step size.

The second stage uses Newton's method to correct the prediction. Introducing new optimization variables $\mathbf{v}_{(i+1)}^{(j)}$ initialized as $\mathbf{v}_{(i+1)}^{(1)} = \mathbf{t}_{(i)}$, Moore-Penrose corrections are constructed as follows [38]:

$$\begin{aligned} \mathbf{y}_{(i+1)}^{(j+1)} &= \mathbf{y}_{(i+1)}^{(j)} + \Delta\mathbf{y}_{(i+1)}^{(j)} = \mathbf{y}_{(i+1)}^{(j)} - \mathbf{G}_{\mathbf{y}}^{-1}\left(\mathbf{y}_{(i+1)}^{(j)}, \mathbf{v}_{(i+1)}^{(j)}\right)\mathbf{G}\left(\mathbf{y}_{(i+1)}^{(j)}, \mathbf{v}_{(i+1)}^{(j)}\right) \\ \mathbf{v}_{(i+1)}^{(j)+1} &= \mathbf{v}_{(i+1)}^{(j)} + \Delta\mathbf{v}_{(i+1)}^{(j)} = \mathbf{v}_{(i+1)}^{(j)} - \mathbf{G}_{\mathbf{y}}^{-1}\left(\mathbf{y}_{(i+1)}^{(j)}, \mathbf{v}_{(i+1)}^{(j)}\right)\mathbf{R}\left(\mathbf{y}_{(i+1)}^{(j)}, \mathbf{v}_{(i+1)}^{(j)}\right) \end{aligned} \tag{1.52}$$

with

$$\begin{gathered} \mathbf{G}(\mathbf{y}, \mathbf{v}) = \begin{bmatrix} \mathbf{h}(\mathbf{y}) \\ \mathbf{0} \end{bmatrix}, \qquad \mathbf{G}_{\mathbf{y}}(\mathbf{y}, \mathbf{v}) = \begin{bmatrix} \mathbf{J}(\mathbf{y}) \\ \mathbf{v}^{\mathrm{T}} \end{bmatrix}, \\ \mathbf{R}(\mathbf{y}, \mathbf{v}) = \begin{bmatrix} \mathbf{J}(\mathbf{y})\,\mathbf{v} \\ \mathbf{0} \end{bmatrix} \end{gathered} \tag{1.53}$$

where subscripts and superscripts have been omitted for brevity.

A summary of the continuation procedure is proposed in Fig. 1.5.

When embedded in a continuation scheme, Hill's stability analysis can be efficiently performed, since $\mathbf{h}_{\mathbf{z}}$ is obtained as a by-product from the correction stage in Eqs. (1.52-1.53). Unstable and stable portions of the NFRC can be then distinguished, depending whether or not their solutions possess one or several Floquet exponents in the right side of the imaginary plane.

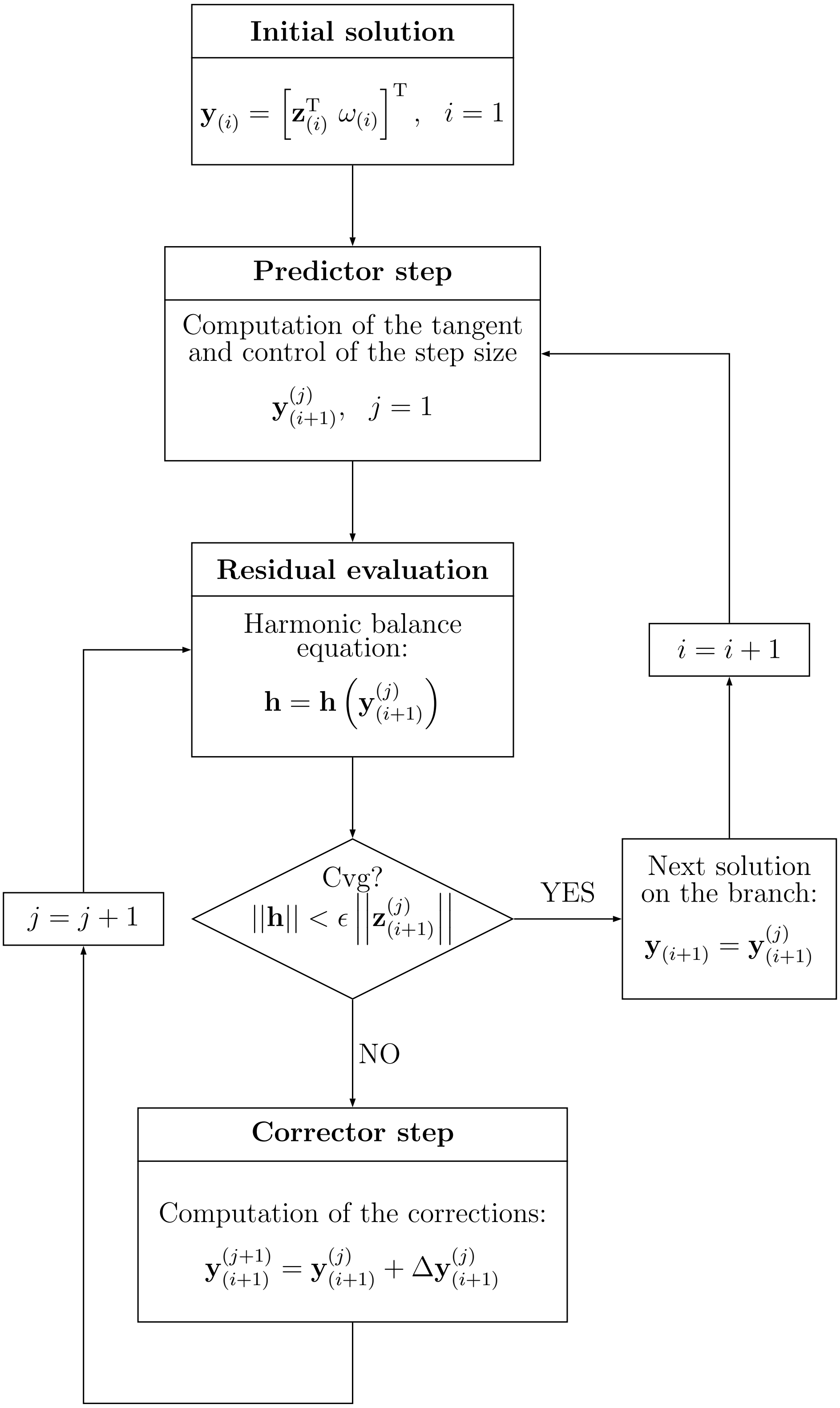

Figure 1.5: Algorithm for the continuation of periodic solutions.

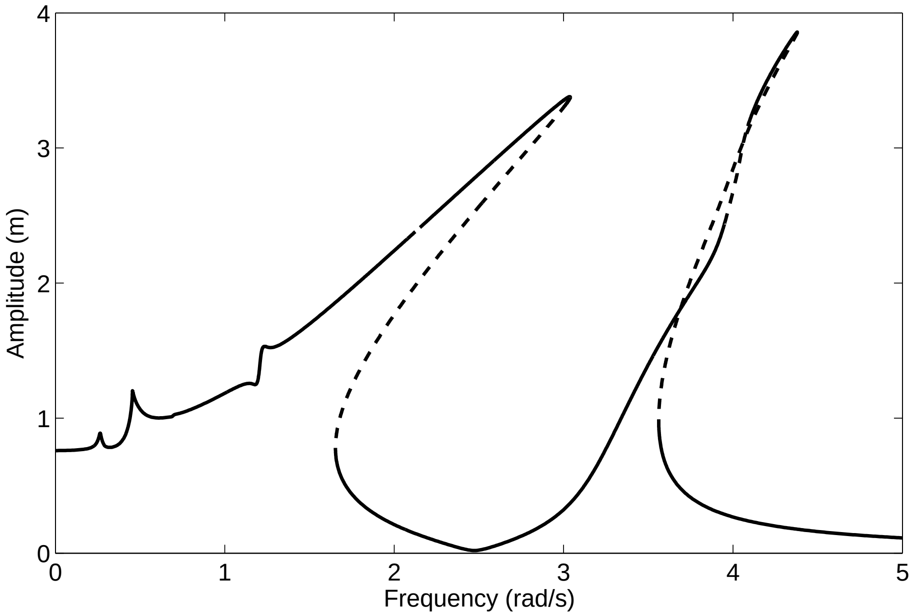

Figure 1.6: NRFC and stability analysis of the coupled Duffing system at $x_1$, for $f = 2\,\mathrm{N}$. Stable and unstable branches are represented with solid and dashed lines, respectively.

Fig. 1.6 shows the NFRC of the coupled Duffing system, computed for $N_H = 5$ and $N = 512$. It features two main peaks, related to fundamental resonances. Stability changes are observed at several locations.

The parameters related to the HB approximation strongly affect the quality of the NFRC, in particular the number of harmonics $N_H$ and the number of time samples $N$ considered in the Fourier operator $\mathbf{\Gamma}(\omega)$. Besides, if a large predictor step size $s_{(i)}$ allows for fast computation, it leads to a poor discretization of the branch. In order to overcome this tradeoff, a common practice consists in updating the step size at each continuation iteration $(i)$. The step size is controlled so that the corrector step requires on average the desirable number of iterations $I_{opt}$. At each step, the step size is updated according to the ratio between $I_{opt}$ and the previous number of iterations $I_{(i-1)}$ [144]:

$$s_{(i)} = \frac{I_{opt}}{I_{(i-1)}} s_{(i-1)} \tag{1.54}$$

Figs. 1.7(a-c) represent different portions of the NRFC of the coupled Duffing system, in the vicinity of the first resonance. Fig. 1.7(a) illustrates that a certain number of harmonics is required to accurately represent the NRFC. At low frequencies, several superharmonic resonances cannot be captured for $N_H = 1$ or 3. Precaution should be therefore taken when selecting the number of harmonics. A solution to this problem was proposed by Grolet *et al.* in [72], who automatically adapted the number of harmonics for each DOF during the continuation process. In Fig. 1.7(b), inaccuracies around the resonance peak are observed for low values of $N$, which can be explained by the aliasing effect. The parameter $I_{opt}$ for continuation is finally studied in Fig. 1.7(c), which depicts the truncation of the peak that occurs for higher values of $I_{opt}$.

### 1.3.2 Detection of Bifurcations

In theory, stability changes occur at particular points called *bifurcations*, which play a key role in the dynamics of nonlinear systems. In this section, codimension-1 bifurcations are of interest as only one parameter varies along the branch (*i.e.*, the forcing frequency $\omega$). Although a complete description of bifurcations and of their normal form is beyond the scope of this dissertation (see, *e.g.*, [107, 171] for a more complete treatment), the existence of three different bifurcation mechanisms can be pointed out, as illustrated in Fig. 1.8.

#### Singular Bifurcation Point

A singular point is detected when a Floquet multiplier leaves the unit circle along the real axis through +1 or, equivalently, when a Floquet exponent crosses the imaginary axis through 0 (see Figs. 1.8(a-b)). The term *singular* refers to the fact that at this point, the Jacobian matrix $\mathbf{h_z}$ is singular: if $\mathbf{h_z}$ is singular, then $\mathbf{B}$ in Eq. (1.46) is singular as well, which means that at least one Floquet exponent is 0.

There exist two families of singular bifurcations:

- Fold bifurcation (also called saddle node, limit point or turning point): the branch comes from one side and turns back, which means that the active parameter (*e.g.*, the frequency $\omega$) increases then decreases, or decreases then increases, along the branch. As a consequence, a fold bifurcation indicates the presence of two existing solutions in its vicinity, and often determines the lower or upper boundary of a bistable region. For a vibration problem, fold bifurcations are usually present in the vicinity of resonance peaks, which results in an amplitude jump in the response of the system to stepped-sine or swept-sine excitations.

- Bifurcation point (BP): two branches are connected. The two branches either meet and exchange stability (transcritical bifurcation), or one branch loses stability and a stable branch emanates from the point (pitchfork bifurcation).

From a mathematical viewpoint, fold bifurcations verify

$$\mathbf{h}_\omega \notin \mathrm{range}\left(\mathbf{h_z}\right) \tag{1.55}$$

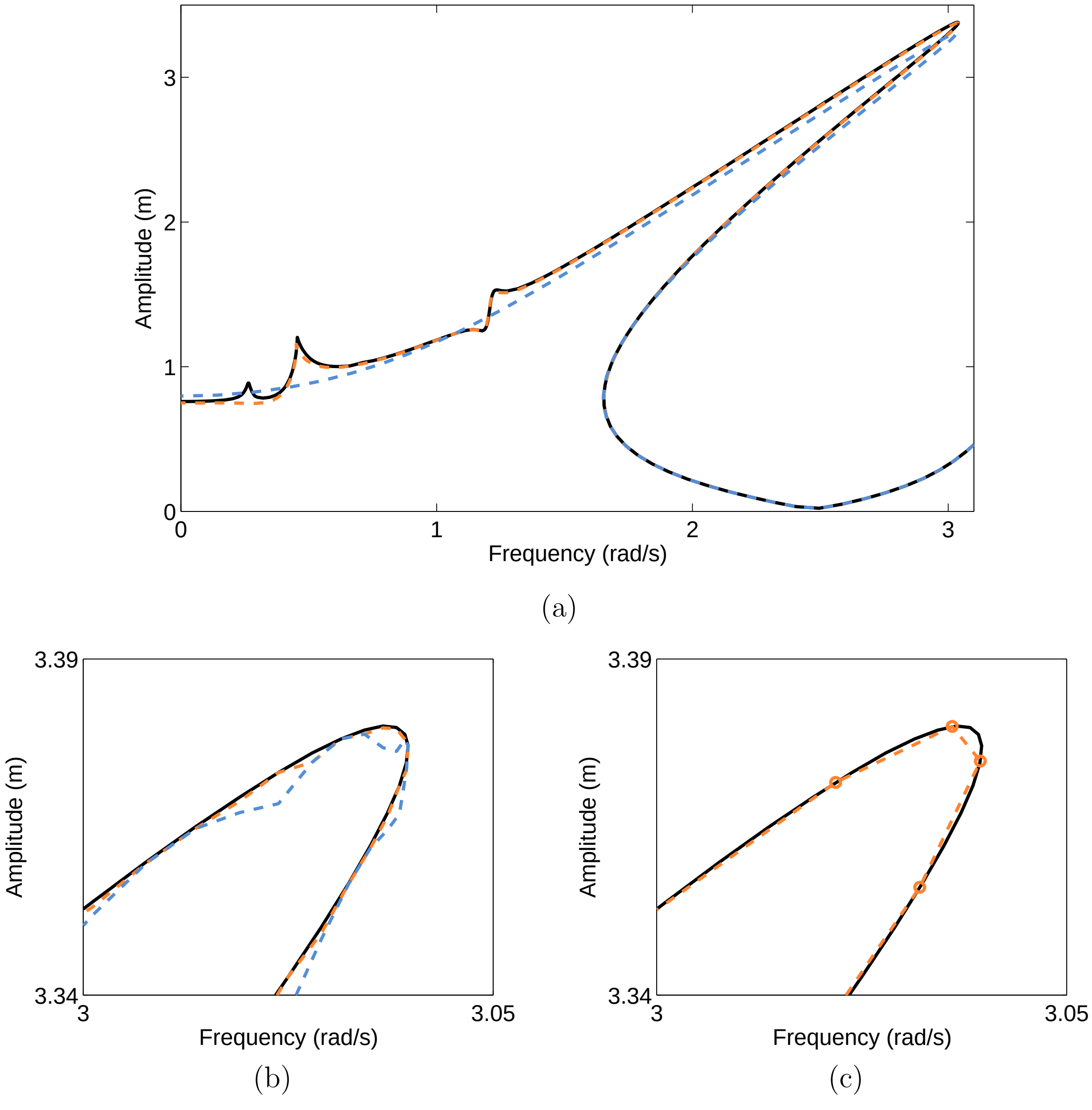

(a)

(b)

(c)

Figure 1.7: NFRC of the coupled Duffing system at $x_1$, for $f = 2\,\mathrm{N}$. Influence of the HB and continuation parameters for a reference configuration with $N_H = 5$, $N = 512$ and $I_{opt} = 3$ (in black). (a) $N_H = 3$ (in orange) and $N_H = 1$ (in blue). (b) $N = 128$ (in orange) and $N = 64$ (in blue). (c) $I_{opt} = 5$ (in orange).

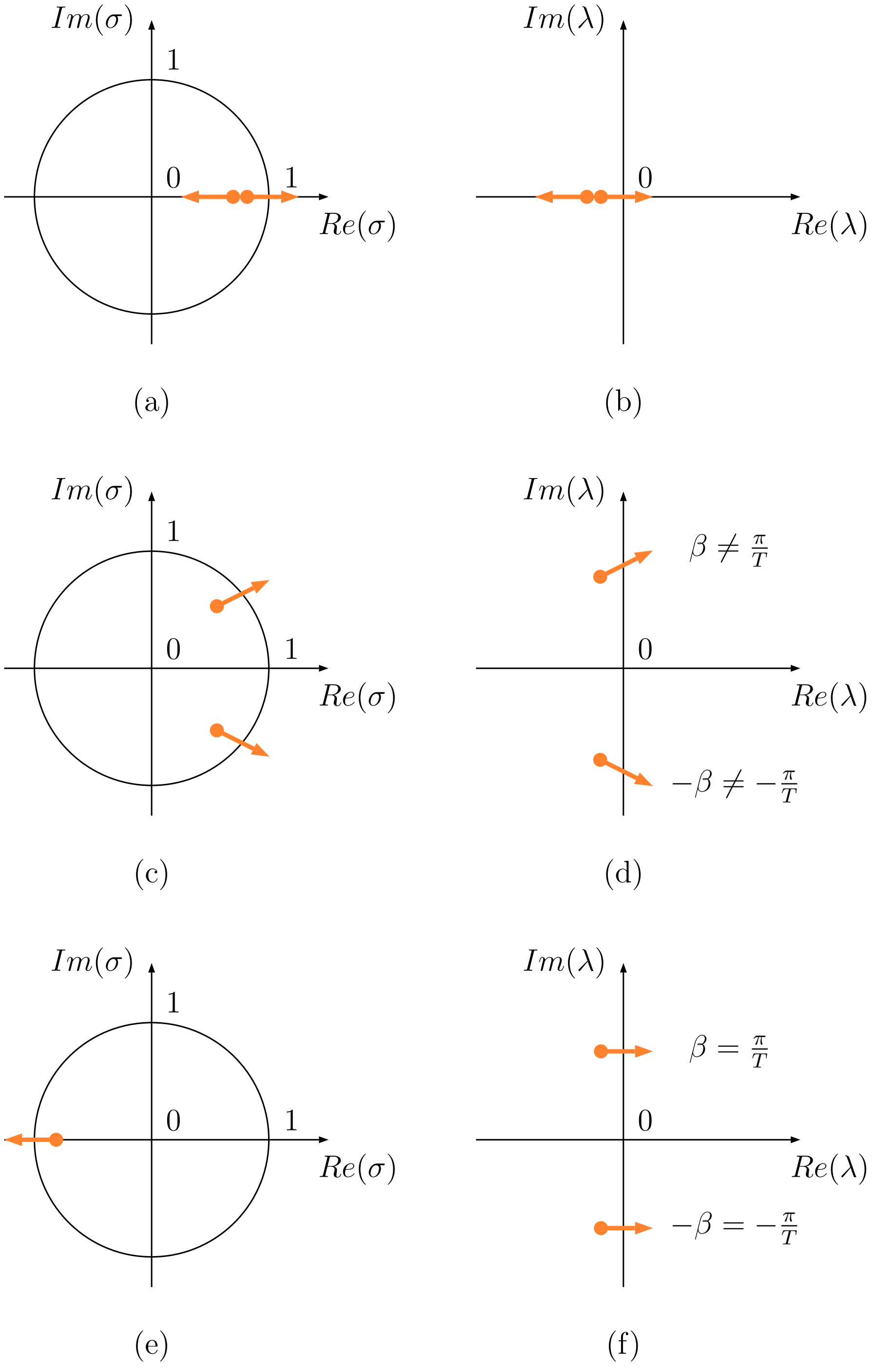

Figure 1.8: Mechanisms for the loss of stability of a periodic solution, illustrated with Floquet multipliers (left column) and Floquet exponents (right column). First row: singular point; second row: Neimark-Sacker bifurcation; third row: period doubling bifurcation.

whereas

$$\mathbf{h}_\omega \in \text{range}\left(\mathbf{h}_\mathbf{z}\right) \tag{1.56}$$

is true for BPs [171]. Fold bifurcations and BPs can then be distinguished by observing whether the attachment of $\mathbf{h}_\omega$ as an extra column to the Jacobian matrix $\mathbf{h}_\mathbf{z}$, *i.e.*, the construction of the extended Jacobian matrix $\mathbf{J}$ defined in Eq. (1.49), removes its singularity or not. More specifically, if the rank of the matrix is increased from $(2N_H + 1)\, n - 1$ to $(2N_H + 1)\, n$, then the singular point is a fold bifurcation. If the matrix built in Eq. (1.49) is still rank-deficient, then the singular point is a BP.

BPs bring another challenge to the continuation procedure, *i.e.*, the possibility to switch from one branch to the other. If no switching method is implemented, the continuation usually extends the same branch through the BP. In order to compute the second branch, the predictor step should be adapted. This relates to the problem of finding the two tangent directions at the BP, which has been discussed in the literature (see, *e.g.*, [19, 94]), and recently applied to turbomachinery [152].

### Neimark-Sacker Bifurcation

A Neimark-Sacker (NS) bifurcation (also called bifurcation into a torus or Hopf bifurcation) is detected when a pair of Floquet multipliers leaves the unit circle as complex conjugates or, equivalently, when a pair of Floquet exponent crosses the imaginary axis as complex conjugates through any value but $\pm\frac{i\pi}{T}$, where $T$ is the period of oscillation (see Fig. 1.8(c-d)).

At a NS bifurcation, another branch of solutions called *quasiperiodic* (QP) oscillations emanates. Along this new branch, the system oscillates with a combination of the forcing frequency $\omega$ and at least another frequency $\omega_2$. The frequencies $\omega$ and $\omega_2$ are incommensurate, which means that the ratio $\omega/\omega_2$ is irrational. The evolution of the envelope frequency $\omega_2$ is usually unknown and intrinsic to the system, in the exception of some cases where the forcing itself is QP [76, 119]. In the vicinity of the NS bifurcation however, the pulsation $\omega_2$ can be approximated by $\beta$, the imaginary part in absolute value of the pair of Floquet exponents (see Fig. 1.8(d)).

### Period Doubling Bifurcation

A period doubling (PD) bifurcation (also called flip bifurcation) is detected when a pair of Floquet multipliers leaves the unit circle along the real axis through $-1$ or, equivalently, when a pair of Floquet exponent crosses the imaginary axis as complex conjugates through $\pm\frac{i\pi}{T}$ (see Fig. 1.8(e-f)).

At a PD bifurcation, another branch of solution emanates, similarly to the scenario described for NS bifurcations. The new branch possesses periodic solutions, with a period doubled compared to the solutions of the original branch. When they appear in cascade, PD doubling bifurcations can lead to chaos [185].

### Test Functions for the Detection of Bifurcations

In order to detect bifurcations along a NFRC, we monitor *test functions* $\phi$ during the numerical continuation process. The roots of these test functions indicate the presence of bifurcations.

According to their algebraic definition, fold bifurcation and BPs are characterized by a rank deficiency of the Jacobian matrix $\mathbf{h}_{\mathbf{z}}$. A candidate for a common test function is therefore

$$\phi_{F,BP} = \det\left(\mathbf{h}_{\mathbf{z}}\right) \tag{1.57}$$

where $\det(\cdot)$ denotes the determinant of the matrix. In order to distinguish between fold and BPs, the rank deficiency of $\mathbf{J}$ in Eq. (1.49) can be exploited. As a consequence, a more dedicated test function for BPs is [67]

$$\phi_{BP} = \det\begin{pmatrix} \mathbf{h}_{\mathbf{z}} & \mathbf{h}_{\omega} \\ \multicolumn{2}{c}{\mathbf{t}^{\mathrm{T}}} \end{pmatrix} \tag{1.58}$$

While the test functions in Eqs. (1.57-1.58) build on the algebraic definitions of fold bifurcations and BPs, another test function for fold bifurcations and BPs based on Hill's method (see Eq. (1.47)), is

$$\phi_{F,BP} = \det\left(\tilde{\mathbf{B}}\right) \tag{1.59}$$

Bifurcations for which a pair of Floquet exponents crosses the imaginary axis as complex conjugates, *i.e.* NS and PD bifurcations, can be detected using the theory of the *bialternate product* of a matrix. The bialternate product $\mathbf{P}_{\odot}$ of a $m \times m$ matrix $\mathbf{P}$,

$$\mathbf{P}_{\odot} = 2\mathbf{P} \odot \mathbb{I}_m \tag{1.60}$$

is a matrix of dimension $m(m-1)/2$ constructed from the rearrangement of the components of $\mathbf{P}$ [68, 74]. The bialternate product has the property to be singular when two eigenvalues of $\mathbf{P}$, $\mu_1$ and $\mu_2$, are such that

$$\mu_1 + \mu_2 = 0 \tag{1.61}$$

which is true for two purely imaginary or real conjugates. For NS and PD bifurcations, when the test function

$$\phi_{NS,PD} = \det\left(\tilde{\mathbf{B}}_{\odot}\right) \tag{1.62}$$

goes through 0, the Floquet exponents should be controlled to select the correct type of bifurcation. For two purely imaginary conjugates, NS or PD bifurcations are detected.

Two real conjugates are associated with a *neutral saddle point*, which is not considered as a bifurcation and can be ignored [66].

For the detection of a NS or PD bifurcation, the computation of the eigenvalues $\tilde{\boldsymbol{\lambda}}$ could in principle be avoided by applying the bialternate product directly to matrix $\mathbf{B}$. However, $\mathbf{B}$ contains spurious eigenvalues, which might lead to erroneous bifurcation detections, as illustrated in Fig. 2.10(a) in Chapter 2. Moreover, as the size of the bialternate product of a matrix rapidly increases with its dimension, the manipulation of the $2n \times 2n$ matrix $\tilde{\mathbf{B}}$ is more efficient than the $(2N_H + 1)\, 2n \times (2N_H + 1)\, 2n$ matrix $\mathbf{B}$. The diagonal shape of $\tilde{\mathbf{B}}$ implies that $\tilde{\mathbf{B}}_{\odot}$ is also diagonal, which allows for a fast evaluation of its terms.

The test functions in Eqs. (1.57-1.62) involve determinants, which is computationally demanding for large-scale structures. To overcome this issue for fold bifurcations, a solution consists in considering the geometrical folding of the branch. A fold bifurcation is thereby detected when the $i_\omega$-th component of the tangent prediction $\mathbf{t}$ related to the active parameter $\omega$ changes sign [67]:

$$\phi_F = t_{i_\omega} \tag{1.63}$$

For BPs, NS and PD bifurcations, the so-called *bordering technique* can be employed to avoid the computation of determinants. This method replaces the evaluation of the determinant of a matrix $\mathbf{G}$ with the evaluation of a scalar function $g$ which vanishes at the same time as the determinant [19, 69]. The function $g$ is obtained by solving the bordered system

$$\begin{bmatrix} \mathbf{G} & \mathbf{p} \\ \mathbf{q}^* & 0 \end{bmatrix} \begin{bmatrix} \mathbf{w} \\ g \end{bmatrix} = \begin{bmatrix} \mathbf{0} \\ 1 \end{bmatrix} \tag{1.64}$$

where $(\cdot)^*$ denotes conjugate transpose, and vectors $\mathbf{p}$ and $\mathbf{q}$ can be arbitrarily fixed as long as they ensure the nonsingularity of the system in Eq. (1.64). When $\mathbf{G}$ is almost singular, $\mathbf{p}$ and $\mathbf{q}$ are chosen close to the null vectors of $\mathbf{G}^*$ and $\mathbf{G}$, respectively [19]. When constructed as in Eq. (1.64), $g$ is directly related to the determinant of $\mathbf{G}$, by Cramer's rule

$$g = \frac{\det \begin{pmatrix} \mathbf{G} & \mathbf{0} \\ \mathbf{q}^* & 1 \end{pmatrix}}{\det \begin{pmatrix} \mathbf{G} & \mathbf{p} \\ \mathbf{q}^* & 0 \end{pmatrix}} = \frac{\det(\mathbf{G})}{\det \begin{pmatrix} \mathbf{G} & \mathbf{p} \\ \mathbf{q}^* & 0 \end{pmatrix}} \tag{1.65}$$

Fig. 1.9 summarizes the methodology for bifurcation detection, when stability analysis is performed with Hill's method.

The bifurcations of the coupled Duffing system are studied in Fig. 1.10. In Fig. 1.10(a), fold bifurcations, BPs and NS bifurcations are detected along the branch, which is consistent with the scenarios for stability changes observed for the Floquet exponents. Fold bifurcations can be found, in particular, close to the two resonance peaks. A branch of periodic solutions emanate from the BPs, as depicted in 1.10(b). QP oscillations appear

1. Detection of fold bifurcations:

$$\phi_F = t_{i_\omega}$$

2. Detection of bifurcation points (BPs):

$$\phi_{BP} = g_{BP}$$

   from the bordering system in Eq. (1.64) with $\mathbf{G}_{BP} = \begin{bmatrix} \mathbf{h}_{\mathbf{z}} & \mathbf{h}_\omega \\ \multicolumn{2}{c}{\mathbf{t}^{\mathrm{T}}} \end{bmatrix}$.

3. Detection of Neimark-Sacker (NS) and period doubling (PD) bifurcations:

$$\phi_{NS,PD} = g_{NS,PD}$$

   from the bordering system in Eq. (1.64) with $\mathbf{G}_{NS,PD} = \tilde{\mathbf{B}}_{\odot}$.

   When $\phi_{NS,PD} = 0$, matrix $\tilde{\mathbf{B}}$ has $\mu_1$ and $\mu_2$ among its eigenvalues, with

$$\mu_1 + \mu_2 = 0$$

   - If $\mu_{1,2} = \pm i\beta$ with $\beta \neq \pi/T$, a NS bifurcation is detected.
   - If $\mu_{1,2} = \pm i\beta$ with $\beta = \pi/T$, a PD bifurcation is detected.
   - If $\mu_{1,2} = \pm\beta$ with $\beta \in \mathbb{R}_0$, a neutral saddle point is detected.

Figure 1.9: Test functions for the detection of codimension-1 bifurcations of NFRCs.

in the vicinity of the NS bifurcations, which is represented in Fig. 1.10(c) for a forcing frequency of $\omega = 4\,\mathrm{rad/s}$. Although this single QP oscillation is obtained through time integration, one should note that the spectral basis of the HB formalism can be extended to two or more incommensurate frequencies, in order to compute the branch of QP solutions between the bifurcations. For more details about the implementation, interested readers may refer to [146, 169] for systems with monoharmonic excitation, and [76, 119] for applications with bi-periodic excitations.

Test functions for fold bifurcation and BP are shown in Figs. 1.11 and 1.12, respectively. Fig. 1.11(c) confirms that the test function based on the determinant of $\mathbf{h_z}$ takes very large values compared to the last component of the predictor step in Fig. 1.11(b). It is also interesting to note that, in Fig. 1.11(b), the test function approaches zero but does not become negative in the vicinity of the superharmonic resonances. This behavior is due to the fact that the resonance peaks almost bend in this region. In Fig. 1.12, similar conclusions can be drawn regarding BPs, as the test function based on the bordering technique takes reasonable values while the test function based on the determinant in Eq. (1.58) does not.

## 1.4 Computation of Bifurcation Curves

Even if there exists a large body of literature on HB applied to nonlinear systems, very few studies attempted to use the method for localizing and tracking bifurcations in parameter space. In electrical engineering, bifurcation tracking limited to a single-harmonic approximation was carried out [110]. With the method developed by Piccardi, PD and fold curves can be obtained [154], together with conditions for codimension-2 bifurcations [155], but this procedure cannot describe NS bifurcations. Traversa *et al.* investigated a bifurcation tracking technique adapted to fold, PD and NS bifurcations [192] by appending to the HB equation system an equation which describes the considered bifurcations through the Floquet multipliers. However, the resolution of the extra equation with the secant method makes the implementation inefficient when the size of the system increases. In [203], Xie *et al.* applied the HB method to study bifurcations of rotating systems. The sensitivity of other points along NFRCs, *e.g.*, resonance peaks, was studied most often for design optimization purposes [42, 151].

Building a general framework for the localization and tracking of bifurcations starts with the construction of an *augmented system* [19], herein consisting of Eq. (1.21) to which one or several equations defining the detected bifurcation are appended. The choice of this extension is crucial as it directly affects the efficiency and robustness of the methodology. A first approach, using the so-called *standard augmented systems*, builds on eigenvectors to create a set of extra equations. Its coupling with the HB method was demonstrated in

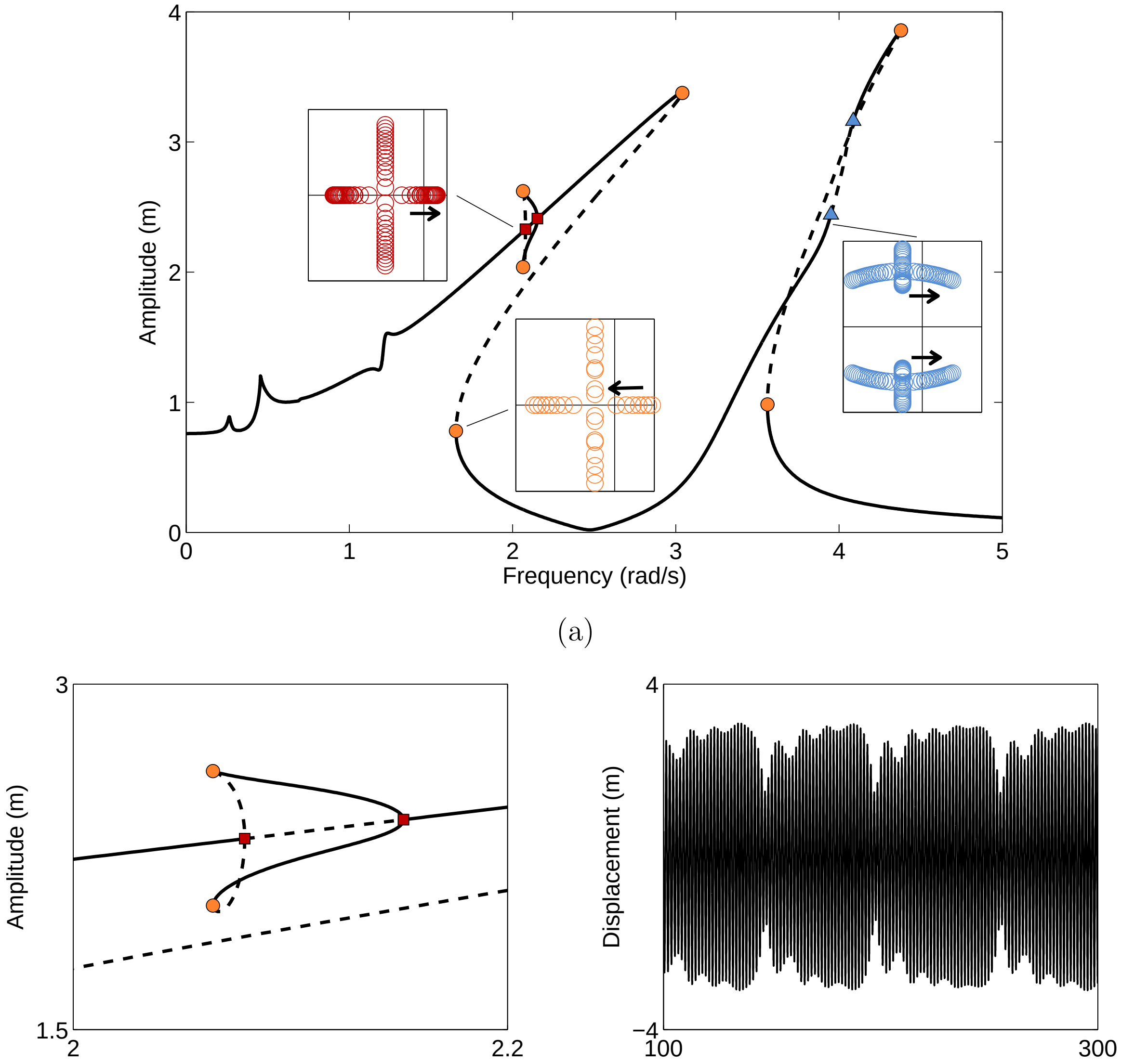

(a)

(b)

(c)

Figure 1.10: Bifurcation analysis of the coupled Duffing system at $x_1$, for $f = 2\,\mathrm{N}$. (a) Stable and unstable solutions are represented with solid and dashed lines. Fold bifurcations, BPs and NS bifurcations are represented with orange circle, red square and blue triangle markers, respectively. Insets display the evolution of Floquet exponents. (b) Close-up of the NRFC in the vicinity of the BPs and the emanating branch. (c) QP oscillations observed at $x_1$, for a forcing frequency of $\omega = 4\,\mathrm{rad/s}$.

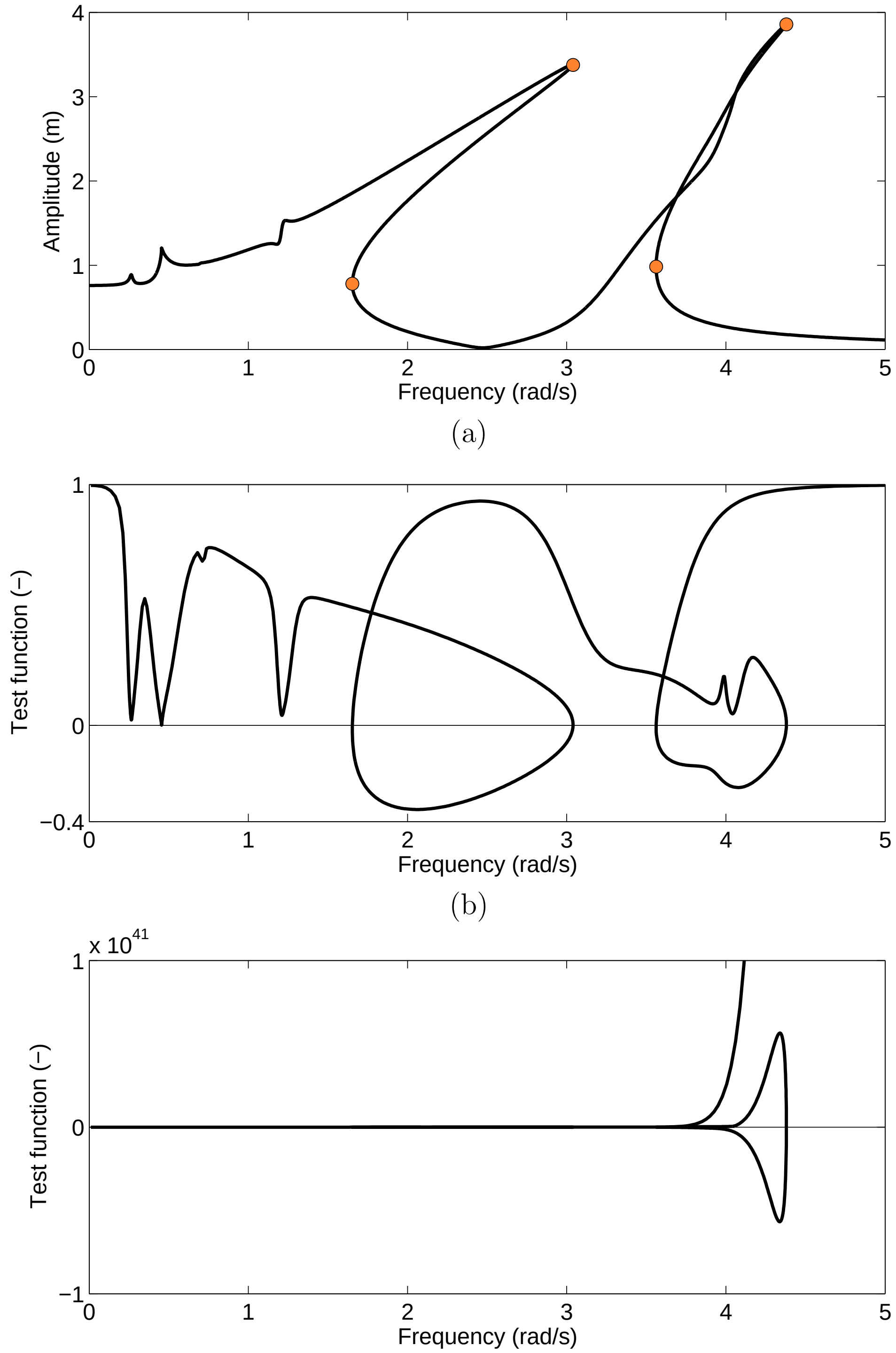

(a)

(b)

(c)

Figure 1.11: Test functions for fold bifurcation detection. (a) NRFC (black line) and fold bifurcations (orange circle markers); (b) test function based on the tangent vector; (c) test function based on the determinant.

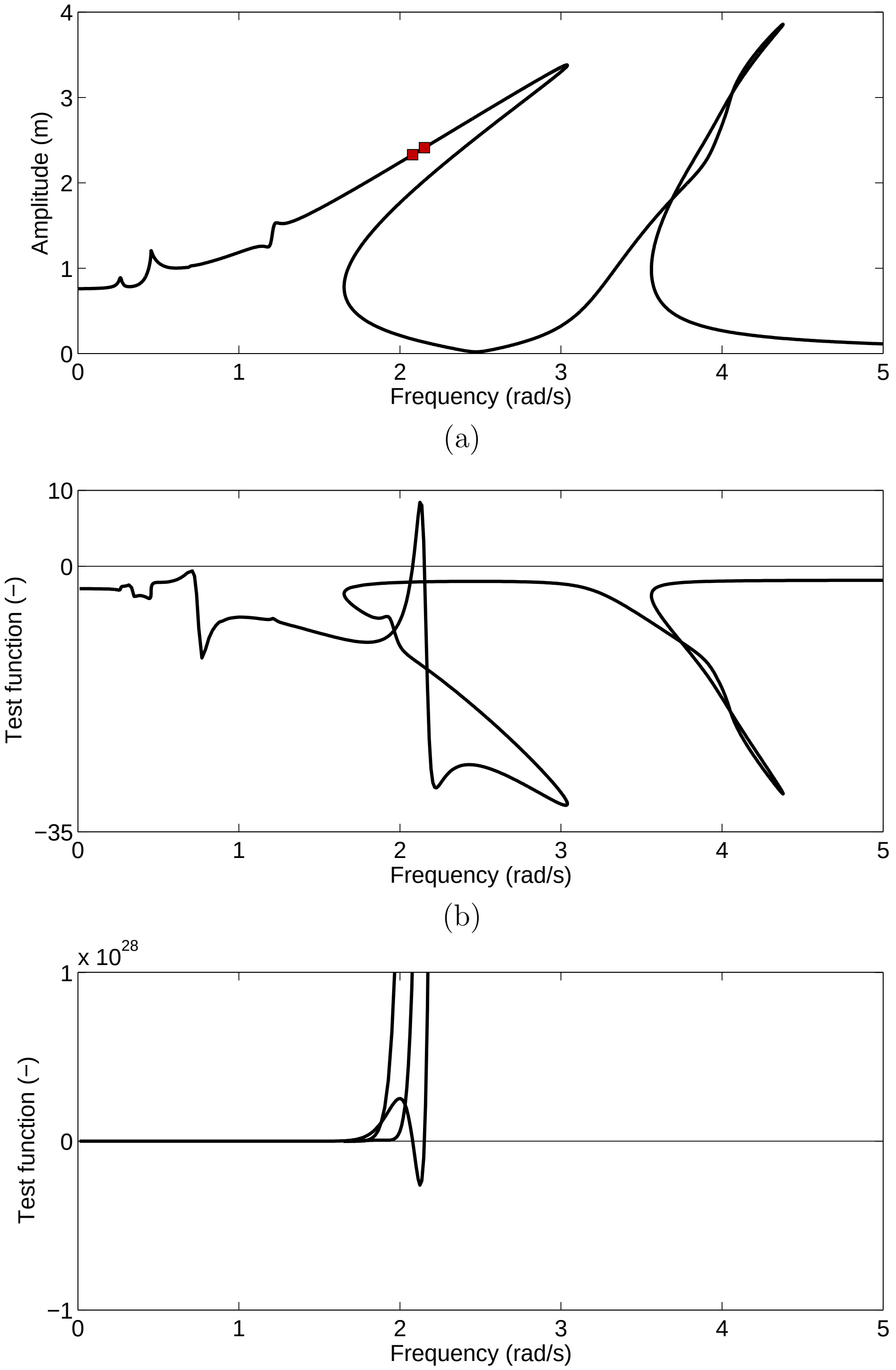

Figure 1.12: Test functions for BP detection. (a) NRFC (black line) and BP bifurcations (red square markers); (b) test function based on the bordering technique; (c) test function based on the determinant.

[202, 203]. Another approach consists in adding a single scalar equation to Eq. (1.21):

$$\mathbf{h}_{aug}\left(\mathbf{z},\omega,\kappa\right)=\left[\begin{array}{c}\mathbf{h}\left(\mathbf{z},\omega,\kappa\right)\\ \phi\left(\mathbf{z},\omega,\kappa\right)\end{array}\right]=\mathbf{0} \tag{1.66}$$

where $\kappa$ is the additional parameter for the tracking procedure. The system in Eq. (1.66) is referred to as a *minimally augmented system* [69]. By construction, minimally augmented systems involve much less unknowns than standard augmented systems.

The bordering technique is employed herein to define the extra equation in Eq. (1.66). For fold bifurcations and BPs, $\phi = g$ results from the resolution of the bordered system in Eq. (1.64) with $\mathbf{G} = \mathbf{h}_{\mathbf{z}}$. For NS and PD bifurcations, $\mathbf{G} = \tilde{\mathbf{B}}_{\odot}$ is considered in the bordered system. Applying the bordering technique may seem inefficient at first sight, as the extra equation hides the resolution of a bordered system. However, this resolution can be efficiently implemented, especially for the diagonal matrix $\tilde{\mathbf{B}}_{\odot}$. Besides, as for standard augmented systems [202], block elimination techniques can be used [69].

Once a bifurcation is detected along a NFRC, it can be localized by solving Eq. (1.66) where $\kappa$ is fixed to its original value, using a Newton-Raphson algorithm. In order to track the bifurcation in the codimension-2 parameter space, the continuation procedure presented in Section 1.3.1 needs to be updated to account for the additional equation describing the bifurcation, and the additional parameter $\kappa$. More specifically, the vectors $\mathbf{y}$ and $\mathbf{h}$, and the matrix $\mathbf{J}$ in Eqs. (1.48-1.53) have to be augmented as follows:

$$\mathbf{y}_{aug}=\left[\mathbf{z}^{\mathrm{T}}\ \omega\ \kappa\right]^{\mathrm{T}} \tag{1.67}$$

$$\mathbf{h}_{aug}=\left[\begin{array}{c}\mathbf{h}\left(\mathbf{y}_{aug}\right)\\ g\left(\mathbf{y}_{aug}\right)\end{array}\right] \tag{1.68}$$

$$\mathbf{J}\left(\mathbf{y}_{aug}\right)=\left[\begin{array}{ccc}\mathbf{h}_{\mathbf{z}}\left(\mathbf{y}_{aug}\right) & \mathbf{h}_{\omega}\left(\mathbf{y}_{aug}\right) & \mathbf{h}_{\kappa}\left(\mathbf{y}_{aug}\right)\\ \mathbf{g}_{\mathbf{z}}\left(\mathbf{y}_{aug}\right) & g_{\omega}\left(\mathbf{y}_{aug}\right) & g_{\kappa}\left(\mathbf{y}_{aug}\right)\end{array}\right] \tag{1.69}$$

where the subscripts $\mathbf{z}$, $\omega$ and $\kappa$ denote the derivation with respect to the components of $\mathbf{z}$, $\omega$ and $\kappa$, respectively.

In the Newton-Raphson algorithm for bifurcation localization, or in Eqs. (1.67-1.69) for bifurcation tracking, the computation of the derivatives of the additional equation is required. In that regard, the bordering technique is attractive, as analytical expressions can be formulated [69]. The derivatives of $g$ with respect to $\alpha$, where $\alpha$ denotes a component of $\mathbf{z}$ or one of the two active parameters $\omega$ or $\kappa$, are found as

$$g_{\alpha}=-\mathbf{v}^{*}\mathbf{G}_{\alpha}\mathbf{w} \tag{1.70}$$

where $\mathbf{G}_{\alpha}$ is the derivative of $\mathbf{G}$ with respect to $\alpha$, and where $\mathbf{w}$ and $\mathbf{v}$ come from the resolution of the bordered system and its transposed version:

$$\left[\begin{array}{cc}\mathbf{G} & \mathbf{p}\\ \mathbf{q}^{*} & 0\end{array}\right]\left[\begin{array}{c}\mathbf{w}\\ g\end{array}\right]=\left[\begin{array}{c}\mathbf{0}\\ 1\end{array}\right] \tag{1.71}$$

$$\begin{bmatrix} \mathbf{G} & \mathbf{p} \\ \mathbf{q}^* & 0 \end{bmatrix}^* \begin{bmatrix} \mathbf{v} \\ e \end{bmatrix} = \begin{bmatrix} \mathbf{0} \\ 1 \end{bmatrix} \tag{1.72}$$

As a result, the only term that has to be evaluated is $\mathbf{G}_\alpha$. For fold bifurcations and BPs,

$$\mathbf{G}_\alpha = \mathbf{h}_{z\alpha} \tag{1.73}$$

where $\mathbf{h}_{z\alpha}$ is the derivative of the Jacobian $\mathbf{h}_\mathbf{z}$ with respect to $\alpha$, which we compute through finite differences.

For NS and PD bifurcations, the properties of bialternate products allow to write [68]

$$\mathbf{G}_\alpha = \frac{\partial}{\partial\alpha}\left(\tilde{\mathbf{B}}_\odot\right) = \left(\frac{\partial}{\partial\alpha}\left(\tilde{\mathbf{B}}\right)\right)_\odot = \begin{bmatrix} \frac{\partial\tilde{\lambda}_1}{\partial\alpha} & & & \\ & \frac{\partial\tilde{\lambda}_2}{\partial\alpha} & & \\ & & \ddots & \\ & & & \frac{\partial\tilde{\lambda}_{2n}}{\partial\alpha} \end{bmatrix}_\odot \tag{1.74}$$

Finite differences can be used to compute the derivatives of the Floquet exponents. However, this means that the eigenvalues of matrix $\mathbf{B}$ in Eq. (1.46) have to be computed for each perturbation of the components of $\mathbf{z}$, and for the perturbation of the two continuation parameters. This represents a total of $n\left(2N_H+1\right)+2$ resolutions of the eigenvalue problem to construct $\mathbf{J}_{aug}$, which is cumbersome for large systems. Instead, we propose to compute the derivatives using the properties of eigenvalue derivatives discussed by Van der Aa *et al.* in [1]:

$$\frac{\partial\tilde{\lambda}_i}{\partial\alpha} = \left(\mathbf{\Lambda}^{-1}\frac{\partial\mathbf{B}}{\partial\alpha}\mathbf{\Lambda}\right)_{(\xi_i,\xi_i)} \tag{1.75}$$

where $\mathbf{\Lambda}$ is the eigenvector matrix of $\mathbf{B}$, and $\boldsymbol{\xi}$ is the localization vector containing the index of the $2n$ Floquet exponents $\tilde{\boldsymbol{\lambda}}$ among the eigenvalues $\boldsymbol{\lambda}$, *i.e.*, $\tilde{\lambda}_i = \lambda_{\xi_i}$. An analytical expression relating the derivative of $\mathbf{B}$ with respect to $\alpha$ in function of $\mathbf{h}_{z\alpha}$ can then be obtained from Eq. (1.46).

Eq. (1.75) holds as long as there are no repeated eigenvalues, which is verified for most situations except when a pair of complex conjugate turns into a pair of real eigenvalues (see Fig. 1.10). Since the transition occurs very quickly, it is reasonable to assume that Eq. (1.75) is valid. For other scenarios with repeated eigenvalues, expressions for the derivatives can be found in [1].

The evaluation of the $\left(2N_H+1\right)n+2$ terms $g_\alpha$ represents the main burden of the method when there is a large number of nonlinear DOFs. In this case, parallel computing could help reduce the computational cost of the algorithm. For structures with few localized nonlinearities, one can take advantage of the fact that $\mathbf{h}_{z\alpha}$ is a null matrix when $\alpha$ corresponds to Fourier coefficients of linear DOFs.

Fig. 1.13 illustrates the methodology for bifurcation tracking, in a codimension-2 parameter space with the forcing frequency $\omega$ and the nonlinear stiffness $\mu$. The bifurcation curves are accompanied with NFRCs computed for several values of $\mu$. In Fig. 1.13(a), while the other bifurcations evolve smoothly, the fold bifurcation located near the second resonance peak exhibits a more complex trajectory. This behavior can be related to the presence of an isolated response curve, an interesting dynamical phenomenon discussed in the next chapters. Fig. 1.13(b) shows that lowering the value of $\mu$ leads to the elimination of the NS bifurcations.

## 1.5 Computation of Nonlinear Normal Modes

Besides the study of forced responses, a common practice in engineering consists in examining vibrating systems through their modal features. More specifically, the study of the underlying undamped and unforced system is sought. In this section, the generalization of modal analysis to nonlinear structures using the outlined HB formalism is introduced.

### 1.5.1 The Concept of Nonlinear Normal Modes

The concept of a normal mode is central in the theory of linear vibrating systems. In addition to their obvious physical interpretation, the linear normal modes (LNMs) have interesting mathematical properties. They can be used to decouple the governing equations of motion; *i.e.*, a linear system vibrates as if it were made of independent oscillators governed by the eigensolutions. The invariance property of LNMs and the modal superposition directly result from this decoupling. In addition, LNMs are relevant dynamical features that can be exploited for various purposes including model reduction (*e.g.*, substructuring techniques [14]), experimental modal analysis [53], finite element model updating [56] and structural health monitoring [40].

Any attempt to apply traditional linear analysis to nonlinear systems results, at best, in a suboptimal design. In this context, nonlinear normal modes (NNMs) offer a solid theoretical tool for interpreting a wide class of nonlinear dynamical phenomena, yet they have a clear conceptual relation to the LNMs. During the normal mode motion of a linear conservative system, each system component moves with the same frequency and with a fixed ratio amongst the displacements of the components. Targeting a straightforward nonlinear extension of the LNM concept, Rosenberg defined an NNM as a vibration in unison of the systems, *i.e.*, a synchronous oscillation [165]. This definition requires that all material points of the system reach their extreme values and pass through zero simultaneously, and allows all displacements to be expressed in terms of a single reference displacement. Kerschen *et al.* recently extended Rosenberg's definition of NNMs to (non-necessarily synchronous) periodic motions of the system [98]. Shaw and Pierre proposed a generalization of Rosenberg's definition that provides a direct and elegant extension of the NNM concept to damped systems [174]. Their geometric-based definition of an NNM as a two-dimensional invariant manifold in phase space was later exploited in [161].

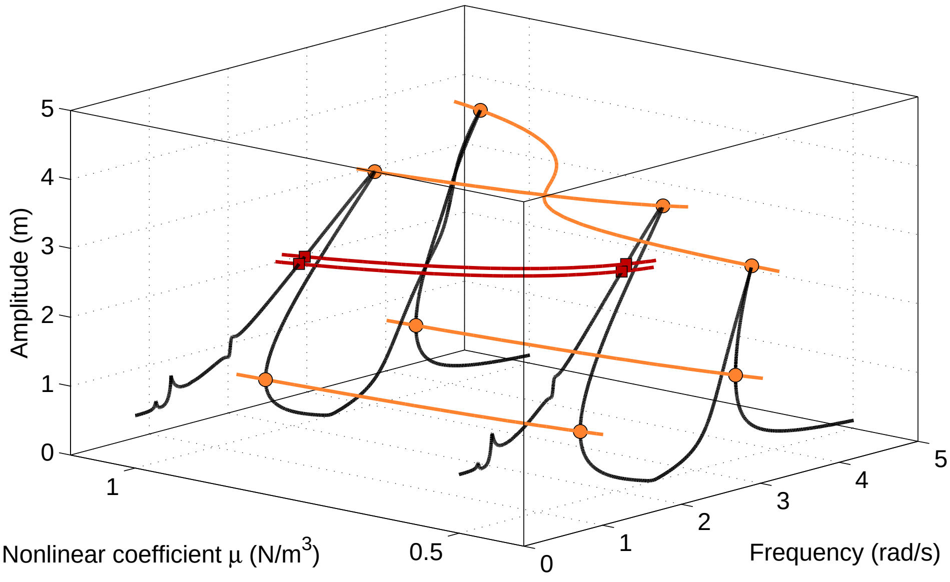

(a)

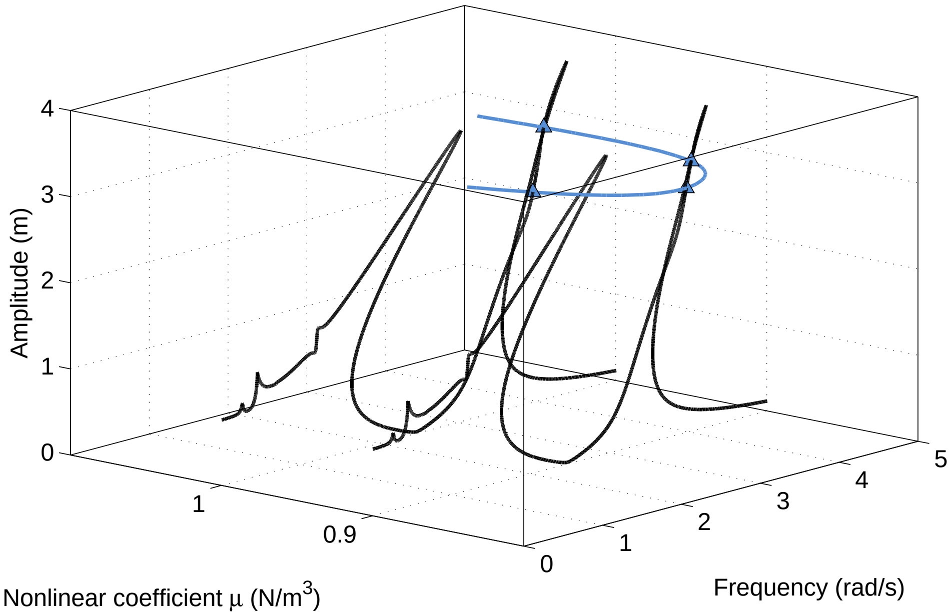

(b)

Figure 1.13: Bifurcation tracking of the coupled Duffing system for $f = 2\,\mathrm{N}$, with respect to the forcing frequency $\omega$ and the nonlinear stiffness $\mu$. (a) NRFCs computed for $\mu = 1$ and $\mu = 0.5$, branches of fold bifurcations (in orange) and BPs (in red). (b) NRFCs computed for $\mu = 1$ and $\mu = 0.9$, and branch of NS bifurcations (in blue).

The main appealing features of the NNMs are that they are capable of handling strongly nonlinear regimes of motion and that they have the potential to address the individualistic nature of nonlinear systems. Moreover, their fundamental properties directly capture some features of nonlinear systems [98]:

1. **Frequency-energy dependence**
   A peculiar property of nonlinear systems is the frequency-energy dependence of their oscillations, *e.g.*, through hardening or softening behaviors. The evolution of NNMs along their backbone accounts for this dependence, as illustrated in Section 1.5.2. In some cases, the evolution of the modal properties results in the localization phenomenon, where vibration energy gets localized in a specific part of the structure.
2. **Internal resonances**
   During a general motion of the system, NNMs may interact. In the presence of these interactions, NNMs with well-separated fundamental frequencies can exchange energy. This coupling between NNMs will be discussed in Chapters 2 and 3.
3. **Relations with forced responses**
   For structures with low damping, the NNM backbone traces the locus of the resonance peaks. Chapter 3 will be devoted to the relations between NNMs and resonances.

A large body of literature has addressed the qualitative and quantitative analysis of nonlinear phenomena using NNMs (see, *e.g.*, [90, 122, 130, 190]). Through various applications, NNMs have served several purposes. For instance, NNM theory was used for the study of nonlinear absorbers (see, *e.g.*, [96]). In [43, 44], Dou *et al.* built on NNMs to optimize the dynamical features of nonlinear structures. A strategy based on NNMs was proposed in [104] for the convergence of reduced-order models. In aeroelasticity, the evolution of limit cycle oscillations was predicted with NNMs [51]. For a more comprehensive review of the applications of NNMs, interested readers may refer to [11].

### 1.5.2 Implementation with the HB Method

The extended definition of NNMs [98] is particularly attractive when targeting a numerical computation of the NNMs, as it enables the use of algorithms for the continuation of periodic solutions [162]. Some of the techniques introduced in Section 1.2, *e.g.*, the shooting and harmonic balance methods, have therefore proved useful in this context. In particular, the computation of NNMs and of their interactions could be substantially improved thanks to the natural filtering property of the HB approximation [100, 124]. Nonlinear Fourier-based modal analysis was also adapted to non-conservative autonomous dynamical systems thanks to generalized Fourier series with slow and fast time scales [101, 112].

The computation of NNMs amounts to finding periodic solutions of the underlying Hamiltonian structure

$$\mathbf{M}\ddot{\mathbf{x}} + \mathbf{K}\mathbf{x} + \mathbf{f}_{nl}(\mathbf{x}) = \mathbf{0} \tag{1.76}$$

To this end, a HB formalism similar to that presented in Section 1.2.1 is applied, where damping and externel forces are removed, which yields

$$\mathbf{h}_{ham}\left(\mathbf{z}, \omega\right) = \left(\boldsymbol{\nabla}^2 \otimes \mathbf{M}\right)\mathbf{z} + \left(\mathbb{I}_{2N_H+1} \otimes \mathbf{K}\right)\mathbf{z} + \mathbf{b}_{nl} = \mathbf{0} \tag{1.77}$$

where $\mathbf{b}_{nl}$ is the vector of the Fourier coefficients of the nonlinear forces, defined as

$$\mathbf{f}_{nl}(\mathbf{x}) = \left(\mathbf{Q}(t) \otimes \mathbb{I}_n\right)\mathbf{b}_{nl} \tag{1.78}$$

However, the problem is not well-posed: if $\mathbf{x}(t)$ is a periodic solution verifying Eq. (1.76), then $\mathbf{x}(t+T)$ is a solution as well. In order to remove this indeterminacy, the phase of the solutions has to be prescribed, with the help of a phase condition [129, 171]. Most phase conditions impose one of the unknowns to be set to 0, *e.g.*, for time-domain methods, the initial displacement or velocity of a DOF [144] and, for frequency-domain methods, the Fourier coefficient of a DOF [93]. In this manuscript, the latter condition is employed which, in addition to Eq. (1.77), yields the equation of a NNM motion:

$$\mathbf{h}_{NNM} = \begin{bmatrix} \mathbf{h}_{ham}\left(\mathbf{z}, \omega\right) \\ z_i \end{bmatrix} = \mathbf{0} \tag{1.79}$$

where $z_i$ is a component of $\mathbf{z}$.

In its current formulation, $\mathbf{h}_{NNM} : \mathbb{R}^{(2N_H+1)n+1} \to \mathbb{R}^{(2N_H+1)n+1}$ is not compatible with the continuation procedure, as the matrices to invert in Eq. (1.52) are not square. A first solution consists in solving these overdetermined equations using Moore-Penrose pseudoinverse [144]. A more elegant approach recasts the system into a square problem, by adding an artificial damping parameter $d$ in the equations of motion [126]:

$$\mathbf{M}\ddot{\mathbf{x}} + d\mathbf{C}\dot{\mathbf{x}} + \mathbf{K}\mathbf{x} + \mathbf{f}_{nl}(\mathbf{x}) = \mathbf{0} \tag{1.80}$$

Although the system in Eq. (1.80) is not conservative, a branch of periodic solutions can be computed and the parameter $d$ will naturally appear equal to zero in the continuation process.

The in-phase and out-of-phase NNMs of the coupled Duffing system computed using the outlined procedure are shown in Fig. 1.14. Fig. 1.14(a) depicts the two branches of NNMs in the so-called frequency-energy plot. The evolution of the natural frequencies is represented with respect to the total energy in the system, *i.e.*, the potential and kinetic energy that is conserved throughout the periodic oscillation. At low energy, the nonlinear forces are negligible and the frequency of the NNMs is close to the linear frequency. As energy increases, however, a clear hardening of the structure can be noticed, which is explained by the presence of the two hardening Duffing oscillators. The NNM motions

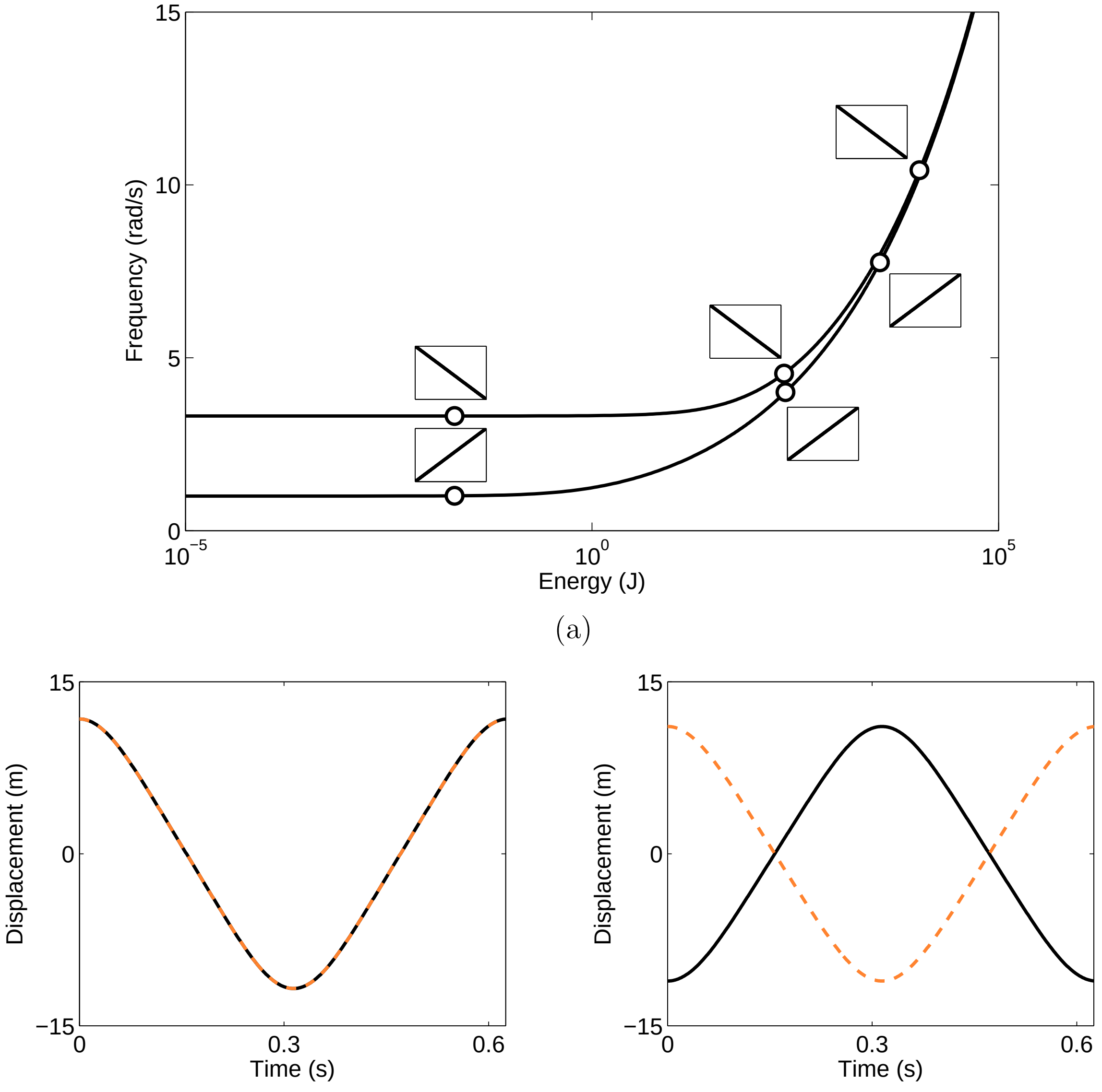

(a)

(b)

(c)

Figure 1.14: NNMs of the coupled Duffing system. (a) Frequency-energy plot. NNM motions depicted in the configuration space are inset; (b) in-phase NNM computed at a frequency $\omega = 10\,\mathrm{rad/s}$; (c) out-of-phase NNM computed at a frequency $\omega = 10\,\mathrm{rad/s}$. The displacements $x_1$ and $x_2$ are represented with solid black and dashed orange lines, respectively.

in Fig. 1.14(a) show that the in-phase and out-of-phase vibrations are conserved at high energy levels, which is also confirmed in Figs. 1.14(b) and (c).

Stability analysis can also be applied to NNMs through Hill's method, with the procedure described in Section 1.2.3. A NNM is stable if all Floquet exponents are located along the imaginary axis, and is unstable otherwise. A difference between a forced periodic response and a NNM lies in the fact that, for the latter, there is always a pair of Floquet exponents located at 0. Similarly to the forced and damped case, stability changes occur through bifurcations, *e.g.*, through fold or symmetry-breaking bifurcations [144]. Stability and bifurcations of NNMs are not investigated in this manuscript, but one should note that the bifurcation detection and tracking methodology presented for NFRCs should be adapted, due to the presence of the pair of Floquet exponents at 0.

## 1.6 Concluding Remarks

The main contribution of this chapter was to propose a harmonic balance formalism for the computation of periodic solutions of nonlinear systems, including their stability and bifurcations. The proposed methodology relies on Hill's method and Floquet exponents, and is coupled to a continuation algorithm in order to trace out nonlinear frequency response curves, the nonlinear normal mode backbones and bifurcation curves.

Particular attention was devoted to the computational efficiency of the algorithm, which motivated the use of bordering techniques and the development of a new procedure for tracking Neimark-Sacker bifurcations based on eigenvalue derivatives. If the dynamics can be modeled with a relatively low number of harmonics, as it is the case for all applications investigated in this thesis, Hill's method is very advantageous for stability and bifurcation analyses. If more harmonics are needed, solving the resulting eigenvalue problem can substantially increase the computational burden; the computation of the monodromy matrix through time integrations is then an efficient alternative.

Thanks to the developed algorithm, bifurcation and modal analyses of large-scale engineering structures with localized nonlinearities is within reach. The real-world spacecraft structure in Chapter 2 serves to demonstrate the capabilities of our method.

# Chapter 2

# Bifurcation and Modal Analysis of a Spacecraft Structure

**Abstract**

This second chapter carries out bifurcation and modal analysis of a real-world spacecraft structure using the harmonic balance method developed in Chapter 1. The computation of nonlinear normal modes and bifurcations reveals that the satellite possesses complex dynamics including modal interactions, mode localization, isolated resonances and quasiperiodic oscillations. Bifurcation tracking is then used to illustrate how the quasiperiodic oscillations can be completely eliminated. This chapter also adopts a wider perspective by discussing the importance of bifurcation and modal analysis in the complete design cycle of engineering structures.

## 2.1 Introduction

To thoroughly investigate the intrinsic features of real-world structures vibrating in nonlinear regimes of motion, the nonlinear analysis framework presented in Fig. 2.1 is adopted in this chapter. It builds on several successive steps:

1. **Measure:**
   The measurement campaign usually serves two purposes. First, experimental data are used to reveal nonlinear behaviors or to confirm their presence. The second objective is to acquire experimental data sets for the identification step. Because the response of a nonlinear system does not scale with the amplitude of the input, data should be measured at several excitation levels. While data obtained at low level may help study the underlying linear model, data at high level usually capture nonlinearities more accurately.

2. **Identify a nonlinear model:**
   During this step, a nonlinear model of the structure that possesses good predictive capability is sought. The nonlinearities are first identified from the experimental data using techniques such as the restoring force surface (RFS) method [121], the reverse path method [125] or nonlinear subspace identification [131]. The nonlinearities are then introduced in an updated finite element model that describes the underlying linear structure.

3. **Understand and uncover nonlinear phenomena:**
   The identified model is exploited for understanding the dynamics observed experimentally but also for uncovering nonlinear phenomena that could have been missed during the test campaign. Direct time integration methods can be used, such as Runge-Kutta or Newmark schemes [61], but we propose to exploit the bifurcation and modal analysis methodology developed in Chapter 1 for an easier and more thorough interpretation.

4. **Improve the structural design:**
   From the observations made during the previous step, the structural analyst can precisely quantify the impact of nonlinearities. If design modifications are necessary to achieve the requested system performance, we propose to utilize bifurcation tracking for the update of selected design parameters.

The outlined design methodology is demonstrated in this chapter using a spacecraft structure, whose description is provided in Section 2.2. In Section 2.3, experimental data are analyzed to assess the nonlinear behavior of the structure. The identification of a numerical model is then described in Section 2.4. Based on this model and on the continuation tools developed in Chapter 1, Sections 2.5 and 2.6 study the nonlinear normal modes and the bifurcation curves of the system, respectively. In Section 2.7, bifurcation tracking is employed to improve the design of the spacecraft. In Sections 2.5, 2.6 and 2.7, a particular

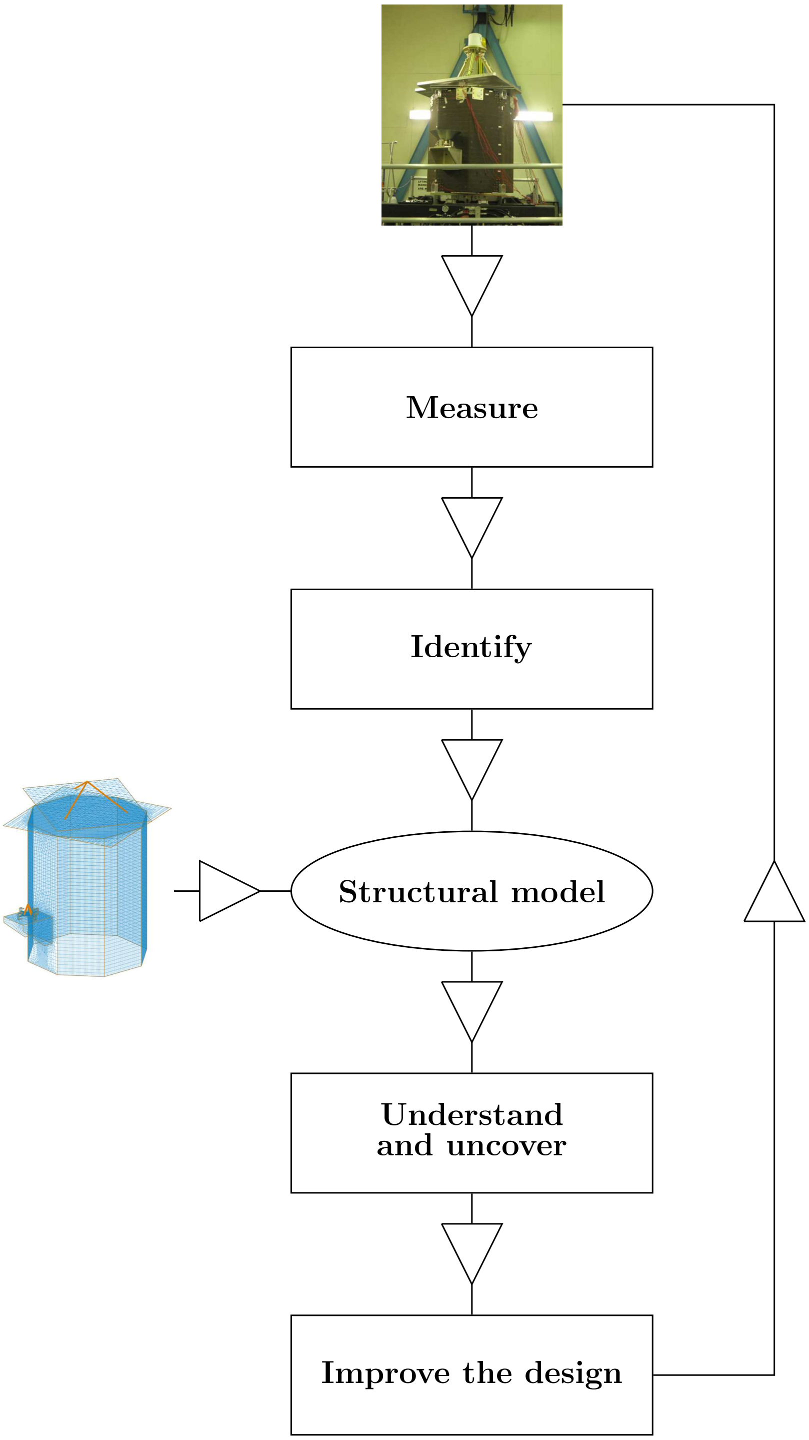

Figure 2.1: Design cycle of nonlinear engineering structures, from measurements to design.

attention is given to the computational performance of harmonic balance (HB) and of the bifurcation tools. Finally, the conclusions of the chapter are drawn in Section 2.8.

## 2.2 Description of the SmallSat Spacecraft

The SmallSat structure was conceived by EADS-Astrium (now Airbus Defence and Space) as a low-cost platform for small satellites in low earth orbits [166]. It is a monocoque tube structure which is 1.2 m in height and 1 m in width. It is composed of eight flat faces for equipment mounting purposes, creating an octagon shape. The spacecraft structure supports a dummy telescope mounted on a baseplate through a tripod. A prototype of the spacecraft is represented in Fig. 2.2(a).

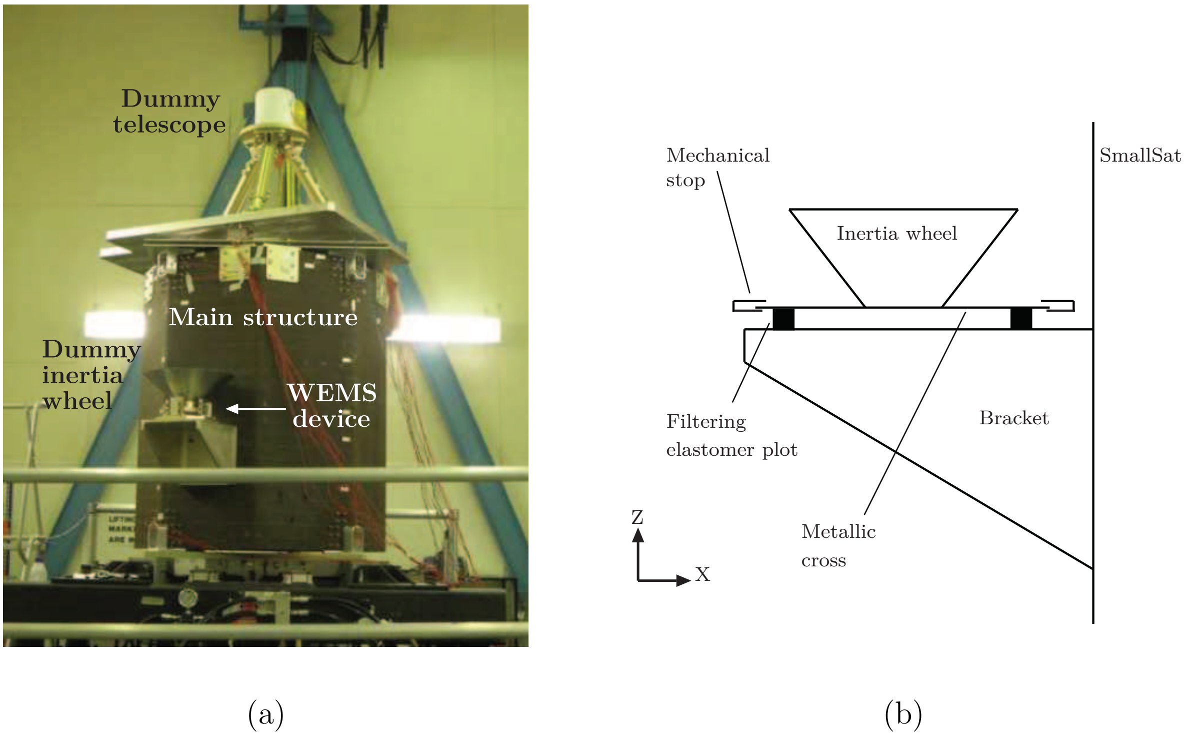

(a) (b)

Figure 2.2: SmallSat spacecraft. (a) Photograph; (b) schematic of the WEMS, the nonlinear vibration isolation device.

As depicted in Fig. 2.2(b), a support bracket connects to one of the eight walls the so-called *wheel elastomer mounting system* (WEMS) which is loaded with an 8-kg dummy inertia wheel. The WEMS acts as a mechanical filter which mitigates high-frequency disturbances coming from the inertia wheel through the presence of a soft elastomeric interface between its mobile part, *i.e.*, the inertia wheel and a supporting metallic cross, and its fixed part, *i.e.*, the bracket and by extension the spacecraft. Moreover, the WEMS incorporates eight mechanical stops, covered with a thin layer of elastomer to prevent metal-metal impacts, and designed to limit the axial and lateral motions of the inertia wheel during launch. The mechanical stops account for 4 localized nonlinear connections (NC), with axial and lateral components for each NC, and give rise to the strongly nonlinear dynamical phenomena that will be studied in this chapter.

## 2.3 Vibration Test Campaign

The experimental data sets analyzed in this section were acquired during a test campaign carried out by Airbus Defence and Space, Siemens-LMS and the University of Liège in Stevenage, UK. It consisted of a series of swept-sine base excitations applied to the structure for different sweep rates and directions. Fig. 2.3 displays the raw acceleration time histories measured vertically on the instrument panel at 0.1 g and 1 g levels. For confidentiality reasons, clearances and displacements are given through dimensionless quantities throughout the chapter.

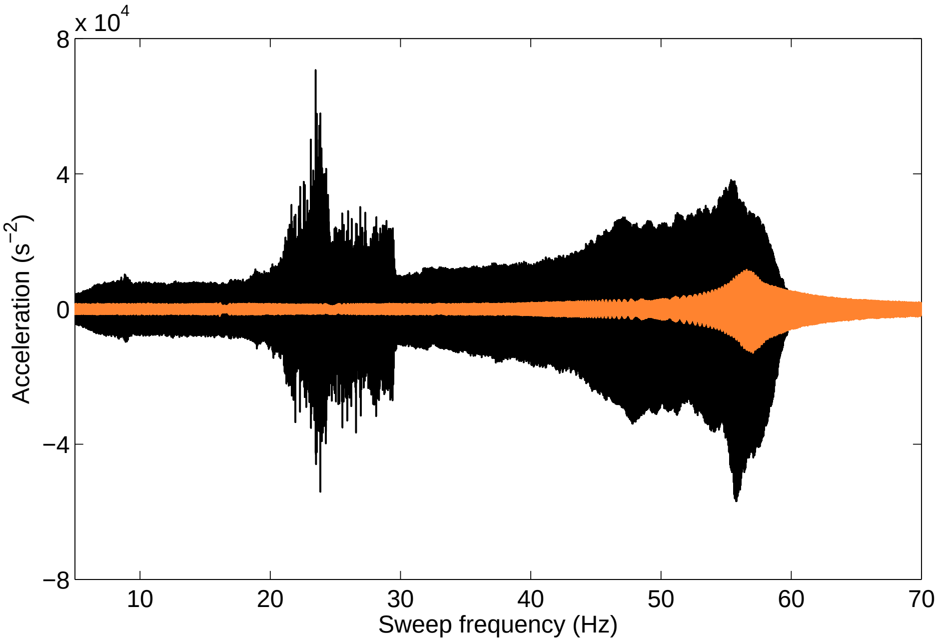

Figure 2.3: Raw acceleration time histories measured on the instrumental panel at 0.1 g (in orange) and 1 g (in black) base excitation levels, obtained for a frequency sweep up [134].

At 0.1 g, the response at the instrument panel presents a single resonance, located around 56 Hz, which is assumed linear in view of the low level of the excitation. At 1 g, this resonance is slightly shifted to lower frequencies, but a second resonance appears between 20 and 30 Hz. A particular feature of this second resonance is that it cannot be predicted by linear modal analysis, as there exists no mode in this frequency range that involves a motion of the instrument panel [134]. Clearly, this nonlinear resonance of the instrument panel deserves further investigation, not only because it is intriguing but also because it is associated with the greatest response amplitude, at an important location due to the presence of the telescope.

## 2.4 Identification of a Nonlinear Model

The identification of the SmallSat's NCs of the WEMS was performed by applying the restoring force surface (RFS) method to the experimental data [134]. Each NC was modeled using piecewise-linear functions, *i.e.*, a trilinear spring in the axial direction (elastomer in traction/compression plus two stops), a bilinear spring in the radial direction (elastomer in shear plus one stop) and a linear spring in the third direction (elastomer in shear). For illustration, the stiffness curve identified for NC1 is displayed in Fig. 2.4. A clear hardening in this connection can be observed, due to the impacts of the metallic cross with the mechanical stops, together with some asymmetry, which is explained by the prestress in the elastomers due to gravity.

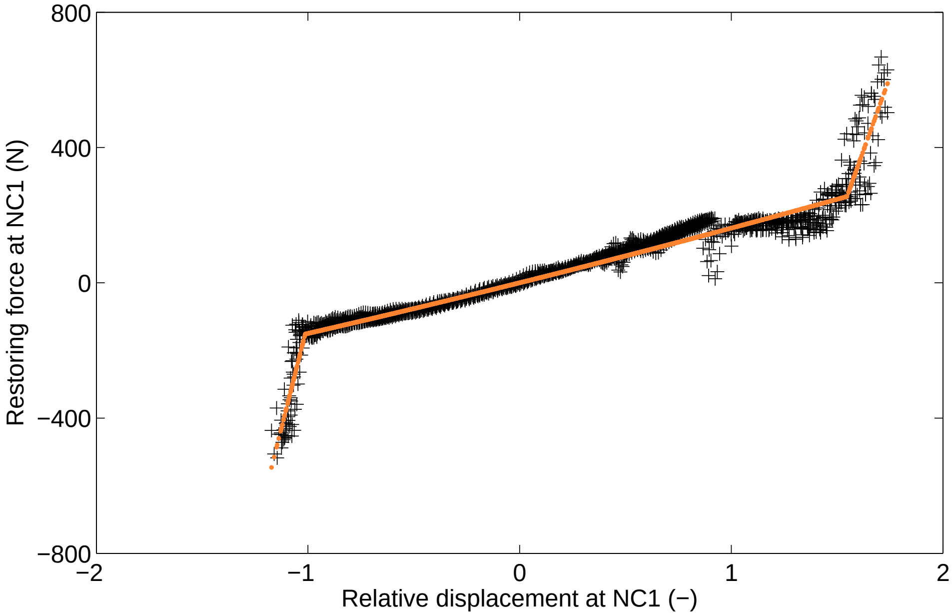

Figure 2.4: Stiffness curve of NC1 identified with the RFS method (in black) and fitted with a trilinear model (in orange).

To build a complete structural model of the satellite, the identified nonlinearities, *i.e.*, the trilinear springs in the axial direction and the bilinear springs in the lateral direction, were integrated in a detailed finite element model (FEM) of the underlying linear structure comprising $150,000$ degrees of freedom (DOFs). To avoid numerical issues, $C^1$ continuity in the close vicinity of the clearances was enforced by regularizing the piecewise-linear functions with third-order Hermite polynomials polynomials.

The FEM, shown in Fig. 2.5, consists of shell elements for the main structure, the metallic cross of the WEMS device and the instrument baseplate, and point masses for the inertia wheel and the dummy telescope. Proportional damping was considered for the main structure, and the high dissipation in the elastomer plots was described using lumped dashpots. As shown in Table 2.1, the modes of the underlying linear structure are densely packed, and the corresponding damping ratios are all beyond 2%.

| Mode | Natural frequency ($Hz$) | Damping ratio (%) |
|---|---|---|
| 1 | 8.06 | 10.10 |
| 2 | 9.14 | 8.03 |
| 3 | 20.44 | 11.96 |
| 4 | 21.60 | 21.04 |
| 5 | 22.06 | 11.55 |
| 6 | 28.75 | 6.23 |
| 7 | 32.49 | 2.09 |
| 8 | 34.78 | 2.23 |
| 9 | 39.07 | 2.33 |
| 10 | 40.78 | 2.42 |
| 11 | 45.78 | 2.61 |
| 12 | 57.76 | 3.13 |

Table 2.1: Linear resonance frequencies and damping ratios computed from the numerical model.

To achieve tractable calculations, the linear FEM was condensed using the Craig-Bampton reduction technique [14]. More specifically, the FEM was reduced to 10 internal modes and 9 nodes, namely both sides of each nonlinear connection and the inertia wheel, but excluding DOFs in rotation. In total, the reduced-order model hence contains 37 DOFs. The predictions of the resulting nonlinear FEM were verified to be in acceptable agreement with experimental observations for the purpose of our study [134, 163].

To reproduce, at least qualitatively, the experimental time series, a swept-sine excitation (0.5 Hz/min) was applied vertically to the inertia wheel, and Newmark's method used the developed model to calculate the structural response to this excitation. A sampling rate of 3000 Hz was selected for an accurate representation of the higher harmonics of the fundamental forcing frequency. The vertical acceleration of the central node on the instrument panel (P-$Z$) is shown in Fig. 2.6(a) for two forcing levels. It is clearly seen that the large-amplitude resonance at 29 Hz observed for 80 N is nonexistent at 20 N. This behavior is fully consistent with the observations made in Fig. 2.3.

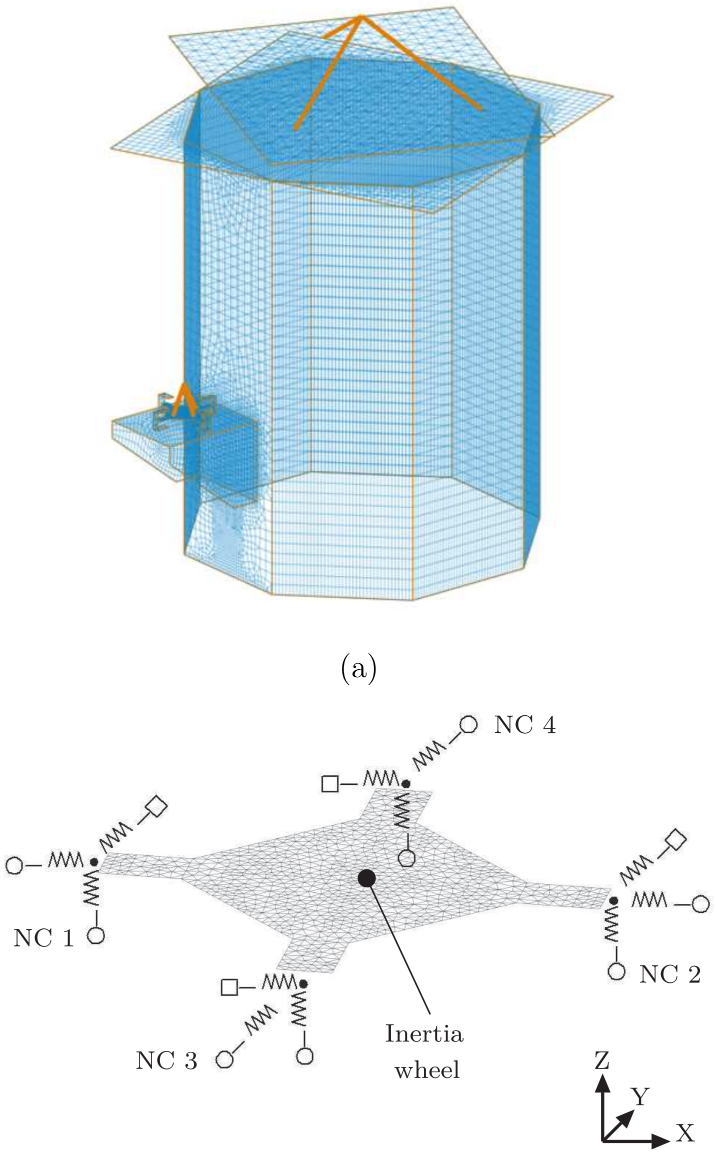

(a)

(b)

Figure 2.5: FEM of the SmallSat. (a) Modeling of the main structure using shell elements; (b) modeling of the WEMS using shell elements, a point mass, linear and nonlinear springs. The linear and nonlinear springs are represented with squares and circles, respectively.

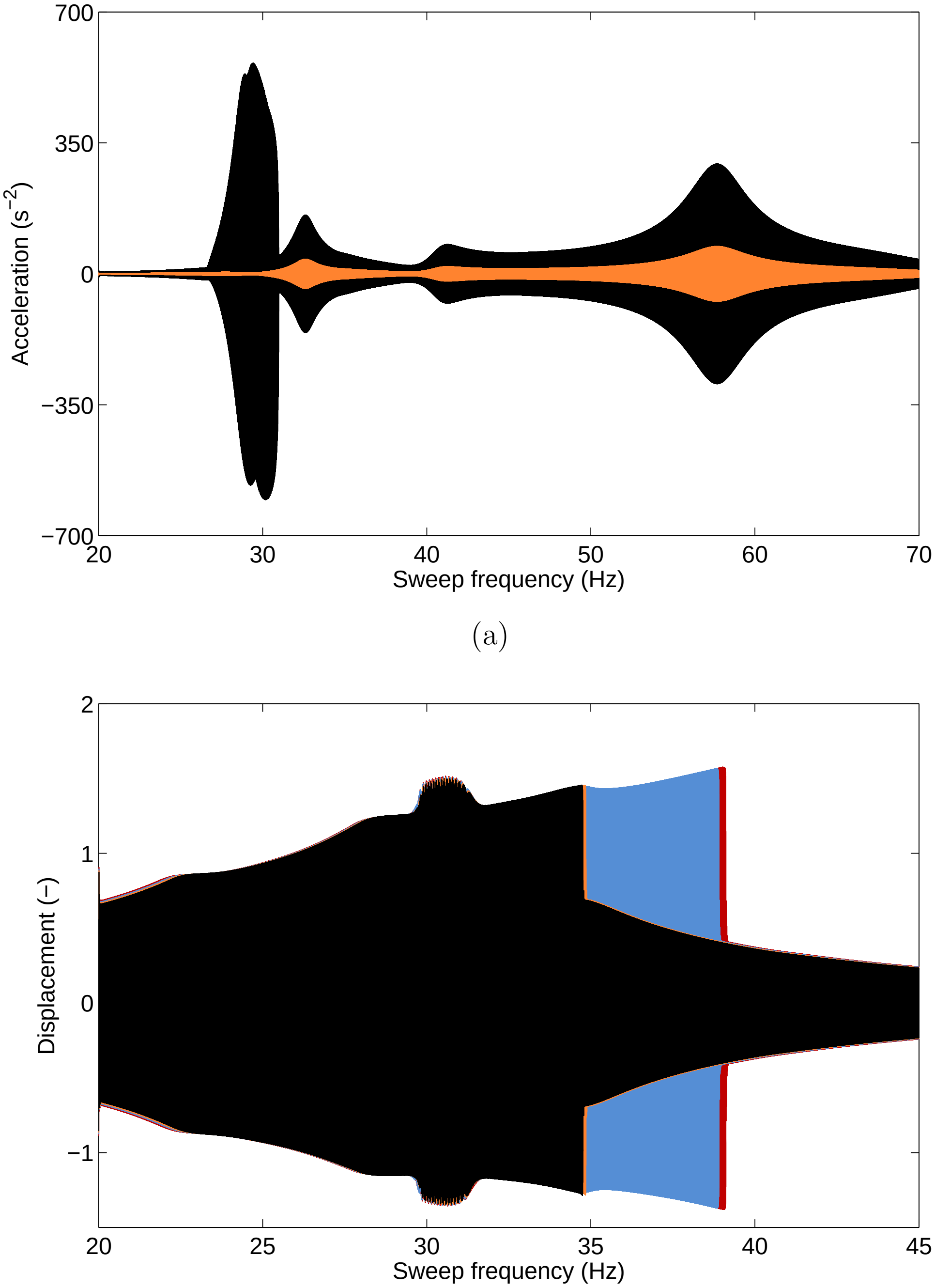

(a)

(b)

Figure 2.6: Time series computed from the numerical model. (a) Swept-sine response in acceleration of the instrument panel at P-$Z$ for a forcing amplitude of $f = 20\,\mathrm{N}$ (in orange) and $f = 80\,\mathrm{N}$ (in black); (b) swept-sine response in displacement of the inertia wheel at NC1-$Z$ for a forcing amplitude $f = 168\,\mathrm{N}$ (in black), $f = 170\,\mathrm{N}$ (in orange), $f = 172\,\mathrm{N}$ (in blue) and $f = 174\,\mathrm{N}$ (in red).

Fig. 2.6(b) depicts the vertical displacement of the node located at NC1 on the inertia wheel side (NC1-$Z$) for forcing amplitudes of 168 N, 170 N, 172 N and 174 N. If the classical jump in amplitude in the vicinity of the resonance can be observed in this figure, a sudden frequency jump is also noticed when the forcing amplitude increases from 170 N to 172 N. This nonlinear phenomenon, which is not often discussed in the literature, deserves deeper investigations, as it is associated with a substantial variation of the resonance frequency. Finally, we note in all time series of Fig. 2.6(b) the presence of an unexpected modulation of the responses envelope between 30 and 31 Hz.

If these simulations confirm the good predictive capabilities of the model and highlight new phenomena, an explanation of the underlying dynamical mechanisms is yet to be provided. This is the objective of Sections 2.5 and 2.6, which apply the NNM theory and bifurcation analysis to the spacecraft, respectively.

## 2.5 Understanding Nonlinear Resonances through Modal Analysis

The continuation method based on the HB method is employed in this section to compute NNMs. The resonance of interest occurs around 29 Hz, which is close to the resonance frequency of the sixth mode of the structure (cf. Table 2.1). NNM6 is computed in Fig. 2.7(a), for a single harmonic component (*i.e.*, $N_H = 1$). At low energy levels, the metallic cross does not interact with the mechanical stops. Consequently, the frequency of the NNMs does not depend on energy, and remains the same as the frequency of the linear mode. For larger energy levels, nonlinearities are activated. The frequency of the NNMs increases suddenly and rapidly, resulting from the nonsmooth and hardening nature of the nonlinearities.

In Fig. 2.7(b), a second harmonic component is added in the Fourier basis. The first part of the branch is similar to that computed with $N_H = 1$, but another branch of solutions emanates from the main branch, referred to as *backbone curve*, and forms a *tongue*. This peculiar nonlinear phenomenon is called *internal resonance* (IR), or *modal interaction*. It is due the fact that, when progressing along the backbone curve, harmonics of the fundamental frequency are generated by the nonlinearities, and may have a frequency close to the oscillation frequency of another NMM of the system. In this situation, a dynamic coupling between the two modes is established together with an energy transfer. Due to the frequency-energy dependence of NNMs, such interactions can develop between modes with incommensurate linear frequencies, which is herein the case for NNM6 and NNM12 (see [97, 115] or Chapters 3 and 4 for other examples).

The ability of the HB algorithm to capture IRs depends on the number of harmonics considered. In Fig. 2.7(a), as only the fundamental frequency is kept in the spectral basis, the 2:1 IR, *i.e.*, the internal resonance involving the fundamental frequency and its

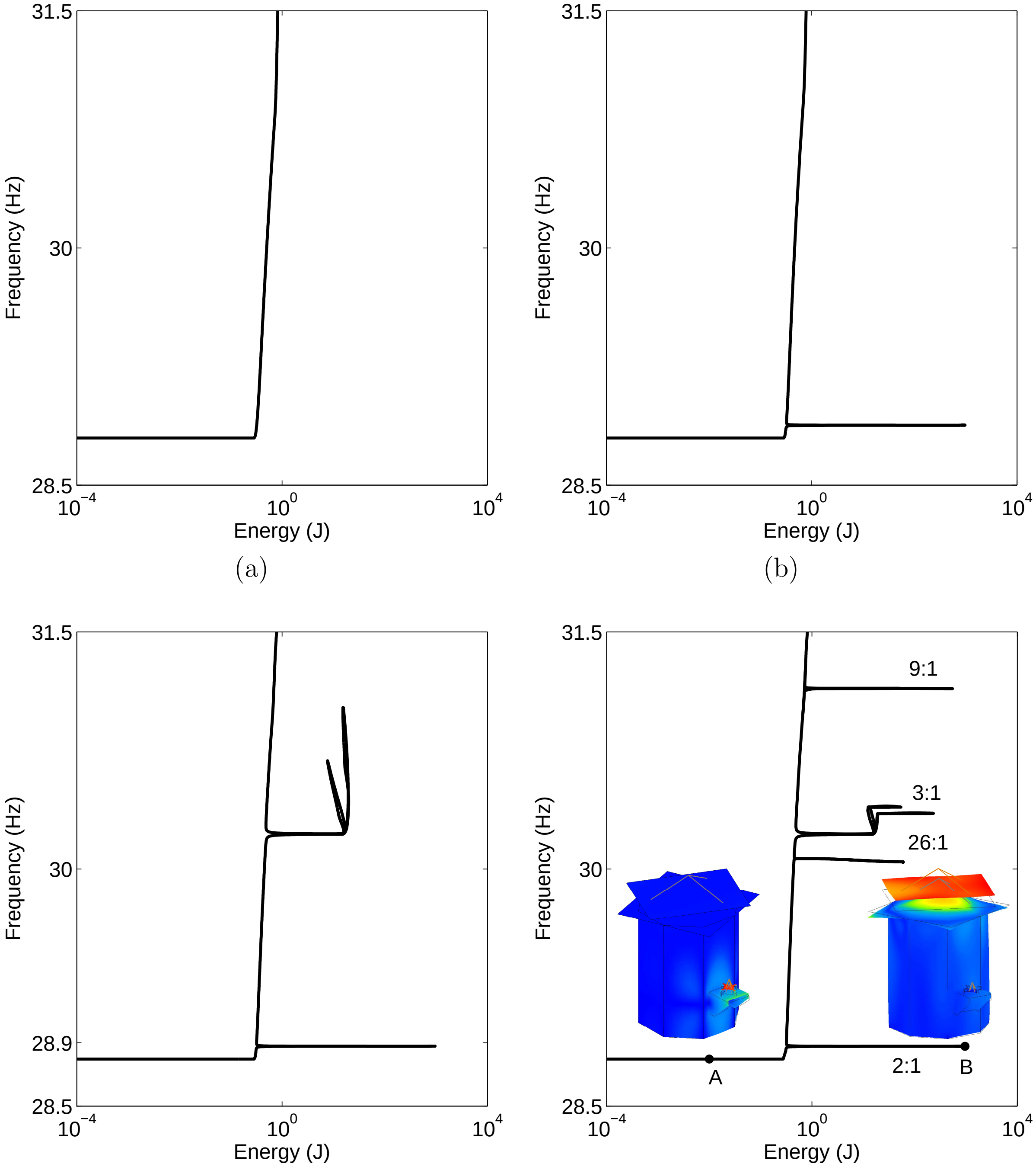

Figure 2.7: Representation of the sixth NNM on the frequency-energy plot. Computation with the harmonic balance method, for (a) $N_H = 1$, (b) $N_H = 2$, and (c) $N_H = 3$ harmonics retained in the Fourier approximation; (d) computation with the shooting technique [163], and representation of the mode shapes at A and B.

second harmonic, cannot be computed. For $N_H = 3$, Fig. 2.7(c) reveals the presence of a 3:1 IR. For comparison, NNM6 computed in [163] with the shooting technique is given in Fig. 2.7(d). This comparison demonstrates that the HB algorithm provides an accurate representation of the backbone curve, even for a single harmonic, and accounts for the presence of IRs up to the limit of its spectral basis. The differences observed between the 3:1 IR tongues can be explained by the fact that this IR involves higher harmonics that are not considered in the spectral basis. As the shooting technique is a time-domain technique, it is able to capture numerous modal interactions along backbone curves, depending on the step size and the sampling frequency used for the continuation algorithm. This feature is interesting for a complete characterization of the modal properties, but it is computationally expensive. The physical significance of the highest IRs is also questionable (see, *e.g.*, the 26:1 IR in Fig. 2.7(d)), if the corresponding oscillation frequencies are outside the range of validity of the reduced-order model. Conversely, the filtering property of the HB method in Figs. 2.7(a-c) proves useful to obtain a rapid estimation of the frequency-energy dependence of a mode, and to represent the IRs that are the most likely to appear in experiments.

In Fig. 2.7(d), the mode shapes related to NNMs computed in the linear regime and at the extremity of the 2:1 IR are depicted. The sixth linear mode shape mainly involves vertical motion of the inertia wheel. Very interestingly, on the 2:1 IR tongue, the mode shape becomes a mixing between the shapes of NNM6 and NNM12 until, at the extremity, the sole second harmonic remains, which completes a transition to NNM12. Located around 28.9 Hz, this latter NNM is associated with strong instrument panel motion. The nonlinear resonance observed in Figs. 2.3 and 2.6(b) can therefore be attributed to a 2:1 modal interaction between the sixth and the twelfth modes of the spacecraft.

## 2.6 Uncovering Nonlinear Phenomena through Bifurcations Analysis

The present section is dedicated to the study of the response of the satellite to harmonic excitation, with the HB analysis tools described in Sections 1.3 and 1.4. More specifically, an explanation of the nonlinear phenomena observed in Fig. 2.6(b) is sought.

### 2.6.1 Convergence of the HB Method

The response for harmonic forcing applied to the vertical DOF of the inertia wheel is computed with $N_H = 9$ harmonics. Fig. 2.8(a) depicts the system's NFRCs at NC1-$Z$ for forcing amplitudes of $f = 50$ N and $f = 155$ N. For a clear assessment of the nonlinear effects, the response amplitudes are normalized with the forcing amplitude. Because the normalized responses for both forcing amplitudes coincide up to 23 Hz, the motion is essentially linear in this frequency range. Conversely, the mode with a linear resonance frequency of 28.8 Hz is greatly affected by the WEMS nonlinearities, because this mode combines bracket deflection with WEMS motion (cf. mode shape A in Fig. 2.7(d)).

The evolution of the normalized harmonic coefficients constructed from Eqs. (1.32-1.33) is shown in Fig. 2.8(b). From 20 to 23 Hz, only the fundamental harmonic participates in the response whereas, in the resonance region, the nonlinearities activate the first fifth harmonics. A constant term and even harmonics contribute to the dynamics because of the asymmetric modeling of the NCs of the WEMS.

In order to further study the effect of the number of harmonics, Fig. 2.9(a) gives the NFRCs computed for $N_H$ varying between 1 and 9. While the approximation for $N_H = 1$ captures the resonance peak with a poor accuracy, a convergence of the curves can be observed for $N_H \geq 5$ in Fig. 2.9(b). For this reason, $N_H = 5$ is considered throughout the rest of the chapter. In Fig. 2.9(c), the computational time required to continue the NFRCs is compared for different values of $N_H$, with stability analysis included or not. The simulations without stability analysis require a computational time that increases almost linearly with $N_H$, except for $N_H = 1$ and 2, which are associated to longer curves. This can be explained by the size of the systems to solve during the continuation procedure, that directly depends on $N_H$. The increase becomes more pronounced when the computation of the Floquet exponents is included, which is due to the growing size of matrix $\mathbf{B}$ in the eigenvalue problem (cf. Eq. (1.46)).

### 2.6.2 Quasiperiodic Oscillations

The bifurcations of the NFRC in Fig. 2.8(a) are now studied. The evolution of Hill's coefficients $\boldsymbol{\lambda}$ and Floquet exponents $\tilde{\boldsymbol{\lambda}}$ in the vicinity of the first Neimark-Sacker (NS) bifurcation is given in Figs. 2.10(a-b). Before the bifurcation, the Floquet exponents lie all in the left-half plane in Fig. 2.10(a), which indicates a stable solution. Conversely, a pair of Hill's coefficients has already crossed the imaginary axis in this figure, which evidences that considering Hill's coefficients leads to misjudgement. After the bifurcation, a pair of complex conjugate Floquet exponents now lies in the right-half plane in Fig. 2.10(b), which means that the system underwent a NS bifurcation and lost stability. A similar scenario is depicted for the first fold bifurcation in Figs. 2.10(c-d) with the difference that a single Floquet exponent crosses the imaginary axis through zero.

The validation of the results is provided in Fig. 2.11(a), where the response to a swept-sine excitation with a forcing amplitude of 155 N computed with a Newmark time integration scheme is superposed to the NFRC. The NFRC provides a very accurate estimation of the envelope of the swept-sine response, except in the region between the two NS bifurcations. The modulation of the displacement's envelope can be explained by the creation of a branch of stable quasiperiodic (QP) solutions at the NS bifurcation near 30 Hz. Fig. 2.11(b) shows the Floquet exponents $\tilde{\boldsymbol{\lambda}}$ obtained with Hill's method for a stable periodic solution at 28 Hz, and the Floquet exponents $\tilde{\boldsymbol{\lambda}}_{TI}$ calculated from the

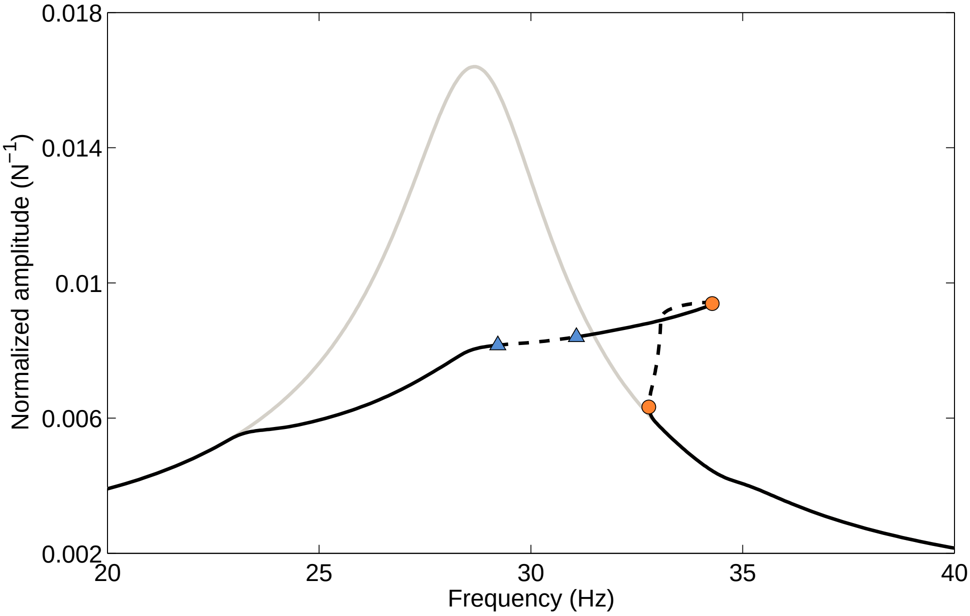

(a)

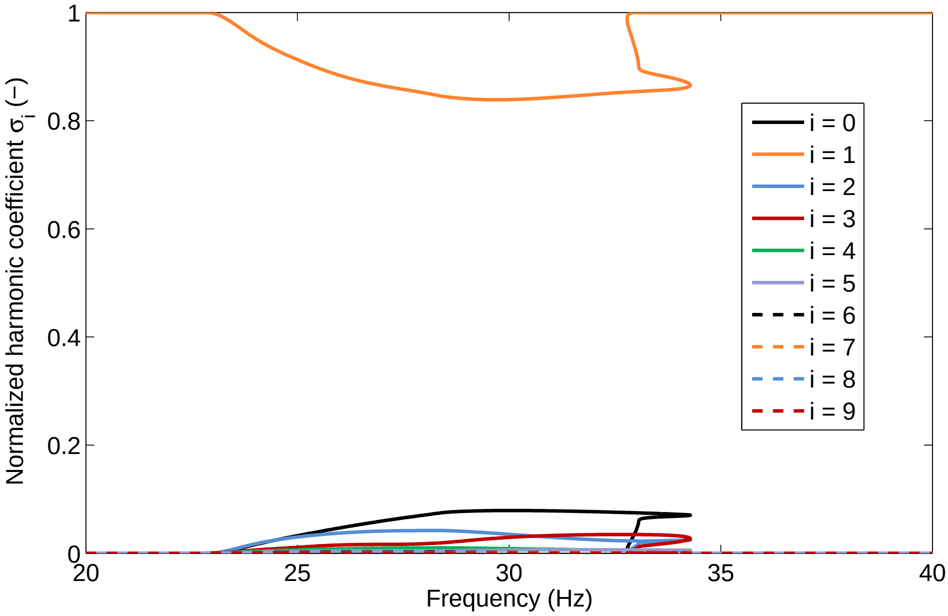

(b)

Figure 2.8: Frequency response at NC1-$Z$. (a) Normalized NFRCs for $f = 50\,\text{N}$ (in grey) and $f = 155\,\text{N}$ (in black). Circle and triangle markers represent fold and NS bifurcations, respectively. The solid and dashed lines represent stable and unstable branches, respectively; (b) harmonic coefficients for $f = 155\,\text{N}$.

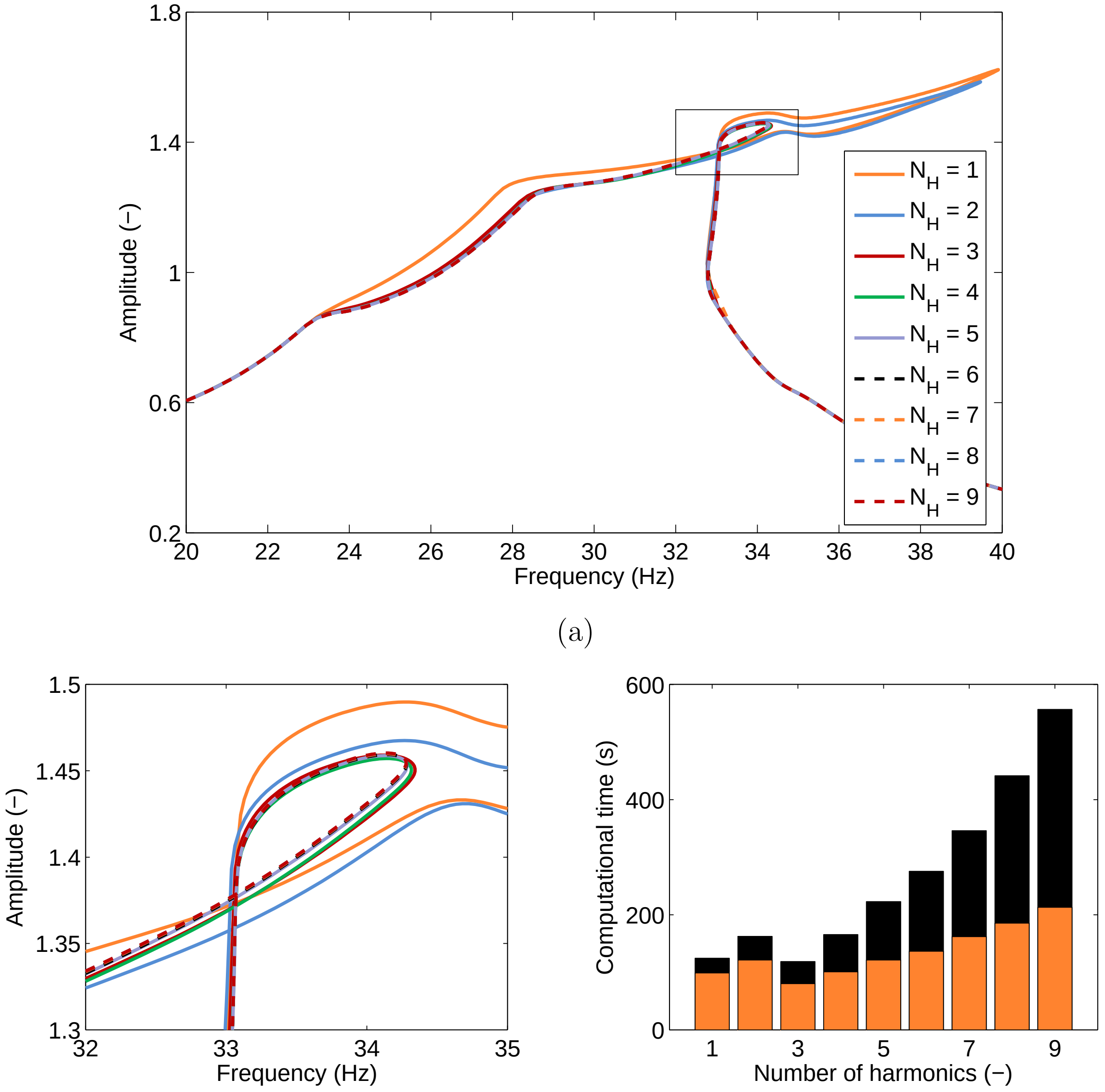

(a)

(b)

(c)

Figure 2.9: Effect of the number of harmonics $N_H$ on the NFRC at NC1-$Z$ for $f = 155\,\mathrm{N}$. (a) Amplitude; (b) close-up of the resonance peak; (c) computational time with (in black) and without (in orange) stability analysis.

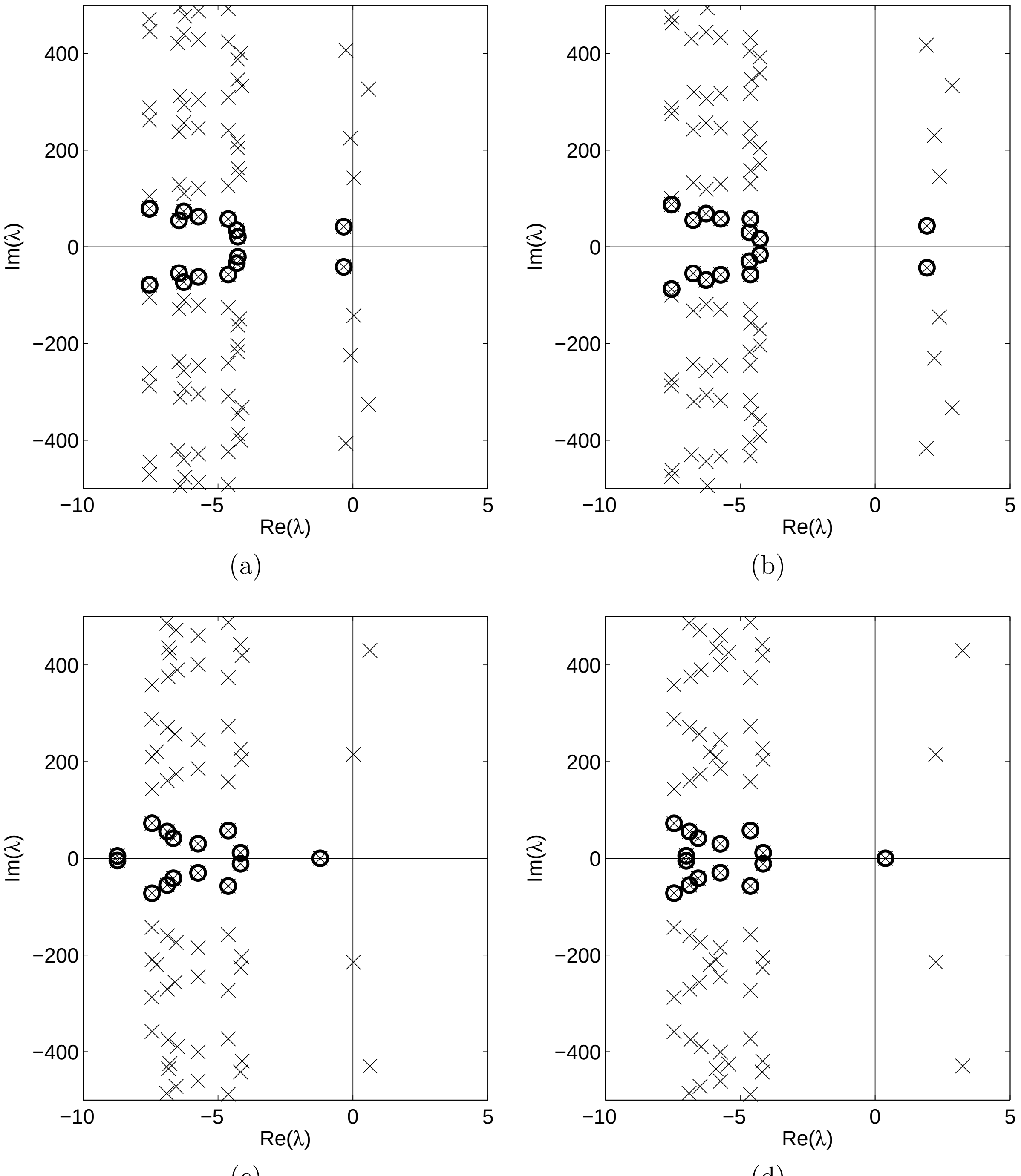

(a) (b)

(c) (d)

Figure 2.10: Hill's coefficient and Floquet exponents. (a) Before the NS bifurcation at $\omega = 29.11\,\mathrm{Hz}$, stable region; (b) after the NS bifurcation at $\omega = 29.8\,\mathrm{Hz}$, unstable region; (c) before the fold bifurcation at $\omega = 34.25\,\mathrm{Hz}$, stable region; (d) after the fold bifurcation at $\omega = 34.28\,\mathrm{Hz}$, unstable region. Hill's coefficients $\boldsymbol{\lambda}$ and Floquet exponents $\tilde{\boldsymbol{\lambda}}$ are denoted with cross and circle markers, respectively.

monodromy matrix evaluated with a Newmark time integration scheme as in [144]. The comparison demonstrates that both Floquet exponent sets are in close agreement, which validates the sorting criterion of Section 1.2.3.

To better characterize the modulation of the displacement's envelope, the structure is now excited harmonically at 28.5 Hz, 29 Hz and 29.5 Hz, which correspond to configurations before, near and after the first NS bifurcation, respectively. In Fig. 2.12(a), after short transients, the response quickly stabilizes on a periodic solution whose amplitude is that predicted by the NFRC. For $\omega = 29$ Hz in Fig. 2.12(b), the steady-state response is still periodic, but the transients feature some modulation. After the NS bifurcation in Fig. 2.12(c), the periodic solution is unstable, and the response exhibits QP oscillations.

As explained in Section 1.3.2, the envelope frequency of the QP oscillations emanating from the NS bifurcations can be predicted by the imaginary part of the purely imaginary Floquet exponents associated to the bifurcations. Fig. 2.13 shows that two exponents cross the imaginary axis around $\beta = 41.8$, which corresponds to a modulation frequency of $\beta/2\pi = 6.65$ Hz. In order to verify this result, Fig. 2.14 displays the FFT of the signals in Fig. 2.12, with the first two seconds of the transients removed. The FFT of the periodic response at $\omega = 28.5$ Hz possesses three peaks, related to the forcing frequency and its second and third harmonics. At $\omega = 29$ Hz, the QP ghost oscillations present in the remaining transients translates into a small peak around 6.65 Hz, which confirms the prediction in Fig. 2.13. Some combinations between the forcing and modulation frequency appear as well, through the two peaks surrounding the main peak at 29 Hz and their second and third harmonics. At $\omega = 29.5$ Hz, the QP signal involves a stronger peak at 6.65 Hz, which gives rise to many other combinations of the different peaks.

### 2.6.3 Frequency Shift

An explanation for the sudden shift of the resonance frequency for a small increment of the forcing amplitude in Fig. 2.6(b) is sought in this section. To this end, the fold bifurcation detected near the resonance peak of the NFRC computed in Fig. 2.8(a) is now tracked in the codimension-2 forcing frequency-forcing amplitude space using the algorithm presented in Section 1.4. Fig. 2.15(a) represents the resulting fold curve, together with the NFRCs of the system computed for different forcing amplitudes. Very interestingly, the algorithm initially tracks the fold bifurcations of the main frequency response, but it then turns back to reveal an *isolated response curve* (IRC), also called *isola*. Such an attractor is rarely observed for real structures in the literature, and will be discussed in greater details in Chapters 3 and 4.

A more convenient representation of the bifurcation curve is given in Fig. 2.15(b), which shows the projection of the fold curve in the forcing amplitude-response amplitude plane. This figure highlights that the IRC is created at $f = 158$ N. The IRC then expands both in frequency and amplitude until $f = 170$ N, for which its merging with the resonance peak occurs. The resonance peak after the merging is characterized by a greater frequency and

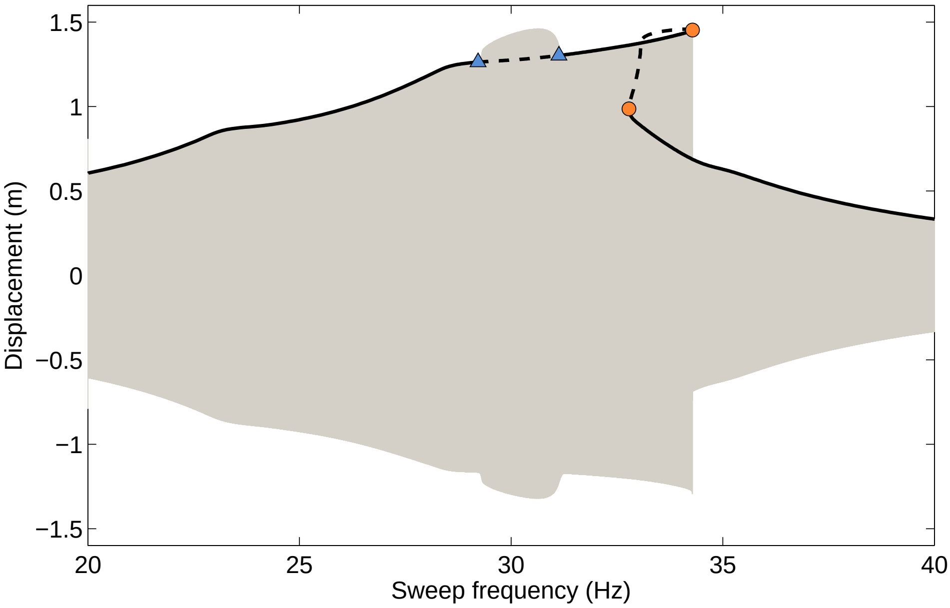

(a)

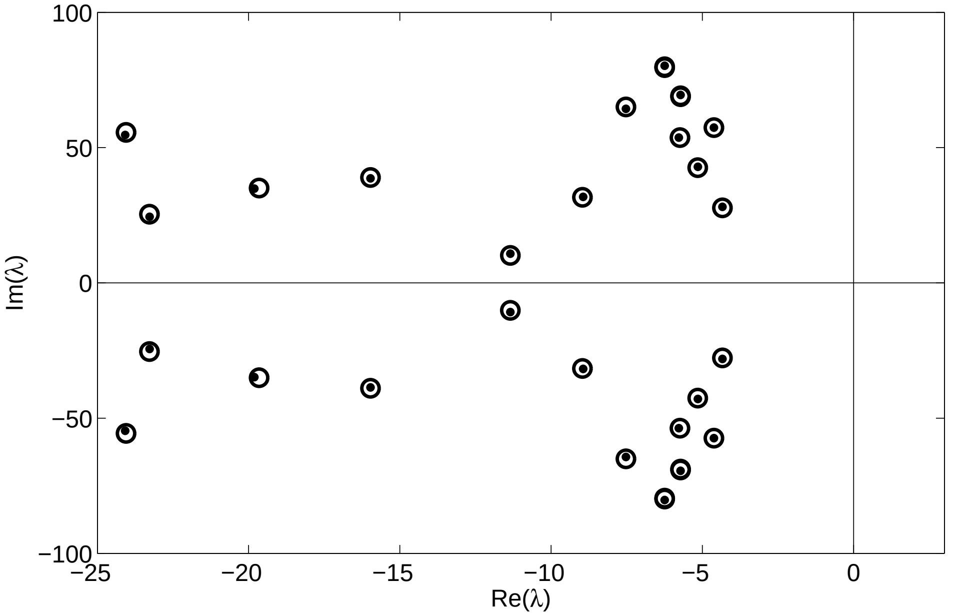

(b)

Figure 2.11: NFRC and stability analysis for $f = 155\,\mathrm{N}$. (a) Comparison between the NFRC (in black) and the swept-sine response calculated at NC1-$Z$ using time integration (in grey); (b) periodic solution at 28 Hz: Floquet exponents $\tilde{\boldsymbol{\lambda}}$ obtained with Hill's method (circle markers), and Floquet exponents $\tilde{\boldsymbol{\lambda}}_{TI}$ obtained with the monodromy matrix from time simulations (dot markers).

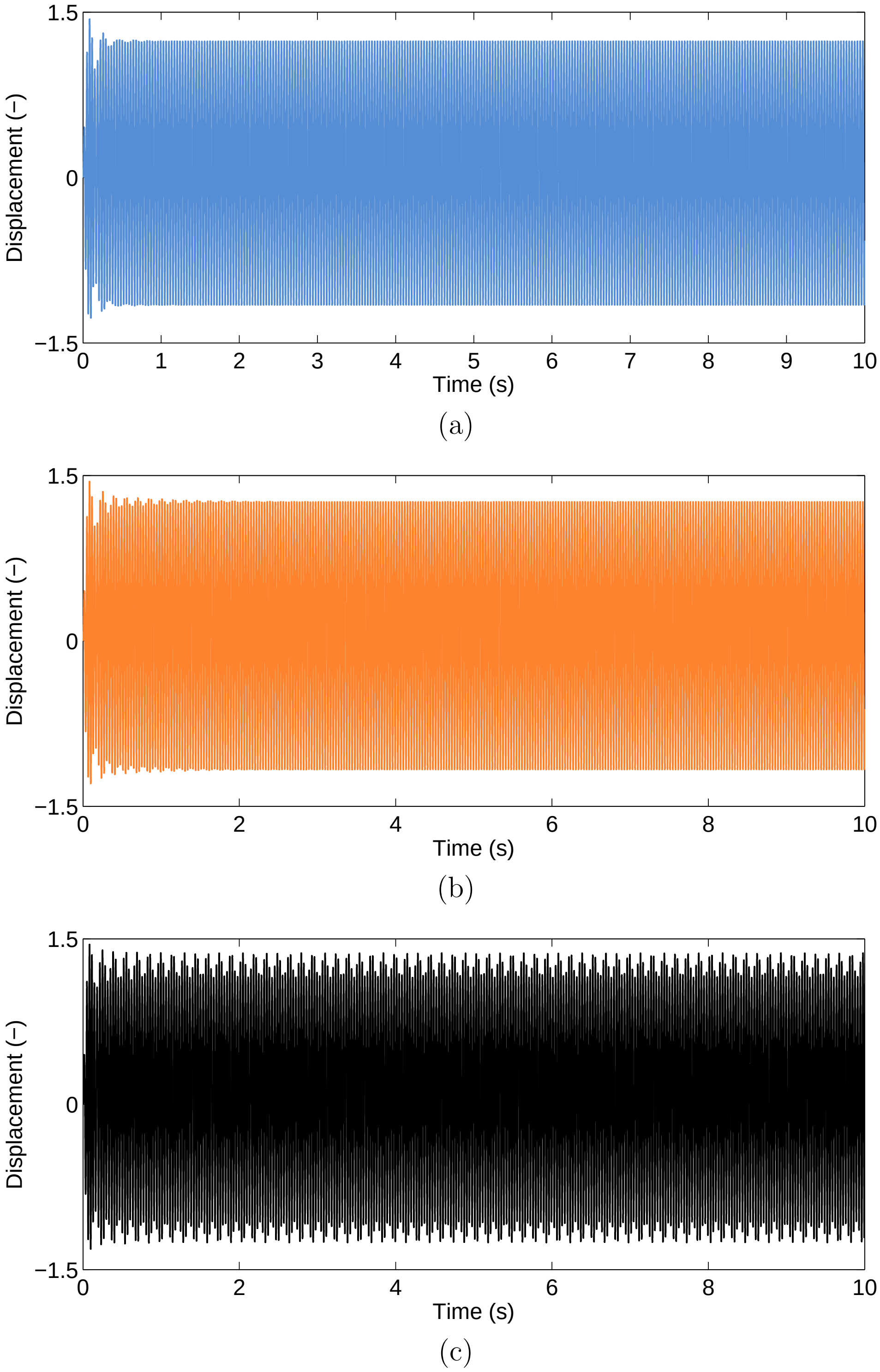

Figure 2.12: Response to sine excitation at NC1-$Z$ applied at $f = 155\,\mathrm{N}$. (a) Forcing frequency $\omega = 28.5\,\mathrm{Hz}$, before the NS bifurcation. (b) Forcing frequency $\omega = 29\,\mathrm{Hz}$, near the NS bifurcation. (c) Forcing frequency $\omega = 29.5\,\mathrm{Hz}$, after the NS bifurcation.

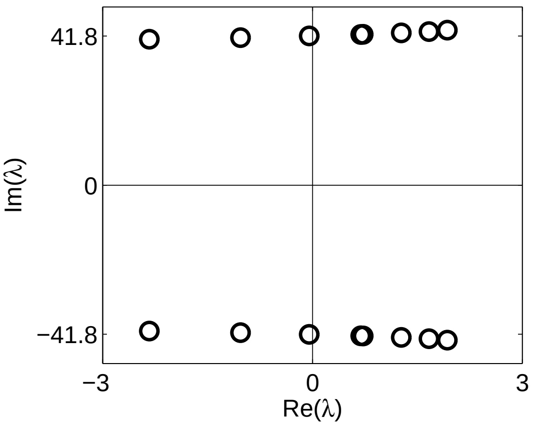

Figure 2.13: Evolution of the Floquet exponents related to the first NS bifurcation.

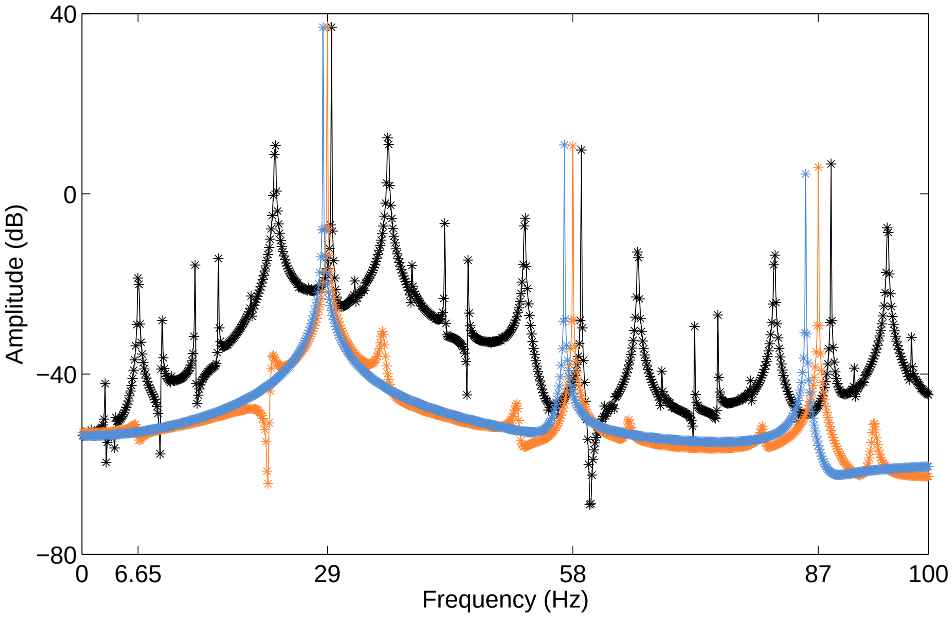

Figure 2.14: Spectral content of the responses in Fig. 2.12. $\omega = 28.5\,\mathrm{Hz}$, before the NS bifurcation (in blue), $\omega = 29\,\mathrm{Hz}$, near the NS bifurcation (in orange), and $\omega = 29.5\,\mathrm{Hz}$, after the NS bifurcation (in black).

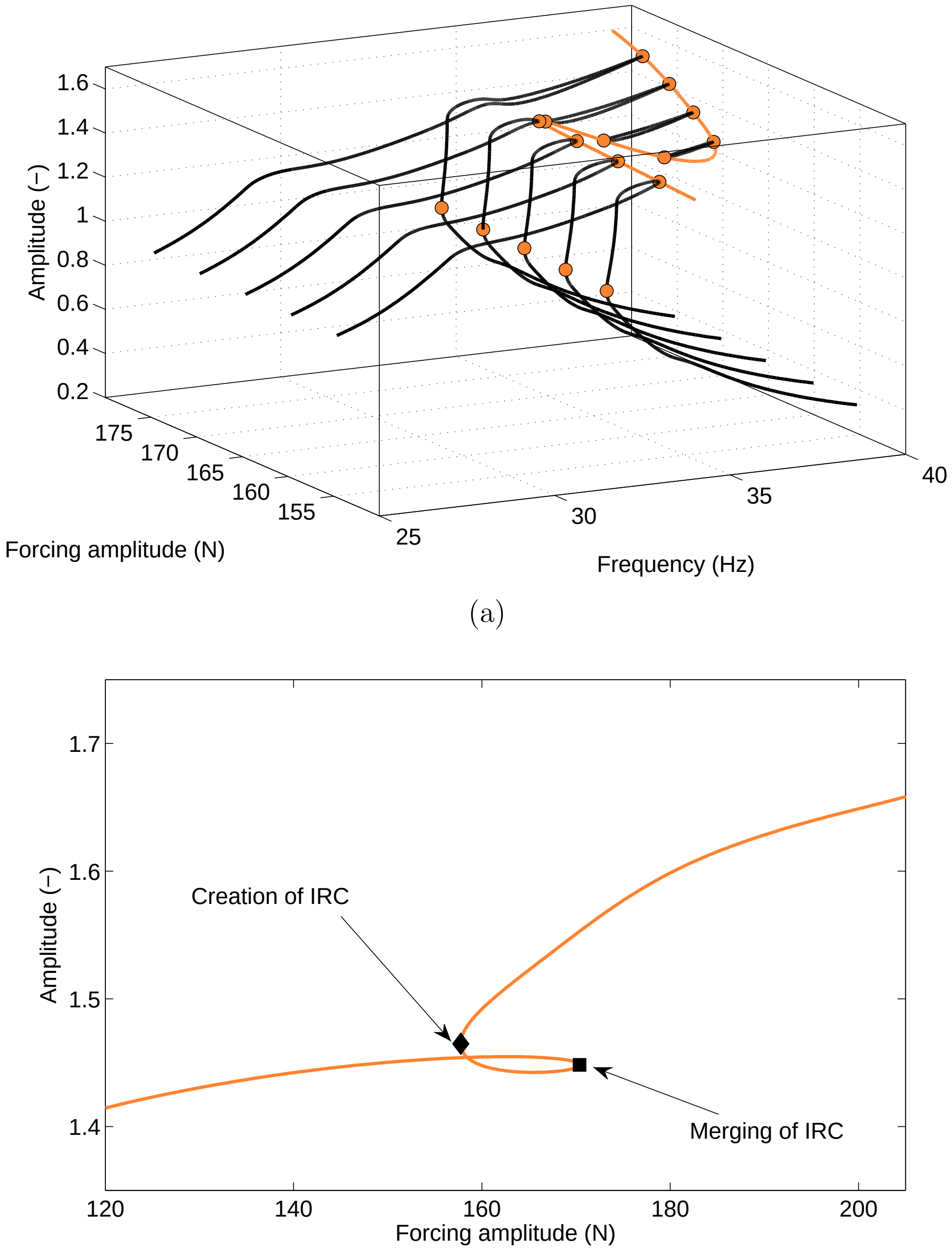

(a)

(b)

Figure 2.15: Tracking of the fold bifurcations of the resonance peak. (a) Three-dimensional space. Branch of fold bifurcations (in orange), NFRCs computed at NC1-$Z$ for $f = 155\,\mathrm{N}$, $160\,\mathrm{N}$, $170\,\mathrm{N}$ and $175\,\mathrm{N}$ (in black). Circle markers depict fold bifurcations; (b) two-dimensional projection of the branch of fold bifurcations.

amplitude. This merging process clearly explains the sudden shift in resonance frequency observed in Fig. 2.6(b).

Although the presence of IRCs is completely missed by the computation of NFRCs, tracking fold bifurcations allows its detection. Bifurcation tracking may therefore offer an efficient alternative to global analysis techniques, such as homotopy method [118], Groebner bases [73] coupled with the HB method, and cell mapping [86].

## 2.7 Nonlinear Design through Bifurcation Analysis

Bifurcation tracking is not only useful for a profound understanding of the system's dynamics, but it can also be used for engineering design. Instead of considering the forcing amplitude as the additional parameter for tracking, one can include a design variable and analyze its influence on the evolution of significant bifurcations.

For the SmallSat structure, Fig. 2.11(a) shows that the amplitude of the QP oscillations is slightly larger than those at resonance. As a consequence, one could try to eliminate the QP oscillations by tuning the axial dashpot $c_{ax}$ of the WEMS device. Fig. 2.16(a) depicts the NS curve computed in the codimension-2 forcing frequency-axial damping space, to which NFRCs obtained for damping values of $c_{ax} = 63\,\mathrm{Ns/m}$ (reference), 80 Ns/m and 85 Ns/m are superposed. This figure demonstrates that the two NS bifurcations, and hence the QP oscillations, disappear for sufficiently high values of damping. The projection of the NS curve in Fig. 2.16(b) shows that the elimination occurs when $c_{ax} = 84\,\mathrm{Ns/m}$. The new and original designs are compared using swept-sine responses in Fig. 2.17, which confirms that an elastomer possessing higher damping leads to the elimination of QP motion.

In Fig. 2.18, the influence of $c_{ax}$ on the fold bifurcation curve discussed in Section 2.6 is investigated. A higher damping does not eliminate the IRC, but rather postpone its creation and merging to higher values of the forcing amplitude.

Finally, the convergence of the HB algorithm for tracking bifurcations is assessed in Fig. 2.19, where the fold and NS curves presented in Figs. 2.15 and 2.16 are recomputed for a number of harmonics $N_H$ varying from 1 to 9. In both cases, a convergence of the results is obtained for $N_H = 5$, with an error of less than 1%. Fig. 2.19(a) also indicates a merged configuration of the NFRC computed with 1 and 2 harmonics at $f = 155\,\mathrm{N}$. This explains the longer curves observed in Fig. 2.9(a).

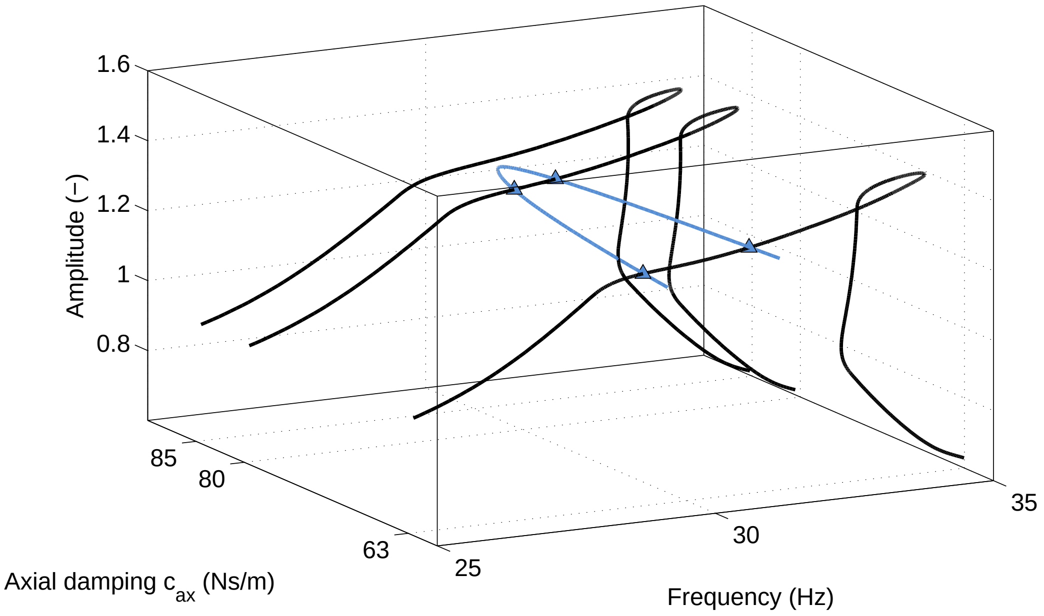

(a)

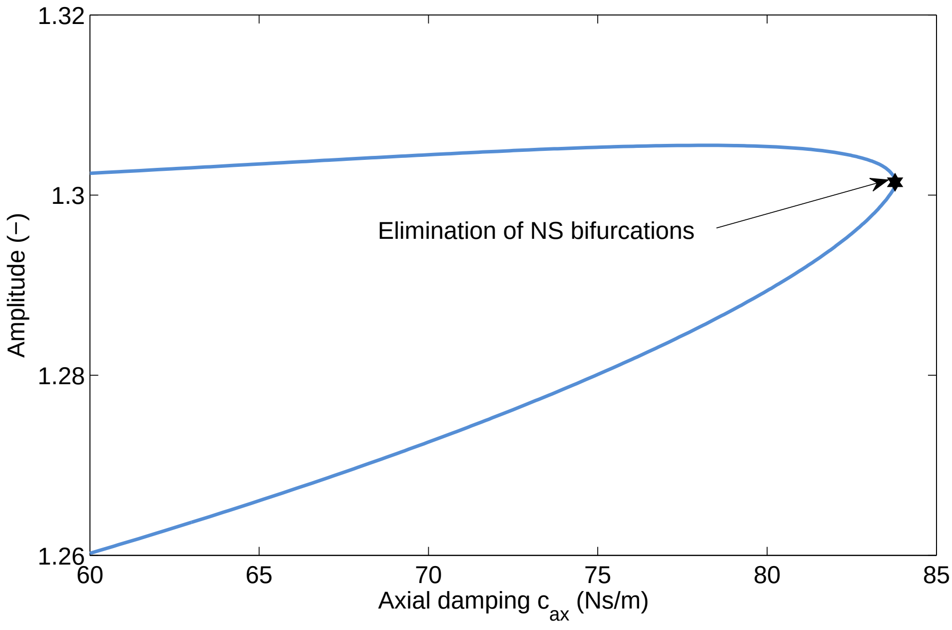

(b)

Figure 2.16: Tracking of the NS bifurcations. (a) Three-dimensional space. Branch of NS bifurcations (in blue), NFRCs computed at NC1-$Z$ for $f = 155\,\mathrm{N}$ and for $c_{ax} = 63\,\mathrm{Ns/m}$, $80\,\mathrm{Ns/m}$ and $85\,\mathrm{Ns/m}$ (in black). Triangle markers depict NS bifurcations; (b) two-dimensional projection of the branch of NS bifurcations.

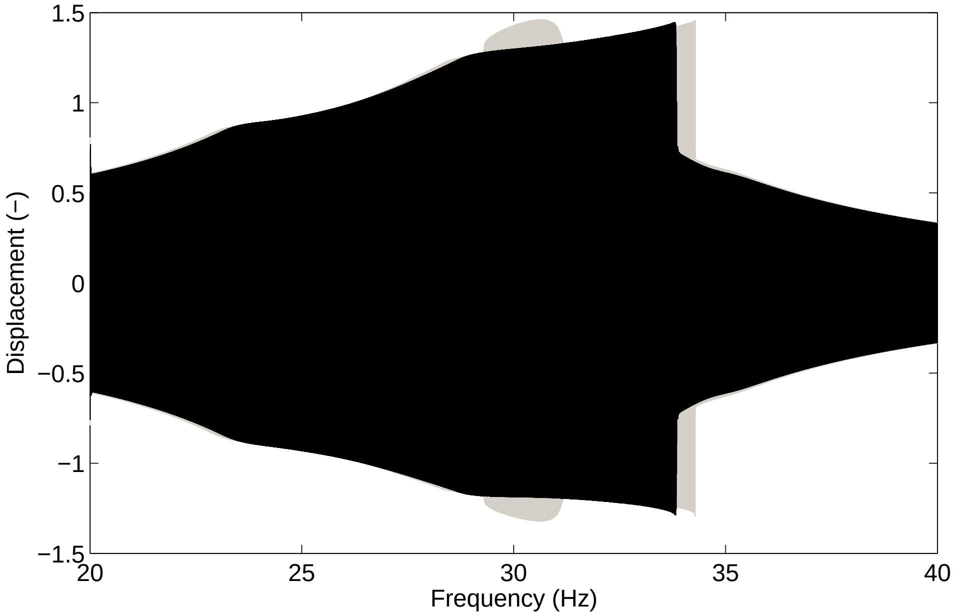

Figure 2.17: Influence of the damping value $c_{ax}$ on the response at NC1-$Z$ to swept-sine excitation, computed for $f = 155\,\mathrm{N}$ and for $c_{ax} = 63\,\mathrm{Ns/m}$ (in grey) and $c_{ax} = 85\,\mathrm{Ns/m}$ (in black).

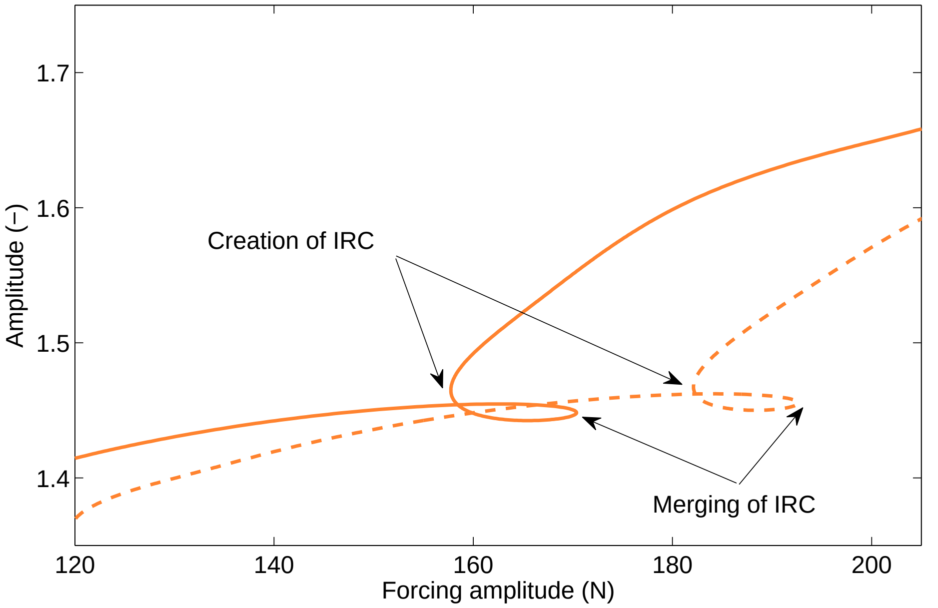

Figure 2.18: Influence of the damping value $c_{ax}$ on the fold bifurcation curves, computed for a value of $c_{ax} = 63\,\mathrm{Ns/m}$ (in solid line) and $c_{ax} = 85\,\mathrm{Ns/m}$ (in dashed line).

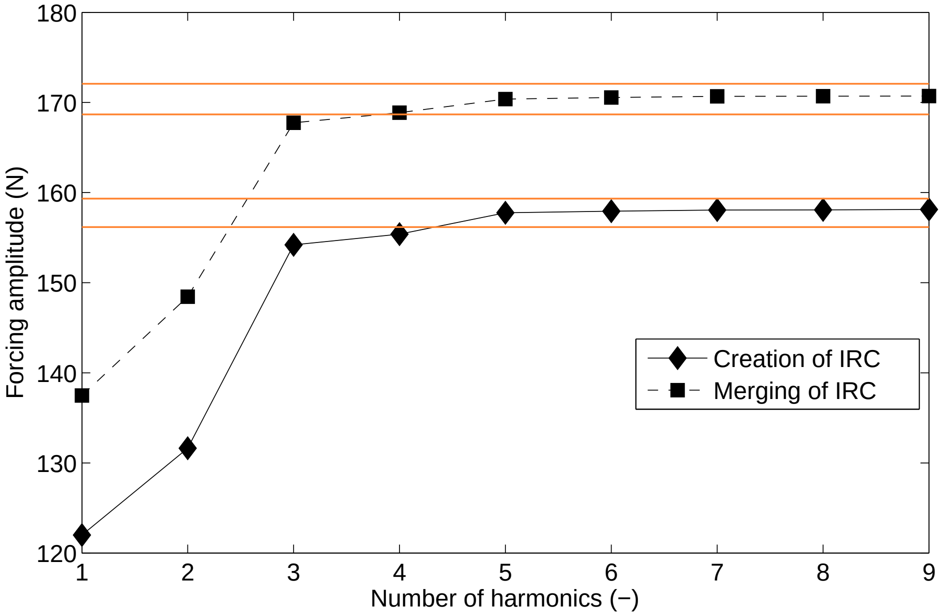

(a)

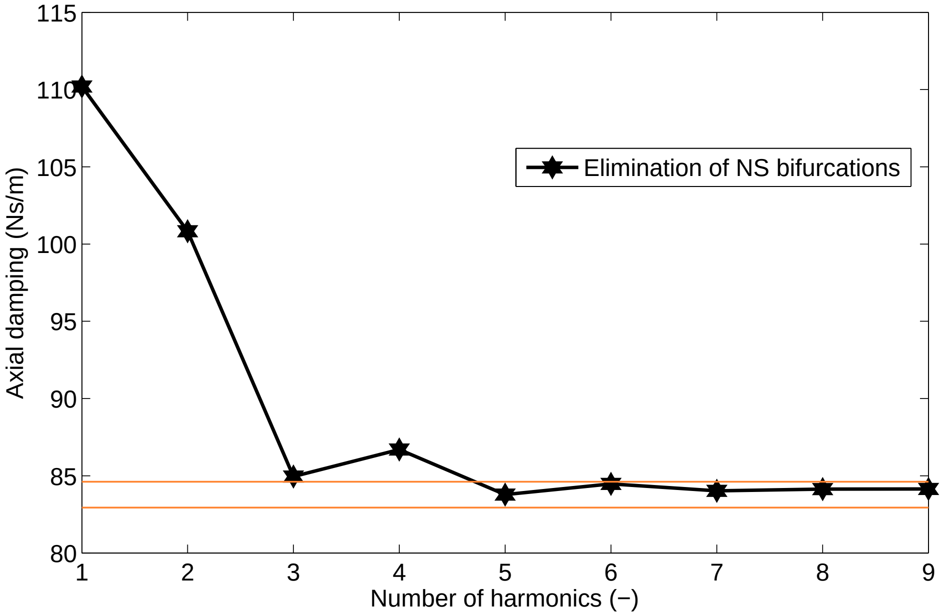

(b)

Figure 2.19: Convergence of the bifurcation tracking algorithm with respect to the number of harmonics $N_H$. (a) Fold bifurcations; (b) NS bifurcations. For both figures, the orange lines give $+1\%$ and $-1\%$ variations with respect to $N_H = 5$.

## 2.8 Concluding Remarks

In this chapter, the harmonic balance method was applied to a real-world aerospace structure possessing coupled modes, significant nonproportional damping and several localized nonlinearities. The results given by our method were carefully validated using direct numerical simulations for the nonlinear frequency response curves, and using the monodromy matrix for the Floquet exponents. The convergence of the algorithm was also assessed, and it was found that a relatively small number of harmonics was required even in strongly nonlinear regimes of motion.

The bifurcation and modal analysis capabilities of the harmonic balance method proved very helpful for a better understanding of the experimental nonlinear resonance, for uncovering quasiperiodic oscillations and isolated response curves that were not highlighted during the test campaign, and for the elimination of the quasiperiodic oscillations through damping modification. In this context, it is clear that the harmonic balance method can play a key role in the design cycle of nonlinear engineering structures.

Isolated response curves were shown to give rise to a substantial shift in resonance frequency, hence, they represent potentially dangerous dynamical attractors. Chapters 3 and 4 provide a more detailed characterization of isolated resonances, both numerically and experimentally. Specifically, we uncover their relation with the nonlinear normal modes in the next chapter.

# Chapter 3

# Relating Nonlinear Resonances and Nonlinear Normal Modes

---

### Abstract

The objective of the present chapter is to investigate fundamental and isolated resonances of nonlinear structures using the nonlinear normal modes (NNMs). In particular, this study explores the connections between NNMs and isolated response curves (IRCs), that are separate from the main forced response but merge with it for higher forcing levels. An energy balance methodology expressed in the harmonic balance formalism demonstrates that the creation of IRCs is directly related to the presence of internal resonances. Fold bifurcation tracking is then employed to characterize merging scenarios. These concepts are illustrated using a cantilever beam with a nonlinear spring at its free end.

# 3.1 Introduction

Chapters 1 and 2 employed the concept of nonlinear normal mode (NNM) to characterize the energy dependence of the natural frequencies of a structure. The occurrence of interactions between NNMs also gave rise to new, unexpected resonances in the frequency response. Similarly to their linear counterpart, NNMs reflect the deformation at resonance of the structure [195]. The main resonance peaks of nonlinear systems, referred to as *fundamental resonances*, can therefore be predicted by NNMs, expressed either as invariant manifolds [190], as a branch of periodic solutions [98], or through their normal forms [25, 83, 84]. This property has been used for various applications, such as nonlinear system identification [85], model updating [106, 148], or model reduction [20, 116, 147, 191].

In the present chapter, we propose to use NNMs for the analysis of another type of resonance, the so-called *isolated resonance*. Isolated resonances are related to the presence of *isolated response curves* (IRCs), also termed isolas or detached resonance curves, which represent an intriguing feature of nonlinear dynamics. They correspond to closed loops of solutions which are, by definition, detached from the main nonlinear frequency response curve (NFRC) [171]. IRCs can lie inside the main resonance peaks [58], or outside [4, 47]. They may thus go easily undetected, whether it be numerically employing continuation techniques, or experimentally applying sine-sweep excitations. However, an increase in forcing amplitude or the variation of another system's parameter may cause the merging of the IRC with the NFRC. This merging may result in dramatic frequency and amplitude shifts of the resonance location, as for the spacecraft studied in Chapter 2. This renders IRCs dangerous for systems likely to operate in nonlinear regimes of motion. IRCs may for instance limit the practical applicability of nonlinear absorbers [64, 182], as shown in Chapter 5. IRCs were also found in other applications, such as shimmying wheels [189] and structures with cyclic symmetry [168], which demonstrates their generic character.

This chapter is organized as follows. In Section 3.2, the case study which serves for illustrating the developments of this chapter is introduced. In Section 3.3, two methods, namely the nonlinear phase lag quadrature criterion and the energy balance criterion, are presented to relate NNMs to the fundamental resonances. Both methodologies are applied in Section 3.4 to predict isolated resonances. Fold bifurcation tracking is then employed for validating the predictions, and for characterizing the merging scenarios. The conclusions of the chapter are finally given in Section 3.5.

# 3.2 Description of the Nonlinear Cantilever Beam

In this chapter, the numerical model of a cantilevered beam with a cubic nonlinear spring attached at its free end is considered [142]. A schematic of the beam is shown in Fig. 3.1. It is 0.7 m in length, with a width and thickness of 0.014 m, and is constructed of structural steel with a Young's modulus of 205 GPa and a density of 7800 kg/m$^3$. A lumped mass of $m = 0.5$ kg is added at a distance $a = 0.31$ m from the fixed end. The addition of the mass lowers the second natural frequency most, while having a minimal effect on the first mode. As will be seen in Fig. 3.7, this added mass shifts the location of a 3:1 internal resonance (IR) with NNM2 on the first NNM branch. A linear finite element model (FEM) of the planar beam was created using 20 Euler-Bernoulli beam elements, giving it a total of 60 degrees of freedom (DOF). The cubic nonlinear spring has a coefficient of $k_{nl} = 6\,10^9$ N/m$^3$.

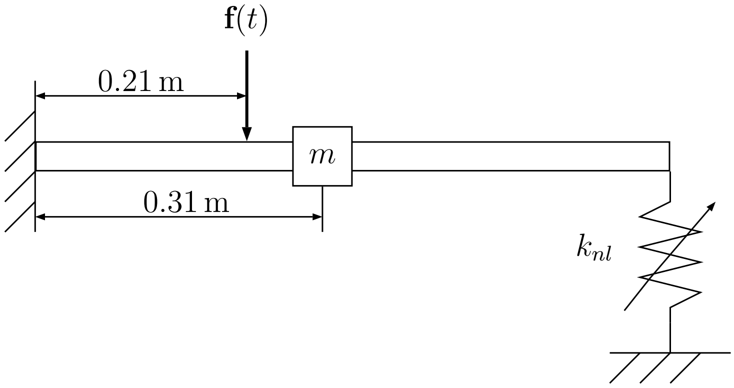

Figure 3.1: Schematic of a cantilever beam with a cubic nonlinear spring and a modifying lumped mass.

A mass and stiffness proportional damping model is used, defining the damping matrix as

$$\mathbf{C} = \kappa\,(a\mathbf{K} + b\mathbf{M}) \tag{3.1}$$

with $a = -0.0391$ and $b = 1.47\,10^{-4}$, where $\kappa$ is a parameter initially set to 1. Table 3.1 gives the natural frequencies and associated damping ratios for the first five modes. For excited configurations, forcing is applied vertically at 0.21 m from the clamping.

| Mode | Natural frequency ($Hz$) | Damping ratio (%) |
|---|---|---|
| 1 | 21.99 | 1.00 |
| 2 | 108.48 | 5.55 |
| 3 | 395.02 | 18.22 |
| 4 | 701.96 | 32.37 |
| 5 | 1861.52 | 85.85 |

Table 3.1: Linear natural frequencies and damping ratios of the nonlinear beam.

As for the spacecraft structure in Chapter 2, condensation of the underlying linear model can be effectively achieved using the Craig-Bampton reduction technique [14]. The reduced-order model keeps the nonlinear node at the tip of the beam, together with the excited node. The FEM is thereby reduced to 2 physical DOFs (excluding horizontal displacement and rotation), and 5 internal modes are sufficient to ensure an acceptable correspondence with the full system. The harmonic balance (HB) continuation tools presented in Chapter 1 for NFRCs and NNMs can then be employed on the resulting model. In this chapter, 9 harmonics are considered in the HB approximation.

## 3.3 Relating Fundamental Resonances and Nonlinear Normal Modes

NNM motions are known to appear in the vicinity of nonlinear resonance peaks. This feature is illustrated in Fig. 3.2, which compares the first resonance peak of the nonlinear beam at different levels $f$ of harmonic forcing, with the projection of the first NNM. The NNM backbone traces the locus of the resonance peaks; it is therefore clear that the resonant response of a structure can be characterized through the excitation of the corresponding NNM.

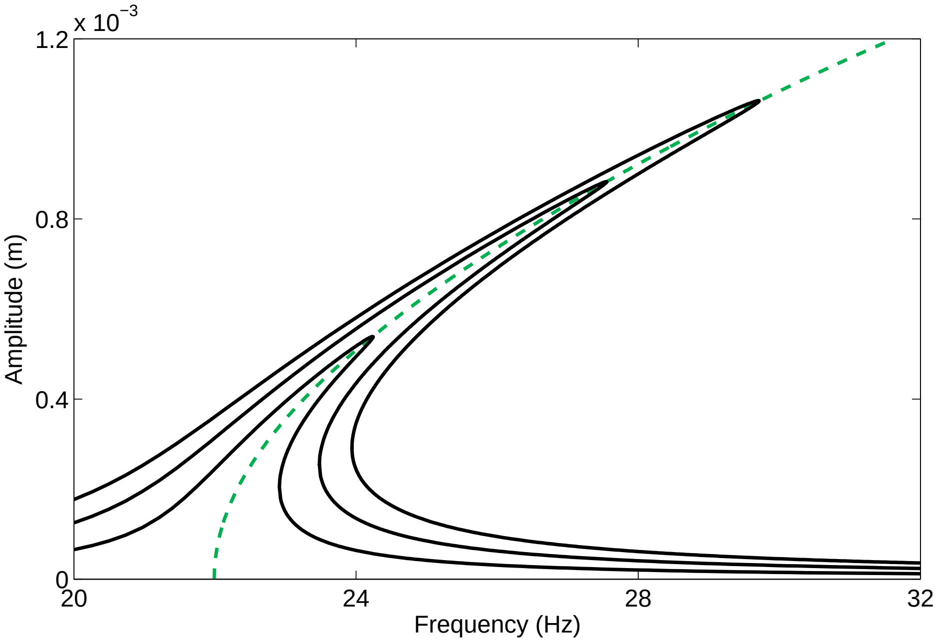

Figure 3.2: Relation between the backbone of the first NNM of the beam and the fundamental resonance. The solid lines represent the NFRCs computed for $f = 0.5\,\text{N}$, $f = 1\,\text{N}$, and $f = 1.5\,\text{N}$, and the dashed line depicts the projection of NNM1 in the frequency-response amplitude plane.

Although the use of a single-point and monoharmonic forcing is often sufficient to isolate NNM motions, as in Fig. 3.2, the procedure is approximate. Following the HB formalism, however, a rigorous procedure can be derived to determine the forcing profile required to appropriate a NNM. In Chapter 1, the equations of motion for forced periodic solutions of a damped system, and for free periodic responses of its underlying Hamiltonian, *i.e.*, for its NNMs, were written as:

$$\begin{aligned} \mathbf{h}\left(\mathbf{z},\omega\right) &= \left(\boldsymbol{\nabla}^2 \otimes \mathbf{M}\right)\mathbf{z} + \left(\boldsymbol{\nabla} \otimes \mathbf{C}\right)\mathbf{z} + \left(\mathbb{I}_{2N_H+1} \otimes \mathbf{K}\right)\mathbf{z} + \mathbf{b}_{nl} - \mathbf{b}_{ext} = \mathbf{0} \quad (3.2) \\ \mathbf{h}_{ham}\left(\mathbf{z},\omega\right) &= \left(\boldsymbol{\nabla}^2 \otimes \mathbf{M}\right)\mathbf{z} + \left(\mathbb{I}_{2N_H+1} \otimes \mathbf{K}\right)\mathbf{z} + \mathbf{b}_{nl} = \mathbf{0} \quad (3.3) \end{aligned}$$

where $\mathbf{b}_{nl}$ and $\mathbf{b}_{ext}$ are the vectors of the Fourier coefficients of the nonlinear and external forces, respectively, defined as

$$\begin{aligned} \mathbf{f}_{nl}(t) &= \left(\mathbf{Q}(t) \otimes \mathbb{I}_n\right)\mathbf{b}_{nl} \quad (3.4) \\ \mathbf{f}_{ext}(t) &= \left(\mathbf{Q}(t) \otimes \mathbb{I}_n\right)\mathbf{b}_{ext} \quad (3.5) \end{aligned}$$

Subtracting Eq. (3.3) from Eq. (3.2) then yields

$$\mathbf{b}_{ext} = \left(\boldsymbol{\nabla} \otimes \mathbf{C}\right)\mathbf{z} \quad (3.6)$$

Eq. (3.6) reveals an important relationship between the forced responses and the NNMs of the system. That is, if all harmonics of the external forces cancel out the harmonics of the damping forces, then the periodic response satisfies exactly the equations of motion (3.3) of the NNM.

In spite of these developments, two questions remain open:

1. How can resonance points be precisely located along a NFRC?
2. How can the NNM appropriation rule in Eq. (3.6) be simplified for single-point, monoharmonic forcing?

The present section provides an answer to these two questions, through the construction of the nonlinear phase lag quadrature and the energy energy balance criteria.

## 3.3.1 Nonlinear Phase Lag Quadrature Criterion

We start by rewriting the approximation of the displacements and forces in the complex domain:

$$\begin{aligned} \mathbf{x}(t) &= \sum_{k=1}^{N_H} \mathrm{Re}\left(\mathbf{X}_k e^{ik\omega t}\right) \quad (3.7) \\ \mathbf{f}_{nl}(t) &= \sum_{k=1}^{N_H} \mathrm{Re}\left(\mathbf{F}_{nl,k} e^{ik\omega t}\right) \quad (3.8) \\ \mathbf{f}_{ext}(t) &= \sum_{k=1}^{N_H} \mathrm{Re}\left(\mathbf{F}_{ext,k} e^{ik\omega t}\right) \quad (3.9) \end{aligned}$$

where $\mathbf{X}_k$, $\mathbf{F}_{nl,k}$ and $\mathbf{F}_{ext,k}$ correspond to the $n \times 1$ vectors containing the complex amplitude of the displacements, nonlinear and external forces, respectively, for the $k$-th harmonic frequency.

By substituting Eqs. (3.7-3.9) and the time derivatives of the displacement vector into the equations of motion (1.1), each harmonic can be balanced to give two relations:

$$-k^2\omega^2\mathbf{M}\mathbf{X}_k + \mathbf{K}\mathbf{X}_k + \mathbf{F}_{nl,k} = 0 \tag{3.10}$$

$$ik\omega\mathbf{C}\mathbf{X}_k = \mathbf{F}_{ext,k} \tag{3.11}$$

Expressions (3.10) and (3.11) are equivalent to Eqs. (3.3) and (3.6), respectively. However, their geometric interpretation, illustrated in Fig. 3.3, provides useful information about how the multi-point, multiharmonic forcing is adjusted when a NNM motion is appropriated. It demonstrates that at resonance, each harmonic of the displacement is 90 degrees out of phase with respect to the force harmonics. This so-called nonlinear phase lag quadrature criterion thus indicates when a NNM motion has been isolated from a NFRC [142], and is the nonlinear extension of the linear phase lag quadrature criterion [61].

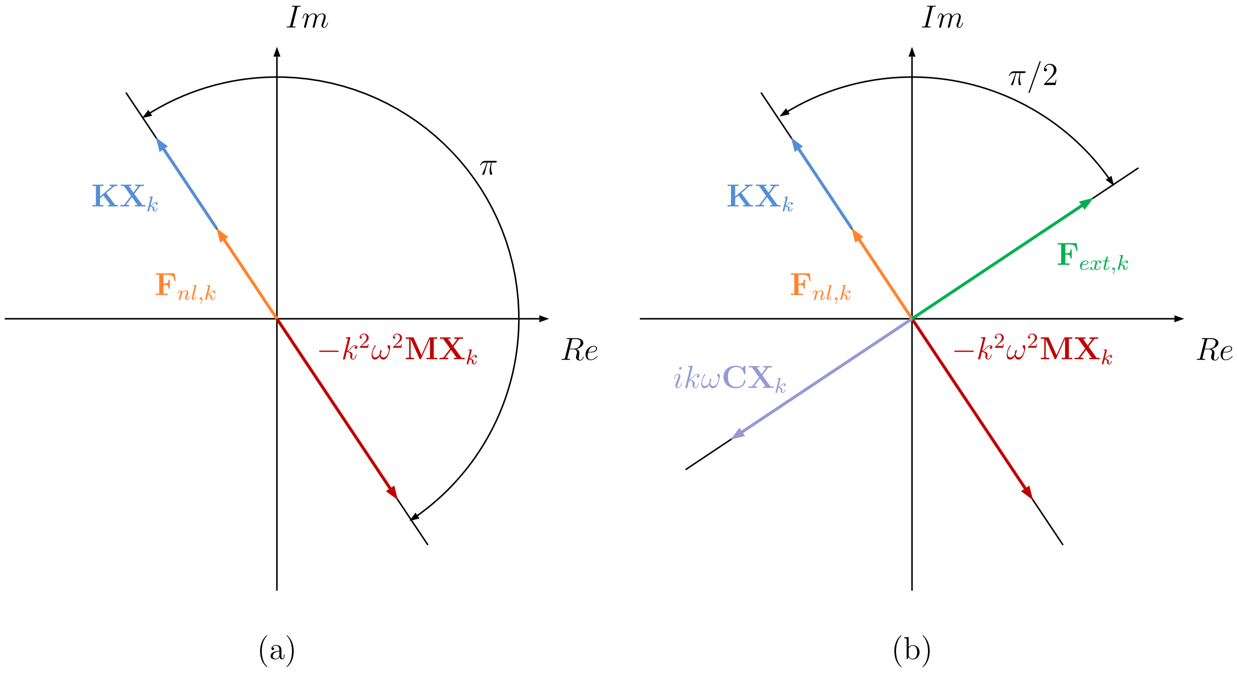

Figure 3.3: Schematic representation of the nonlinear phase lag quadrature criterion for the harmonic $k$, inspired by [61, 150]. (a) NNM motion; (b) NNM motion at the resonance of a damped system.

In [143], Peeters *et al.* defined a multiharmonic mode indicator function (MIF) which indicates when the 90-degree phase lag condition is obtained. As shown experimentally and numerically in [49, 103, 142, 143, 204], the phase lag quadrature criterion also proves accurate for single-point, monoharmonic forcing profile. In this case, the associated MIF can be defined as

$$\Delta_1 = \frac{\mathrm{Re}(\mathbf{X}_1)^* \mathrm{Re}(\mathbf{X}_1)}{\mathbf{X}_1^* \mathbf{X}_1} \tag{3.12}$$

where the operator $(\cdot)^*$ represents the complex conjugate transpose. Using the complex amplitude of the fundamental harmonic, $\mathbf{X}_1$, of the computed NFRC, resonance occurs when $\Delta_1$ is equal to one. Eq. (3.12) can also be written using the formalism of Eq. (1.2) with the vectors $\mathbf{s}_1^x$ and $\mathbf{c}_1^x$ of the Fourier coefficients related to the sine and cosine of the fundamental frequency, respectively, which reads

$$\Delta_1 = \frac{\left(\mathbf{c}_1^x\right)^{\mathrm{T}} \left(\mathbf{c}_1^x\right)}{\left(\mathbf{c}_1^x\right)^{\mathrm{T}} \left(\mathbf{c}_1^x\right) + \left(\mathbf{s}_1^x\right)^{\mathrm{T}} \left(\mathbf{s}_1^x\right)} \tag{3.13}$$

where the operator $(\cdot)^{\mathrm{T}}$ denotes the transpose.

Thanks to the MIF, the resonances of the beam at the different forcing levels can be accurately located along the NFRC in Fig. 3.4.

### 3.3.2 Energy Balance Criterion

The motivation in this section is to determine the parameters of the forcing that appropriates a given NNM. A first analytical attempt in this direction [82, 83] used the second-order normal form theory to develop a nonlinear extension of the energy balance criterion [61]. Because this method assumes weak nonlinearity, we employ herein a numerical viewpoint to tackle strongly nonlinear regimes of motion.

We first consider a linear system that oscillates in a linear normal mode denoted as $\mathbf{x}(t)$. The damping forces instantaneously exert a distributed force $\mathbf{C}\dot{\mathbf{x}}(t)$ and the total energy dissipated over one period of oscillation $T$ is

$$E_{diss} = \int_0^T P_{diss}\, dt = \int_0^T \dot{\mathbf{x}}(t)^{\mathrm{T}} \mathbf{C} \dot{\mathbf{x}}(t)\, dt \tag{3.14}$$

where $P_{diss}$ is the power dissipated at any instant. Similarly, an arbitrary forcing function $\mathbf{f}_{ext}(t)$ inputs energy into the system as

$$E_{in} = \int_0^T P_{in}\, dt = \int_0^T \dot{\mathbf{x}}(t)^{\mathrm{T}} \mathbf{f}_{ext}(t)\, dt \tag{3.15}$$

where $P_{in}$ is the power input into the system at any instant. At resonance, the energy dissipated by the damping forces must match the total energy input to the system over the period $T$ [61]. The balance is enforced by setting

$$E_{diss} = E_{in} \tag{3.16}$$

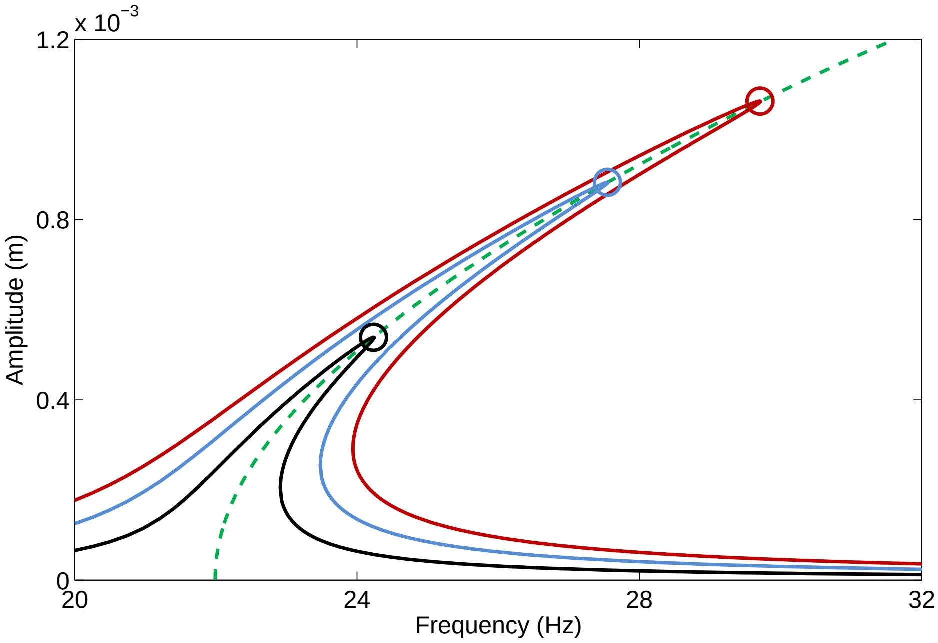

(a)

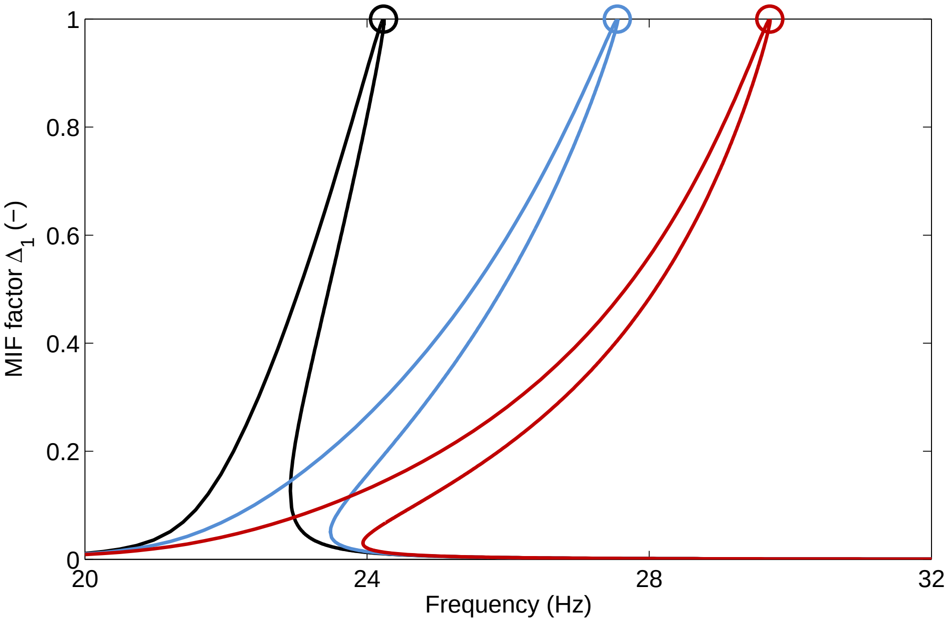

(b)

Figure 3.4: Location of resonances. (a) NFRCs computed at beam tip for $f = 0.5\,\mathrm{N}$ (in black), $f = 1\,\mathrm{N}$ (in blue) and $1.5\,\mathrm{N}$ (in red), and projection of NNM1 in the frequency-response amplitude plane (dashed line); (b) MIF. Circle markers denote solutions with $\Delta_1 = 1$.

Employing the HB formalism for nonlinear systems, $P_{diss}$ reads

$$P_{diss} = \dot{\mathbf{x}}(t)^{\mathrm{T}}\mathbf{C}\dot{\mathbf{x}}(t) = \mathbf{z}^{\mathrm{T}}\left[\left(\mathbf{Q}(t)\boldsymbol{\nabla}\otimes\mathbb{I}_n\right)^{\mathrm{T}}\mathbf{C}\left(\mathbf{Q}(t)\boldsymbol{\nabla}\otimes\mathbb{I}_n\right)\right]\mathbf{z} \tag{3.17}$$

Considering the expression of the transpose of the Kronecker tensor product and its the mixed-product property

$$\left(\mathbf{A}\otimes\mathbf{B}\right)^{\mathrm{T}} = \mathbf{A}^{\mathrm{T}}\otimes\mathbf{B}^{\mathrm{T}} \tag{3.18}$$

$$\left(\mathbf{A}\otimes\mathbf{B}\right)\left(\mathbf{C}\otimes\mathbf{D}\right) = \left(\mathbf{AC}\right)\otimes\left(\mathbf{BD}\right) \tag{3.19}$$

Eq. (3.17) can be rewritten as

$$\begin{aligned} P_{diss} &= \mathbf{z}^{\mathrm{T}}\left[\left(\boldsymbol{\nabla}^{\mathrm{T}}\mathbf{Q}^{\mathrm{T}}(t)\otimes\mathbb{I}_n\right)\left(1\otimes\mathbf{C}\right)\left(\mathbf{Q}(t)\boldsymbol{\nabla}\otimes\mathbb{I}_n\right)\right]\mathbf{z} \\ &= \mathbf{z}^{\mathrm{T}}\left[\left(\boldsymbol{\nabla}^{\mathrm{T}}\mathbf{Q}^{\mathrm{T}}(t)\otimes\mathbb{I}_n\right)\left(\mathbf{Q}(t)\boldsymbol{\nabla}\otimes\mathbf{C}\right)\right]\mathbf{z} \\ &= \mathbf{z}^{\mathrm{T}}\left[\left(\boldsymbol{\nabla}^{\mathrm{T}}\mathbf{Q}^{\mathrm{T}}(t)\mathbf{Q}(t)\boldsymbol{\nabla}\right)\otimes\mathbf{C}\right]\mathbf{z} \end{aligned} \tag{3.20}$$

The only term that depends on time in Eq. (3.20) is the vector $\mathbf{Q}(t)$ which, due to the fact that it represents an orthogonal trigonometric basis, verifies the property

$$\frac{2}{T}\int_0^T \mathbf{Q}^{\mathrm{T}}(t)\mathbf{Q}(t)dt = \mathbb{I}_{2N_H+1} \tag{3.21}$$

Computing $E_{diss}$ as the integral of Eq. (3.20) yields

$$\begin{aligned} E_{diss} &= \mathbf{z}^{\mathrm{T}}\left[\boldsymbol{\nabla}^{\mathrm{T}}\left(\int_0^T \mathbf{Q}^{\mathrm{T}}(t)\mathbf{Q}(t)\,dt\right)\boldsymbol{\nabla}\otimes\mathbf{C}\right]\mathbf{z} \\ &= \frac{\mathbf{z}^{\mathrm{T}}\left(\boldsymbol{\nabla}^{\mathrm{T}}\boldsymbol{\nabla}\otimes\mathbf{C}\right)\mathbf{z}T}{2} \end{aligned} \tag{3.22}$$

Depending on the assumption on the forcing profile, different expressions of the input energy can be derived. Considering a general multi-point and multiharmonic forcing $\mathbf{f}_{ext}(t) = \left(\mathbf{Q}(t)\otimes\mathbb{I}\right)\mathbf{b}_{ext}$, $P_{in}$ is computed as

$$\begin{aligned} P_{in} &= \mathbf{z}^{\mathrm{T}}\left[\left(\mathbf{Q}(t)\boldsymbol{\nabla}\otimes\mathbb{I}_n\right)^{\mathrm{T}}\left(\mathbf{Q}(t)\otimes\mathbb{I}_n\right)\right]\mathbf{b}_{ext} \\ &= \mathbf{z}^{\mathrm{T}}\left[\left(\boldsymbol{\nabla}^{\mathrm{T}}\mathbf{Q}^{\mathrm{T}}(t)\otimes\mathbb{I}_n\right)\left(\mathbf{Q}(t)\otimes\mathbb{I}_n\right)\right]\mathbf{b}_{ext} \\ &= \mathbf{z}^{\mathrm{T}}\left[\left(\boldsymbol{\nabla}^{\mathrm{T}}\mathbf{Q}^{\mathrm{T}}(t)\mathbf{Q}(t)\right)\otimes\mathbb{I}_n\right]\mathbf{b}_{ext} \end{aligned} \tag{3.23}$$

The input energy $E_{in}$ is:

$$\begin{aligned} E_{in} &= \mathbf{z}^{\mathrm{T}}\left[\boldsymbol{\nabla}^{\mathrm{T}}\left(\int_0^T \mathbf{Q}^{\mathrm{T}}(t)\mathbf{Q}(t)\,dt\right)\otimes\mathbb{I}_n\right]\mathbf{b}_{ext} \\ &= \frac{\mathbf{z}^{\mathrm{T}}\left(\boldsymbol{\nabla}^{\mathrm{T}}\otimes\mathbb{I}_n\right)\mathbf{b}_{ext}T}{2} \end{aligned} \tag{3.24}$$

Balancing Eqs. (3.22) and (3.24) reads

$$\frac{\mathbf{z}^{\mathrm{T}}\left(\boldsymbol{\nabla}^{\mathrm{T}}\boldsymbol{\nabla}\otimes\mathbf{C}\right)\mathbf{z}T}{2}=\frac{\mathbf{z}^{\mathrm{T}}\left(\boldsymbol{\nabla}^{\mathrm{T}}\otimes\mathbb{I}_n\right)\mathbf{b}_{ext}T}{2} \tag{3.25}$$

yielding, after simplification,

$$\mathbf{b}_{ext}=\left(\boldsymbol{\nabla}\otimes\mathbf{C}\right)\mathbf{z} \tag{3.26}$$

We thus retrieve Eq. (3.6), which demonstrates that the energy balance also holds for NNMs of nonlinear systems.

Considering now the more practical case of a monoharmonic force applied on a single DOF $l$, $\mathbf{f}_{ext}(t)=f\mathbf{e}_l\sin(\omega t)$, where $\mathbf{e}_l$ is a $n\times 1$ vector of zeros with a value of one at the component $l$:

$$\begin{aligned}P_{in} &= \mathbf{z}^{\mathrm{T}}\left(\mathbf{Q}(t)\boldsymbol{\nabla}\otimes\mathbb{I}_n\right)^{\mathrm{T}}\left(f\mathbf{e}_l\sin(\omega t)\right)\\ &= \mathbf{z}^{\mathrm{T}}\left[\left(\boldsymbol{\nabla}^{\mathrm{T}}\mathbf{Q}^{\mathrm{T}}(t)\otimes\mathbb{I}_n\right)\left(\sin(\omega t)\otimes 1\right)\right]f\mathbf{e}_l\\ &= \mathbf{z}^{\mathrm{T}}\left[\left(\boldsymbol{\nabla}^{\mathrm{T}}\mathbf{Q}^{\mathrm{T}}(t)\sin(\omega t)\right)\otimes\mathbb{I}_n\right]f\mathbf{e}_l\end{aligned} \tag{3.27}$$

Given that

$$\int_0^T \mathbf{Q}^{\mathrm{T}}(t)\sin(\omega t)\;dt=\frac{T\mathbf{e}_2}{2} \tag{3.28}$$

where $\mathbf{e}_2$ is a $(2N_H+1)\times 1$ vector of zeros with a value of one at the second component, we obtain

$$\begin{aligned}E_{in} &= \mathbf{z}^{\mathrm{T}}\left[\boldsymbol{\nabla}^{\mathrm{T}}\left(\int_0^T \mathbf{Q}^{\mathrm{T}}(t)\sin(\omega t)\;dt\right)\otimes\mathbb{I}_n\right]f\mathbf{e}_l\\ &= f\frac{\mathbf{z}^{\mathrm{T}}\left(\boldsymbol{\nabla}^{\mathrm{T}}\mathbf{e}_2\otimes\mathbb{I}_n\right)\mathbf{e}_lT}{2}\end{aligned} \tag{3.29}$$

Finally, the energy balance for a mono-point, monoharmonic forcing can be expressed as

$$\frac{\mathbf{z}^{\mathrm{T}}\left(\boldsymbol{\nabla}^{\mathrm{T}}\boldsymbol{\nabla}\otimes\mathbf{C}\right)\mathbf{z}T}{2}=f\frac{\mathbf{z}^{\mathrm{T}}\left(\boldsymbol{\nabla}^{\mathrm{T}}\mathbf{e}_2\otimes\mathbb{I}_n\right)\mathbf{e}_lT}{2} \tag{3.30}$$

or, equivalently,

$$f=\frac{\mathbf{z}^{\mathrm{T}}\left(\boldsymbol{\nabla}^{\mathrm{T}}\boldsymbol{\nabla}\otimes\mathbf{C}\right)\mathbf{z}}{\mathbf{z}^{\mathrm{T}}\left(\boldsymbol{\nabla}^{\mathrm{T}}\mathbf{e}_2\otimes\mathbb{I}_n\right)\mathbf{e}_l} \tag{3.31}$$

This relation represents an important result because, given a forcing frequency $w$, a specific NNM $\mathbf{z}$ and the damping matrix $\mathbf{C}$, it estimates the forcing amplitude $f$ that excites the system at resonance with associated NNM motion $\mathbf{x}(t)$.

Considering the backbone of the first NNM of the beam depicted in the frequency-energy plot (FEP) in Fig. 3.5(a), the forcing amplitude calculated through Eq. (3.31) is shown in Fig. 3.5(b). Fig. 3.6 superposes the crosses in Fig. 3.5(b) corresponding to forcing amplitudes of 0.5 N, 1 N and 1.5 N to Fig. 3.4. The crosses and the circles correspond very well in Fig. 3.6, indicating an excellent agreement between the predictions of energy balance and the actual resonance peaks detected with the MIF.

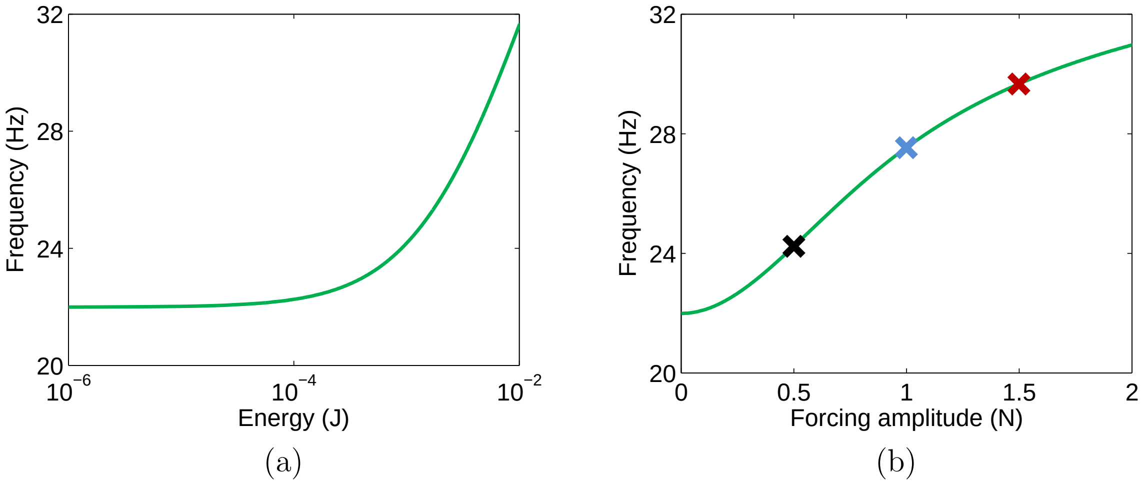

Figure 3.5: Energy balance applied to NNM1. (a) FEP of the portion studied; (b) forcing amplitude predicted by energy balance. Cross markers indicate forcing amplitudes of interest.

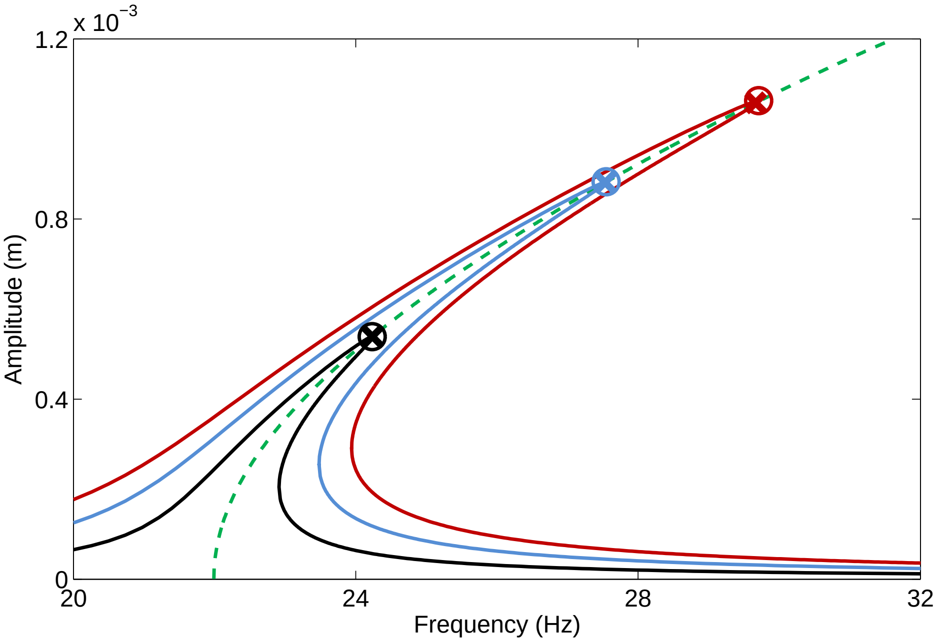

Figure 3.6: Comparison between the resonances detected with the MIF in Fig. 3.4 (circle markers) and the NNM motions determined from the energy balance criterion in Fig 3.5 (cross markers). NFRCs computed at beam tip for $f = 0.5\,\mathrm{N}$ (in black), $f = 1\,\mathrm{N}$ (in blue) and $1.5\,\mathrm{N}$ (in red), and projection of NNM1 in the frequency-response amplitude plane (dashed line).

## 3.4 Relating Isolated Resonances and Nonlinear Normal Modes

The purpose of this section is to apply the nonlinear phase lag quadrature and energy balance criteria in the presence of modal interactions.

### 3.4.1 Detection of Modal Interactions

The FEP shown in Fig. 3.7 is computed in a larger energy range. It presents two distinct features, namely a backbone, and tongues that emanate from the backbone. The tongues are related to IRs, as they occur when two or more NNMs interact (cf. Section 2.5). For a better visualization of the IRs, Fig. 3.7 displays the frequency-energy behavior of the higher-order NNMs after dividing the frequency by various integers. By shifting these NNMs down the frequency axis, it is possible to observe the location where the backbones of higher modes intersect with the NNM1 backbone and cause an IR to occur. Considering the IR at approximately 37 Hz, the 1/3rd frequency branch of the NNM2 branch intersects the backbone of NNM1. This causes NNM1 to bifurcate and create a 3:1 IR tongue that has solutions where NNM1 and NNM2 interact. The other two IRs along NNM1 are 9:1 and 7:1 interactions with NNM3 near 44 Hz and 57 Hz, respectively.

The response at each of the points (a-d) along NNM1 is presented in Figs. 3.7(a-d) for the vertical displacement at the tip of the beam. At low energy, the response in Fig. 3.7(a) is dominated by the first linear mode. At higher energies, other harmonics contribute to the overall response, especially as one enters IRs, where the time series shows a strong, multiharmonic response at an integer frequency ratio of the interacting nonlinear mode. For example, the time response of point (b) clearly shows the contribution of a third harmonic due to the 3:1 resonance with NNM2. The same observations hold for the other IRs, with oscillations at the 9th and 7th harmonics of the fundamental frequency in Figs. 3.7(c) and (d), respectively.

### 3.4.2 Detection of Isolated Resonances

The result of energy balance applied to both the backbone and the tongues of IR of the FEP of the beam is depicted in Fig. 3.8. If only one resonance can be excited at low forcing amplitudes, the folding for $f = 22.3\,\mathrm{N}$ reveals the existence of multiple resonance scenarios beyond this forcing amplitude. For instance, for $f = 25\,\mathrm{N}$, three resonances depicted by crosses in Fig. 3.8 can be triggered.

For verification, the NFRCs for $f = 5\,\mathrm{N}$, 25 N, 32.5 N and 40 N are displayed in Figs. 3.9(a-d), respectively. At 5 N, a single resonance is detected by the MIF. At 25 N, an isolated response curve (IRC) appears in the NFRC. As predicted in Fig. 3.8, three resonances

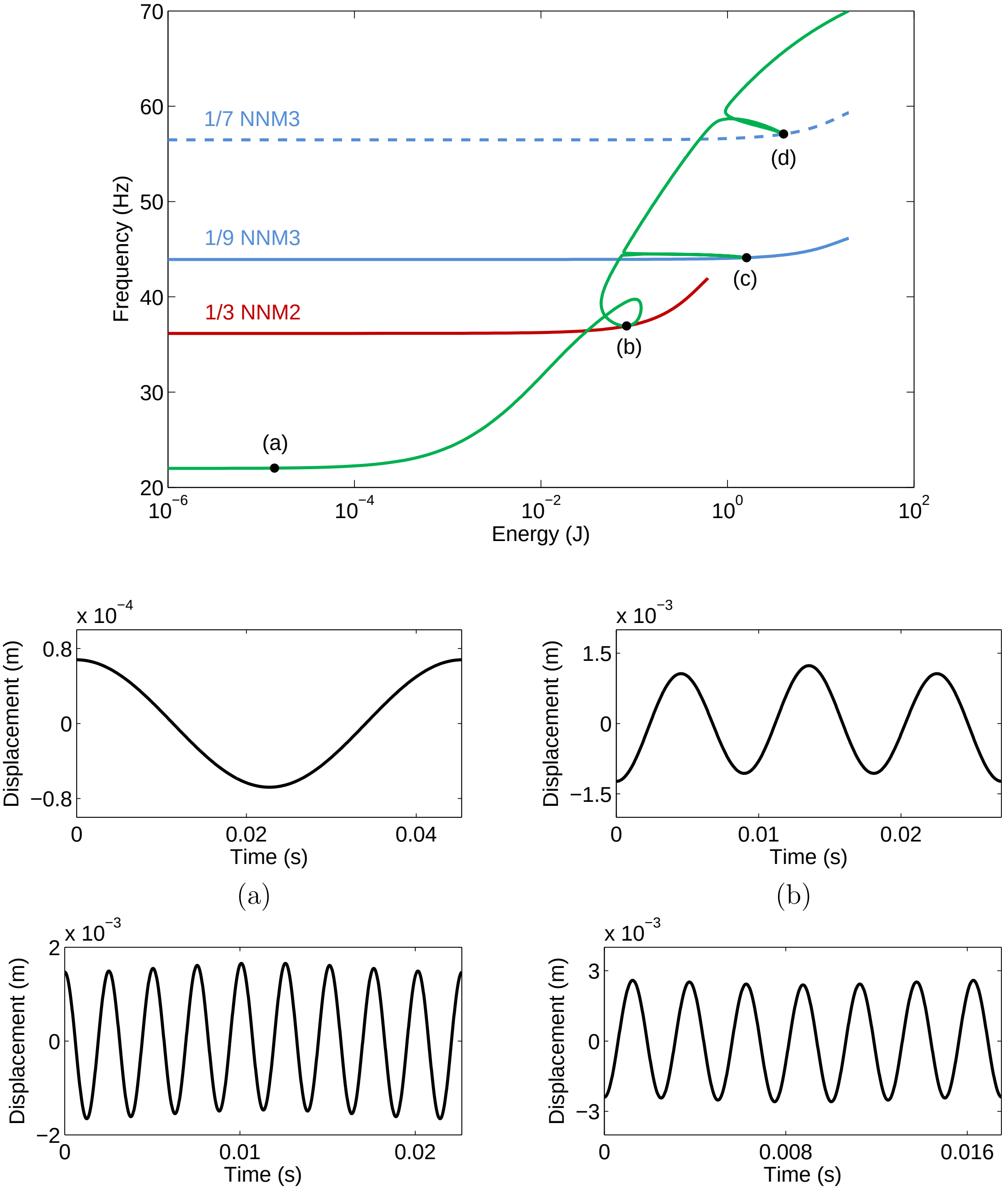

(a) (b)

(c) (d)

Figure 3.7: NNMs of the nonlinear beam. First NNM (in green), second NNM with a frequency divided by 3 (in red), third NNM with a frequency divided by 9 (solid blue line) and by 7 (dashed blue line). The time series of the vertical displacement at the tip of the beam and related to the NNMs represented with the black dots are given in (a), (b), (c) and (d).

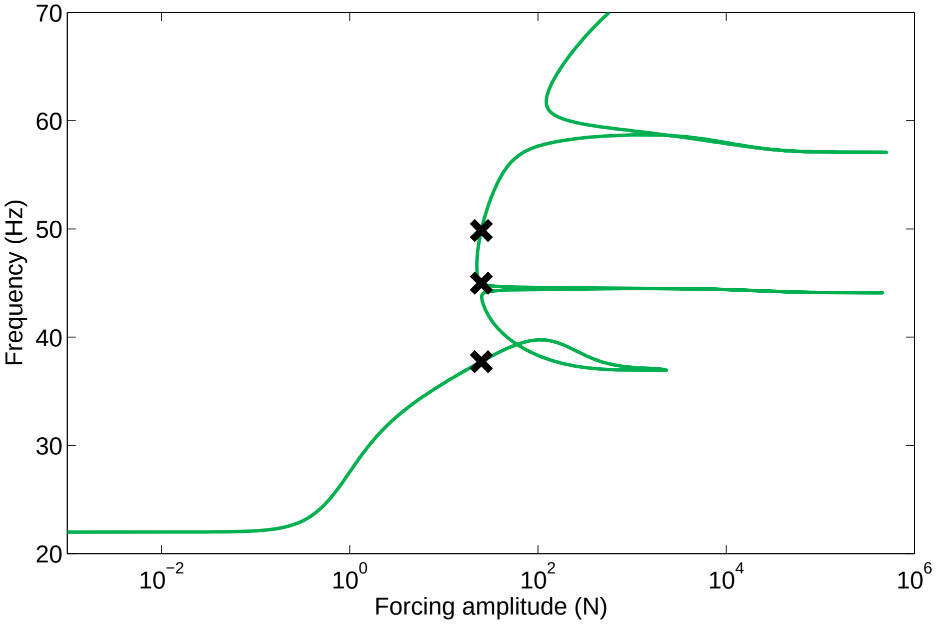

Figure 3.8: Forcing amplitude required to excite the NNMs of Fig. 3.7. Cross markers indicate NNM motions for $f = 25\,\mathrm{N}$.

exist, one on the main branch and two at the extremities of the IRC. At 32.5 N, the IRC expands along the backbone of the FEP until it merges with the main resonance peak at 40 N. An interesting observation in Fig. 3.9(d) is that this merging occurs in the vicinity of the 3:1 IR tongue, which shows the predominant role played by modal interactions in the creation and elimination of IRCs.

In summary, coupling the NNM theory with the energy balance methodology offers a way to unveil the presence of IRCs and to estimate the forcing amplitude at which these IRCs are created.

### 3.4.3 Fold Bifurcation Tracking

As discussed in Sections 1.3.2 and 2.6, fold bifurcations can be found near fundamental and isolated resonances. The tracking of fold bifurcations is thus applied to the nonlinear beam, which is illustrated in Fig. 3.10. As for the satellite, the branch of fold bifurcations turns back to reveal the IRC. The IRC is created when $f = 20.7\,\mathrm{N}$ and its merging with the fundamental resonance occurs for $f = 33\,\mathrm{N}$.

Fig. 3.11 shows the comparison between energy balance, which relies on the undamped, unforced dynamics, and fold bifurcations, which are in direct relation with forced, damped responses. On the main branch of Fig. 3.11, the predictions of energy balance are seen to be in very good agreement with the fold bifurcation branch, which means that the former

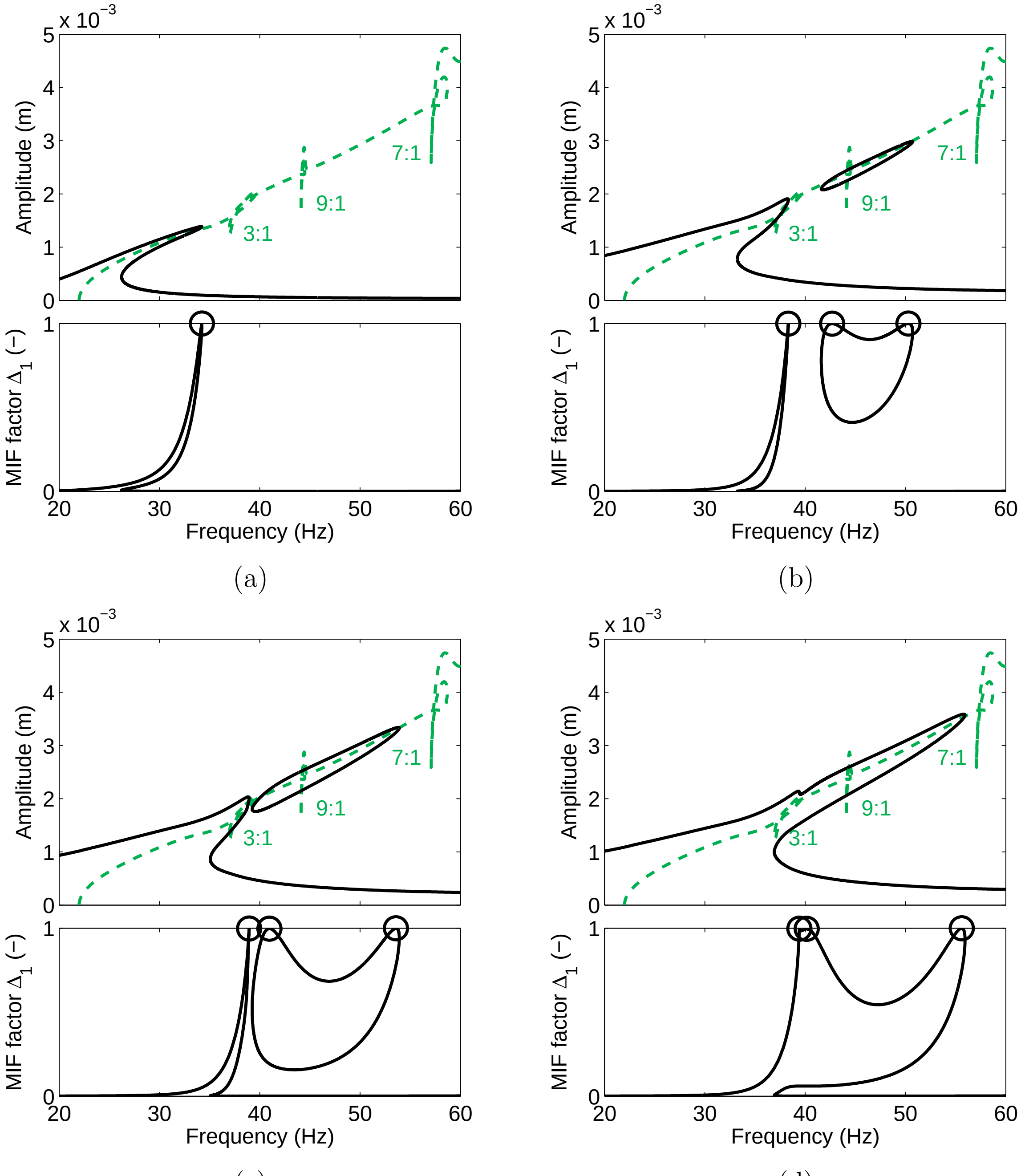

(a) (b)

(c) (d)

Figure 3.9: Multiple resonance scenarios for (a) $f = 5\,\mathrm{N}$, (b) $f = 25\,\mathrm{N}$, (c) $f = 32.5\,\mathrm{N}$ and (d) $f = 40\,\mathrm{N}$. In the top plots, solid and dashed line represent NFRCs and the projection of NNM1 in the frequency-response amplitude plane.

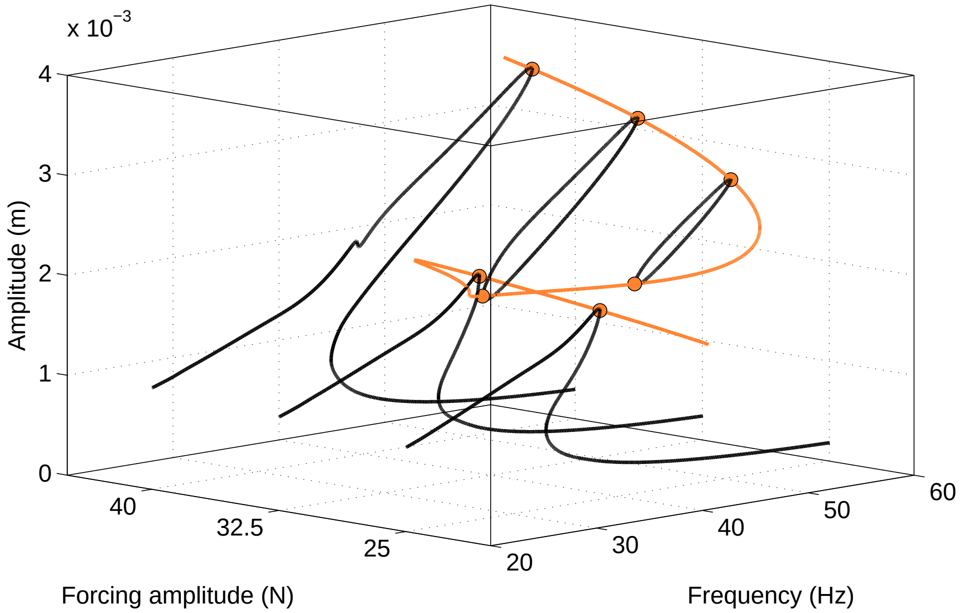

Figure 3.10: Branch of fold bifurcations (in orange) and NFRCs computed at the tip of the beam for $f = 25\,\mathrm{N}$, $32.5\,\mathrm{N}$, and $40\,\mathrm{N}$ (in black). Circle markers depict fold bifurcations.

technique can predict well the fundamental resonances and the creation of IRCs. However, the energy balance curve cannot predict accurately when the IRC merges with the main branch, which is due to the fact that the merging phenomenon is strongly affected by the damping forces, and involves higher harmonics of the fundamental frequency that are not considered in the energy balance. In addition, the energy balance curve exhibits foldings related to 9:1 and 7:1 IRs that are not found in the fold bifurcation branch.

Interestingly, the additional resonance scenarios can be triggered by a decrease in damping. For $\kappa = 0.1$ in Fig. 3.12(a), a new pair of fold bifurcations is created near $f = 1.3\,\mathrm{N}$ in the vicinity of the 7:1 IR. For $\kappa = 0.05$ in Fig. 3.12(b), another pair of bifurcations appears near $f = 15\,\mathrm{N}$ where the 9:1 IR occurs. To validate these findings, Figs. 3.13 and 3.14 present the complete NFRCs for $\kappa = 0.05$ and $f = 1.28\,\mathrm{N}$, 1.4 , $15\,\mathrm{N}$, $16\,\mathrm{N}$ and $25\,\mathrm{N}$. For $f = 1.28\,\mathrm{N}$, there exist two small IRCs which merge together in the vicinity of the 9:1 IR at $f = 1.4\,\mathrm{N}$. As shown in Fig. 3.14(a) for $f = 15\,\mathrm{N}$, this *super-IRC* expands along the NNM backbone, and a new IRC is also created in the vicinity of the 7:1 IR. For $f = 16\,\mathrm{N}$, the super IRC merges with the main resonance near the 3:1 IR (see Fig. 3.14(b)). Finally, the remaining IRC also connects to the main resonance close to the 3:1 IR when the forcing amplitude reaches $25\,\mathrm{N}$ in Fig. 3.14(c).

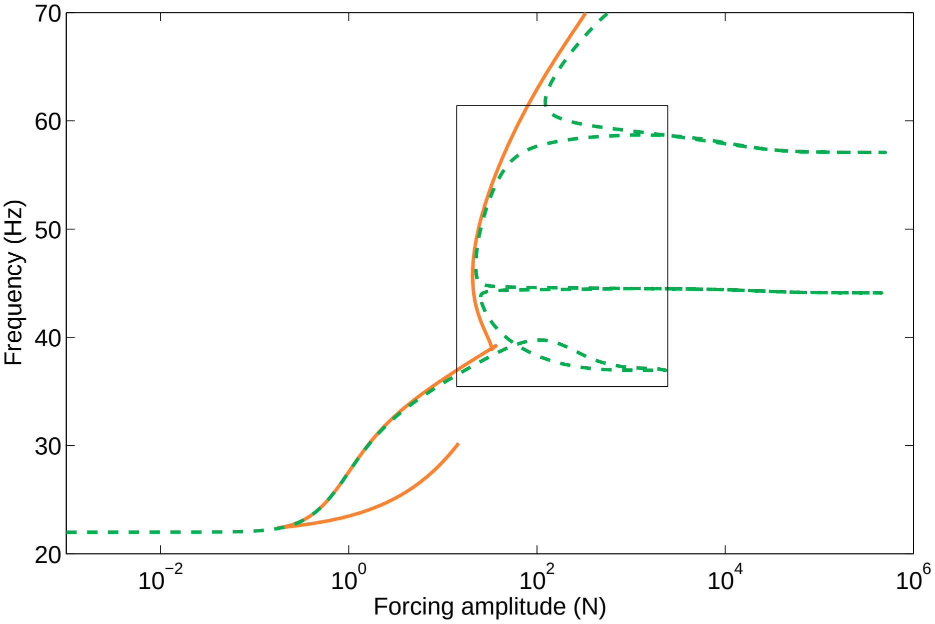

(a)

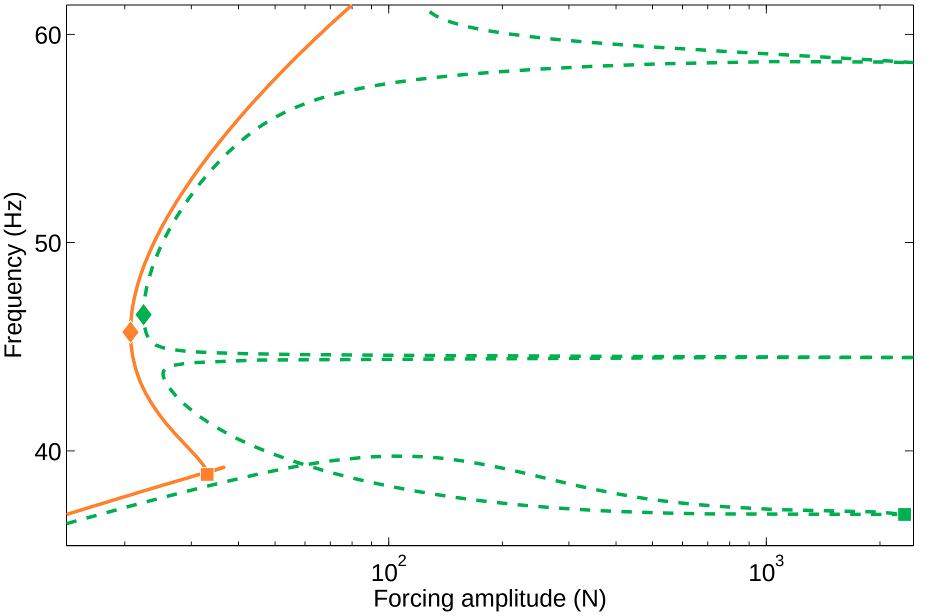

(b)

Figure 3.11: Prediction of IRCs using NNM1. (a) Forcing amplitudes required to excite the solutions along NNM1 and computed from the energy balance criterion (in green), and fold bifurcation curve (in orange); (b) close-up. The diamond and square markers indicate the creation of new solutions and their elimination, respectively.

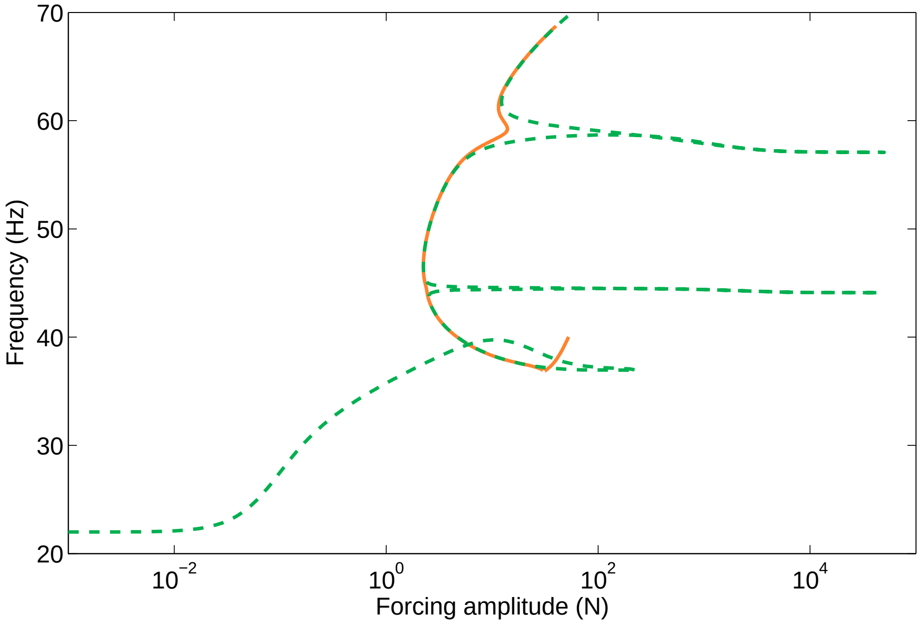

(a)

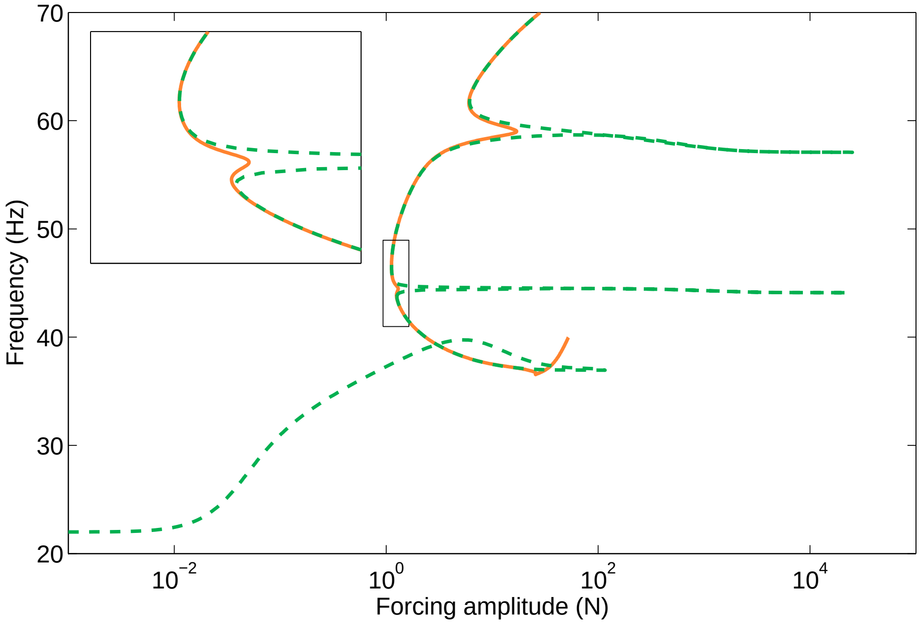

(b)

Figure 3.12: Influence of damping on the prediction of IRCs using NNM1. (a) $\kappa = 0.1$; (b) $\kappa = 0.05$. Forcing amplitudes required to excite the solutions along NNM1 computed from the energy balance criterion (in green), and fold bifurcation curve (in orange).

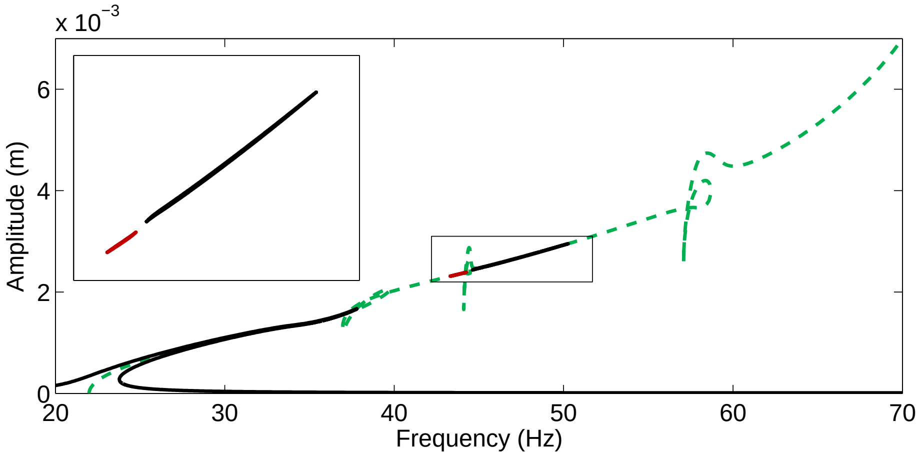

(a)

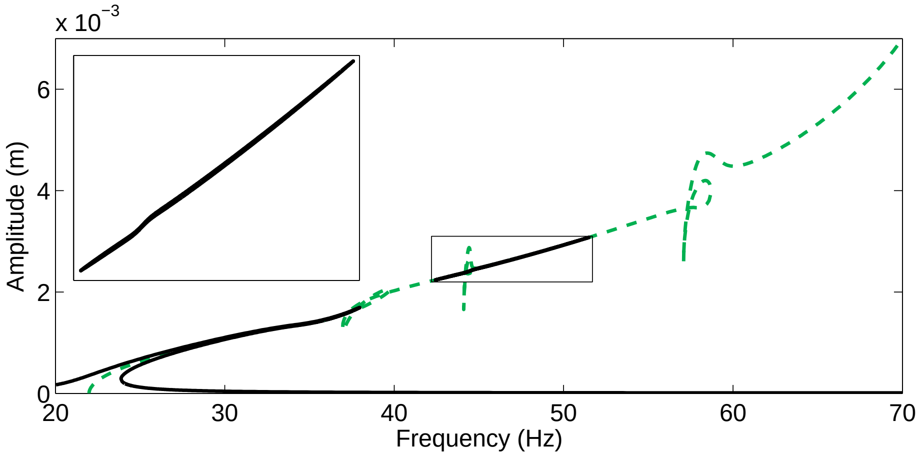

(b)

Figure 3.13: NFRCs (in black and red) and NNM1 (in green) computed for $\kappa = 0.05$. (a) $f = 1.28\,\mathrm{N}$; (b) $f = 1.4\,\mathrm{N}$.

### 3.4.4 IRC Merging Scenarios

For completeness, we mention that two different scenarios for the merging of IRCs exist, as schematized in Fig. 3.15. For the generic scenario called mushroom formation [10], a new pair of fold bifurcations is created during the merging process. The degenerate case rather involves the elimination of two fold bifurcations.

For $\kappa = 0.5$, the merging of the IRC near the 7:1 IR is degenerate, as confirmed in the close-up in Fig. 3.16(a); it can therefore be detected through the tracking of the fold bifurcations of the fundamental resonance, shown in Fig. 3.12(b). Conversely, the merging of the IRC around the 3:1 IR in Fig. 3.16(b) is generic. Because the merging process involves new bifurcations that do not belong to the bifurcation curve associated with the fundamental resonance, this scenario cannot be inferred from Fig. 3.12(b).

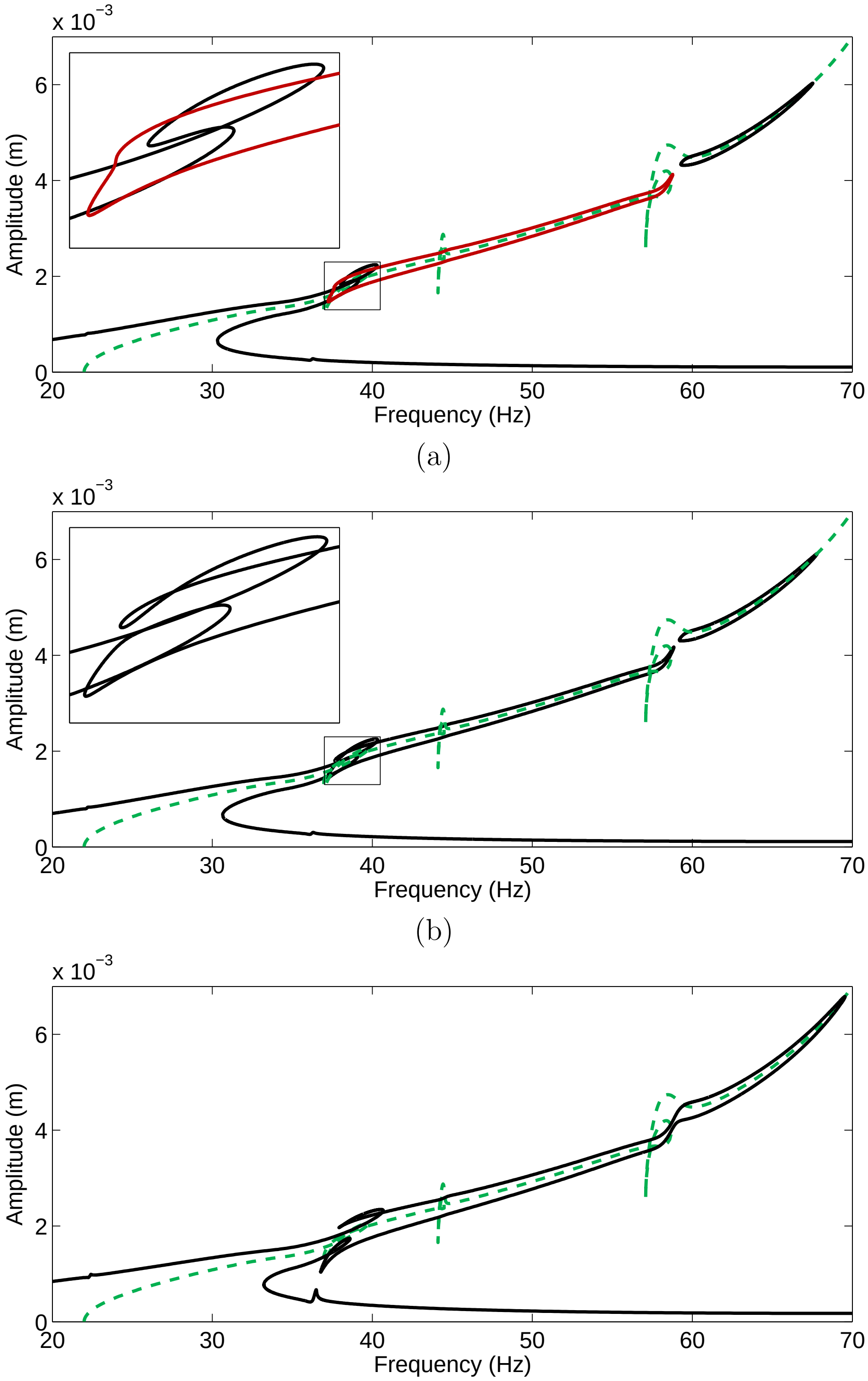

(a)

(b)

(c)

Figure 3.14: NFRCs (in black and red) and NNM1 (in green) computed for $\kappa = 0.05$. (a) $f = 15\,\mathrm{N}$; (b) $f = 16\,\mathrm{N}$; (c) $f = 25\,\mathrm{N}$.

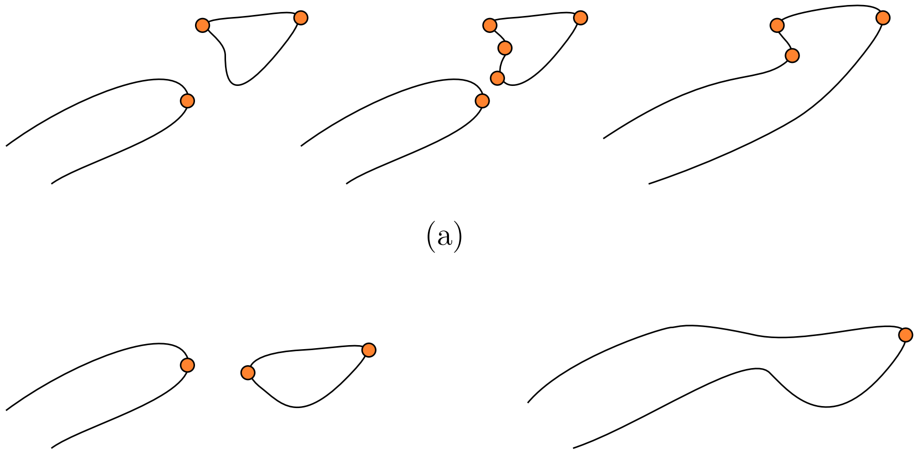

(a)

(b)

Figure 3.15: Schematic representation of IRCs and their (a) generic and (b) degenerate merging scenarios. NFRCs and fold bifurcations are represented with black lines and orange circle markers, respectively.

## 3.5 Concluding Remarks

The objective of this chapter was to reveal the intimate connection between nonlinear resonances and nonlinear normal modes. To establish the link that exists between these two concepts, the nonlinear phase quadrature and energy balance criteria were introduced.

Thanks to this theoretical framework, we could relate the creation of isolated response curves to the presence of interactions between nonlinear normal modes. It was shown that, for sufficiently low damping, very complex scenarios which involve the creation of several isolated curves that can merge together or with the fundamental resonance can exist. The tracking of fold bifurcations also proved useful for the study of isolated resonances, in particular for accurately predicting the forcing amplitudes at which mergings can occur. We note that there exist other mechanisms for the creation of isolated resonances, *e.g.*, involving isolated branches of nonlinear normal modes [85].

To provide further evidence of the existence and practical importance of isolated resonances, the next chapter studies the dynamics of an experimental two-degree-of-freedom system.

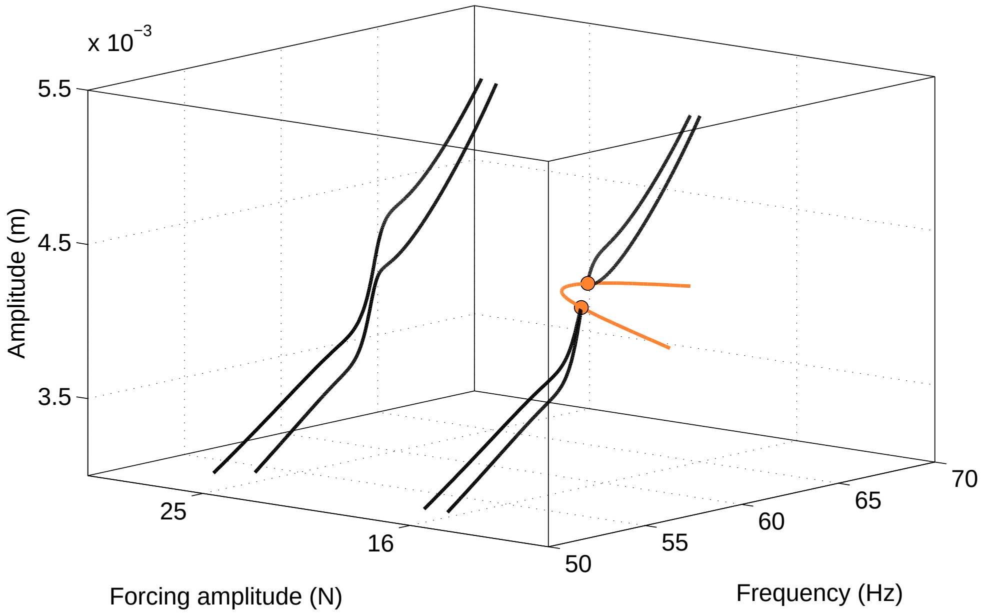

(a)

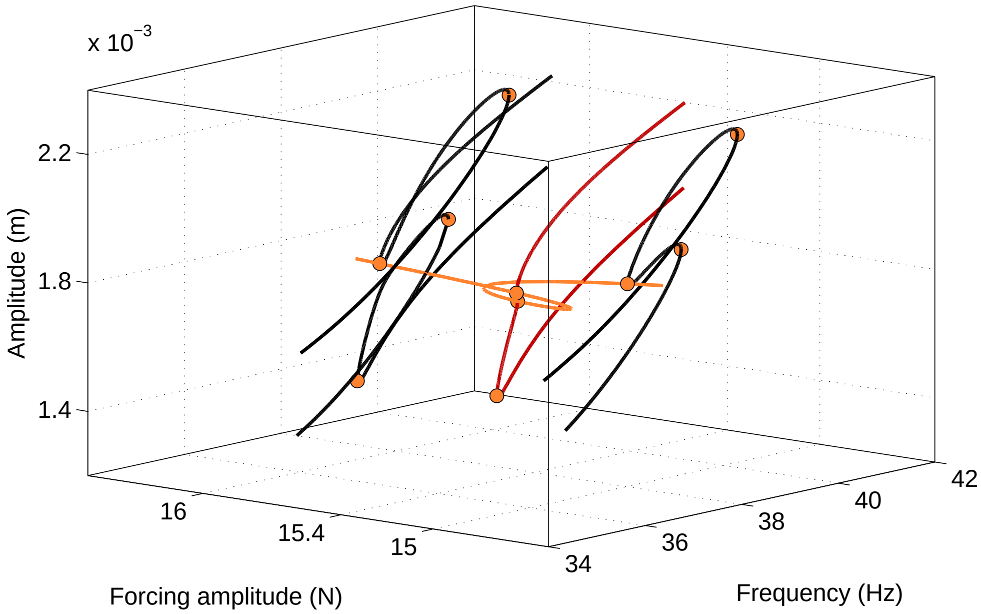

(b)

Figure 3.16: Merging of the IRC with the NFRC for the nonlinear cantilever beam. (a) Degenerate scenario near the 7:1 IR; (b) generic scenario near the 3:1 IR. NFRCs are represented with black and red lines, and orange circle markers denote fold bifurcations. For clarity, not all responses are displayed in (b).

# Chapter 4

# Experimental Characterization of Isolated Response Curves

### Abstract

In this chapter, the observation and characterization of isolated response curves (IRCs) are experimentally reported in the case of a nonlinear system consisting of two masses sliding on a horizontal guide. Transverse springs connect one of the masses to a support to provide a nonlinear restoring force, and the displacements of the support are prescribed with harmonic motion. The existence of an IRC in this system is related to a 3:1 internal resonance between its two fundamental modes. The observed IRC is studied in detached and merged conditions using swept-sine excitations. The main findings are validated using a numerical model.

## 4.1 Introduction

Chapter 3 established the link that exists between the internal resonances (IRs) in the undamped, unforced system and the isolated response curves (IRCs) of the damped, forced system. It was shown that the Hamiltonian dynamics highlights the possible scenarios for the creation of IRCs and that the amount of damping in the system dictates which scenario will be eventually realized. The objective of the present chapter is to provide an experimental demonstration of the creation and merging of IRCs in the context of a 3:1 IR between two nonlinear normal modes.

In the mechanical engineering literature, very few studies have been devoted to the experimental investigation of IRCs. In [58], Gatti *et al.* analyzed the dynamics of a Duffing oscillator attached to a shaker, and detected IRCs in the simulations performed on the numerical model of the set-up. The authors assessed the influence of the system's parameters on the domain of the IRC in [57]. In [60], remote attractors were detected in the response of an impacting pendulum. Gourc *et al.* also found IRCs while performing targeted energy transfer with a nonlinear energy sink [64]. To the best of our knowledge, however, no experimental set-up dedicated to the analysis of IRCs has been proposed so far.

The chapter is organized as follows. Section 4.2 presents the dedicated nonlinear set-up comprising two masses sliding on an horizontal guide. The response of the set-up to swept-sine excitations are investigated in Section 4.3 to reveal IRCs. In order to gain deeper understanding of the dynamics in play and to validate the experimental results, a numerical model is constructed in Section 4.4. The conclusions of the study are summarized in Section 4.5. Experimental data exploited in this chapter were collected during a stay at Duke University (NC, USA), in collaboration with Prof. L.N. Virgin.

## 4.2 Construction of an Experimental Set-Up Featuring an Internal Resonance

The experimental set-up comprises two masses sliding on an horizontal guide, as shown in Fig. 4.1. The masses are connected together and to the ground through steel extension springs, whose lengths and stiffnesses determine the static equilibrium of the system. Two transverse bungee chords are attached to the first mass to provide a nonlinear restoring force in the direction of motion. Damping in the system is mainly due to the bearings of the slide and to the rubber present in the chords. According to the discussions in Chapter 3, the set-up should ideally feature low damping; lubricant was used to attenuate friction in the bearings.

The displacement of the transverse chord supports is prescribed to impart motion to the two masses using a Scotch yoke flywheel [199]. The Scotch yoke converts rotational motion

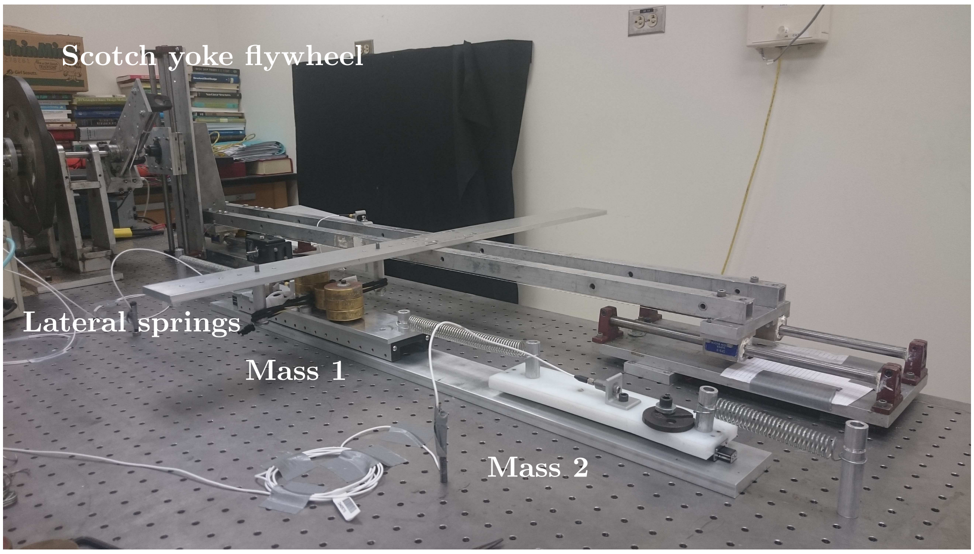

(a)

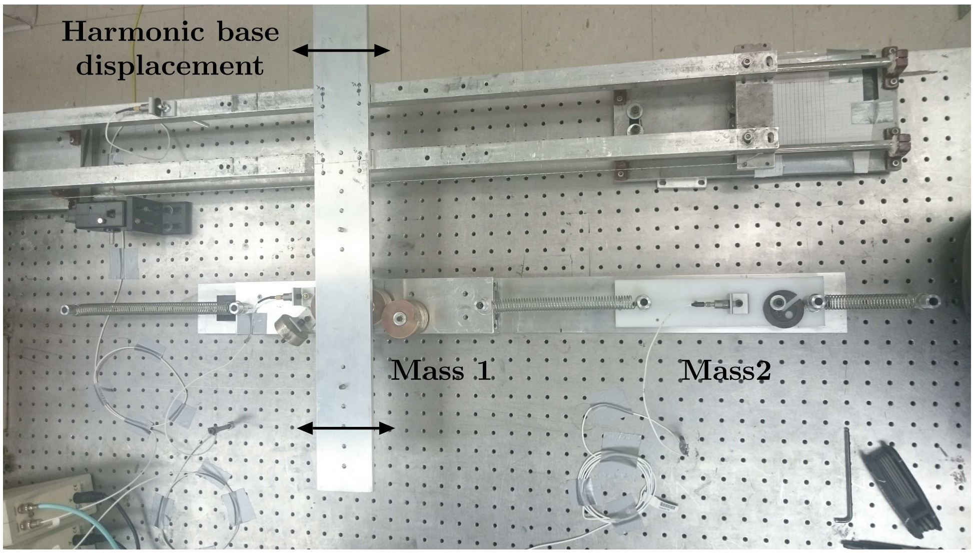

(b)

Figure 4.1: Experimental set-up. (a) Side view; (b) top view.

into a unidirectional harmonic displacement $d \sin(\omega t)$, where $d$ is the base displacement amplitude, and $\omega$ the excitation frequency. The frequency $\omega$ is limited to 2.8 Hz in the present experimental test rig, and the base displacement $d$ is set manually but can be accurately estimated.

Because the bungee chords are excited in their transverse direction, a geometrical nonlinearity is activated for sufficiently large base displacements. At rest, the chords are loosely connected to the support in order to create a connection with a nearly essentially nonlinear characteristic. A numerical study in [132] on a similar system demonstrated that this limited pre-stress facilitates the creation of IRCs. Fig. 4.2 shows an experimental qualitative estimate of the nonlinear restoring force using the restoring force surface (RFS) method [134]. The force features a clear hardening for moderate displacements, and a linear tangent for larger values.

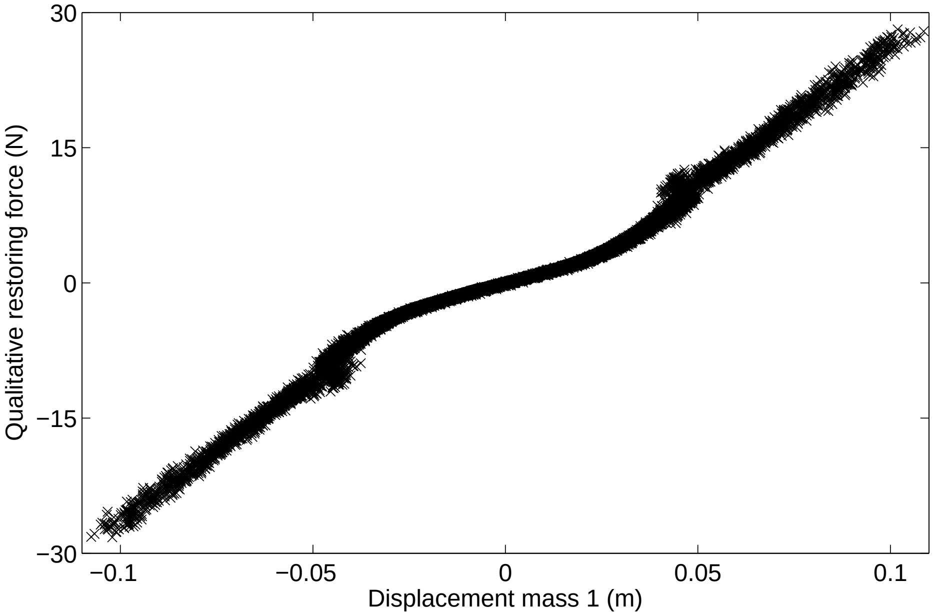

Figure 4.2: Experimental qualitative restoring force of the transverse connection, calculated for $d = 5.9\,\text{mm}$.

To realize an IRC, our target is a 3:1 IR between the first (in-phase) and second (out-of-phase) modes of the system. Because a strong hardening of the in-phase mode is expected, the masses, chords and springs are adapted to achieve a ratio between the two linear natural frequencies of the system greater than 3 and smaller than 5. Doing so, a 3:1 ratio between the resonance frequencies of the two modes can be realized for sufficiently large base displacements.

Due to the limitation of the excitation frequency, the second mode of the system cannot be directly observed to verify its resonance frequency. Instead, the time series of the free-decay analysis in Fig. 4.3(a) are utilized to extract the resonance frequencies of the modes using the wavelet transform in Fig. 4.3(b). The first mode exhibits a clear hardening, whereas the dependence on energy of the second mode is negligible. The resonance frequency of the second mode at low energy level is 6.45 Hz; for the first mode, due to the dependence on energy and the friction occurring at low amplitude, the resonance frequency is estimated around 1.5-1.6 Hz.

A weak second and a strong third harmonics of the excitation frequency are also present in Fig. 4.3(b). As anticipated, the combination of the energy dependence and the third harmonic involves a 3:1 IR between the in-phase and the out-of-phase modes, evidenced around 6.45 Hz for a fundamental frequency of 2.15 Hz in Fig. 4.3(b). This IR is also responsible for the distortion in the response of the second mass in Fig. 4.3(a).

## 4.3 Experimental Realization of IRCs

### 4.3.1 Evidence of IRCs

As discussed for the SmallSat spacecraft in Fig. 2.6(b), a method to reveal the presence of IRCs is to record the responses to swept-sine excitations of increasing amplitudes. This is carried out in Fig. 4.4 for values of $d$ ranging from 3.3 mm to 6 mm. When $d = 3.3$ mm, the geometrical nonlineary is not activated, and the dynamics is predominantly linear. From $d = 4$ mm to 5.7 mm, there is an increase in both amplitude and frequency at resonance, which is followed by the classical jump to low-amplitude solution. As $d$ becomes closer to 5.7 mm, the resonance frequency saturates near 2.15 Hz. Increasing $d$ from 5.7 mm to 5.8 mm leads to a dramatic increase (18.6%) in the resonance frequency from 2.15 Hz to 2.55 Hz. At that point, the merging of the main frequency response with an IRC is suspected. Fig. 4.5 depicts the sweep-up and sweep-down responses of mass 1 for a base amplitude of 5.9 mm, *i.e.*, after the merging of the IRC. Jumps down and up occur around 2.55 Hz and 1.8 Hz, respectively, which means that the system possesses a very large bistable region.

To bring additional experimental evidence of the IRC, time series corresponding to motions on the detached IRC are depicted in Fig. 4.6. To realize these time series, a base excitation of 5 mm and 2.38 Hz is considered. The system initially vibrates at low amplitudes, and a series of perturbations are applied to excite the IRC. Around $t = 10$ s, a high-amplitude motion stabilizes, which confirms the existence of the IRC. From there on, a sweep up followed by a jump around $t = 70$ s locates the right extremity of the stable portion of the IRC at 2.47 Hz. Between $t = 70$ s and $t = 110$ s, the excitation is swept back to 2.38 Hz, when a new series of perturbations is applied. At $t = 125$ s, the system is back on the IRC, and a sweep down permits to travel along the IRC until $t = 240$ s. This new jump locates the left extremity of the stable portion of the IRC at 2.16 Hz. Since the basin of attraction of the IRC shrinks as the limits of its stable part are reached, it might have happened that the system jumped before the actual change in stability. A solution

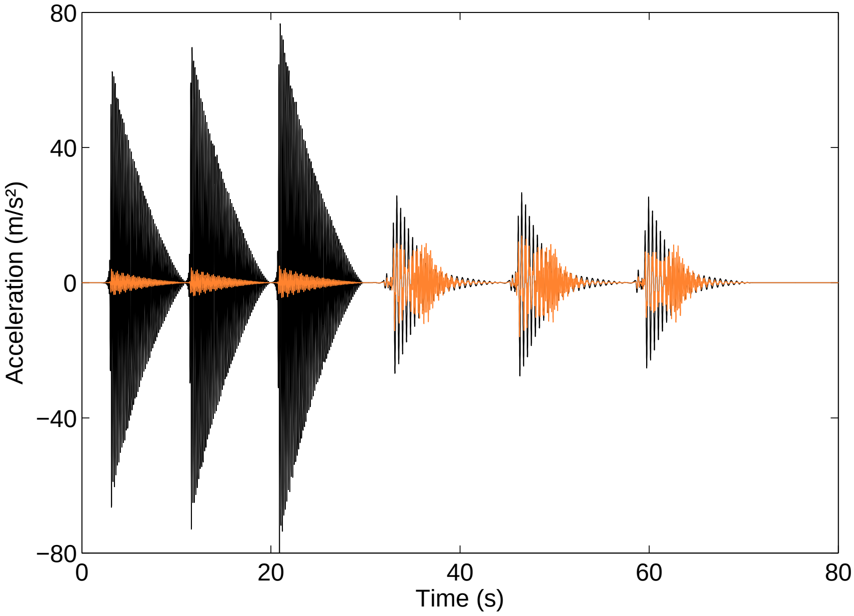

(a)

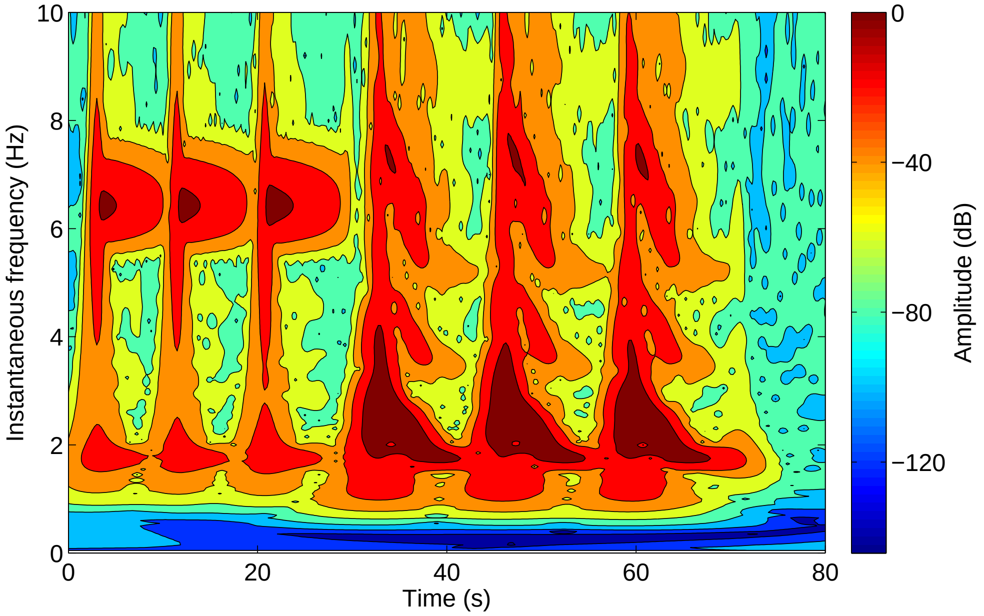

(b)

Figure 4.3: Free-decay analysis. (a) Displacements measured on mass 1 (in black) and mass 2 (in orange) in response to three impacts applied to mass 2 followed by three impacts applied to mass 1; (b) wavelet transform of mass 1 acceleration.

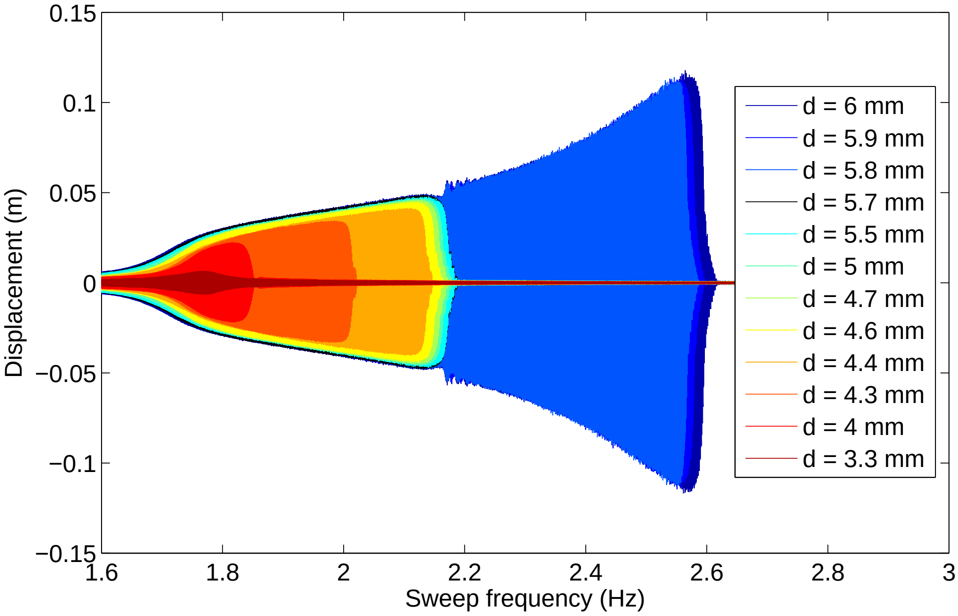

Figure 4.4: Responses of mass 1 to swept-sine excitations for different values of the base displacement $d$.

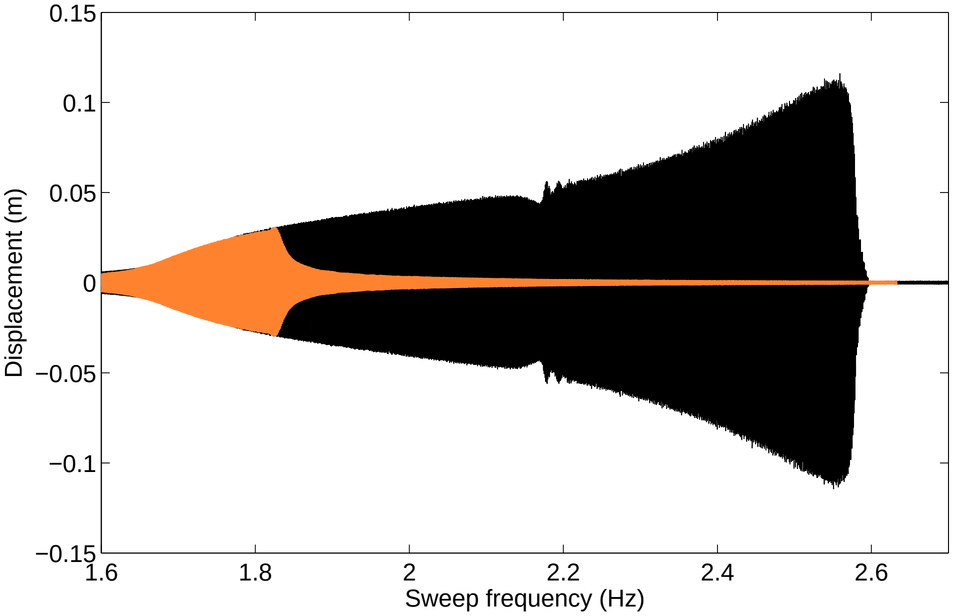

Figure 4.5: Response of mass 1 to swept-sine excitations with positive (in black) and negative (in orange) sweep rates, for $d = 5.9\,\mathrm{mm}$.

to this problem would be to perform stochastic interrogation in the frequency range of interest [199] or experimental continuation [17, 177].

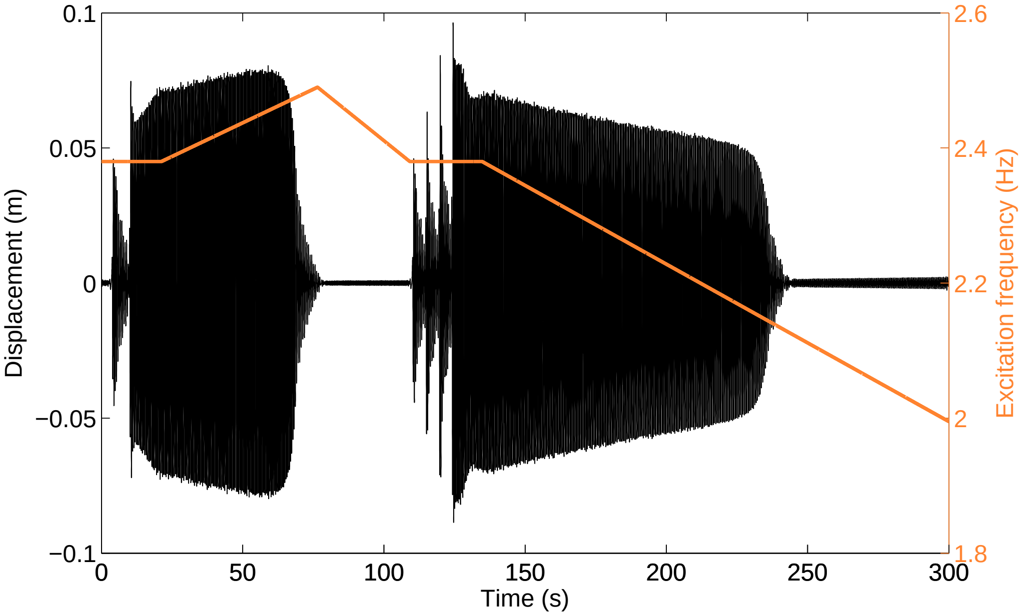

Figure 4.6: Realization of periodic solutions on the detached IRC by perturbations. The amplitude and initial frequency of the base excitation are $d = 5\,\mathrm{mm}$ and $\omega = 2.38\,\mathrm{Hz}$, respectively. The black and orange lines depict the displacement of mass 1 and the excitation frequency, respectively.

Further characterization of the IRC before merging is provided in Fig. 4.7. As the base displacement is increased from 4.5 mm to 4.9 mm, the main resonance peak and the left extremity of the IRC are seen to saturate in the vicinity of 2.15 Hz. Conversely, the right extremity of the IRC continues to expand toward greater frequencies, which confirms the growth of the IRC before the merging.

### 4.3.2 Relation with the 3:1 Internal Resonance

As observed in Figs. 4.4 and 4.7, both the main resonant response and the IRC saturates near 2.15 Hz before merging occurs. Since 2.15 Hz is precisely the third of the resonance frequency of the second mode, it is clear that the merging process occurs in the vicinity of the 3:1 IR between the in-phase and out-of-phase modes. This experimental result is thus the confirmation of the theoretical finding of Chapter 3 that modal interactions are one possible dynamical mechanism for the creation of IRCs. A closer investigation after merging is carried out in Fig. 4.8, which shows both acceleration signals near 2.15 Hz for $d = 5.9\,\mathrm{mm}$. A strong modulation of the time series is observed in Figs 4.8(a-b). The wavelet transform in Fig. 4.8(c) reveals the presence of a significant third harmonic component, the frequency of which coincides with the frequency of the out-of-phase mode. We refer the interested reader to [136] and [137] for videos of the swept-sine responses

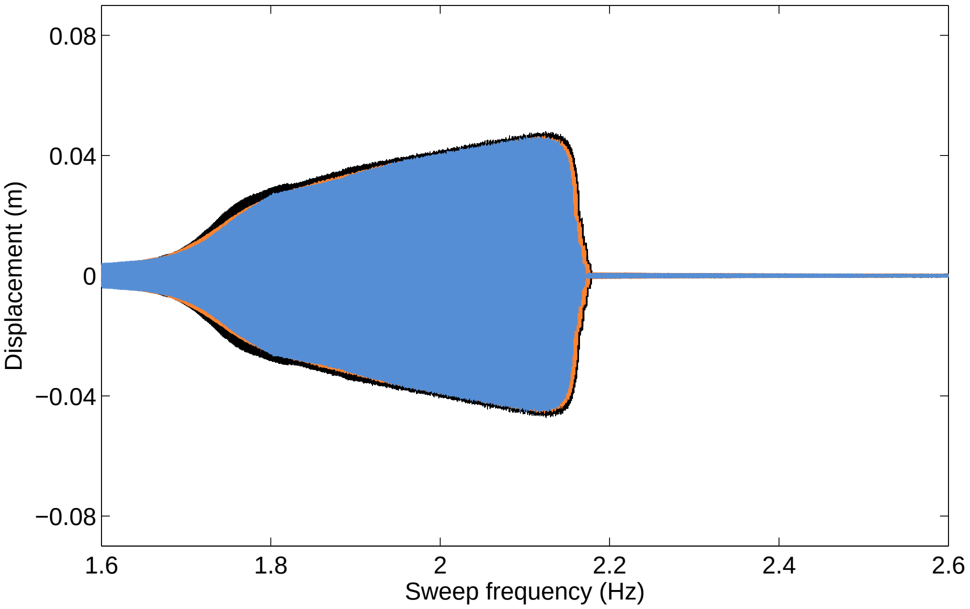

(a)

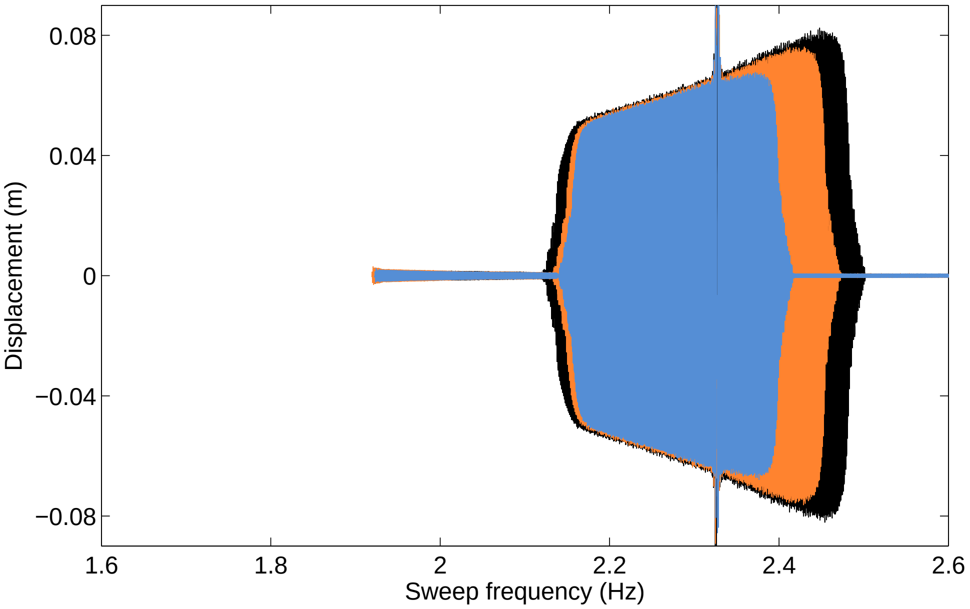

(b)

Figure 4.7: Evolution of (a) the main frequency response and (b) the IRC at mass 1, for $d = 4.5\,\mathrm{mm}$ (in blue), $4.7\,\mathrm{mm}$ (in orange) and $4.9\,\mathrm{mm}$ (in black). Sweep-up and sweep-down responses are superposed. IRCs are stabilized through perturbations at 2.33 Hz.

recorded near the merging region for isolated ($d = 5.7\,\mathrm{mm}$) and merged configuration ($d = 6\,\mathrm{mm}$), respectively. Both videos highlight the contributions of the third harmonic of the excitation frequency.

The response of the two masses for a stepped-sine excitation at 2.17 Hz is displayed in Fig. 4.9. The 3:1 IR is clearly visible in Fig. 4.9(b), whereas the modulation observed in Fig. 4.8 is repeated in Fig 4.9(a), which seems to relate to quasiperiodic oscillations with an envelope frequency of 0.1 Hz.

## 4.4 Model-Based Investigation of IRCs

### 4.4.1 Construction of a Numerical Model

A schematic representation of the set-up is provided in Fig. 4.10. Its equations of motion can be derived as

$$\begin{aligned} m_1\ddot{x}_1 + c_1\dot{x}_1 + k_1x_1 + k_2\left(x_1 - x_2\right) + f_{nl}\left(x\right) &= 0 \\ m_2\ddot{x}_2 + c_2\dot{x}_2 + k_2\left(x_2 - x_1\right) + k_3x_2 &= 0 \end{aligned} \tag{4.1}$$

where $x_1$ and $x_2$ are the absolute displacements of $m_1$ and $m_2$, respectively, $x = x_1 - d\sin\left(\omega t\right)$ is the displacement of $m_1$ relative to the displacement of the base, $k_1$, $k_2$ and $k_3$ are linear stiffness coefficients, and $c_1$ and $c_2$ are linear viscous damping coefficients. $f_{nl}$ represents the horizontal projection of the restoring force associated with the two transverse chords. This force can be theoretically written as

$$f_{nl}(x) = 2F\cos\left(\theta\right) = 2k\left(\sqrt{x^2+l^2} - l_0\right)\frac{x}{\sqrt{x^2+l^2}} = 2k\left(1 - \frac{\lambda}{\sqrt{1+\left(x/l\right)^2}}\right)x \tag{4.2}$$

where $F$ is the restoring force in the direction of a chord, $\theta$ is the angle between this direction and the horizontal, $k$, $l$ and $l_0$ denote the stiffness, length and natural length of the transverse chords, respectively, and $\lambda = l_0/l$ is the prestress parameter. The Taylor series expansion of Eq. (4.2) around 0 reads

$$f_{nl}(x) = 2k(1-\lambda)x + \frac{k\lambda}{l^2}x^3 + R_3(x). \tag{4.3}$$

Eq. (4.3) indicates the presence of a linear term in the restoring force that is related to the prestress of the chord, whereas the third-order term in the restoring force increases with $\lambda$. This confirms that limited prestress should be used to increase the nonlinear contribution in the transverse connection.

Several assumptions are associated to the model proposed in Eqs. (4.1):

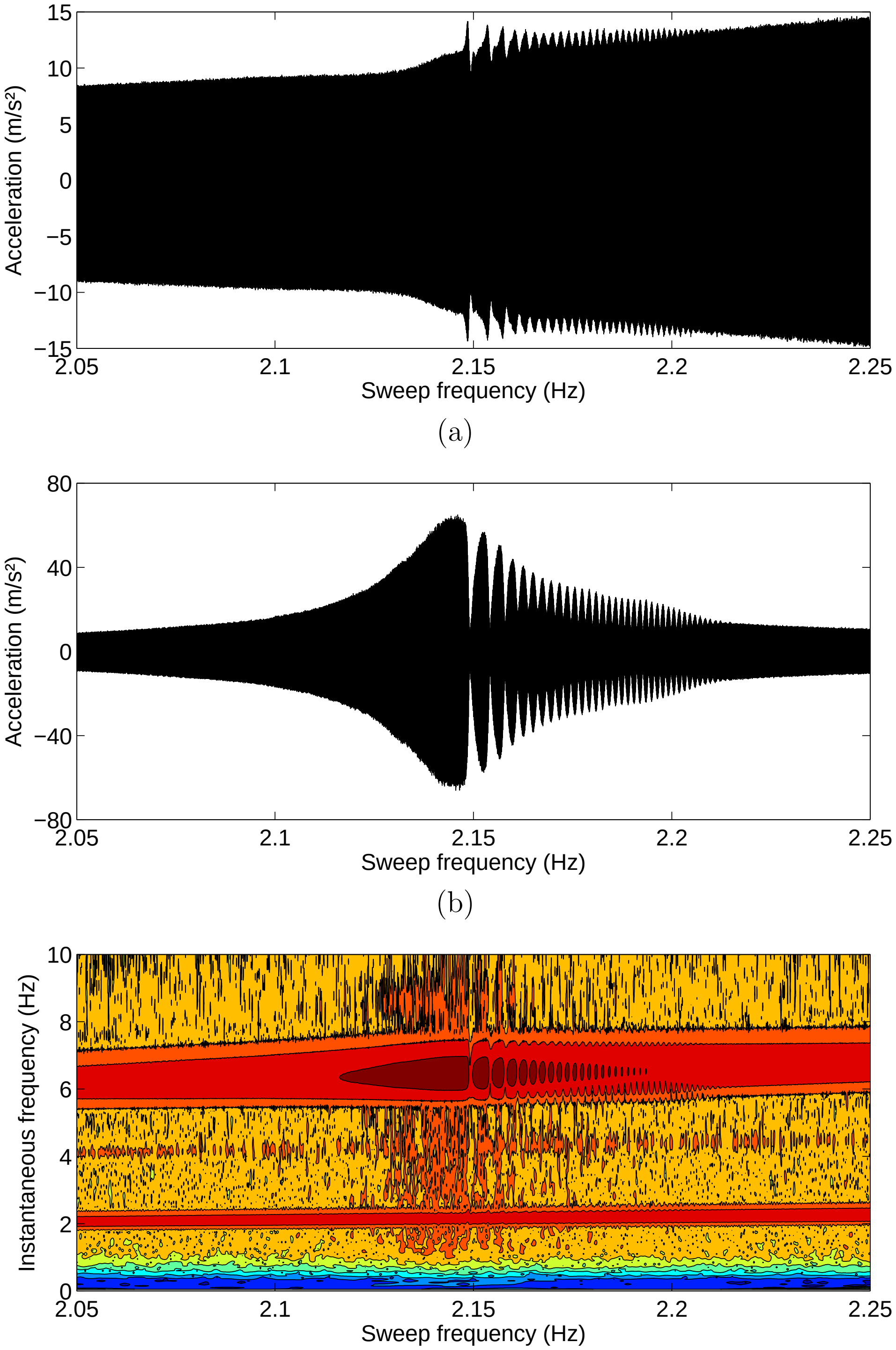

(a)

(b)

(c)

Figure 4.8: Close-up on the merging region. Accelerations of (a) mass 1 and (b) mass 2, and (c) wavelet transform of mass 2 acceleration in response to swept-sine excitations for $d = 5.9\,\mathrm{mm}$.

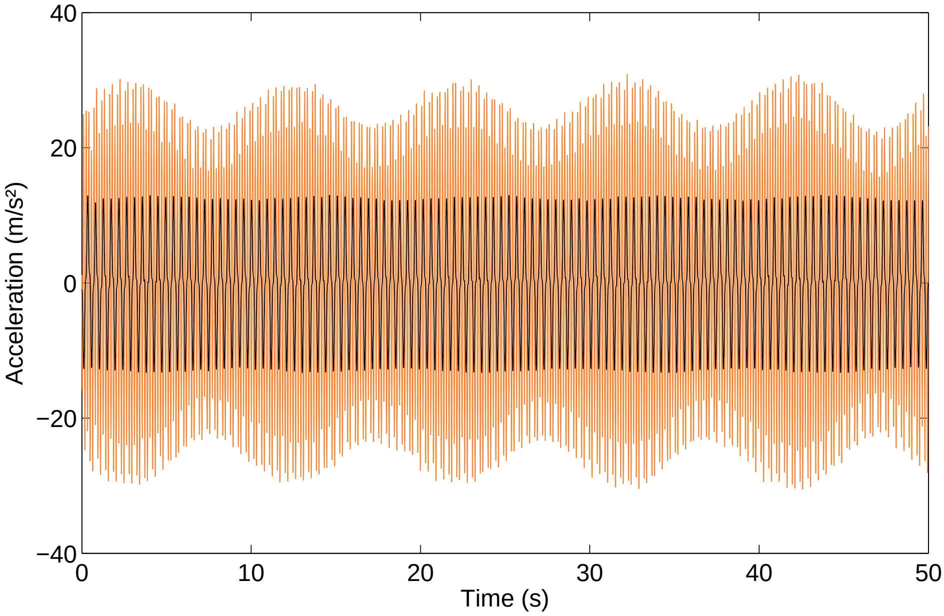

(a)

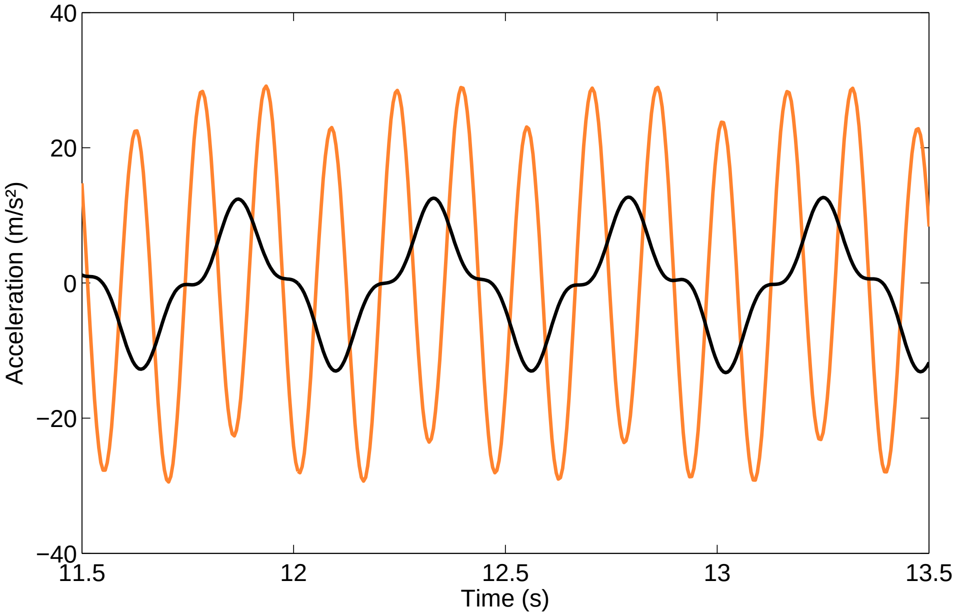

(b)

Figure 4.9: Evidence of the 3:1 IR. (a) Time series for the acceleration of mass 1 (in black) and 2 (in orange), for $d = 5.9\,\mathrm{mm}$ and $\omega = 2.17\,\mathrm{Hz}$; (b) close-up.

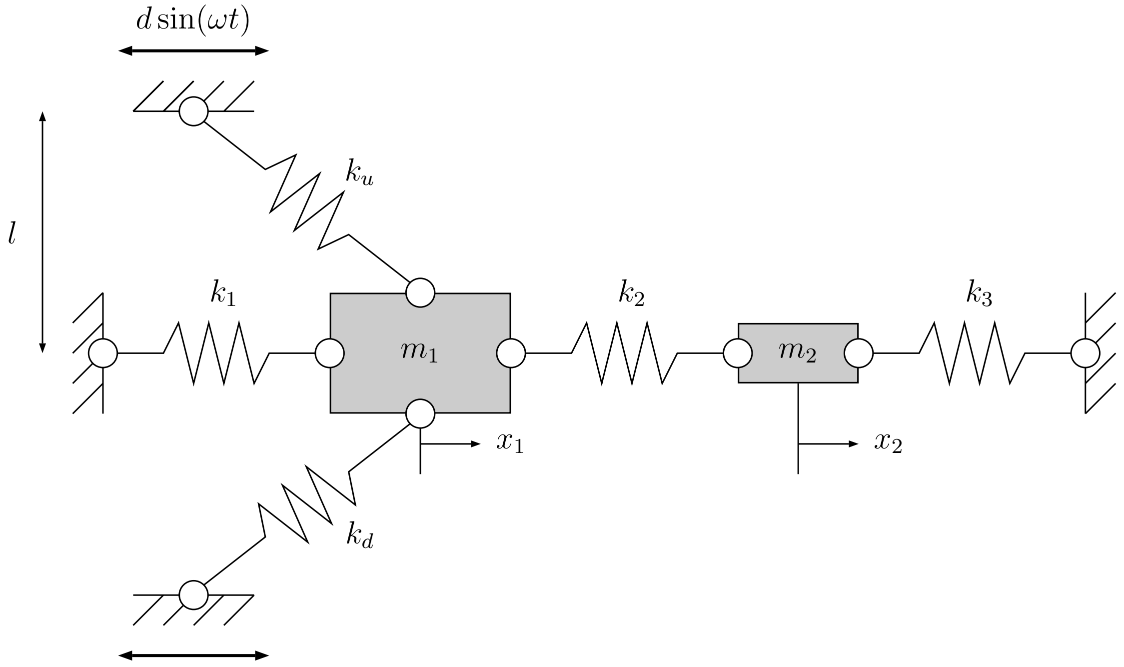

Figure 4.10: Schematic representation of the set-up.

- **Slides:** A linear viscous damping model is used for the interaction between the ground and the two slides. Friction is thereby neglected, whereas it was noted to affect the motion of the masses at low amplitude.
- **Horizontal springs:** As large-amplitude oscillations of the masses are observed, the linear stiffness model proposed for the extension springs is questionable. Damping effects are also neglected.
- **Transverse chords:** Given the structure of the bungee chords, the linear stiffness model used in Eq. (4.2) represents a strong assumption. No damping is considered, whereas one could expect a hysteretic behavior of the rubber composing the chords.

The two mass constants in Eqs. (4.1) can be easily estimated from the set-up, and the other parameters of the model are manually adjusted in order to correlate some of the fundamental experimental results. More specifically, a merging of the IRC occurring in the simulations between $d = 5.7\,\mathrm{mm}$ and $d = 5.8\,\mathrm{mm}$ is sought, with realistic response amplitudes. Table 4.1 lists the values considered in this section, and Table 4.2 provides the corresponding modal parameters. Very low damping is attributed to the second mass and the second mode, to increase their contributions in the IR region.

Fig. 4.11 shows the nonlinear restoring force of the model in Eq. (4.2) computed with the values of Table 4.1. The numerical and experimental restoring forces share the same features, except for low relative displacements where linear contributions are observed in

| $m_1$ (kg) | $m_2$ (kg) | $k_1$ (N/m) | $k_2$ (N/m) | $k_3$ (N/m) |
|---|---|---|---|---|
| 3.49 | 0.46 | 135.0 | 261.8 | 485.6 |
| $k$ (N/m) | $l$ (m) | $\lambda$ (-) | $c_1$ (Ns/m) | $c_2$ (Ns/m) |
| 503.7 | $3.5\ 10^{-2}$ | 0.98 | 2.25 | 0.085 |

Table 4.1: Parameters of the numerical model.

| Mode | Natural frequency ($Hz$) | Damping ratio (%) |
|---|---|---|
| 1 | 1.52 | 3.33 |
| 2 | 6.46 | 0.24 |

Table 4.2: Linear resonance frequencies and damping ratios computed from the numerical model.

the experiments in Fig. 4.2, whereas they are limited in Fig. 4.11, due to the large value considered for $\lambda$.

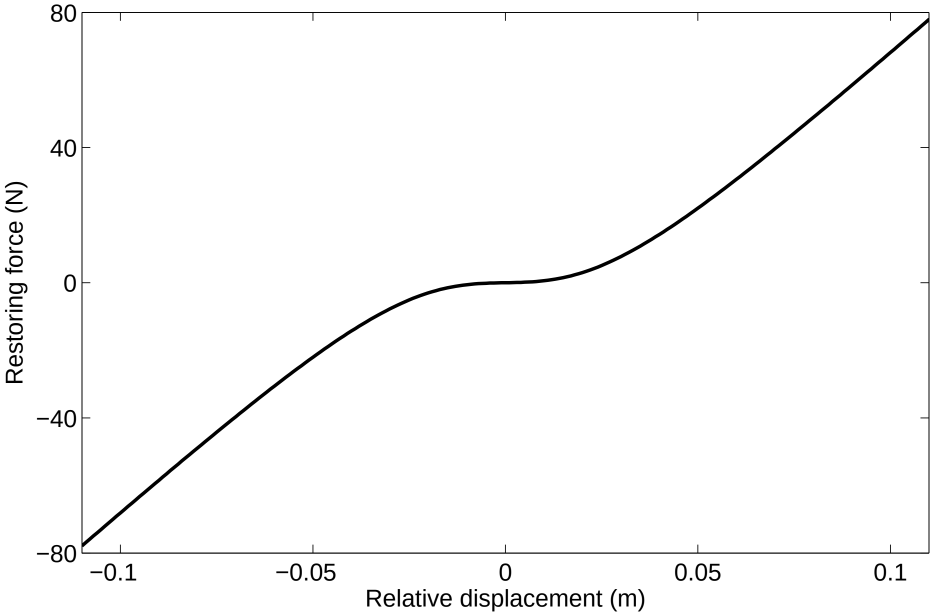

Figure 4.11: Numerical restoring force of the transverse connection.

### 4.4.2 NNMs and NFRCs of the Numerical Model

The continuation tools developed in Chapter 1 are now applied to the model for 9 harmonics retained in the Fourier approximation. Modal analysis is carried out in Fig. 4.12, where the two branches of nonlinear normal modes (NNMs) are depicted. The energy dependence is strong for the first NNM and negligible for the second, which is consistent with the observations made in Fig. 4.3(b). Fig. 4.12 also confirms the presence of a 3:1 IR near 2.15 Hz. Regarding the mode shapes, the in-phase NNM mostly involves a motion of mass 1, except in the IR region where it interacts with the out-of-phase NNM. Conversely, the shape of the out-of-phase NNM is barely affected by the energy level, and exhibits larger oscillations of mass 2.

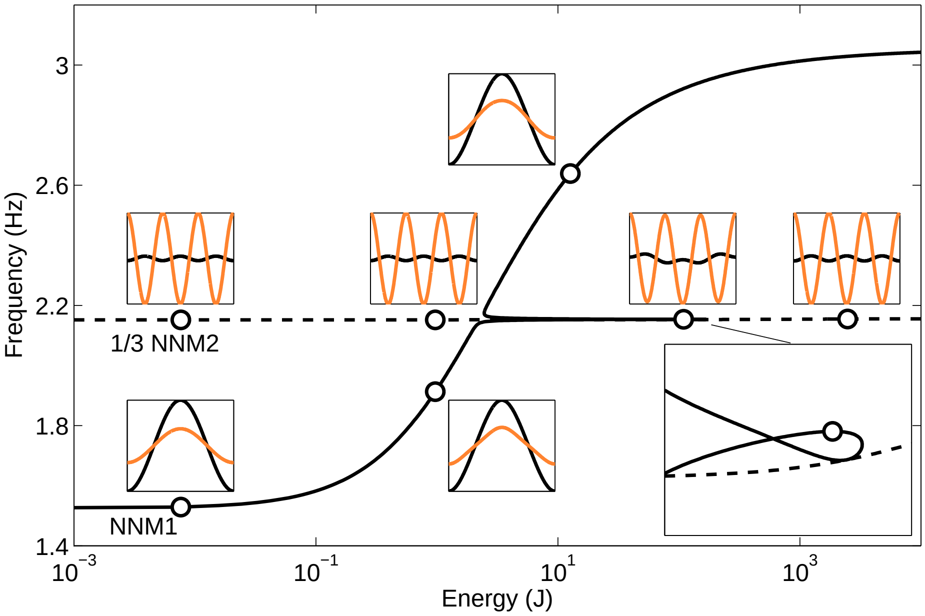

Figure 4.12: In-phase (solid line) NNM, and out-of-phase (dashed line) NNM with a frequency divided by 3. NNM time series of $x_1$ (in black) and $x_2$ (in orange) are inset.

In Figs. 4.13 and 4.14, the nonlinear frequency response curve (NFRC) of the model is compared to the experimental swept-sine responses, for $d = 5.7\,\mathrm{mm}$ and $d = 5.9\,\mathrm{mm}$, respectively. For the sake of clarity, the IRC is not represented in the former case. The superposition of the NFRCs and the experimental time series demonstrate the capabilities of the model to capture the dynamics of the system, especially in the merging region. In particular, the sudden increase in displacement of mass 2 in the vicinity of the 3:1 IR is represented, which can be attributed to the energy exchange between the in-phase and out-of-phase mode. On the other hand, the discrepancies for the amplitudes of the two masses at the 3:1 IR, at resonance and at low amplitude can be attributed to the inaccurate estimation of the damping forces.

Neimark-Sacker (NS) bifurcations are detected in the merging region in Fig. 4.14, which

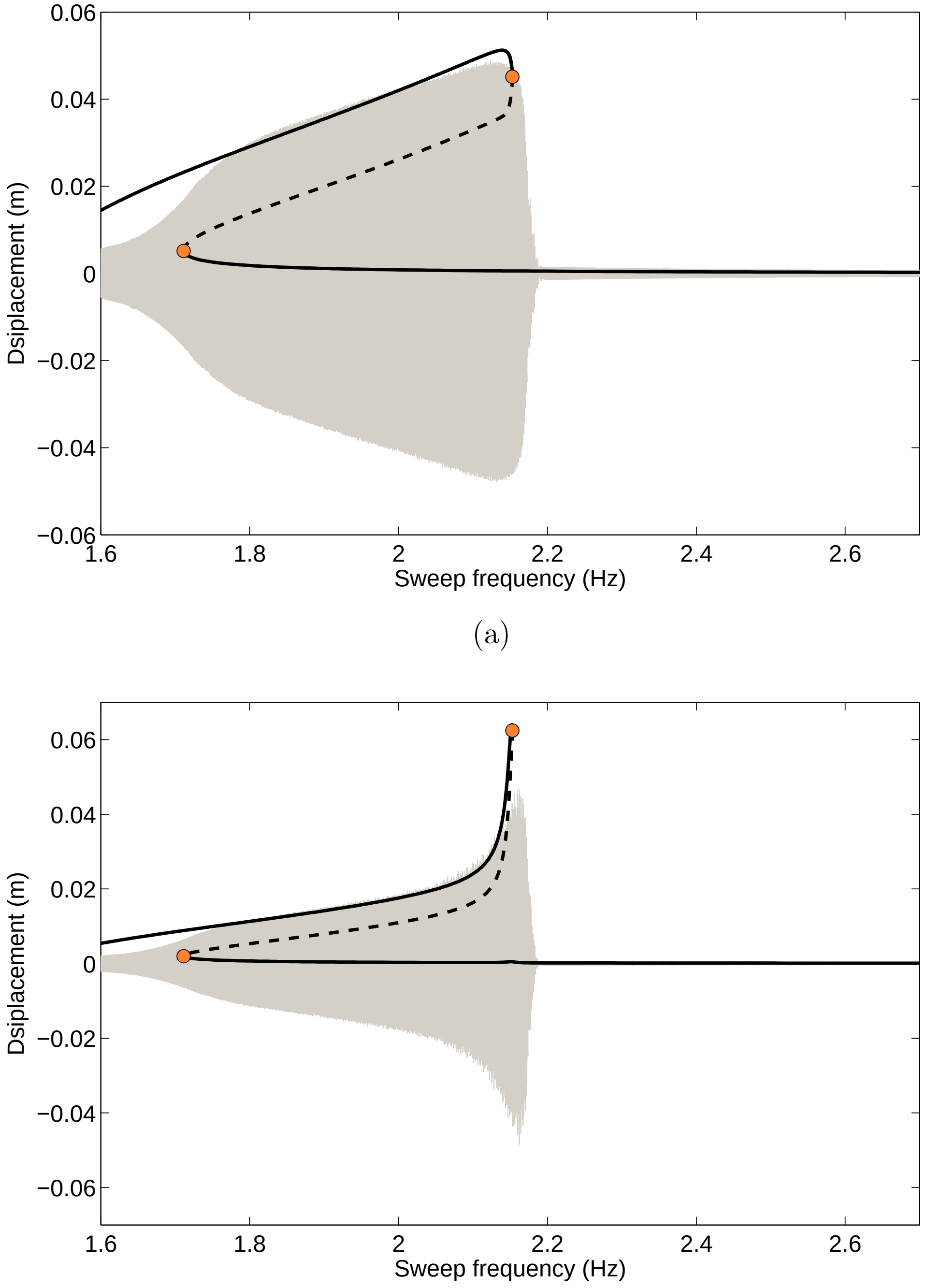

(a)

(b)

Figure 4.13: Comparison between the experimental swept-sine response (in grey) and the NFRCs (in black), before the merging, for $d = 5.7\,\text{mm}$. (a) Mass 1; (b) mass 2. Solid and dashed line represent stable and unstable solutions along the NFRC, respectively. Fold bifurcations are depicted with circle markers.

seems to explain the modulated oscillations observed in Fig. 4.9. In Fig. 4.15, time integration is performed at 2.196 Hz in the unstable region between the third and fourth NS bifurcation. Stable QP oscillations are obtained, which present strong resemblance with the experimental time series presented in Fig. 4.9.

Bifurcation tracking is finally employed in Fig. 4.16 for the fold bifurcations detected in Figs. 4.13 and 4.14. The curve indicates the creation of the IRC for $d = 4.1$ mm, and its merging for $d = 5.8$ mm. Moreover, from $d = 4.1$ mm, the left fold bifurcation of the IRC converges slowly toward the merging point, whereas the right bifurcation rapidly moves to larger amplitudes. This is consistent with the saturation phenomenon reported in Fig. 4.7.

### 4.4.3 Influence of the Internal Resonance

Experiments and simulations confirmed that the presence of the IRC is closely related to the 3:1 IR. We now investigate the effects of the modification of the IR location. To this end, the NNMs computed for several values of the parameter $m_2$ are displayed in Fig. 4.17. Increasing the value of $m_2$ is shown to have a limited influence on the first mode, but a strong impact on the second mode, whose natural frequency decreases. This involves, in turn, a shift of the 3:1 IR to lower frequencies.

The influence of the internal resonance on the responses of the system is studied both experimentally and numerically in Fig. 4.18. For the reference configuration in Figs. 4.18(a-b), the merging of the IRC occurs around 2.15 Hz. When $m_2$ is augmented up to 0.526 kg, the IR is detected at 2.02 Hz (see Figs. 4.18(c-d)). For this configuration, the IRC still exists. Increasing $m_2$ to 0.868 kg eventually leads to the disappearance of the 3:1 IR from the frequency response in Figs. 4.18(e-f).

In order to understand the influence of the IR on the IRC from another viewpoint, the projections of the fold bifurcation curve for the three values of $m_2$ studied are given in Fig. 4.19. This figure shows that the merging of the IRC occurs at lower amplitude and lower base displacement as $m_2$ decreases, until it disappears for $m_2 = 0.868$ kg.

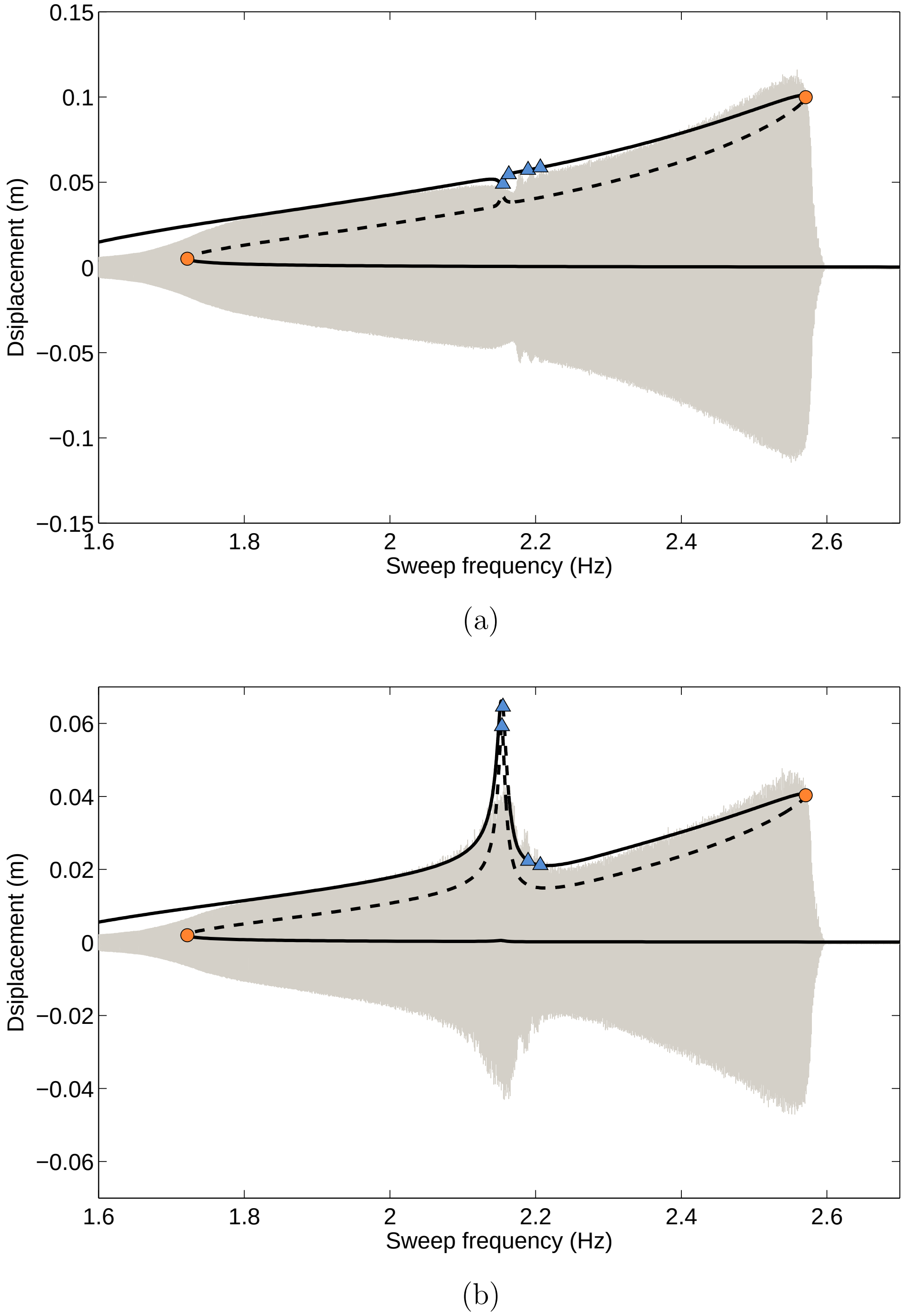

Figure 4.14: Comparison between the experimental swept-sine response (in grey) and the NFRCs (in black), after the merging, for $d = 5.9\,\mathrm{mm}$. (a) Mass 1; (b) mass 2. Solid and dashed line represent stable and unstable solutions along the NFRC, respectively. Fold and NS bifurcations are depicted with circle and triangle markers, respectively.

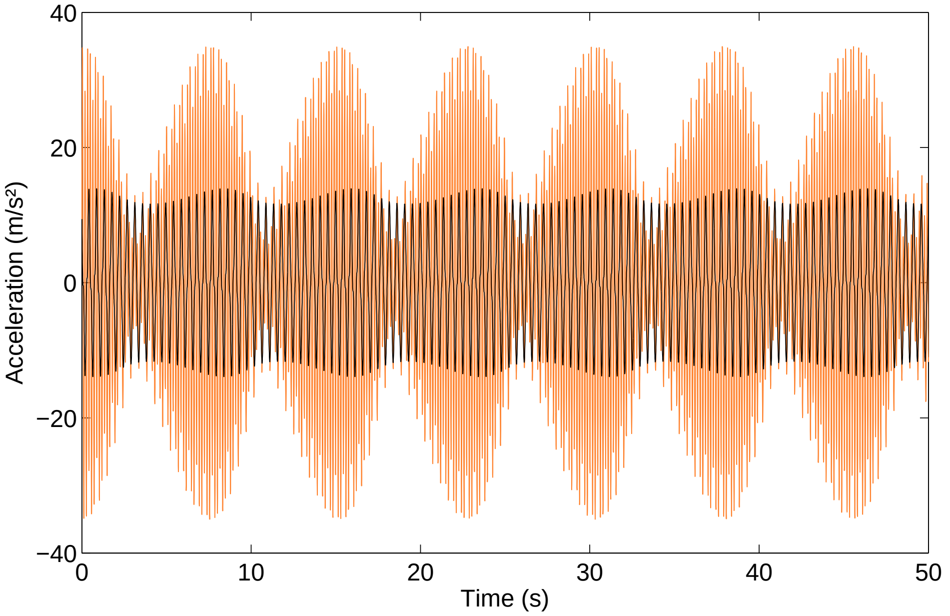

(a)

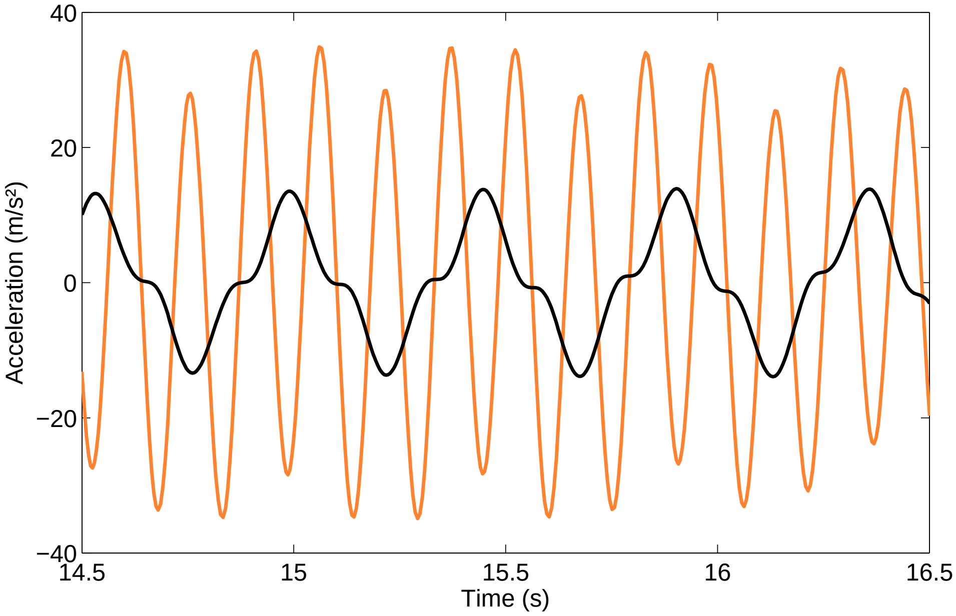

(b)

Figure 4.15: Quasiperiodic oscillations obtained from time integration. (a) Time series for the acceleration of mass 1 (in black) and 2 (in orange), for $d = 5.9\,\mathrm{mm}$ and $\omega = 2.196\,\mathrm{Hz}$; (b) close-up.

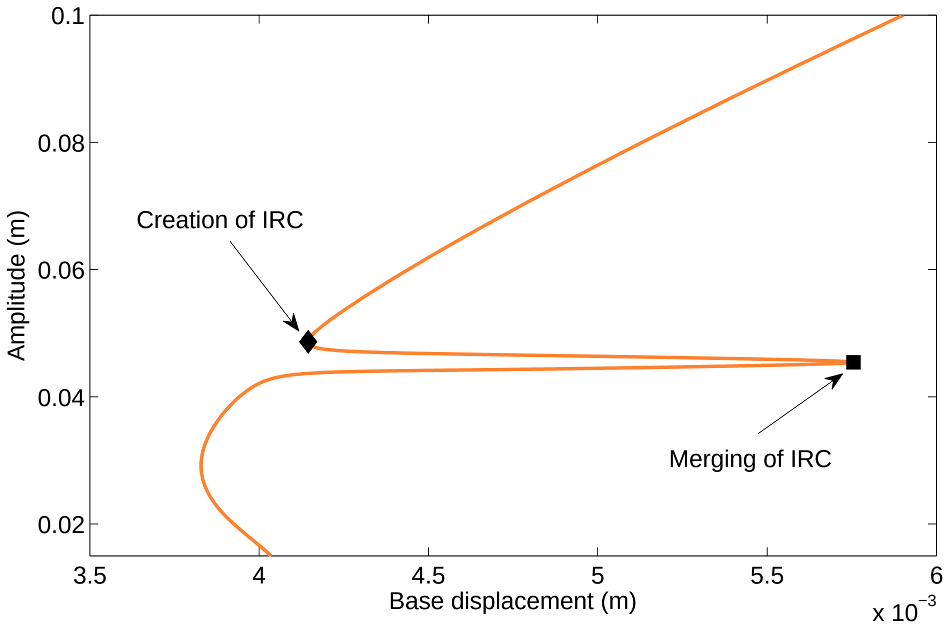

Figure 4.16: Projection of the branch of fold bifurcations in the base displacement-response amplitude plane.

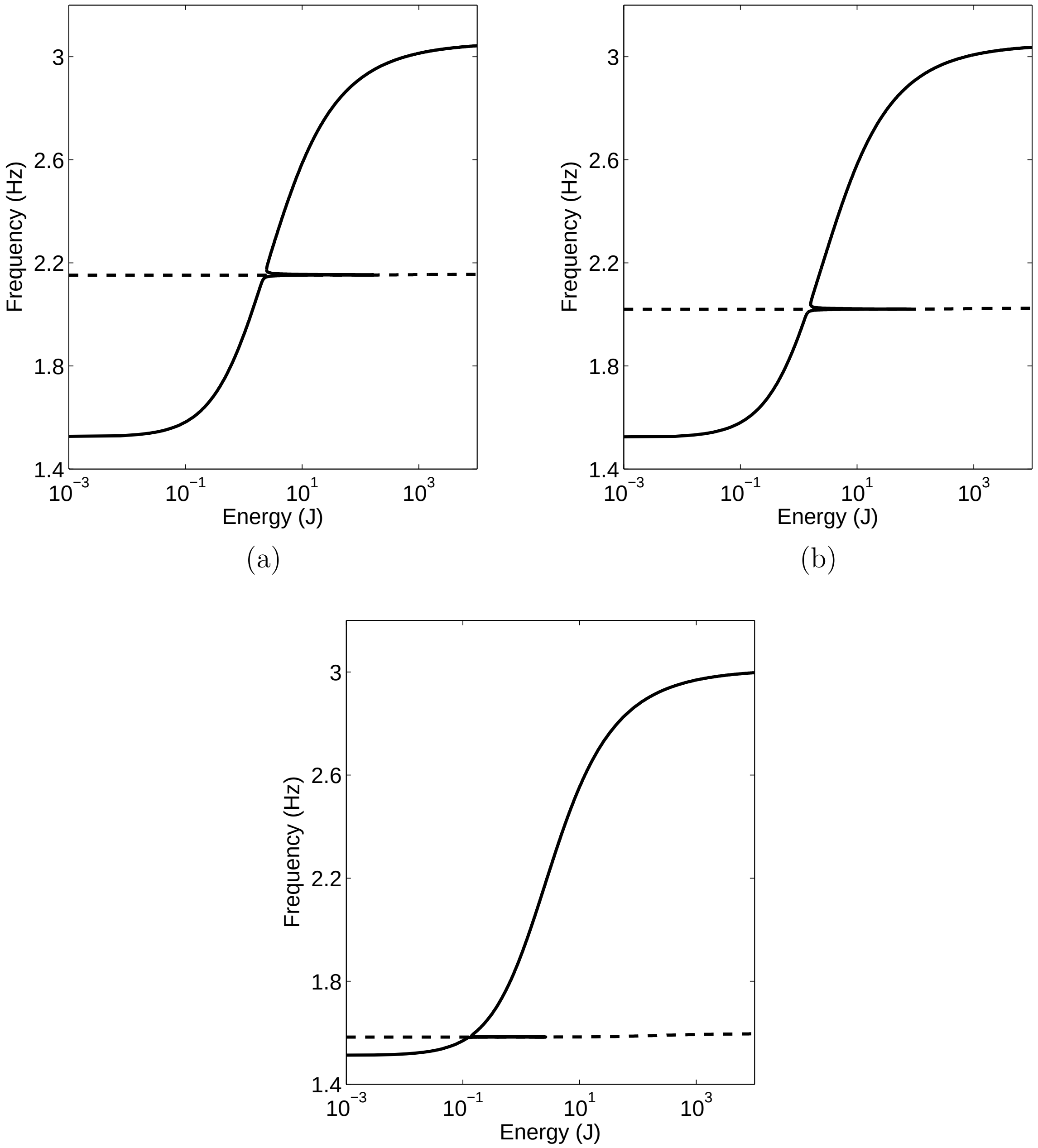

(a)

(b)

(c)

Figure 4.17: Influence of $m_2$ on NNM1 (solid line), and on NNM2 with a frequency divided by 3 (dashed line). (a) $m_2 = 0.464\,\mathrm{kg}$ (reference); (b) $m_2 = 0.526\,\mathrm{kg}$; (c) $m_2 = 0.868\,\mathrm{kg}$.

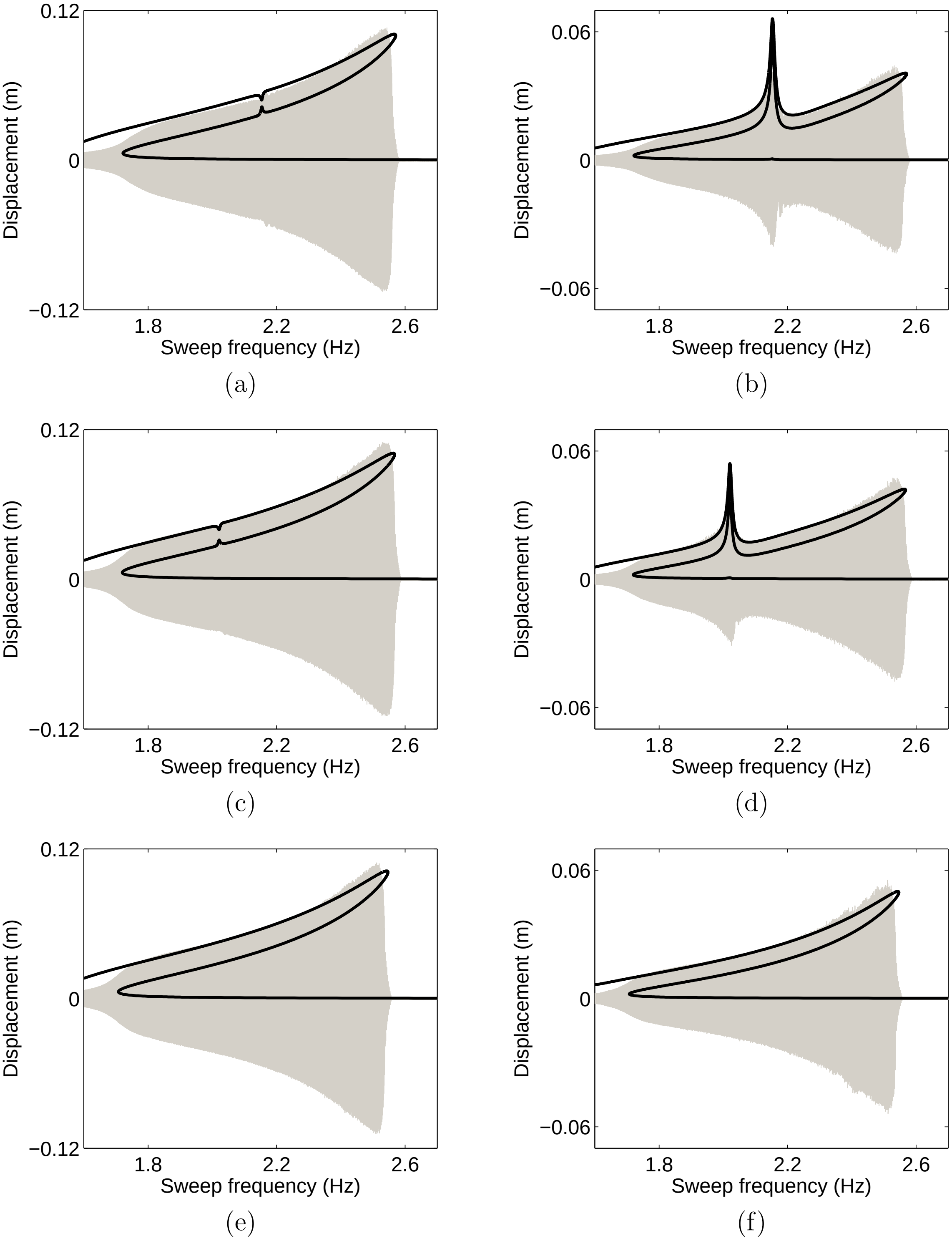

(a) (b) (c) (d) (e) (f)

Figure 4.18: Influence of $m_2$ on the forced response of mass 1 (left column) and mass 2 (right column), for $d = 5.9\,\mathrm{mm}$. (a-b) $m_2 = 0.464\,\mathrm{kg}$ (reference); (c-d) $m_2 = 0.526\,\mathrm{kg}$; (e-f) $m_2 = 0.868\,\mathrm{kg}$. The experimental swept-sine responses and the numerical NFRCs are represented with grey and black lines, respectively.

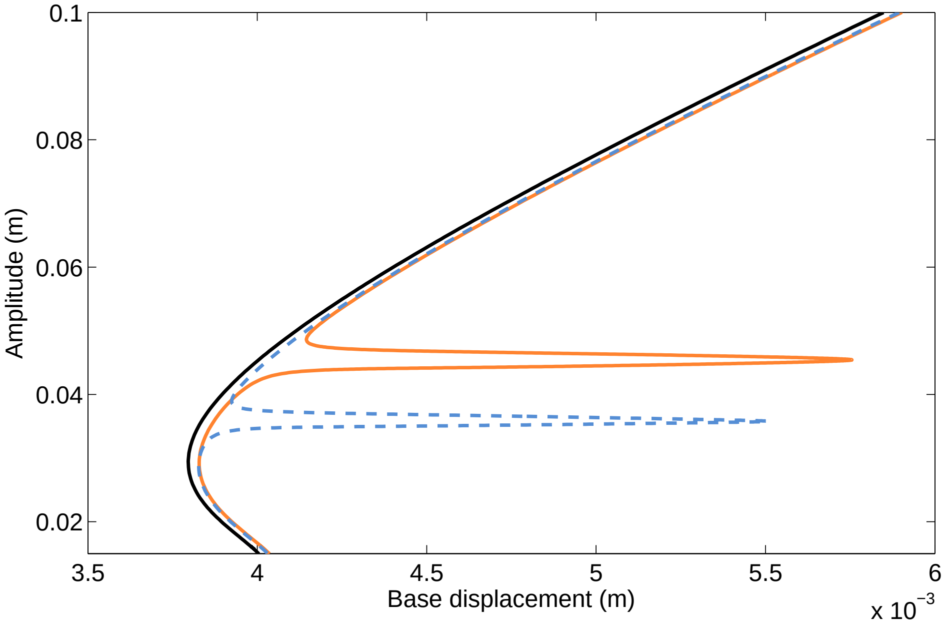

Figure 4.19: Influence of $m_2$ on the projection of the branch of fold bifurcations in the base displacement-response amplitude plane. The orange, blue and black curves denote the configurations with $m_2 = 0.464\,\mathrm{kg}$ (reference), $m_2 = 0.526\,\mathrm{kg}$ and $m_2 = 0.868\,\mathrm{kg}$, respectively.

## 4.5 Concluding Remarks

This chapter provided the experimental evidence for isolated resonance curves (IRCs). Thanks to a dedicated set-up featuring a 3:1 internal resonance between the in-phase and out-of-phase modes, the stable portion of an IRC and its merging with the fundamental resonance branch were carefully characterized combining swept-sine, stepped and impulsive excitations. As a consequence of the merging, the IRC was responsible for a sudden and substantial increase in the resonance frequency of the in-phase mode. Experiments also validated the theoretical finding of Chapter 3 that internal resonances are one possible mechanism for creating IRCs.

The experimental observations could be faithfully reproduced using a numerical model of the experimental set-up. This model also shed light on the strong modulation of the time series in the merging region, which corresponds to quasiperiodic oscillations triggered by Neimark-Sacker bifurcations. Overall, this chapter thus offered a better understanding of IRCs and their influence of the system's dynamics.

# Chapter 5

# Performance and Robustness of the Nonlinear Tuned Vibration Absorber

### Abstract

This chapter addresses the intentional use of nonlinearities for mitigating a nonlinear resonance of a mechanical system. A new nonlinear absorber, termed the nonlinear tuned vibration absorber (NLTVA), is introduced. One unconventional aspect of the NLTVA is that the mathematical form of its restoring force is tailored according to the nonlinear restoring force of the primary system. The NLTVA parameters are then determined using a nonlinear generalization of Den Hartog's equal-peak method. In order to assess the robustness of the absorber, a methodology combining bifurcation tracking and global analysis is proposed to identify boundaries in the NLTVA parameter space delimiting regions of safe operation. The sensitivity of these boundaries to uncertainty in the NLTVA parameters is also investigated. The mitigation of the resonant vibrations of a Duffing oscillator is considered to illustrate the developments throughout the chapter.

## 5.1 Introduction

A recent trend in the technical literature is to exploit nonlinear dynamical phenomena instead of avoiding them, as is the common practice. For instance, reference [21] demonstrates a new mechanism for tunable rectification that uses bifurcations and chaos. In [5], a new strategy for engineering low-frequency noise oscillators is developed through the coupling of modes in internal resonance conditions. A cascade of parametric resonances is proposed by Strachan et al. as a basis for the development of passive frequency dividers [184].

Nonlinearity is also more and more utilized for vibration absorption [4, 29, 55, 157] and energy harvesting [16, 71, 91, 160]. For instance, a nonlinear energy sink (NES), *i.e.*, an absorber with essential nonlinearity [194], can extract energy from virtually any mode of a host structure [95]. The NES can also carry out targeted energy transfer, which is an irreversible channeling of vibrational energy from the host structure to the absorber [96]. This absorber has been applied for various purposes including seismic mitigation [135], aeroelastic instability suppression [87, 196], acoustic mitigation [18] and chatter suppression [65]. This makes nonlinear vibration absorbers suitable candidates for vibration mitigation of nonlinear primary structures. However, the performance of existing absorbers is known to exhibit marked sensitivity to motion amplitudes. For instance, there exists a well-defined threshold of input energy below which no significant energy dissipation can be induced in an NES [194]. Likewise, the saturation phenomenon – characteristic of autoparametric vibration absorbers – occurs only when the forcing amplitude exceeds a certain threshold [138].

This chapter builds upon previous developments [198, 197] to introduce a new nonlinear vibration absorber for mitigating the vibrations around a nonlinear resonance. The absorber is termed the nonlinear tuned vibration absorber (NLTVA), because its nonlinear restoring force is tuned according to the nonlinear restoring force of the host structure. In other words, we propose to synthesize the absorber's load-deflection characteristic so that the NLTVA can mitigate the considered nonlinear resonance in wide ranges of motion amplitudes. Interestingly, this objective is similar in essence to what was achieved with centrifugal pendulum vibration absorbers in rotating machinery [37, 175], whose natural frequency scales with the rate of engine rotation. In the same way, Lacarbonara et al. [109] proposed a carefully-tuned secondary pendulating mass in order to reduce the vibrations of a planar pendulum in a relatively large interval of disturbance amplitudes. In this work, the tuning procedure of the NLTVA relies on the nonlinear generalization of Den Hartog's equal-peak method, whose linear version is widely used for designing linear vibration absorbers [23, 80]. The basic idea of the nonlinear tuning rule is to select the nonlinear coefficient of the absorber that ensures equal peaks in the nonlinear receptance function for an as large as possible range of forcing amplitudes.

The purposeful introduction of nonlinearity can enhance system performance. However, it can also give rise to complicated dynamical phenomena, which linear systems cannot.

If quasiperiodic (QP) regimes of motion can be favorable for vibration absorption with essential nonlinearity [181], they were found to be detrimental for a nonlinear absorber possessing both linear and nonlinear springs [173]. This highlights that no general conclusion can be drawn regarding the influence of quasiperiodic attractors. In [64, 182], the applicability of nonlinear absorbers is affected by the presence of isolated response curves (IRCs). In view of the potentially adverse effects of the aforementioned nonlinear attractors, another objective of the present chapter is to identify boundaries in the NLTVA parameter space delimiting safe, unsafe and unacceptable operations. The sensitivity of these boundaries to uncertainty in the NLTVA parameters is also investigated. To this end, a rigorous methodology combining the harmonic balance continuation tools developed in Chapter 1 with global analysis is proposed.

The chapter is organized as follows. In Section 5.2, the tuning procedure for linear vibration absorbers is briefly reviewed. Section 5.3 introduces the salient features of the NLTVA, and discusses its performance. Specifically, this section demonstrates that equal peaks in the frequency response of the coupled system can be maintained in nonlinear regimes of motion. Section 5.4 reveals that systems featuring a NLTVA can exhibit IRCs and QP regimes of motion. Based on the existence and location of these attractors, regions of safe, unsafe and unacceptable NLTVA operations are defined. Section 5.5 studies the sensitivity of attenuation performance and of the three regions of NLTVA operation to variations of the different absorber parameters. The conclusions of the present study are drawn in Section 5.6.

## 5.2 The Linear Tuned Vibration Absorber

The dynamics of a harmonically-forced, lightly-damped, Duffing oscillator with an attached linear tuned vibration absorber (LTVA) is considered in this section:

$$\begin{aligned} m_1\ddot{x}_1 + c_1\dot{x}_1 + k_1x_1 + k_{nl1}x_1^3 + c_2(\dot{x}_1 - \dot{x}_2) + k_2(x_1 - x_2) &= f\sin(\omega t) \\ m_2\ddot{x}_2 + c_2(\dot{x}_2 - \dot{x}_1) + k_2(x_2 - x_1) &= 0 \end{aligned} \tag{5.1}$$

where $x_1(t)$ and $x_2(t)$ are the displacements of the harmonically-forced primary system and of the absorber, respectively. The parameters of the primary oscillator are listed in Table 5.1.

| $m_1$ (kg) | $k_1$ (N/m) | $c_1$ (N/ms) | $k_{nl1}$ (N/m$^3$) |
|---|---|---|---|
| 1 | 1 | 0.002 | 1 |

Table 5.1: Parameters of the primary system.

The underlying linear version of the vibration absorption problem in Eqs. (5.1), *i.e.*, with $k_{nl1} = 0$, has been widely studied in the literature over the past century. For an undamped primary system ($c_1 = 0$), Den Hartog realized that the receptance function of the primary mass passes through two invariant points independent of absorber damping. He proposed to adjust the absorber stiffness to have two fixed points of equal heights in the receptance curve and to select the absorber damping so that the curve presents a horizontal tangent through one of the fixed points. This laid down the foundations of the so-called equal-peak method. Den Hartog [80] and Brock [23] derived approximate analytic formulas for the absorber stiffness and damping, respectively. Interestingly, it is only recently that an exact closed-form solution to this classic problem could be derived [8]:

$$\begin{aligned}
\lambda = \frac{\omega_{n2}}{\omega_{n1}} &= \sqrt{\frac{k_2 m_1}{k_1 m_2}} = \frac{2}{1+\epsilon}\sqrt{\frac{2\left[16+23\epsilon+9\epsilon^2+2(2+\epsilon)\sqrt{4+3\epsilon}\right]}{3(64+80\epsilon+27\epsilon^2)}} \\
\mu_2 &= \frac{c_2}{2\sqrt{k_2 m_2}} = \frac{1}{4}\sqrt{\frac{8+9\epsilon-4\sqrt{4+3\epsilon}}{1+\epsilon}}
\end{aligned} \tag{5.2}$$

where $\omega_{n1}$ and $\omega_{n2}$ are the natural frequencies of the primary system and of the absorber, respectively, $\epsilon = m_2/m_1$ is the mass ratio and $\mu_2$ is the damping ratio. Equivalently, Eqs. (5.2) can be rewritten as

$$\begin{aligned}
k_2 &= \frac{8\epsilon k_1\left[16+23\epsilon+9\epsilon^2+2(2+\epsilon)\sqrt{4+3\epsilon}\right]}{3(1+\epsilon)^2(64+80\epsilon+27\epsilon^2)} \\
c_2 &= \sqrt{\frac{k_2 m_2(8+9\epsilon-4\sqrt{4+3\epsilon})}{4(1+\epsilon)}}
\end{aligned} \tag{5.3}$$

A LTVA tuned according to Eqs. (5.3) minimizes the maximum response amplitude of an undamped linear primary system. These conditions can be generalized to damped systems [7, 8], and are still widely used, as discussed in the review paper [186].

The performance of the LTVA applied to the nonlinear damped primary system in Eqs. (5.1) is now investigated. An absorber with a mass ratio $\epsilon = 5\%$ is selected for obvious practical reasons. Table 5.2 gives the parameters of the LTVA calculated from Eqs. (5.3). Even if the formulas are strictly valid only for an undamped primary system, they are still used herein in view of the very light damping $c_1$ considered. Fig. 5.1 shows the nonlinear frequency response curves (NFRCs) of the primary mass for various forcing amplitudes $f$ ranging from 0.001 N to 0.07 N, computed with the continuation tools developed in Chapter 1 for 5 harmonics. At 0.001 N in Fig. 5.1(a), the system behaves linearly, and two peaks of equal amplitude can be observed in accordance with linear theory. When the forcing amplitude is increased, the cubic nonlinearity of the primary system is activated. At 0.02 N, Fig. 5.1(b) shows a slight detuning of the absorber, but this detuning is not yet too detrimental to the absorber's performance. At 0.06 N in Fig. 5.1(c), the LTVA is no longer effective due to the important difference in the amplitude of the two resonances. A hardening behavior characteristic of cubic springs with positive coefficients is also present in the second resonance peak; it indicates that the regime of motion is no longer weakly nonlinear. When the forcing amplitude increases from 0.06 N to 0.07 N, the LTVA becomes completely detuned by the nonlinear effects. The primary mass displacement increases by a factor of 2 between Figs. 5.1(c) and (d), which is a clear sign of the absence of superposition principle for this coupled system. Because of the frequency-energy dependence of nonlinear oscillations and of the narrow bandwidth of the LTVA, this absorber can only be effective in weakly nonlinear regimes of motion.

| $m_2$ (kg) | $k_2$ (N/m) | $c_2$ (N/ms) |
|---|---|---|
| 0.05 | 0.0454 | 0.0128 |

Table 5.2: Parameters of the LTVA for $\epsilon = 0.05$.

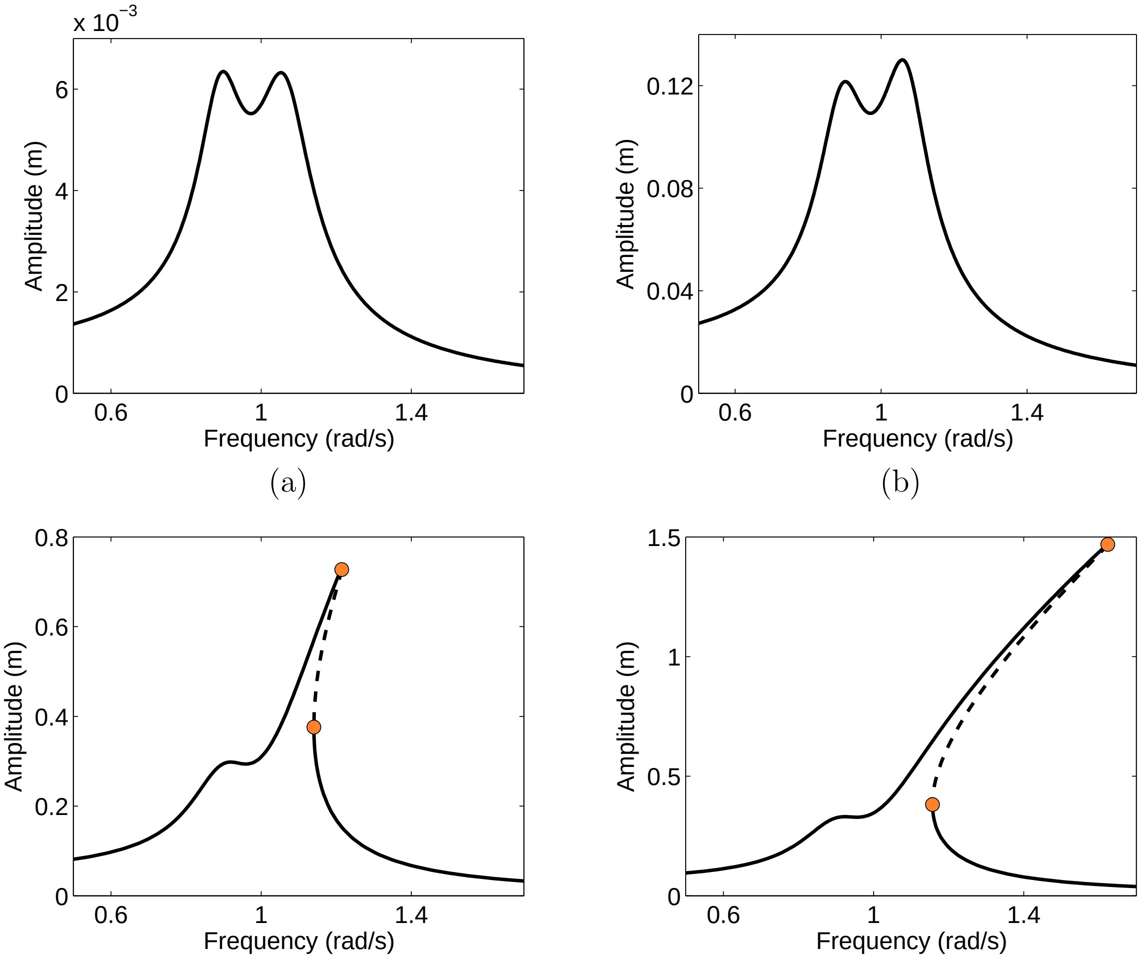

(a) (b) (c) (d)

Figure 5.1: NFRCs of the Duffing oscillator with an attached LTVA. (a) $f = 0.001$ N; (b) $f = 0.02$ N; (c) $f = 0.06$ N; (d) $f = 0.07$ N. The solid and dashed lines represent stable and unstable solutions, respectively. Fold bifurcations are depicted with circle markers.

## 5.3 The Nonlinear Tuned Vibration Absorber

In view of the results presented in the previous section, it is meaningful to examine the performance of nonlinear absorbers for vibration mitigation of nonlinear primary structures. However, as pointed out in the introductory section, an increased bandwidth may come at the price of a marked sensitivity to external forcing amplitude.

To mitigate a nonlinear resonance in an as large as possible range of forcing amplitudes, we introduce the nonlinear tuned vibration absorber (NLTVA). One unconventional feature of this absorber is that the mathematical form of its nonlinear restoring force is not imposed a priori, as it is the case for most existing nonlinear absorbers.

### 5.3.1 Synthesis of the Nonlinear Restoring Force of the Absorber

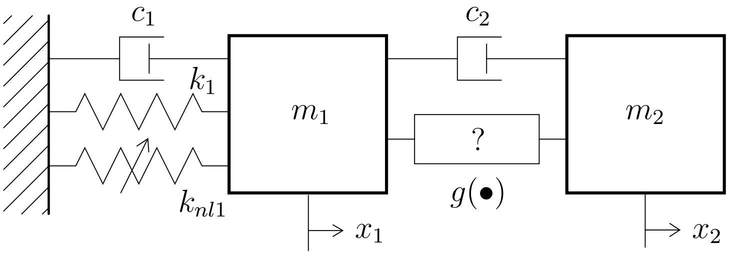

Figure 5.2: Schematic representation of a NLTVA attached to a Duffing oscillator.

The dynamics of a Duffing oscillator with an attached NLTVA is considered, as depicted in Fig. 5.2:

$$\begin{aligned} m_1\ddot{x}_1 + c_1\dot{x}_1 + k_1x_1 + k_{nl1}x_1^3 + c_2(\dot{x}_1 - \dot{x}_2) + g(x_1 - x_2) &= f\sin(\omega t) \\ m_2\ddot{x}_2 + c_2(\dot{x}_2 - \dot{x}_1) - g(x_1 - x_2) &= 0 \end{aligned} \tag{5.4}$$

The NLTVA is assumed to have a generic smooth restoring force $g\left(x_1 - x_2\right)$ with $g(0) = 0$. Defining the dimensionless time $\tau = \omega_{n1}t$, where $\omega_{n1} = \sqrt{k_1/m_1}$, and applying the transformation $r(t) = x_1(t) - x_2(t)$ yields

$$\begin{aligned} x_1'' + 2\mu_1x_1' + x_1 + \frac{4}{3}\tilde{\alpha}_3x_1^3 + 2\mu_2\lambda\epsilon r' + \frac{\epsilon}{m_2\omega_{n1}^2}g\left(r\right) &= F\sin\left(\gamma\tau\right) \\ r'' + 2\mu_1x_1' + x_1 + \frac{4}{3}\tilde{\alpha}_3x_1^3 + 2\mu_2\lambda\left(\epsilon+1\right)r' + \frac{\epsilon+1}{m_2\omega_{n1}^2}g\left(r\right) &= F\sin\left(\gamma\tau\right) \end{aligned} \tag{5.5}$$

where prime denotes differentiation with respect to time $\tau$, $2\mu_1 = c_1/(m_1\omega_{n1})$, $\tilde{\alpha}_3 = 3k_{nl1}/4k_1$, $2\mu_2 = c_2/(m_2\omega_{n2})$, $\lambda = \omega_{n2}/\omega_{n1}$, $\epsilon = m_2/m_1$, $F = f/k_1$ and $\gamma = \omega/\omega_{n1}$. $\omega_{n2}$ is the linearized frequency of the NLTVA.

Expanding $g(r)$ in Taylor series around $r = 0$ and normalizing the system using $q_1 = x_1/F$ and $q_2 = r/F$, we obtain

$$
\begin{aligned}
q_1'' + 2\mu_1 q_1' + q_1 + \frac{4}{3}\tilde{\alpha}_3 F^2 q_1^3 + 2\mu_2\lambda\epsilon q_2' + \lambda^2\epsilon q_2 + \frac{\epsilon}{m_2\omega_{n1}^2}\sum_{k=2}^{\infty}\frac{F^{k-1}}{k!}\left.\frac{\mathrm{d}^k g}{\mathrm{d}r^k}\right|_{r=0} q_2^k &= \sin(\gamma\tau)\\
q_2'' + 2\mu_1 q_1' + q_1 + \frac{4}{3}\tilde{\alpha}_3 F^2 q_1^3 + 2\mu_2\lambda(\epsilon+1) q_2' + \lambda^2(\epsilon+1) q_2 + \frac{\epsilon+1}{m_2\omega_{n1}^2}\sum_{k=2}^{\infty}\frac{F^{k-1}}{k!}\left.\frac{\mathrm{d}^k g}{\mathrm{d}r^k}\right|_{r=0} q_2^k &= \sin(\gamma\tau)
\end{aligned}
\tag{5.6}
$$

where $\omega_{n2} = \sqrt{\mathrm{d}g/\mathrm{d}q_2|_{q_2=0}/m_2}$.

In Eqs. (5.6), the linear terms are independent of the forcing amplitude $F$, which confirms that a purely linear absorber attached to a linear oscillator is effective irrespective of the considered forcing amplitude. Focusing now on the complete system, $F$ appears in the nonlinear coefficients of both the primary system and the absorber, which reminds that it is equivalent to consider the system strongly nonlinear or strongly excited. Specifically, Eqs. (5.6) show that the forcing amplitude modifies linearly the quadratic terms, quadratically the cubic terms and so on. This suggests that, if an optimal set of absorber parameters is chosen for a specific value of $F$, variations of $F$ will detune the nonlinear absorber, unless the nonlinear coefficients of the primary system and of the absorber undergo a similar variation with $F$. According to Eqs. (5.6), this can be achieved by selecting the same mathematical function for the absorber as that of the primary system. When coupled to a Duffing oscillator, the NLTVA should therefore possess a cubic spring:

$$
\begin{aligned}
q_1'' + 2\mu_1 q_1' + q_1 + \frac{4}{3}\alpha_3 q_1^3 + 2\mu_2\lambda\epsilon q_2' + \lambda^2\epsilon q_2 + \frac{4}{3}\epsilon\beta_3 q_2^3 &= \sin(\gamma\tau)\\
q_2'' + 2\mu_1 q_1' + q_1 + \frac{4}{3}\alpha_3 q_1^3 + 2\mu_2\lambda(\epsilon+1) q_2' + \lambda^2(\epsilon+1) q_2 + \frac{4}{3}(\epsilon+1)\beta_3 q_2^3 &= \sin(\gamma\tau)
\end{aligned}
\tag{5.7}
$$

where

$$
\alpha_3 = \tilde{\alpha}_3 F^2 \quad \text{and} \quad \beta_3 = \frac{3}{4}\frac{F^2 g'''(r)|_{r=0}}{3! m_2\omega_{n1}^2}. \tag{5.8}
$$

The NLTVA spring should also possess a linear component so that it is effective at low forcing amplitudes where the cubic component of the Duffing oscillator is not activated.

In summary, the proposed nonlinear tuning rule is to choose the mathematical form of the NLTVA's restoring force so that it is a 'mirror' of the primary system.

## 5.3.2 Nonlinear Generalization of the Equal-Peak Method

The next step is to determine the NLTVA parameters, namely $\epsilon$, $\lambda$, $\mu_2$ and $\beta_3$. The mass ratio $\epsilon$ is chosen according to practical constraints. In order to ensure the same performance as the LTVA at low energy levels, the linear parameters $\lambda$ and $\mu_2$ are determined using Eqs. (5.2).

The additional design parameter offered by the NLTVA, *i.e.*, $\beta_3$, is exploited herein to realize equal peaks for various forcing amplitudes. For this purpose, however, an exact analytic estimation of $\beta_3$ is not within reach. Nonetheless, Habib *et al.* demonstrated that $\beta_3$ is almost linearly related to $\alpha_3$ for fixed values of the mass ratio. This relation implies that the nonlinear coefficient of the NLTVA does not depend on forcing amplitude, and can be obtained by an analytical regression formula [77]:

$$\beta_3 = \frac{2\alpha_3\epsilon}{1+4\epsilon} \tag{5.9}$$

In [77], the authors also showed that a linear relation between $\alpha_3$ and $\beta_3$ is only observed when the NLTVA is governed by equations analogous to those of the primary system. This further justifies the proposed synthesis of the absorber's load-deflection curve.

In summary, given $m_1$, $c_1$, $k_1$ and $k_{nl1}$ for a Duffing oscillator and given a mass ratio $\epsilon$, the NLTVA parameters can be determined using the analytical formulas given in Fig. 5.3. These formulas form the basis of a new tuning rule for nonlinear absorbers that may be viewed as a nonlinear generalization of Den Hartog's equal-peak method. Note, however, that there are no invariant points in the nonlinear case. There is thus no complete equivalence with the linear equal-peak method.

$$\begin{aligned}
m_2 &= \epsilon m_1 \\
k_2 &= \frac{8\epsilon k_1\left[16+23\epsilon+9\epsilon^2+2(2+\epsilon)\sqrt{4+3\epsilon}\right]}{3(1+\epsilon)^2(64+80\epsilon+27\epsilon^2)} \\
c_2 &= \sqrt{\frac{k_2 m_2(8+9\epsilon-4\sqrt{4+3\epsilon})}{4(1+\epsilon)}} \\
k_{nl2} &= \frac{2\epsilon^2 k_{nl1}}{(1+4\epsilon)}
\end{aligned}$$

Figure 5.3: Tuning procedure for the NLTVA.

For the parameters of the primary system in Table 5.1, the NLTVA parameters determined from Fig. 5.3 are given in Table 5.3. Fig. 5.4 compares the respective performance of the NLTVA and the LTVA. For $f = 0.001\,\mathrm{N}$ in Fig. 5.4(a), the LTVA and NLTVA exhibit similar performance as they operate in a linear regime. For higher forcing levels, resonance peaks of equal amplitude are maintained for the NLTVA, which substantially improves the performance of the LTVA. For a more global comparison between the two absorbers, Fig. 5.4(e) represents the amplitude of the resonance peaks of the Duffing oscillator as a function of $f$. If the LTVA gets rapidly detuned, the amplitude of the two resonance peaks for the NLTVA remains almost identical. In addition, the amplitude is almost linearly related to forcing amplitude, as if the system would obey the superposition principle. This result is unexpected in view of the strongly nonlinear regimes investigated. It therefore seems that adding a properly chosen nonlinearity to an already nonlinear system can somehow linearize the dynamics of the coupled system. On the contrary, the amplitude of the resonance peaks for the LTVA exhibits a marked nonlinear dependence with respect to forcing amplitude.

| $m_2$ (kg) | $k_2$ (N/m) | $c_2$ (N/ms) | $k_{nl2}$ (N/m$^3$) |
|---|---|---|---|
| 0.05 | 0.0454 | 0.0128 | 0.0042 |

Table 5.3: Parameters of the NLTVA.

## 5.4 Robustness of the NLTVA

In Fig. 5.5, the dynamics of the NLTVA is investigated for larger forcing amplitudes. The main observation is that the NLTVA performance (in terms of $H_\infty$ optimization) is always superior to that of the LTVA. However, between $f = 0.12$ N and $f = 0.18$ N, the two main resonance peaks co-exist with two additional solutions, which raises the question of the NLTVA robustness.

Considering the multivaluedness of the system's response in Fig. 5.5, this section aims at uncovering the dynamical attractors that the system may exhibit. The proposed methodology combines bifurcation tracking using the algorithm proposed in Chapter 1, and global analysis.

### 5.4.1 Adverse Dynamics

Fig. 5.6 presents the NFRCs of the primary mass with an attached NLTVA, computed for several forcing amplitudes. For $f = 0.005$ N in Fig. 5.6(a), neither of the nonlinearities are activated, and the linear result is retrieved. For $f = 0.09$ N in Fig. 5.6(b), the resonance peaks bend forward as a result of the hardening nature of the cubic springs, and the resonance frequencies increase. Notwithstanding this nonlinear behavior, resonance peaks of equal amplitude are obtained thanks to the NLTVA.

Slightly increasing forcing amplitude triggers the appearance of two different bifurcations. For $f = 0.098$ N, a pair of fold bifurcations modifies the stability along the frequency response in Fig. 5.6(c). For $f = 0.11$ N in Fig. 5.6(d), a pair of Neimark-Sacker (NS) bifurcations changes stability as well, but it also generates a stable branch of quasiperiodic (QP) solutions that was computed using direct time integrations. Since approximately equal peaks are maintained in Figs. 5.6(c-d) and since QP oscillations have amplitudes comparable to those of the resonance peaks, the NLTVA can still be considered as effective.

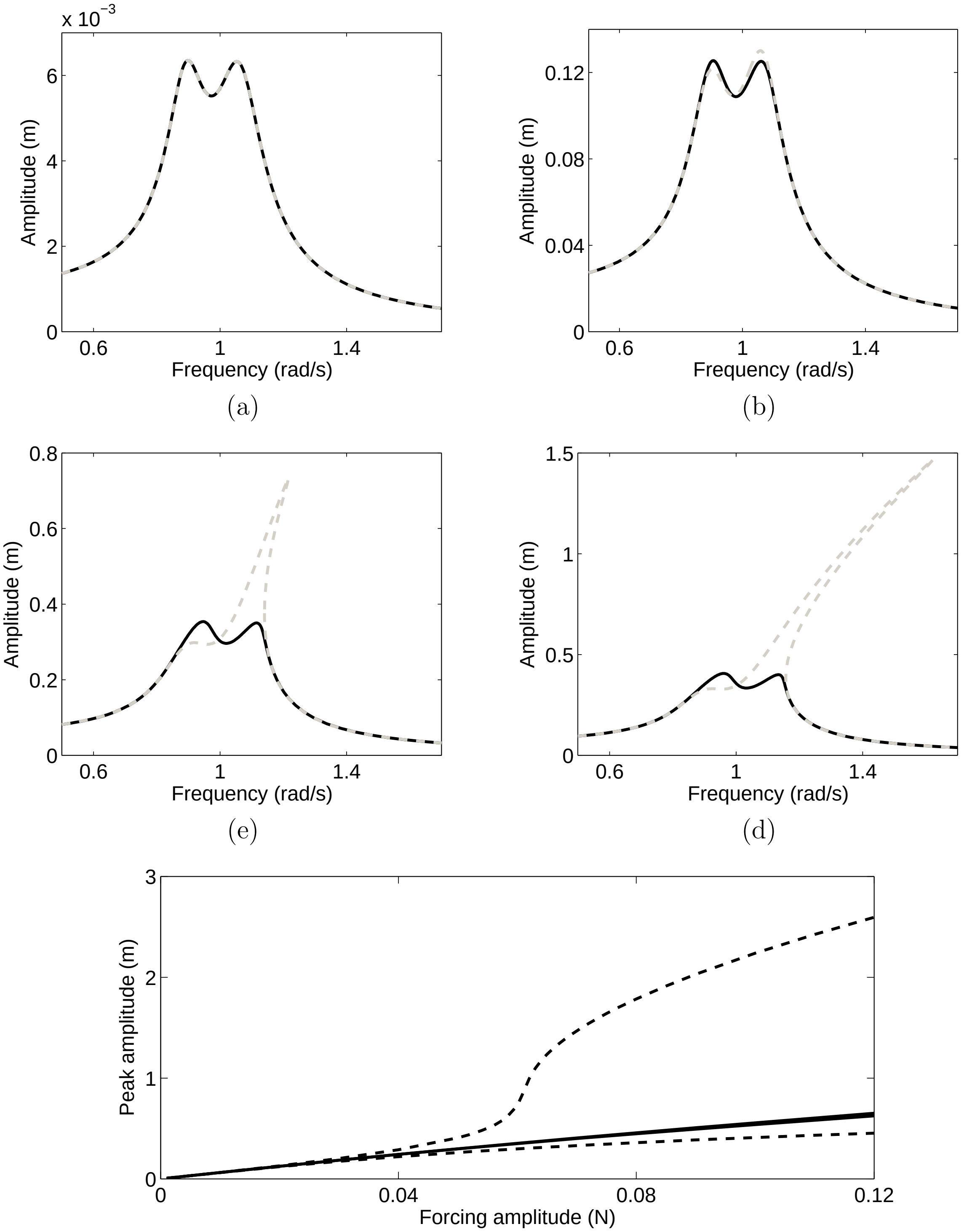

(a)

(b)

(e)

(d)

(e)

Figure 5.4: Frequency response of the Duffing oscillator with an attached NLTVA (solid line) and LTVA (dashed line). (a-d) NFRCs for $f = 0.001\,\mathrm{N}$, $f = 0.02\,\mathrm{N}$, $f = 0.06\,\mathrm{N}$ and $f = 0.07\,\mathrm{N}$; (e) evolution of the resonance peaks.

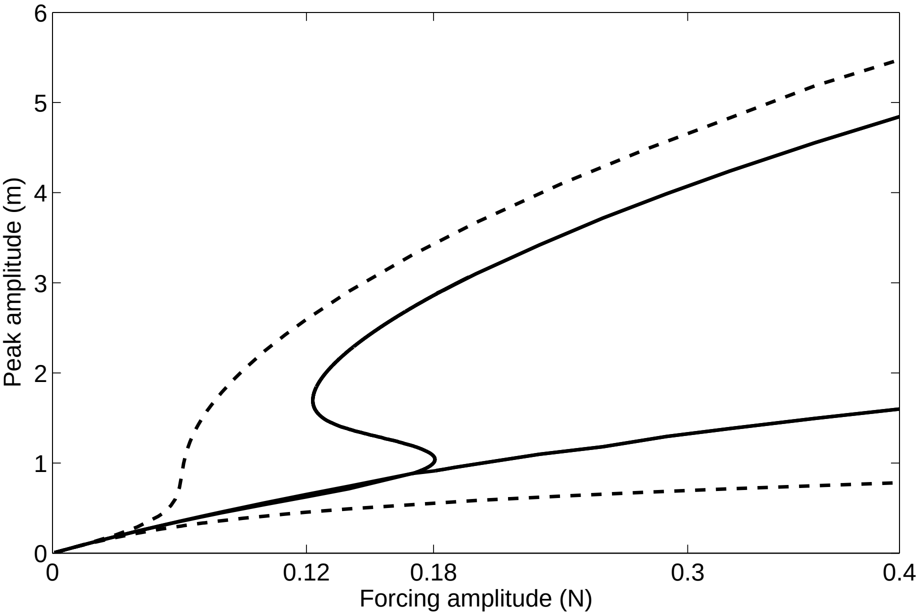

Figure 5.5: Robustness of the NLVTA (solid line) and LTVA (dashed line).

For $f = 0.15\,\mathrm{N}$, a new pair of fold bifurcations creates an isolated response curve (IRC) between 1.57 and 2.32 rad/s in Fig. 5.6(e). This IRC is associated with large amplitudes of motion, but it remains far enough from the desired operating frequency range of the NLTVA. In addition, the left portion of the IRC between 1.57 and 1.73 rad/s is unstable, and, hence, not physically realizable. The IRC also possesses a NS bifurcation, but no stable branch of QP oscillations could be found in its vicinity.

For larger forcing amplitudes, the IRC expands and eventually merges with the second resonance peak for $f = 0.19\,\mathrm{N}$, as depicted in Fig. 5.6(f). This merging eliminates the fold bifurcation characterizing the second resonance peak and the fold bifurcation on the left of the IRC, and causes a very substantial increase in the amplitude of the second resonance. Unlike the IRCs studied in Chapters 3 and 4 that were associated to internal resonances, the presence of the IRC is herein related to a branch of detached nonlinear normal modes.

## 5.4.2 Bifurcation Tracking

QP oscillations and IRCs represent adverse dynamics that deserve further investigation. Since their creation occurs through NS and fold bifurcations, respectively, these bifurcations are now tracked with respect to $\omega$ and $f$ and projected onto the forcing amplitude-response amplitude plane for interpretation. Fig. 5.7(a) represents the loci of the fold bifurcations of Fig. 5.6. Branch A is related to the bifurcations in the neighbourhood of the first resonance peak, whereas branch B corresponds to the bifurcations in the vicinity

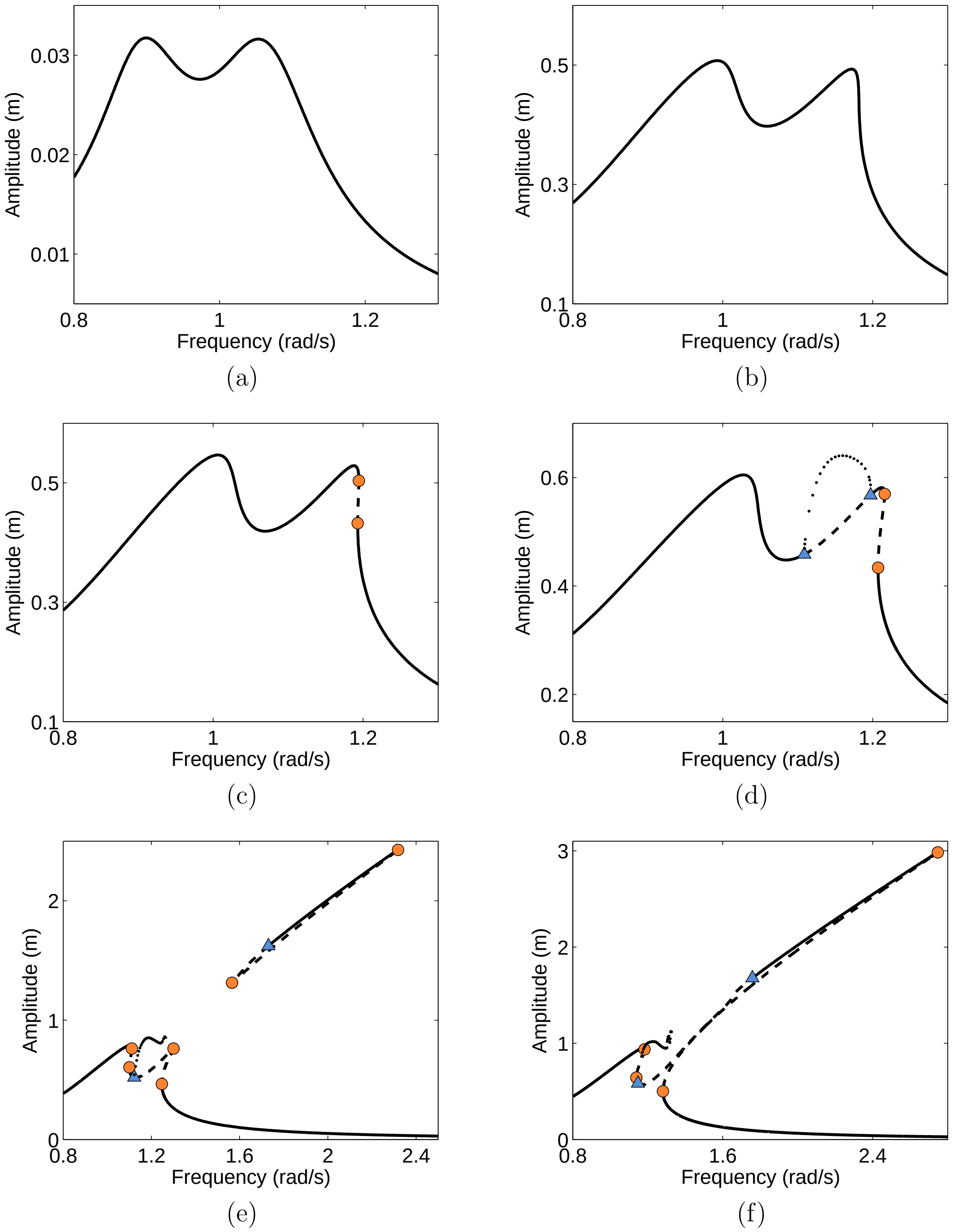

(a) (b)

(c) (d)

(e) (f)

Figure 5.6: NFRCs of the Duffing oscillator with an attached NLTVA. (a) $f = 0.005\,\mathrm{N}$; (b) $f = 0.09\,\mathrm{N}$; (c) $f = 0.098\,\mathrm{N}$; (d) $f = 0.11\,\mathrm{N}$; (e) $f = 0.15\,\mathrm{N}$; (f) $f = 0.19\,\mathrm{N}$. Stable (solid lines), unstable (dashed lines) and QP (dotted line) branches. Fold and NS bifurcations are depicted with circle and triangle markers, respectively.

of the second resonance peak. Because the IRC merges with this latter peak, branch B indicates the creation and elimination of the IRC, represented with diamond and square markers, respectively. The IRC appears around 0.12 N and merges with the main branch around 0.18 N. It can also be observed that branches A and B overlap between 0.13 and 0.17 N, which is another manifestation of the proposed nonlinear equal-peak method.

Fig. 5.7(b) displays the branch of NS bifurcations and indicates that the stable QP branch between the two resonance peaks is created when $f = 0.095\,\mathrm{N}$ (star marker). One also notes that Bogdanov-Takens bifurcations, associated with a pair of Floquet exponents at zero [107], are detected at the intersections of the fold and NS curves. At these intersections, NS bifurcations turn into neutral saddle points (cf. Section 1.3.2).

### 5.4.3 Global Analysis

The previous two sections have highlighted the different dynamical attractors of the coupled system (5.4) together with their locations in the $f$-$\omega$ parameter space. Since the stable QP solutions between the two resonances are associated with acceptable amplitudes, they are not considered as a great concern. However, one should stress that NS bifurcations can trigger torus breakdown and phase locking with large-amplitude attractors [2]. Despite detailed numerical simulations and co-dimension 2 bifurcation analysis in MATCONT [38], no evidence of such behaviors could be observed.

The large-amplitude IRC is more problematic. The likelihood of converging to the safe, low-amplitude periodic solution in the region where the IRC exists should therefore be determined. Given a forcing amplitude and frequency, direct time integrations for a large set of random initial states can provide the basins of attraction, similarly to what was achieved in [48] for a coupled linear oscillator and nonlinear absorber system. To limit the scope of the discussion, the NLTVA is considered at rest, as it would be the case, *e.g.*, during an earthquake, but other configurations were also tested.

For $f = 0.15\,\mathrm{N}$, Fig. 5.8(a) illustrates that the bistable region lies after the NS bifurcation on the IRC, *i.e.*, in the frequency interval between 1.73 and 2.32 rad/s. The basins of attraction of the IRC in this interval are found to be very small compared to those of the main branch, as shown in Figs. 5.8(c-f). This finding is confirmed in Fig. 5.9 where the ratio between the areas of the basins of attraction of the IRC and of the low-amplitude periodic solution does not exceed 6% for the considered range of initial conditions. The basins of attraction of the IRC are also located at a considerable distance from the origin, meaning that high-energy initial conditions have to be imparted to the system to excite the IRC. It can finally be shown that the basins of attraction of the IRC remain small for other forcing amplitudes and that the low-amplitude solution is the only stable solution between 1.57 and 1.73 rad/s, as confirmed in Fig. 5.8(a).

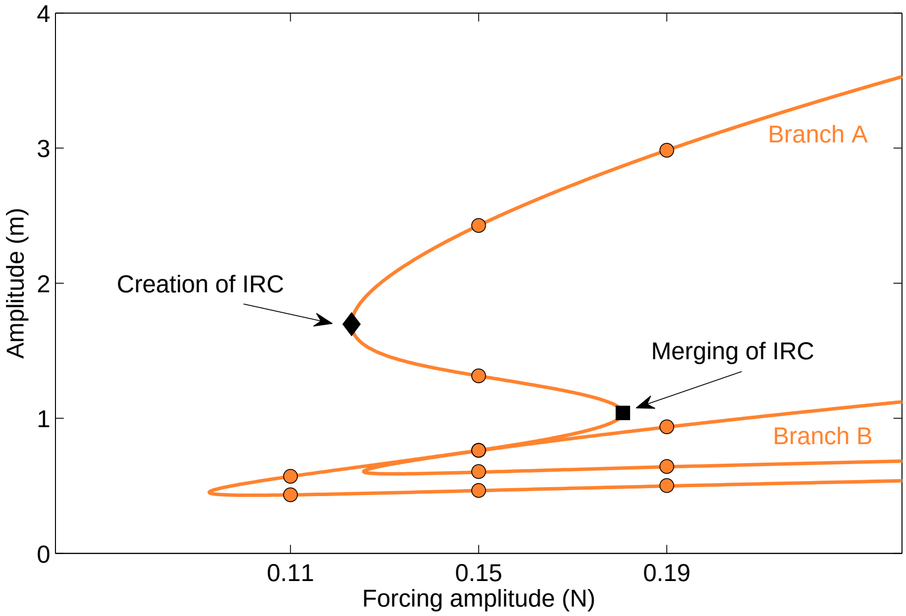

(a)

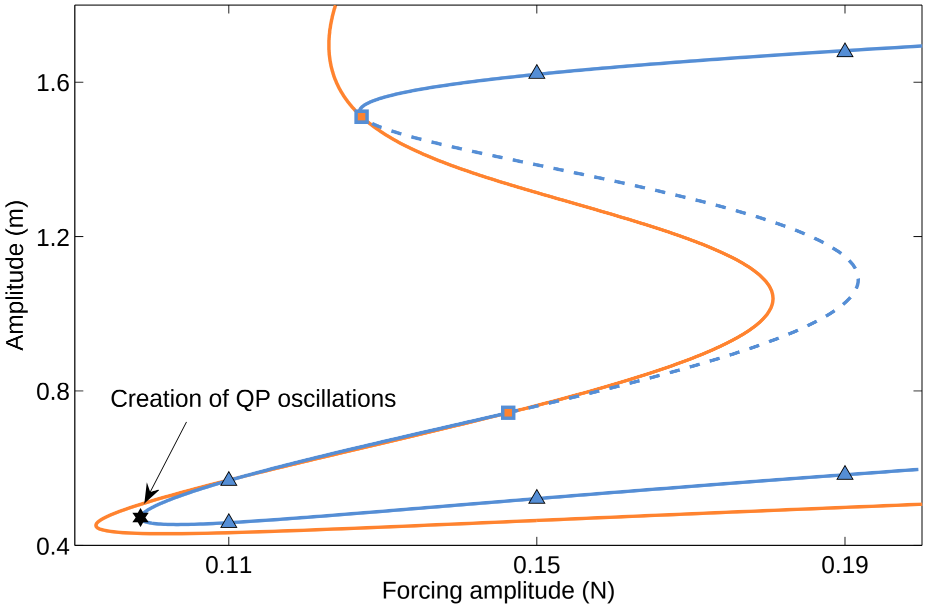

(b)

Figure 5.7: Projection of the bifurcation branches onto the forcing amplitude-response amplitude plane. (a) Fold bifurcations; (b) NS bifurcations. Circle and triangle markers represent the fold and NS bifurcations in Figs. 5.6(d-f), respectively, and square markers denote Bogdanov-Takens bifurcations.

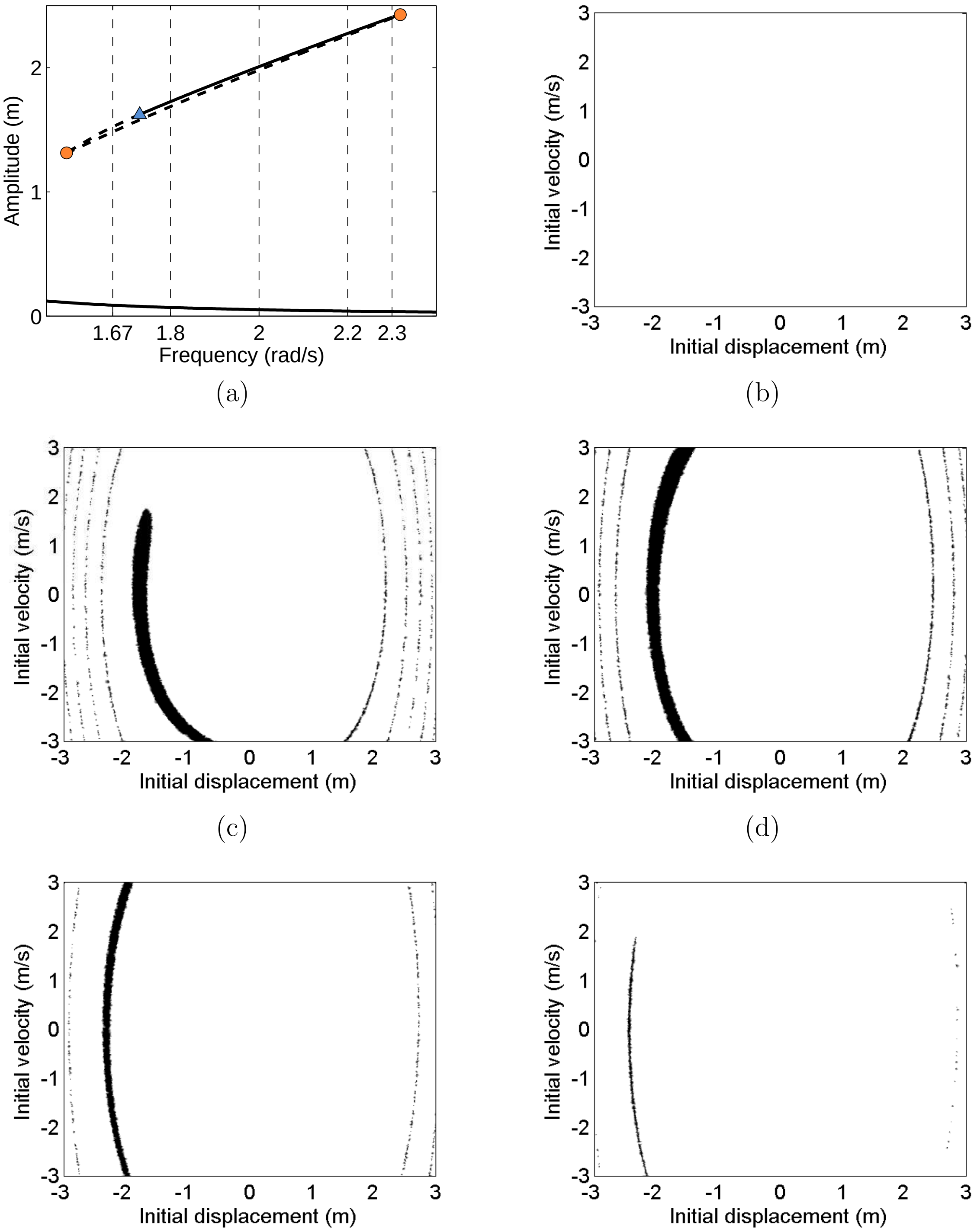

(a) (b)

(c) (d)

(e) (f)

Figure 5.8: Basins of attraction of the periodic solutions for $f = 0.15\,\mathrm{N}$. (a) Close-up of the NFRC; (b-f) basins of attraction for $\omega = 1.67\,\mathrm{rad/s}$; $\omega = 1.8\,\mathrm{rad/s}$; $\omega = 2\,\mathrm{rad/s}$; $\omega = 2.2\,\mathrm{rad/s}$, and $\omega = 2.3\,\mathrm{rad/s}$, respectively. White and black regions denote the coexisting periodic solutions on the main frequency response and on the IRC, respectively.

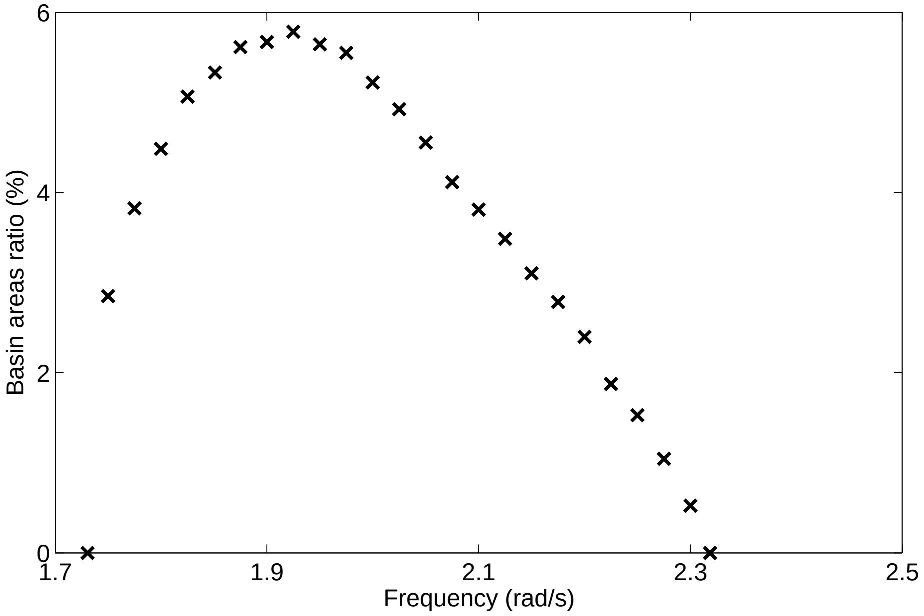

Figure 5.9: Ratio between the areas of the basins of attraction of the IRC and of the main resonance branch for $f = 0.15\,\mathrm{N}$.

## 5.4.4 Safe, Unsafe and Unacceptable NLTVA Operations

Three distinct regions, schematized in Fig. 5.10 and characterized based on branch B of fold bifurcations in Fig. 5.7(a), are defined for the operation of the NLTVA:

1. In the first region, the only branch of periodic solutions is the main branch. QP solutions exist, but they barely degrade NLTVA performance. It is therefore *safe* to operate the NLTVA in this region.
2. The second region presents a large-amplitude IRC. Even if this IRC appears outside the operating frequency range of the NLTVA and if its basins of attraction are small, it is *unsafe* to operate the NLTVA in this region.
3. In the third region, the IRC has merged with the main branch, resulting in a resonance peak of very high amplitude. Even if part of the branch may be unstable due to NS bifurcations, it is *unacceptable* to operate the NLTVA in this region.

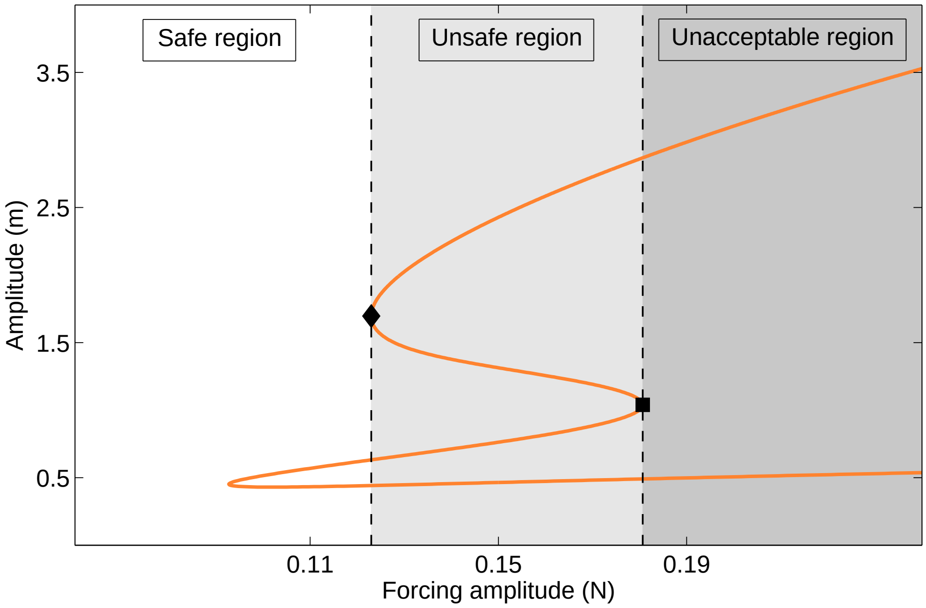

Figure 5.10: Performance regions of the NLTVA. The solid line is the projection of branch B of fold bifurcations onto the forcing amplitude-response amplitude plane, and the diamond and square markers indicate the apparition and merging of the IRCs, respectively.

## 5.5 Sensitivity Analysis of the NLTVA

### 5.5.1 Attenuation Performance in the Safe Region

The effects of variations of the damping and nonlinear stiffness coefficients on performance in the safe region are now studied. Variations of the linear stiffness are not considered herein, because very accurate values of the optimal frequency ratio can easily be obtained through small adjustments of the mass ratio (by, *e.g.*, adding small masses on the NLTVA once it is built).

Fig. 5.11 represents the effects of individual perturbations of ±15% of $c_2$ and $k_{nl2}$ on the amplitude of the resonance peaks in the safe region, *i.e.*, until $f = 0.12\,\mathrm{N}$. Note that these variations are realistic in view of what was achieved with an experimental NLTVA prototype [70]. The NLTVA performance is not significantly degraded and remains largely superior to that of the unperturbed LTVA, clearly highlighting the robustness of NLTVA performance in the safe region. For illustration, Fig. 5.12 depicts the corresponding frequency responses at $f = 0.11\,\mathrm{N}$.

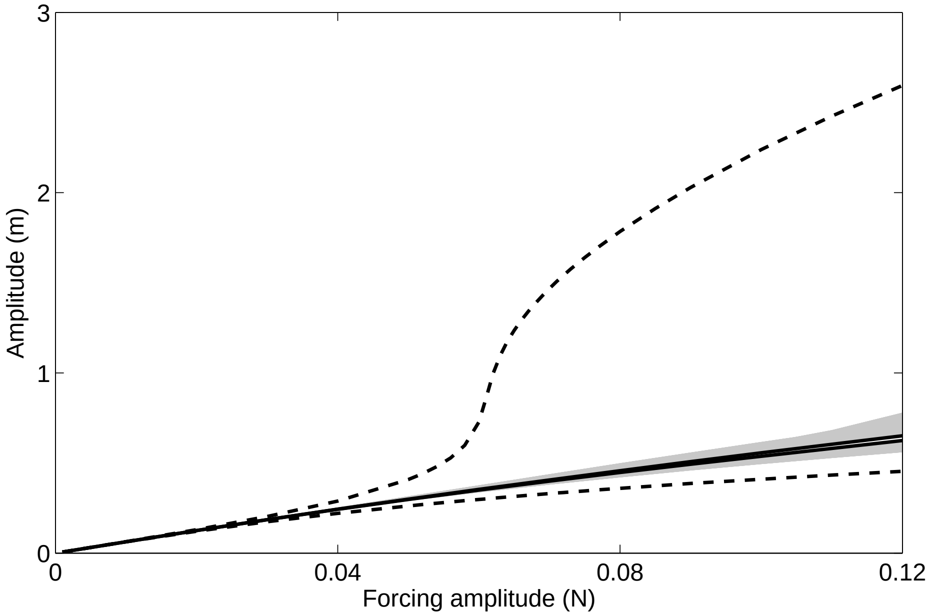

Figure 5.11: Performance of the LVTA/NLTVA for increasing forcing amplitudes. The dashed and solid lines depict the amplitude of the resonances peaks of the Duffing oscillator with an attached LTVA and NLTVA, respectively. The regions in gray show the individual effects of +15% and −15% perturbations of the reference values $c_2$ and $k_{nl2}$ of the NLTVA.

### 5.5.2 Boundaries in NLTVA Parameter Space

In order to assess the influence of the NLTVA parameters on the regions of performance, the dimensionless system (5.7) is considered. More specifically, variations of the parameters with respect to their reference values $\epsilon$, $\mu_2^{opt}$ and $\beta_3^{opt}$ computed from Table 5.3 are examined. Fig. 5.13(a) demonstrates the beneficial influence of larger mass ratios. Not only they correspond to resonance peaks of smaller amplitudes (assuming that fold bifurcations occur in the vicinity of the resonance peaks), but they also postpone both the appearance and the merging of the IRC to greater values of $\alpha_3$. The corresponding boundaries in Fig. 5.13(b) illustrate the clear enlargement of the safe region for greater mass ratios. An interesting observation is that, for $\epsilon < 4\%$, there are no longer QP solutions in the safe region.

Fig. 5.13(c) shows that increasing the damping ratio can translate into a fold bifurcation branch that possesses no folding, meaning that the IRC can be completely eliminated. Specifically, Fig. 5.13(d) confirms that the unsafe and unacceptable regions disappear for $p_\mu = \mu_2/\mu_2^{opt} \approx 144\%$. Such a detuning of the damping coefficient seems interesting, but it is associated with an important decrease in performance in the safe region.

Fig. 5.13(e) illustrates that the nonlinear stiffness coefficient $\beta_3$ has a strong influence on

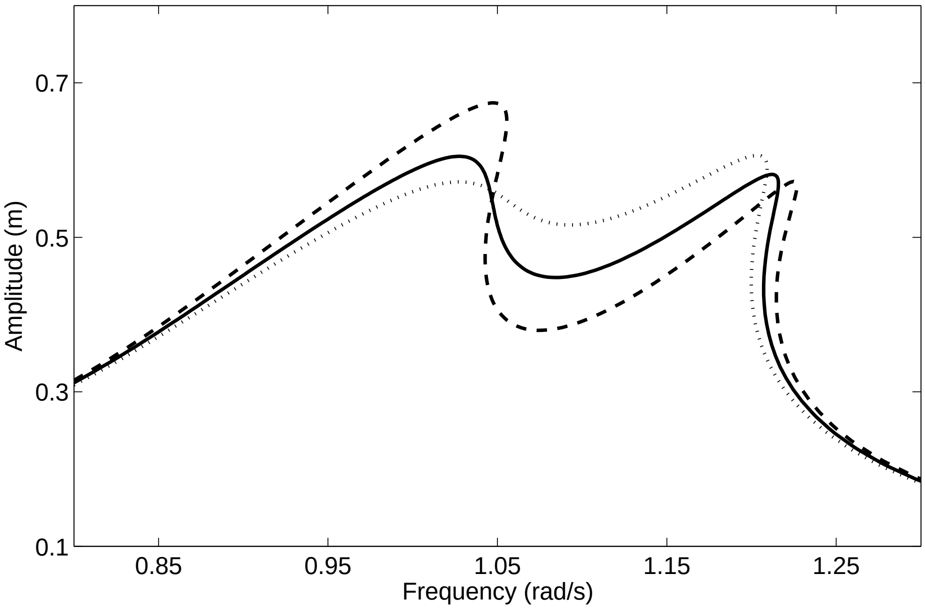

(a)

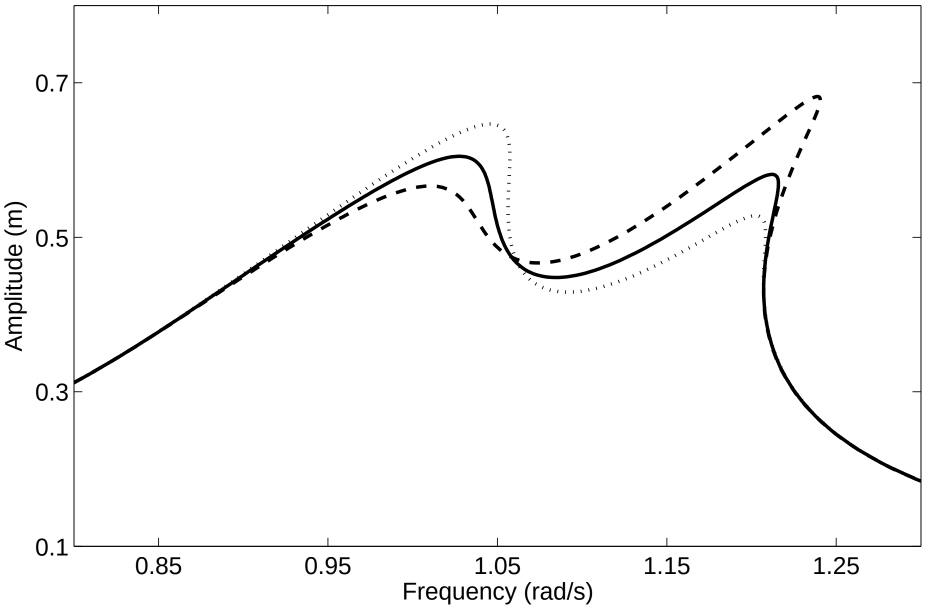

(b)

Figure 5.12: Sensitivity of the NLTVA performance with respect to (a) $c_2$ and (b) $k_{nl2}$ for $f = 0.11\,\text{N}$. The solid line represents the NFRC for the optimal values, the dashed and dotted lines correspond to variations of -15% and 15% with respect to the optimal value, respectively.

the merging of the IRC. Indeed, as plotted in Fig. 5.12(b), greater values of $\beta_3$ reduce the amplitude of the second peak, hence, postponing its merging with the IRC. Increasing $\beta_3$ is also beneficial for delaying the appearance of the IRC and enlarging the safe region, as shown in Fig. 5.13(f). On the other hand, Fig. 5.12(b) evidences that a greater $\beta_3$ increases the amplitude of the first resonant peak, which, in turn, decreases the NLTVA performance.

## 5.6 Concluding Remarks

The purpose of this chapter was the development of a new nonlinear absorber, the nonlineat tuned vibration absorber (NLTVA), for mitigating the vibrations of a nonlinear resonance of a mechanical system. A specific objective was to ensure the effectiveness of the absorber in weakly as well as strongly nonlinear regimes of motion for which the primary system's resonance frequency can undergo substantial variations.

To this end, the additional design parameter offered by nonlinear devices, *i.e.*, the mathematical form of the absorber's restoring force, was exploited thereby synthesizing nonlinearity for enhanced performance. We showed that, if the NLTVA is a 'mirror' of the primary system, a nonlinear counterpart of Den Hartog's equal-peak method can be established. Simple, though accurate, analytic formulas were proposed for this nonlinear equal-peak method. They lead to the design of an absorber with excellent performance in a relatively large range of forcing amplitudes. Interestingly, the coupled system Duffing-NLTVA is found to exhibit dynamics that bear resemblance to that of a linear system.

For very strongly nonlinear regimes, however, inherently nonlinear dynamical instabilities, namely isolated response curves and quasiperiodic solutions, appeared. In view of the potentially adverse effects of these attractors on the performance of the system, the second objective of the chapter was to identify, and possibly enlarge, the safe region of operation of the NLTVA. This was achieved thanks to the combination of several methods, namely the numerical continuation of periodic solutions, bifurcation detection and tracking, and global analysis. It turns out that the best strategy to enlarge the safe region while maintaining excellent NLTVA performance is to increase the mass ratio. If it cannot be further increased because of practical considerations, an alternative is to increase either damping or the nonlinear coefficient of the absorber.

Despite these instabilities, a key result is that the NLTVA performance remained always superior to that of the classical LTVA.

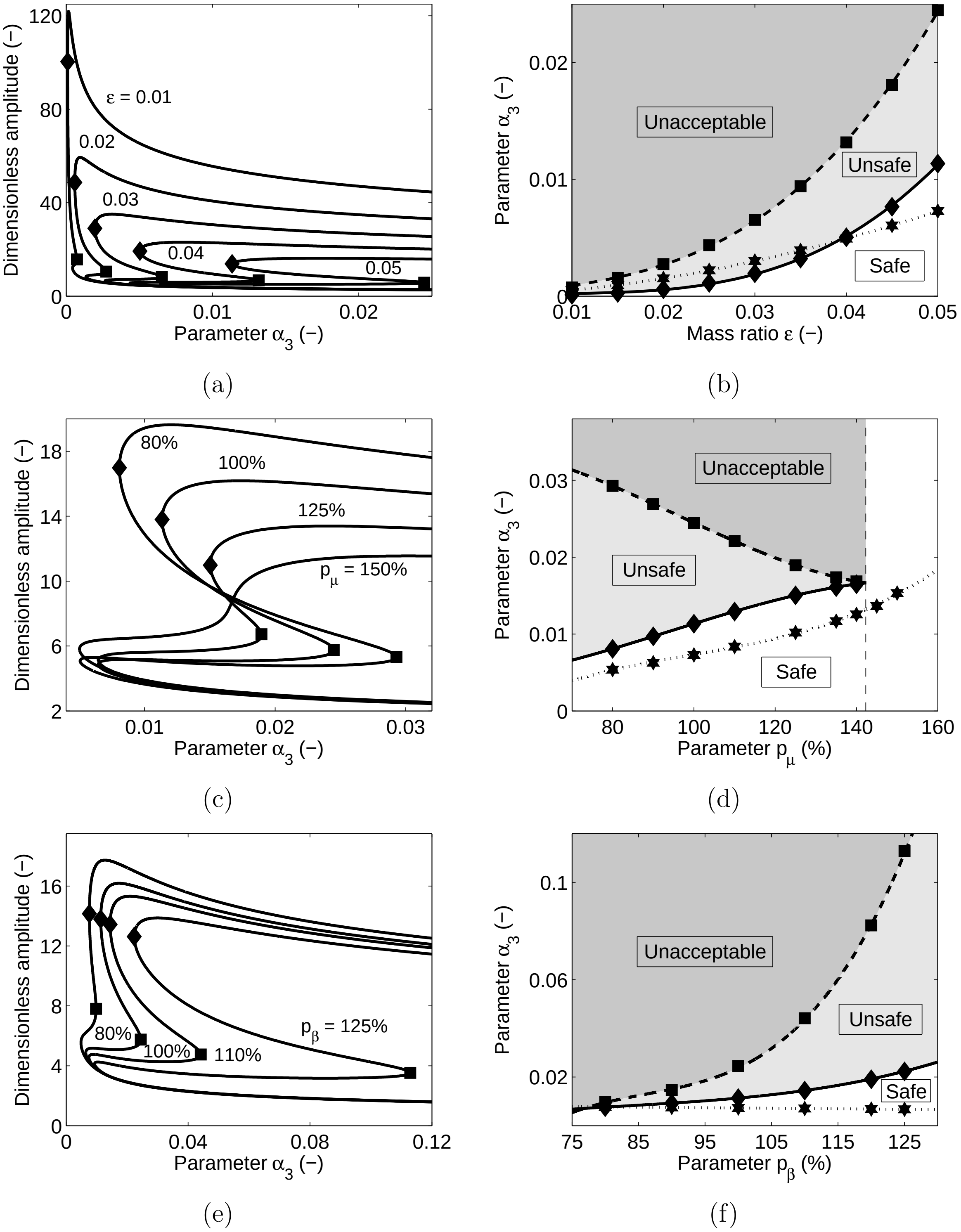

(a) (b)

(c) (d)

(e) (f)

Figure 5.13: Influence of (a-b) $\epsilon$, (c-d) $p_\mu = \mu_2/\mu_2^{opt}$ and (e-f) $p_\beta = \beta_3/\beta_3^{opt}$ on the regions of NLTVA operation. Left column: fold bifurcation branches. Right column: boundaries between safe and unsafe regions (diamond curves), unsafe and unacceptable regions (square curves), and the onset of QP motion (star curves).

# Conclusions

The present doctoral thesis introduced a methodology for advanced nonlinear vibration analysis, aimed toward promoting performance and ensuring robustness in the design cycle of engineering structures. This methodology, illustrated in Fig. C.1, is supported by original numerical techniques developed for bifurcation and modal analysis.

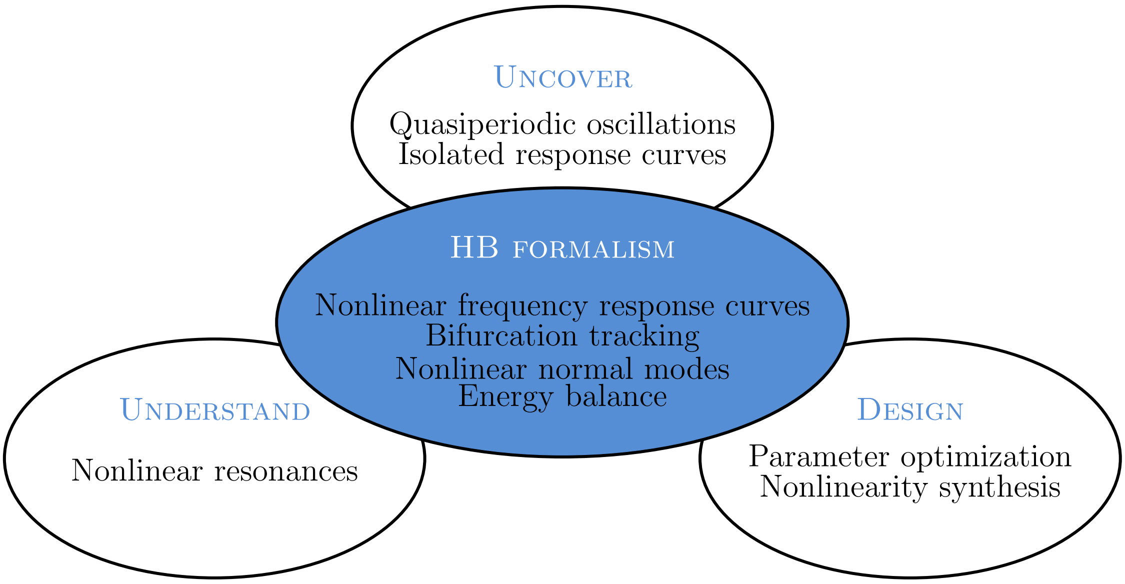

Figure C.1: Harmonic balance-based framework for advanced nonlinear vibration analysis.

The harmonic balance (HB) formalism constitutes the key building block of the proposed framework. In Chapter 1, the HB method was embedded in a continuation procedure to calculate nonlinear frequency response curves (NFRCs) and nonlinear normal modes (NNMs); it was also combined with Hill's method to perform stability analysis. In view of their importance in dynamical systems, bifurcations were systematically detected along NFRCs using adequate test functions, and tracked in the system's parameter space. In this context, our first specific contribution was a new bifurcation tracking algorithm based on bordering techniques and Floquet exponents derivatives. The satellite example in Chapter 2 demonstrated that this algorithm can effectively analyze the nonlinear dynamics exhibited by real-world structures and uncover complex phenomena, including quasiperiodic regimes of motion and isolated response curves. Through parameter modifications that eliminate the undesired dynamical attractors, the proposed bifurcation tracking methodology also paved the way for robust design of nonlinear structures.

The main thrust of Chapter 3 was the study of nonlinear resonances and their relation with NNMs. We developed an energy balance criterion in the HB formalism, enabling direct prediction of isolated response curves based on NNM topology. The merging of these isolated solutions with the NFRC could also be linked to the interactions between NNMs. These theoretical efforts were complemented in Chapter 4 by an experimental test campaign that we carried out at Duke University, during which isolated resonance curves were thoroughly characterized.

The final contribution of this thesis in Chapter 5 took advantage of the additional design flexibility offered by nonlinearities. In collaboration with several researchers of the Space Structures and Systems Laboratory, a new nonlinear vibration absorber, termed the nonlinear tuned vibration absorber, was developed. This absorber targets the mitigation of nonlinear resonances and generalizes to nonlinear systems the well-known equal-peak method proposed by Den Hartog. In this context, the performance and robustness of the absorber, as well as its sensitivity against parameter uncertainties, were successfully assessed using the developed HB-based tools. Even if this nonlinear device can exhibit quasiperiodic oscillations and isolated resonances, a remarkable feature is that it always outperforms the classical linear tuned vibration absorber.

# Perspectives for Future Research

Building on the developments achieved in this doctoral thesis, several directions can be followed for future research. This section reviews three promising directions, and illustrates them with preliminary results.

## Extension of the HB Methodology to Multi-Parameter Bifurcation Tracking

In this manuscript, the HB algorithm was adapted for tracking codimension-1 bifurcations with respect to two parameters (*e.g.*, the forcing frequency and amplitude). Often, the resulting bifurcation curves presented peculiar points associated with important changes in the system's dynamics. For instance, both the creation and merging of IRCs were found to appear at a folding point of the fold bifurcation curve. Because it is interesting to see how these points evolve with respect to a design parameter, one could directly track their evolution by including the selected parameter in the continuation procedure, hence performing three-parameter bifurcation tracking.

As a first step in this direction, the HB bifurcation tracking algorithm was extended to study the evolution of the codimension-2 Bogdanov-Takens (BT) bifurcations highlighted in Fig. 5.7, with respect to $\omega$, $f$ and $k_{nl2}$. As these bifurcations occur at the intersection of fold and Neimark-Sacker bifurcation curves, an augmented system for BT bifurcation tracking can be written as

$$\mathbf{h}_{BT}\left(\mathbf{z}, \omega, f, k_{nl2}\right) = \begin{bmatrix} \mathbf{h}\left(\mathbf{z}, \omega, f, k_{nl2}\right) \\ g_F\left(\mathbf{z}, \omega, f, k_{nl2}\right) \\ g_{NS}\left(\mathbf{z}, \omega, f, k_{nl2}\right) \end{bmatrix} = \mathbf{0} \tag{C.1}$$

where $g_F$ and $g_{NS}$ are computed through the resolution of the bordered system in Eq. (1.64) with $\mathbf{G} = \mathbf{h_z}$ and $\mathbf{G} = \tilde{\mathbf{B}}_{\odot}$, respectively. The main computational burden associated with bifurcation tracking was shown to be related to the evaluation of derivatives of $\mathbf{h_z}$ with respect to the components of $\mathbf{z}$ and the parameters. With the formulation proposed in Eq. (C.1), however, these derivatives can be employed for both $g_F$ and $g_{NS}$, which limits the increase in computational time with respect to the tracking of codimension-1 bifurcations. The calculated branch depicted in Fig. C.2 shows that the BT bifurcations are eliminated when lowering the value of $k_{nl2}$.

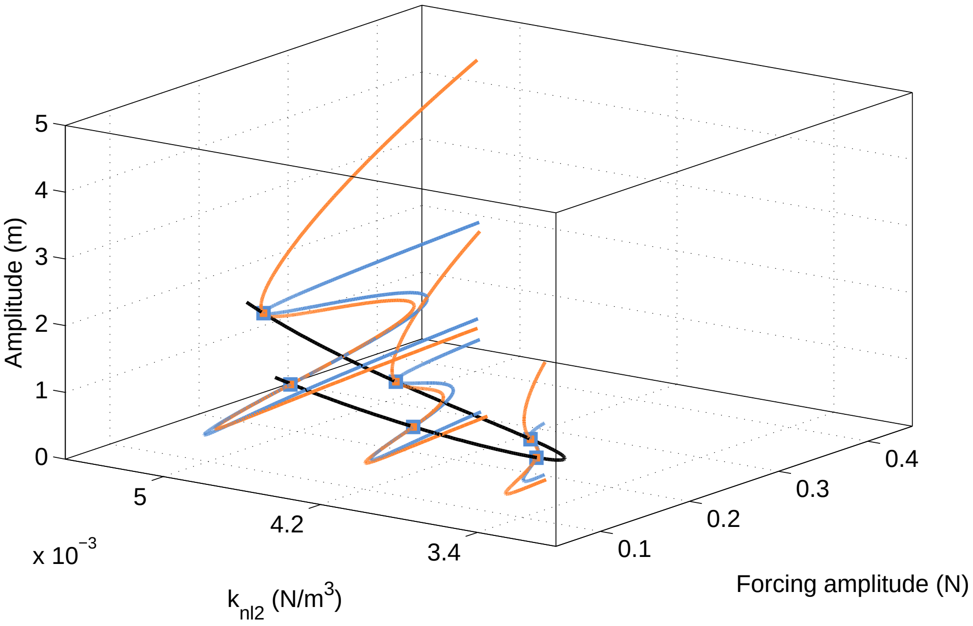

Figure C.2: Projection of the BT bifurcation curve (in black) onto the $f$-$k_{nl2}$-response amplitude space. Fold bifurcation curves and Neimark-Sacker/neutral saddle curves computed for $k_{nl2} = 0.0042\,\mathrm{N/m^3}$ (reference), $0.005\,\mathrm{N/m^3}$ and $0.0034\,\mathrm{N/m^3}$ are represented in orange and blue, respectively.

## Computation of Nonlinear Frequency Responses Curves from Broadband Testing

There is a recent interest in exploring the nonlinear features of a set-up without relying on a physical model. Methods based on online continuation, for instance, construct NFRCs or backbone curves experimentally, by means of a control apparatus [17, 177].

An alternative approach, which we term offline continuation, combines an identification method with the HB formalism. For this purpose, the frequency-domain nonlinear subspace identification (FNSI) technique is employed to obtain a state-space model from measured broadband data [133]. As presented in [63] and illustrated in Fig. C.3, the HB method can then be directly applied to the state-space model for the calculation of the NFRCs of the experimental set-up.

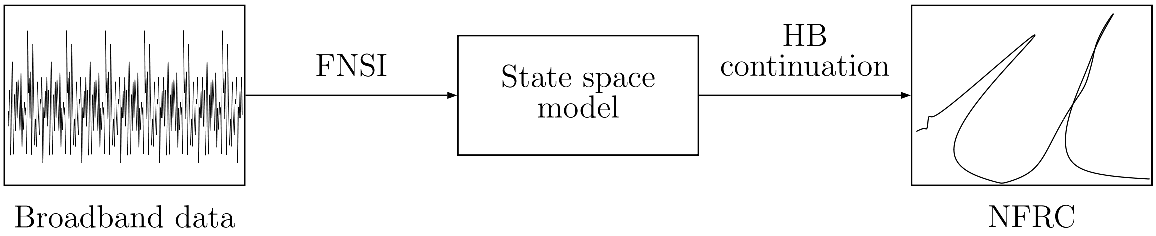

Figure C.3: FNSI-HB continuation procedure.

For illustration, Fig. C.4 displays the NFRC of the two-degree-of-freedom system studied in Chapter 1, constructed only from its response to random-phase multisine excitation.

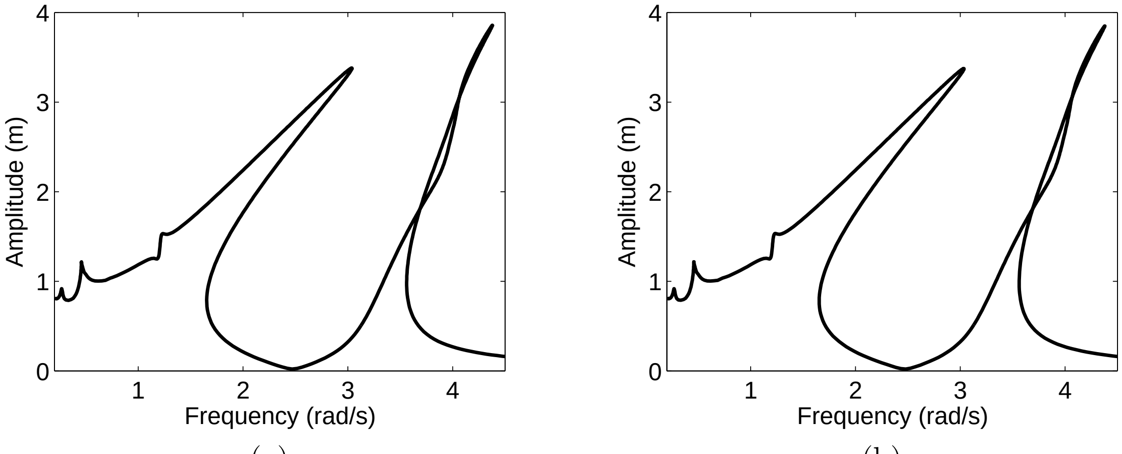

(a) (b)

Figure C.4: NFRC of the (a) theoretical model and (b) identified state-space model.

## Automatic Nonlinearity Synthesis

In Chapter 5, we demonstrated analytically that the mathematical form of the nonlinearity of the nonlinear tuned vibration absorber should be identical to that of the primary system. Thanks to this so-called mirror rule, equal peaks could be enforced in the NRFC of the system for a large range of forcing amplitudes. Another approach to derive this result is to gradually construct the nonlinearity of the absorber, which is modeled using a collection of splines for greater flexibility. Starting from very small displacements, the knots of the first two splines (corresponding to negative and positive displacements, respectively) are moved until the amplitude of two peaks of the NFRC are equal. Freezing the obtained splines, two new splines modeling the nonlinearity for larger negative and positive displacements are again optimized according to the equal-peak criterion. This 'point by point' procedure is repeated until the complete nonlinearity in the forcing range of interest is calculated. Fig. C.5 depicts the result for the nonlinear tuned vibration absorber attached to the Duffing oscillator considered in Chapter 5. For small and moderate displacements, an almost perfect agreement between the nonlinearities constructed analytically and numerically is observed. The deviation at large relative displacements is due to the inherent limitation of analytical developments for strongly nonlinear regimes of motion.

Beside the design of nonlinear absorbers, this automatic synthesis of nonlinearity opens up new horizons for the development of devices that exploit nonlinearity and for the optimization of nonlinear engineering structures to enforce, for instance, linear dynamics [78]. Potentially, intricate shapes can be obtained for the resulting nonlinearity, but this should not be seen as a limitation in view of the advent of topology optimization and additive manufacturing [42, 70].

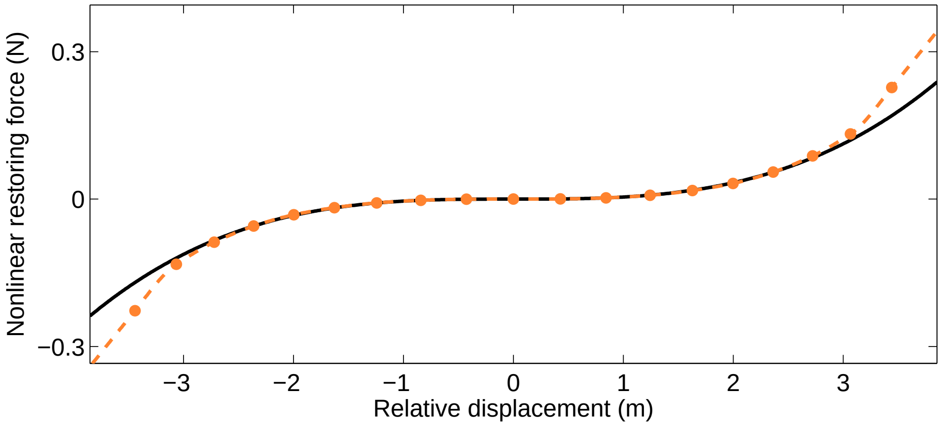

Figure C.5: Comparison between the analytical nonlinearity (in black) and the point-by-point construction (in orange).

# Bibliography

[1] N.P. Van Der Aa, H.G. Ter Morsche, and R.R.M. Mattheij. Computation of eigenvalue and eigenvector derivatives for a general complex-valued eigensystem. *Electronic Journal of Linear Algebra*, 16(1):300–314, 2007.

[2] V.S. Afraimovich and L.P. Shilnikov. Invariant two-dimensional tori, their breakdown and stochasticity. *American Mathematical Society Translations*, 149(2):201–212, 1991.

[3] J.R. Ahlquist, J.M. Carreño, H. Climent, R. de Diego, and J. de Alba. Assessment of nonlinear structural response in A400M GVT. In *Proceedings of the 28th International Modal Analysis Conference (IMAC)*, Jacksonville, FL, 2010.

[4] N.A. Alexander and F. Schilder. Exploring the performance of a nonlinear tuned mass damper. *Journal of Sound and Vibration*, 319(1):445–462, 2009.

[5] D. Antonio, D.H. Zanette, and D. López. Frequency stabilization in nonlinear micromechanical oscillators. *Nature Communications*, 3:806, 2012.

[6] R. Arquier. *Une Méthode de Calcul des Modes de Vibrations Non-Linéaires de Structures*. PhD thesis, Université de la méditerranée (Aix-Marseille II), Marseille, France, 2007.

[7] T. Asami and O. Nishihara. Closed-form exact solution to H$\infty$ optimization of dynamic vibration absorbers (application to different transfer functions and damping systems). *Journal of Vibration and Acoustics*, 125(3):398–405, 2003.

[8] T. Asami, O. Nishihara, and A.M. Baz. Analytical solutions to H$\infty$ and H2 optimization of dynamic vibration absorbers attached to damped linear systems. *Journal of Vibration and Acoustics*, 124(2):284–295, 2002.

[9] U. Ascher, J. Christiansen, and R.D. Russell. A collocation solver for mixed order systems of boundary value problems. *Mathematics of Computation*, 33:659–679, 1979.

[10] D. Avitabile, M. Desroches, and S. Rodrigues. On the numerical continuation of isolas of equilibria. *International Journal of Bifurcation and Chaos*, 22(11):1250277, 2012.

[11] K.V. Avramov and Y.V. Mikhlin. Review of applications of nonlinear normal modes for vibrating mechanical systems. *Applied Mechanics Reviews*, 65(2):020801, 2013.

[12] Y. Azizi, A.K. Bajaj, P. Davies, and V. Sundaram. Prediction and verification of the periodic response of a single-degree-of-freedom foam-mass system by using incremental harmonic balance. *Nonlinear Dynamics*, 82(4):1933–1951, 2015.

[13] S. Baguet and B. Cochelin. On the behaviour of the ANM continuation in the presence of bifurcations. *Communications in Numerical Methods in Engineering*, 19(6):459–471, 2003.

[14] M.C.C. Bampton and J.R.R. Craig. Coupling of substructures for dynamic analyses. *AIAA Journal*, 6(7):1313–1319, 1968.

[15] F. Barillon, J.J. Sinou, J.M. Duffal, and L. Jézéquel. Non-linear dynamics of a whole vehicle finite element model using a harmonic balance method. *International Journal of Vehicle Design*, 63(4):387–403, 2013.

[16] D.A.W. Barton, S.G. Burrow, and L.R. Clare. Energy harvesting from vibrations with a nonlinear oscillator. *Journal of Vibration and Acoustics*, 132(2):021009, 2010.

[17] D.A.W. Barton, B.P. Mann, and S.G. Burrow. Control-based continuation for investigating nonlinear experiments. *Journal of Vibration and Control*, 18(4):509–520, 2012.

[18] R. Bellet, B. Cochelin, P. Herzog, and P.O. Mattei. Experimental study of targeted energy transfer from an acoustic system to a nonlinear membrane absorber. *Journal of Sound and Vibration*, 329(14):2768–2791, 2010.

[19] W.J. Beyn, A. Champneys, E. Doedel, W. Govaerts, Y.A. Kuznetsov, and B. Sandstede. Numerical continuation, and computation of normal forms. *Handbook of Dynamical Systems*, 2:149–219, 2002.

[20] F. Blanc, C. Touzé, J.F. Mercier, K. Ege, and A.S.B. Ben-Dhia. On the numerical computation of nonlinear normal modes for reduced-order modelling of conservative vibratory systems. *Mechanical Systems and Signal Processing*, 36(2):520–539, 2013.

[21] N. Boechler, G. Theocharis, and C. Daraio. Bifurcation-based acoustic switching and rectification. *Nature Materials*, 10(9):665–668, 2011.

[22] F. Bonani and M. Gilli. Analysis of stability and bifurcations of limit cycles in Chua's circuit through the harmonic-balance approach. *IEEE Transactions on Circuits and Systems – Part I: Fundamental Theory and Applications*, 46(8):881–890, 1999.

[23] J.E. Brock. A note on the damped vibration absorber. *Journal of Applied Mechanics*, 13(4):A–284, 1946.

[24] T.M. Cameron and J.H. Griffin. An alternating frequency/time domain method for calculating the steady-state response of nonlinear dynamic systems. *Journal of Applied Mechanics*, 56(1):149–154, 1989.

[25] A. Cammarano, T.L. Hill, S.A. Neild, and D.J. Wagg. Bifurcations of backbone curves for systems of coupled nonlinear two mass oscillator. *Nonlinear Dynamics*, 77(1-2):311–320, 2014.

[26] A. Cardona, T. Coune, A. Lerusse, and M. Geradin. A multiharmonic method for non-linear vibration analysis. *International Journal for Numerical Methods in Engineering*, 37(9):1593–1608, 1994.

[27] A. Cardona, A. Lerusse, and M. Géradin. Fast Fourier nonlinear vibration analysis. *Computational Mechanics*, 22(2):128–142, 1998.

[28] K. Carney, I. Yunis, K. Smith, and C.Y. Peng. Nonlinear dynamic behavior in the Cassini spacecraft modal survey. In *Proceedings of the 15th International Modal Analysis Conference (IMAC)*, Orlando, FL, 1997.

[29] N. Carpineto, W. Lacarbonara, and F. Vestroni. Hysteretic tuned mass dampers for structural vibration mitigation. *Journal of Sound and Vibration*, 333(5):1302–1318, 2014.

[30] Y.K. Cheung and S.L. Lau. Incremental time-space finite strip method for non-linear structural vibrations. *Earthquake Engineering & Structural Dynamics*, 10(2):239–253, 1982.

[31] M. Claeys, J.J. Sinou, J.P. Lambelin, and B. Alcoverro. Multi-harmonic measurements and numerical simulations of nonlinear vibrations of a beam with non-ideal boundary conditions. *Communications in Nonlinear Science and Numerical Simulation*, 2014.

[32] M. Claeys, J.J. Sinou, J.P. Lambelin, and R. Todeschini. Experimental and numerical study of the nonlinear vibrations of an assembly with friction joints. In *Proceedings of the 26th International Conference on Noise and Vibration engineering (ISMA)*, Leuven, Belgium, 2014.

[33] S.T. Clark, F.M. Besem, R.E. Kielb, and J.P. Thomas. Developing a reduced-order model of nonsynchronous vibration in turbomachinery using proper-orthogonal decomposition methods. *Journal of Engineering for Gas Turbines and Power*, 137(5):052501, 2015.

[34] B. Cochelin and C. Vergez. A high order purely frequency-based harmonic balance formulation for continuation of periodic solutions. *Journal of Sound and Vibration*, 324(1):243–262, 2009.

[35] European Commission et al. Flightpath 2050: Europe's vision for aviation. Technical report, High Level Group on Aviation Research, Publications Office of the European Union, Luxembourg, 2011.

[36] H. Dankowicz and F. Schilder. An extended continuation problem for bifurcation analysis in the presence of constraints. *Journal of Computational and Nonlinear Dynamics*, 6(3), 2011.

[37] H.H. Denman. Tautochronic bifilar pendulum torsion absorbers for reciprocating engines. *Journal of Sound and Vibration*, 159(2):251–277, 1992.

[38] A. Dhooge, W. Govaerts, and Y.A. Kuznetsov. MATCONT: A MATLAB package for numerical bifurcation analysis of ODEs. *ACM Transactions on Mathematical Software (TOMS)*, 29(2):141–164, 2003.

[39] G. Dimitriadis. Continuation of higher-order harmonic balance solutions for nonlinear aeroelastic systems. *Journal of Aircraft*, 45(2):523–537, 2008.

[40] S.W. Doebling, C.R. Farrar, M.B. Prime, and D.W. Shevitz. Damage identification and health monitoring of structural and mechanical systems from changes in their vibration characteristics: A literature review. Technical report, Los Alamos National Lab., NM, 1996.

[41] E.J. Doedel, A.R. Champneys, T.F. Fairgrieve, Y.A. Kuznetsov, B. Sandstede, and X. Wang. AUTO97: Continuation and bifurcation software for ordinary differential equations (with homcont). *Users Guide, Concordia University, Montreal, Canada, Available from http://indy.cs.concordia.ca*, 1997.

[42] S. Dou and J.S. Jensen. Optimization of nonlinear structural resonance using the incremental harmonic balance method. *Journal of Sound and Vibration*, 334:239–254, 2015.

[43] S. Dou and J.S. Jensen. Optimization of hardening/softening behavior of plane frame structures using nonlinear normal modes. *Computers & Structures*, 164:63–74, 2016.

[44] S. Dou, B.S. Strachan, S.W. Shaw, and J.S. Jensen. Structural optimization for nonlinear dynamic response. *Philosophical Transactions of the Royal Society A: Mathematical, Physical and Engineering Sciences*, 373(2051):20140408, 2015.

[45] E. Dowelll. *A Modern Course in Aeroelasticity*, volume 217 of *Solid Mechanics and Its Applications*. Springer, New-York, NY, 2015.

[46] C. Duan and R. Singh. Super-harmonics in a torsional system with dry friction path subject to harmonic excitation under a mean torque. *Journal of Sound and Vibration*, 285(4):803–834, 2005.

[47] C. Duan and R. Singh. Isolated sub-harmonic resonance branch in the frequency response of an oscillator with slight asymmetry in the clearance. *Journal of Sound and Vibration*, 314(1):12–18, 2008.

[48] R.P. Eason, A.J. Dick, and S. Nagarajaiah. Numerical investigation of coexisting high and low amplitude responses and safe basin erosion for a coupled linear oscillator and nonlinear absorber system. *Journal of Sound and Vibration*, 333(15):3490–3504, 2014.

[49] D.A. Ehrhardt, R.B. Harris, and M.S. Allen. Numerical and experimental determination of nonlinear normal modes of a circular perforated plate. In *Proceedings of the 32nd International Modal Analysis Conference (IMAC)*, Orlando, FL, USA, 2014.

[50] K. Ekici, K.C. Hall, and E.H. Dowell. Computationally fast harmonic balance methods for unsteady aerodynamic predictions of helicopter rotors. *Journal of Computational Physics*, 227(12):6206–6225, 2008.

[51] C.W. Emory and M.J. Patil. Predicting limit cycle oscillation in an aeroelastic system using nonlinear normal modes. *Journal of Aircraft*, 50(1):73–81, 2013.

[52] K. Engelborghs, T. Luzyanina, and D. Roose. Numerical bifurcation analysis of delay differential equations using DDE-BIFTOOL. *ACM Transactions on Mathematical Software (TOMS)*, 28(1):1–21, 2002.

[53] D.J. Ewins. *Modal Testing: Theory, Practice and Application.* Research Studies Press, Baldock, United Kingdom, 2000.

[54] C.C. Fang. Critical conditions for a class of switched linear systems based on harmonic balance: Applications to DC-DC converters. *Nonlinear Dynamics*, 70(3):1767–1789, 2012.

[55] M. Febbo and S.P. Machado. Nonlinear dynamic vibration absorbers with a saturation. *Journal of Sound and Vibration*, 332(6):1465–1483, 2013.

[56] M. Friswell and J.E. Mottershead. *Finite Element Model Updating in Structural Dynamics*, volume 38 of *Solid Mechanics and Its Applications.* Kluwer Academic Publishers, Dordrecht, The Netherlands, 1995.

[57] G. Gatti and M.J. Brennan. On the effects of system parameters on the response of a harmonically excited system consisting of weakly coupled nonlinear and linear oscillators. *Journal of Sound and Vibration*, 330(18):4538–4550, 2011.

[58] G. Gatti, M.J. Brennan, and I. Kovacic. On the interaction of the responses at the resonance frequencies of a nonlinear two degrees-of-freedom system. *Physica D: Nonlinear Phenomena*, 239(10):591–599, 2010.

[59] R. Genesio and A. Tesi. Harmonic balance methods for the analysis of chaotic dynamics in nonlinear systems. *Automatica*, 28(3):531–548, 1992.

[60] C. George, L.N. Virgin, and T. Witelski. Experimental study of regular and chaotic transients in a non-smooth system. *International Journal of Non-Linear Mechanics*, 2015.

[61] M. Géradin and D.J. Rixen. *Mechanical Vibrations: Theory and Application to Structural Dynamics*. John Wiley & Sons, New-York, NY, 2014.

[62] A. Gopinath, E. Van Der Weide, J.J. Alonso, A. Jameson, K. Ekici, and K.C. Hall. Three-dimensional unsteady multi-stage turbomachinery simulations using the harmonic balance technique. In *Proceedings of the 45th AIAA Aerospace Sciences Meeting and Exhibit*, Reno, NV, 2007.

[63] E. Gourc, C. Grappasonni, J.P. Noël, T. Detroux, and G. Kerschen. Obtaining nonlinear frequency responses from broadband testing. In *Proceedings of the 34th International Modal Analysis Conference (IMAC)*, Orlando, FL, USA, 2016.

[64] E. Gourc, G. Michon, S. Seguy, and A. Berlioz. Experimental investigation and design optimization of targeted energy transfer under periodic forcing. *Journal of Vibration and Acoustics*, 136(2):021021, 2014.

[65] E. Gourc, S. Seguy, G. Michon, A. Berlioz, and B.P. Mann. Quenching chatter instability in turning process with a vibro-impact nonlinear energy sink. *Journal of Sound and Vibration*, 355:392–406, 2015.

[66] W. Govaerts. Numerical bifurcation analysis for ODEs. *Journal of Computational and Applied Mathematics*, 125(1):57–68, 2000.

[67] W. Govaerts, Y.A. Kuznetsov, V. De Witte, A. Dhooge, H.G.E. Meijer, W. Mestrom, A.M. Riet, and B. Sautois. MATCONT and CL MATCONT: Continuation toolboxes in MATLAB. Technical report, Gent University and Utrech University, 2011.

[68] W. Govaerts and B. Sijnave. Matrix manifolds and the jordan structure of the bialternate matrix product. *Linear Algebra and its Applications*, 292(1):245–266, 1999.

[69] W.J.F. Govaerts. *Numerical Methods for Bifurcations of Dynamical Equilibria.* SIAM, Philadelphia, PA, 2000.

[70] C. Grappasonni, G. Habib, T. Detroux, and G. Kerschen. Experimental demonstration of a 3D-printed nonlinear tuned vibration absorber. In *Proceedings of the 33rd International Modal Analysis Conference (IMAC)*, Orlando, FL, 2015.

[71] P.L. Green, K. Worden, K. Atallah, and N.D. Sims. The benefits of duffing-type nonlinearities and electrical optimisation of a mono-stable energy harvester under white Gaussian excitations. *Journal of Sound and Vibration*, 331(20):4504–4517, 2012.

[72] A. Grolet and F. Thouverez. On a new harmonic selection technique for harmonic balance method. *Mechanical Systems and Signal Processing*, 30:43–60, 2012.

[73] A. Grolet and F. Thouverez. Computing multiple periodic solutions of nonlinear vibration problems using the harmonic balance method and Groebner bases. *Mechanical Systems and Signal Processing*, 52:529–547, 2015.

[74] J. Guckenheimer, M. Myers, and B. Sturmfels. Computing Hopf bifurcations I. *SIAM Journal on Numerical Analysis*, 34(1):1–21, 1997.

[75] J. Guillen and C. Pierre. An efficient, hybrid, frequency-time domain method for the dynamics of large-scale dry-friction damped structural systems. In *Proceedings of the IUTAM Symposium on Unilateral Multibody Contacts*, Munich, Germany, 1998.

[76] M. Guskov and F. Thouverez. Harmonic balance-based approach for quasi-periodic motions and stability analysis. *Journal of Vibration and Acoustics*, 134(3):031003, 2012.

[77] G. Habib, T. Detroux, R. Viguié, and G. Kerschen. Nonlinear generalization of Den Hartog' s equal-peak method. *Mechanical Systems and Signal Processing*, 52:17–28, 2015.

[78] G. Habib, C. Grappasonni, and G. Kerschen. Enforcing linear dynamics through the addition of nonlinearity. In *Proceedings of the 34th International Modal Analysis Conference (IMAC)*, Orlando, FL, USA, 2016.

[79] K.C. Hall, J.P. Thomas, and W.S. Clark. Computation of unsteady nonlinear flows in cascades using a harmonic balance technique. *AIAA Journal*, 40(5):879–886, 2002.

[80] J.P. Den Hartog. *Mechanical Vibrations.* McGraw-Hill Book Company, New-York, NY, 1934.

[81] G.W. Hill. On the part of the motion of the lunar perigee which is a function of the mean motions of the sun and moon. *Acta Mathematica*, 8(1):1–36, 1886.

[82] T.L. Hill, A. Cammarano, S.A. Neild, and D.J. Wagg. An analytical method for the optimisation of weakly nonlinear systems. In *Proceedings of the 9th International Conference on Structural Dynamics (EURODYN)*, Porto, Portugal, 2014.

[83] T.L. Hill, A. Cammarano, S.A. Neild, and D.J. Wagg. Interpreting the forced responses of a two-degree-of-freedom nonlinear oscillator using backbone curves. *Journal of Sound and Vibration*, 349:276–288, 2015.

[84] T.L. Hill, A. Cammarano, S.A. Neild, and D.J. Wagg. Out-of-unison resonance in weakly nonlinear coupled oscillators. *Proceedings of the Royal Society of London A: Mathematical, Physical and Engineering Sciences*, 471(2173):20140659, 2015.

[85] T.L. Hill, P.L. Green, A. Cammarano, and S.A. Neild. Fast Bayesian identification of a class of elastic weakly nonlinear systems using backbone curves. *Journal of Sound and Vibration*, 360:156–170, 2016.

[86] C.S. Hsu. *Cell-to-Cell Mapping: A Method of Global Analysis for Nonlinear Systems*, volume 64 of *Applied Mathematical Sciences*. Springer Science & Business Media, New-York, NY, 2013.

[87] S.A. Hubbard, D.M. McFarland, L.A. Bergman, and A.F. Vakakis. Targeted energy transfer between a model flexible wing and nonlinear energy sink. *Journal of Aircraft*, 47(6):1918–1931, 2010.

[88] J.L. Hwang and T.N. Shiau. An application of the generalized polynomial expansion method to nonlinear rotor bearing systems. *Journal of Vibration and Acoustics*, 113(3):299–308, 1991.

[89] V. Jaumouillé, J.J. Sinou, and B. Petitjean. An adaptive harmonic balance method for predicting the nonlinear dynamic responses of mechanical systems–Application to bolted structures. *Journal of Sound and Vibration*, 329(19):4048–4067, 2010.

[90] L. Jezequel and C.H. Lamarque. Analysis of non-linear dynamical systems by the normal form theory. *Journal of Sound and Vibration*, 149(3):429–459, 1991.

[91] M.A. Karami and D.J. Inman. Powering pacemakers from heartbeat vibrations using linear and nonlinear energy harvesters. *Applied Physics Letters*, 100(4):042901, 2012.

[92] S. Karkar, B. Cochelin, and C. Vergez. A high-order, purely frequency based harmonic balance formulation for continuation of periodic solutions: The case of non-polynomial nonlinearities. *Journal of Sound and Vibration*, 332(4):968–977, 2013.

[93] S. Karkar, B. Cochelin, and C. Vergez. A comparative study of the harmonic balance method and the orthogonal collocation method on stiff nonlinear systems. *Journal of Sound and Vibration*, 333(12):2554–2567, 2014.

[94] H.B. Keller. Lectures on numerical methods in bifurcation problems. 1987.

[95] G. Kerschen, J.J. Kowtko, D.M. McFarland, L.A. Bergman, and A.F. Vakakis. Theoretical and experimental study of multimodal targeted energy transfer in a system of coupled oscillators. *Nonlinear Dynamics*, 47(1-3):285–309, 2007.

[96] G. Kerschen, Y.S. Lee, A.F. Vakakis, D.M. McFarland, and L.A. Bergman. Irreversible passive energy transfer in coupled oscillators with essential nonlinearity. *SIAM Journal on Applied Mathematics*, 66(2):648–679, 2006.

[97] G. Kerschen, M. Peeters, J.C. Golinval, and C. Stephan. Nonlinear modal analysis of a full-scale aircraft. *Journal of Aircraft*, 50(5):1409–1419, 2013.

[98] G. Kerschen, M. Peeters, J.C. Golinval, and A.F. Vakakis. Nonlinear normal modes, Part I: A useful framework for the structural dynamicist. *Mechanical Systems and Signal Processing*, 23(1):170–194, 2009.

[99] T.C. Kim, T.E. Rook, and R. Singh. Super-and sub-harmonic response calculations for a torsional system with clearance nonlinearity using the harmonic balance method. *Journal of Sound and Vibration*, 281(3):965–993, 2005.

[100] M. Krack, L. Panning von Scheidt, and J. Wallaschek. A high-order harmonic balance method for systems with distinct states. *Journal of Sound and Vibration*, 332(21):5476–5488, 2013.

[101] M. Krack, L. Panning von Scheidt, J. Wallaschek, C. Siewert, and A. Hartung. Reduced order modeling based on complex nonlinear modal analysis and its application to bladed disks with shroud contact. *Journal of Engineering for Gas Turbines and Power*, 135(10):102502, 2013.

[102] N.M. Krylov and N.N. Bogoliubov. *Introduction to Non-Linear Mechanics*. Number 11 in Annals of Mathematics Studies. Princeton University Press, Princeton, NJ, 1943.

[103] R.J. Kuether and M.S. Allen. Computing nonlinear normal modes using numerical continuation and force appropriation. In *Proceedings of the ASME 2012 International Design Engineering Technical Conferences (IDETC)*, Chicago, IL, USA, 2012.

[104] R.J. Kuether, M.R. Brake, and M.S. Allen. Evaluating convergence of reduced order models using nonlinear normal modes. In *Proceedings of the 32nd International Modal Analysis Conference (IMAC)*, Orlando, FL, 2014.

[105] K.S. Kundert and A. Sangiovanni-Vincentelli. Simulation of nonlinear circuits in the frequency domain. *IEEE Transactions on Computer-Aided Design of Integrated Circuits and Systems*, 5(4):521–535, 1986.

[106] M. Kurt, M. Eriten, D. M. McFarland, L.A. Bergman, and A.F. Vakakis. Methodology for model updating of mechanical components with local nonlinearities. *Journal of Sound and Vibration*, 357:331–348, 2015.

[107] Y.A. Kuznetsov. *Elements of Applied Bifurcation Theory*. Springer Science & Business Media, New-York, NY, 2013.

[108] Y.A. Kuznetsov and V.V. Levitin. CONTENT: A multiplatform environment for analyzing dynamical systems. *User's Guide, Dynamical Systems Laboratory, CWI, Amsterdam, Netherlands, Available by anonymous ftp from ftp.cwi.nl/pub/CONTENT*, 1995-1997.

[109] W. Lacarbonara, R.R. Soper, A.H. Nayfeh, and D.T. Mook. A nonclassical vibration absorber for pendulation reduction. *Journal of Vibration and Control*, 7(3):365–393, 2001.

[110] V. Lanza, M. Bonnin, and M. Gilli. On the application of the describing function technique to the bifurcation analysis of nonlinear systems. *Circuits and Systems II: Express Briefs, IEEE Transactions on*, 54(4):343–347, 2007.

[111] S.L. Lau and Y.K. Cheung. Amplitude incremental variational principle for nonlinear vibration of elastic systems. *Journal of Applied Mechanics*, 48(4):959–964, 1981.

[112] D. Laxalde and F. Thouverez. Complex non-linear modal analysis for mechanical systems: Application to turbomachinery bladings with friction interfaces. *Journal of Sound and Vibration*, 322(4):1009–1025, 2009.

[113] A. Lazarus and O. Thomas. A harmonic-based method for computing the stability of periodic solutions of dynamical systems. *Comptes Rendus Mécanique*, 338(9):510–517, 2010.

[114] B.H.K. Lee, L. Liu, and K.W. Chung. Airfoil motion in subsonic flow with strong cubic nonlinear restoring forces. *Journal of Sound and Vibration*, 281(3):699–717, 2005.

[115] Y.S. Lee, F. Nucera, A.F. Vakakis, D.M. McFarland, and L.A. Bergman. Periodic orbits, damped transitions and targeted energy transfers in oscillators with vibro-impact attachments. *Physica D: Nonlinear Phenomena*, 238(18):1868–1896, 2009.

[116] S. Lenci and G. Rega. Dimension reduction of homoclinic orbits of buckled beams via the non-linear normal modes technique. *International Journal of Non-Linear Mechanics*, 42(3):515–528, 2007.

[117] R. Lewandowski. Computational formulation for periodic vibration of geometrically nonlinear structures–part 2: Numerical strategy and examples. *International journal of solids and structures*, 34(15):1949–1964, 1997.

[118] T.Y. Li. Solving polynomial systems by polyhedral homotopies. *Taiwanese Journal of Mathematics*, 3(3):pp–251, 1999.

[119] H. Liao. Global resonance optimization analysis of nonlinear mechanical systems: Application to the uncertainty quantification problems in rotor dynamics. *Communications in Nonlinear Science and Numerical Simulation*, 19(9):3323–3345, 2014.

[120] L. Liu and E.H. Dowell. Harmonic balance approach for an airfoil with a freeplay control surface. *AIAA Journal*, 43(4):802–815, 2005.

[121] S.F. Masri and T.K. Caughey. A nonparametric identification technique for nonlinear dynamic problems. *Journal of Applied Mechanics*, 46(2):433–447, 1979.

[122] Y.V. Mikhlin and K.V. Avramov. Nonlinears normal modes for vibrating mechanical systems. Review of theoretical developments. *Applied Mechanics Reviews*, 63(6):060802, 2010.

[123] G. Moore. Floquet theory as a computational tool. *SIAM Journal on Numerical Analysis*, 42(6):2522–2568, 2005.

[124] E.H. Moussi, S. Bellizzi, B. Cochelin, and I. Nistor. Nonlinear normal modes of a two degrees-of-freedom piecewise linear system. *Mechanical Systems and Signal Processing*, 64:266–281, 2015.

[125] P. Muhamad, N.D. Sims, and K. Worden. On the orthogonalised reverse path method for nonlinear system identification. *Journal of Sound and Vibration*, 331(20):4488–4503, 2012.

[126] F.J. Munoz-Almaraz, E. Freire, J. Galán, E. Doedel, and A. Vanderbauwhede. Continuation of periodic orbits in conservative and Hamiltonian systems. *Physica D: Nonlinear Phenomena*, 181(1):1–38, 2003.

[127] S. Nacivet, C. Pierre, F. Thouverez, and L. Jezequel. A dynamic Lagrangian frequency-time method for the vibration of dry-friction-damped systems. *Journal of Sound and Vibration*, 265(1):201–219, 2003.

[128] S. Narayanan and P. Sekar. A frequency domain based numeric-analytical method for non-linear dynamical systems. *Journal of Sound and Vibration*, 211(3):409–424, 1998.

[129] A.H. Nayfeh and B. Balachandran. *Applied Nonlinear Dynamics: Analytical, Computational and Experimental Methods.* John Wiley & Sons, New-York, NY, 2008.

[130] A.H. Nayfeh and S.A. Nayfeh. Nonlinear normal modes of a continuous system with quadratic nonlinearities. *Journal of Vibration and Acoustics*, 117(2):199–205, 1995.

[131] J.P. Noël. *A Frequency-Domain Approach to Subspace Identification of Nonlinear Systems: Application to Aerospace Structures.* PhD thesis, Université de Liège, Liège, Belgium, 2014.

[132] J.P. Noël, T. Detroux, G. Kerschen, and L.N. Virgin. Isolated response curves in a base-excited, two-degree-of-freedom, nonlinear system. In *Proceedings of the ASME 2015 International Design Engineering Technical Conferences (IDETC)*, Boston, MA, 2015.

[133] J.P. Noël and G. Kerschen. Frequency-domain subspace identification for nonlinear mechanical systems. *Mechanical Systems and Signal Processing*, 40(2):701–717, 2013.

[134] J.P. Noël, L. Renson, and G. Kerschen. Complex dynamics of a nonlinear aerospace structure: Experimental identification and modal interactions. *Journal of Sound and Vibration*, 333(12):2588–2607, 2014.

[135] F. Nucera, A.F. Vakakis, D.M. McFarland, L.A. Bergman, and G. Kerschen. Targeted energy transfers in vibro-impact oscillators for seismic mitigation. *Nonlinear Dynamics*, 50(3):651–677, 2007.

[136] Video of the experiments presented in Chapter 4 (isolated configuration). `https://youtu.be/7w4JDbcSsxU`, consulted in March 2016.

[137] Video of the experiments presented in Chapter 4 (merged configuration). `https://youtu.be/dqXnpLpiCAY`, consulted in March 2016.

[138] S.S. Oueini and A.H. Nayfeh. Analysis and application of a nonlinear vibration absorber. *Journal of Vibration and Control*, 6(7):999–1016, 2000.

[139] C. Padmanabhan and R. Singh. Analysis of periodically excited non-linear systems by a parametric continuation technique. *Journal of Sound and Vibration*, 184(1):35–58, 1995.

[140] A. Paranjape, N.K. Sinha, and N. Ananthkrishnan. Use of bifurcation and continuation methods for aircraft trim and stability analysis–A state-of-the-art. *Journal of Aerospace Sciences and Technologies*, 60(2):85, 2008.

[141] M.C. Pauzin, S. Mensah, B. Cochelin, and J.P. Lefebvre. High order harmonic balance formulation of free and encapsulated microbubbles. *Journal of Sound and Vibration*, 330(5):987–1004, 2011.

[142] M. Peeters, G. Kerschen, and J.C. Golinval. Dynamic testing of nonlinear vibrating structures using nonlinear normal modes. *Journal of Sound and Vibration*, 330(3):486–509, 2011.

[143] M. Peeters, G. Kerschen, and J.C. Golinval. Modal testing of nonlinear vibrating structures based on nonlinear normal modes: Experimental demonstration. *Mechanical Systems and Signal Processing*, 25(4):1227–1247, 2011.

[144] M. Peeters, R. Viguié, G. Sérandour, G. Kerschen, and J.C. Golinval. Nonlinear normal modes, Part II: Toward a practical computation using numerical continuation techniques. *Mechanical Systems and Signal Processing*, 23(1):195–216, 2009.

[145] L. Peletan, S. Baguet, M. Torkhani, and G. Jacquet-Richardet. A comparison of stability computational methods for periodic solution of nonlinear problems with application to rotordynamics. *Nonlinear Dynamics*, 72(3):671–682, 2013.

[146] L. Peletan, S. Baguet, M. Torkhani, and G. Jacquet-Richardet. Quasi-periodic harmonic balance method for rubbing self-induced vibrations in rotor-stator dynamics. *Nonlinear Dynamics*, 78(4):2501–2515, 2014.

[147] E. Pesheck, C. Pierre, and S.W. Shaw. Accurate reduced-order models for a simple rotor blade model using nonlinear normal modes. *Mathematical and Computer Modelling*, 33(10):1085–1097, 2001.

[148] S. Peter, A. Grundler, P. Reuss, L. Gaul, and R.I. Leine. Towards finite element model updating based on nonlinear normal modes. In *Proceedings of the 33rd International Modal Analysis Conference (IMAC)*, Orlando, FL, 2015.

[149] S. Peter, P. Reuss, and L. Gaul. Identification of sub-and higher harmonic vibrations in vibro-impact systems. In *Proceedings of the 32nd International Modal Analysis Conference (IMAC)*, Orlando, FL, 2014.

[150] S. Peter, R. Riethmüller, and R.I. Leine. Tracking of backbone curves of nonlinear systems using phase-locked-loops. In *Proceedings of the 34th International Modal Analysis Conference (IMAC)*, Orlando, FL, USA, 2016.

[151] E.P. Petrov. Direct parametric analysis of resonance regimes for nonlinear vibrations of bladed disks. *Journal of Turbomachinery*, 129(3):495–502, 2007.

[152] E.P. Petrov. Analysis of bifurcations in multiharmonic analysis of nonlinear forced vibrations of gas-turbine engine structures with friction and gaps. In *Proceedings of the ASME Turbo Expo: Turbine Technical Conference and Exposition*, Montreal, Canada, 2015.

[153] E.P. Petrov and D.J. Ewins. Analytical formulation of friction interface elements for analysis of nonlinear multi-harmonic vibrations of bladed disks. *Journal of Turbomachinery*, 125(2):364–371, 2003.

[154] C. Piccardi. Bifurcations of limit cycles in periodically forced nonlinear systems: The harmonic balance approach. *IEEE Transactions on Circuits and Systems – Part I: Fundamental Theory and Applications*, 41(4):315–320, 1994.

[155] C. Piccardi. Harmonic balance analysis of codimension-2 bifurcations in periodic systems. *IEEE Transactions on Circuits and Systems – Part I: Fundamental Theory and Applications*, 43:1015–1018, 1996.

[156] C. Pierre, A.A. Ferri, and E.H. Dowell. Multi-harmonic analysis of dry friction damped systems using an incremental harmonic balance method. *Journal of Applied Mechanics*, 52(4):958–964, 1985.

[157] N. Poovarodom, S. Kanchanosot, and P. Warnitchai. Application of non-linear multiple tuned mass dampers to suppress man-induced vibrations of a pedestrian bridge. *Earthquake Engineering & Structural Dynamics*, 32(7):1117–1131, 2003.

[158] O. Poudou and C. Pierre. Hybrid frequency-time domain methods for the analysis of complex structural systems with dry friction damping. In *Proceedings of the 44th AIAA/ASME/ASCE/AHS/ASC Structures, Structural Dynamics and Materials Conference*, Norfolk, VA, 2003.

[159] M.J.D. Powell. A hybrid method for nonlinear equations. *Numerical Methods for Nonlinear Algebraic Equations*, 7:87–114, 1970.

[160] D.D. Quinn, A.L. Triplett, A.F. Vakakis, and L.A. Bergman. Energy harvesting from impulsive loads using intentional essential nonlinearities. *Journal of Vibration and Acoustics*, 133(1):011004, 2011.

[161] L. Renson, G. Deliége, and G. Kerschen. An effective finite-element-based method for the computation of nonlinear normal modes of nonconservative systems. *Meccanica*, 49(8):1901–1916, 2014.

[162] L. Renson, G. Kerschen, and B. Cochelin. Numerical computation of nonlinear normal modes in mechanical engineering. *Journal of Sound and Vibration*, 364:177–206, 2016.

[163] L. Renson, J.P. Noël, and G. Kerschen. Complex dynamics of a nonlinear aerospace structure: Numerical continuation and normal modes. *Nonlinear Dynamics*, 79(2):1293–1309, 2015.

[164] P. Ribeiro and M. Petyt. Geometrical non-linear, steady state, forced, periodic vibration of plates, part I: Model and convergence studies. *Journal of Sound and Vibration*, 226(5):955–983, 1999.

[165] R.M. Rosenberg. On nonlinear vibrations of systems with many degrees of freedom. *Advances in Applied Mechanics*, 9(155-242):6–1, 1966.

[166] A.G. Russell. Thick skin, faceted, CFRP, monocoque tube structure for smallsats. In *Proceedings of European Conference on Spacecraft Structures, Materials and Mechanical Testing*, Noordwijk, The Netherlands, 2000.

[167] A.G. Salinger, N.M. Bou-Rabee, R.P. Pawlowski, E.D. Wilkes, E.A. Burroughs, R.B. Lehoucq, and L.A. Romero. LOCA 1.0 library of continuation algorithms: Theory and implementation manual. Technical report, SAND2002-0396, Sandia National Laboratories, Albuquerque, NM, 2002.

[168] E. Sarrouy, A. Grolet, and F. Thouverez. Global and bifurcation analysis of a structure with cyclic symmetry. *International Journal of Non-Linear Mechanics*, 46(5):727–737, 2011.

[169] F. Schilder, H.M. Osinga, and W. Vogt. Continuation of quasi-periodic invariant tori. *SIAM Journal on Applied Dynamical Systems*, 4(3):459–488, 2005.

[170] A. Sénéchal, B. Petitjean, and L. Zoghai. Development of a numerical tool for industrial structures with local nonlinearities. In *Proceedings of the 26th International Conference on Noise and Vibration engineering (ISMA)*, Leuven, Belgium, 2014.

[171] R. Seydel. *Practical bifurcation and stability analysis.* Springer-Verlag, New-York, NY, 2010.

[172] S. Sharma, E.B. Coetzee, M.H. Lowenberg, S.A. Neild, and B. Krauskopf. Numerical continuation and bifurcation analysis in aircraft design: An industrial perspective. *Philosophical Transactions of the Royal Society A: Mathematical, Physical and Engineering Sciences*, 373(2051):20140406, 2015.

[173] J. Shaw, S.W. Shaw, and A.G. Haddow. On the response of the non-linear vibration absorber. *International Journal of Non-Linear Mechanics*, 24(4):281–293, 1989.

[174] S.W. Shaw and C. Pierre. Normal modes for non-linear vibratory systems. *Journal of Sound and Vibration*, 164(1):85–124, 1993.

[175] S.W. Shaw, P.M. Schmitz, and A.G. Haddow. Tautochronic vibration absorbers for rotating systems. *Journal of Computational and Nonlinear Dynamics*, 1(4):283–293, 2006.

[176] S.F. Shen. An approximate analysis of nonlinear flutter problems. *Journal of the Aerospace Sciences*, 26(1):25–32, 1959.

[177] J. Sieber and B. Krauskopf. Control based bifurcation analysis for experiments. *Nonlinear Dynamics*, 51(3):365–377, 2008.

[178] J.J. Sinou and A.W. Lees. A non-linear study of a cracked rotor. *European Journal of Mechanics-A/Solids*, 26(1):152–170, 2007.

[179] S.W. Smith, B. Balachandran, and A.H. Nayfeh. Nonlinear interactions and the Hubble Space Telescope. In *Proceedings of the AIAA Astrodynamics Conference*, Hilton Head Island,SC, 1992.

[180] S.C. Stanton, B.A.M. Owens, and B.P. Mann. Harmonic balance analysis of the bistable piezoelectric inertial generator. *Journal of Sound and Vibration*, 331(15):3617–3627, 2012.

[181] Y. Starosvetsky and O.V. Gendelman. Response regimes of linear oscillator coupled to nonlinear energy sink with harmonic forcing and frequency detuning. *Journal of Sound and Vibration*, 315(3):746–765, 2008.

[182] Y. Starosvetsky and O.V. Gendelman. Vibration absorption in systems with a nonlinear energy sink: Nonlinear damping. *Journal of Sound and Vibration*, 324(3):916–939, 2009.

[183] S. Stoykov and S. Margenov. Numerical computation of periodic responses of nonlinear large-scale systems by shooting method. *Computers and Mathematics with Applications*, 367(5):2257–2267, 2014.

[184] B.S. Strachan, S.W. Shaw, and O. Kogan. Subharmonic resonance cascades in a class of coupled resonators. *Journal of Computational and Nonlinear Dynamics*, 8(4):041015, 2013.

[185] S.H. Strogatz. *Nonlinear Dynamics and Chaos: With Applications to Physics, Biology, Chemistry, and Engineering.* Addison-Wesley, Reading, MA, 1994.

[186] J.Q. Sun, M.R. Jolly, and M.A. Norris. Passive, adaptive and active tuned vibration absorbers–A survey. *Journal of Mechanical Design*, 117(B):234–242, 1995.

[187] D. Süß and K. Willner. Investigation of a jointed friction oscillator using the multiharmonic balance method. *Mechanical Systems and Signal Processing*, 52:73–87, 2015.

[188] K.Y. Sze, S.H. Chen, and J.L. Huang. The incremental harmonic balance method for nonlinear vibration of axially moving beams. *Journal of Sound and Vibration*, 281(3):611–626, 2005.

[189] D. Takács, G. Stépán, and S.J. Hogan. Isolated large amplitude periodic motions of towed rigid wheels. *Nonlinear Dynamics*, 52(1-2):27–34, 2008.

[190] C. Touzé and M. Amabili. Nonlinear normal modes for damped geometrically nonlinear systems: Application to reduced-order modelling of harmonically forced structures. *Journal of Sound and Vibration*, 298(4):958–981, 2006.

[191] C. Touzé, M. Amabili, and O. Thomas. Reduced-order models for large-amplitude vibrations of shells including in-plane inertia. *Computer Methods in Applied Mechanics and Engineering*, 197(21):2030–2045, 2008.

[192] F.L. Traversa, F. Bonani, and S.D. Guerrieri. A frequency-domain approach to the analysis of stability and bifurcations in nonlinear systems described by differential-algebraic equations. *International Journal of Circuit Theory and Applications*, 36(4):421–439, 2008.

[193] M. Urabe. Galerkin's procedure for nonlinear periodic systems. *Archive for Rational Mechanics and Analysis*, 20(2):120–152, 1965.

[194] A.F. Vakakis, O.V. Gendelman, L.A. Bergman, D.M. McFarland, G. Kerschen, and Y.S. Lee. *Nonlinear Targeted Energy Transfer in Mechanical and Structural Systems*, volume 156 of *Solid Mechanics and Its Applications.* Springer Science & Business Media, New-York, NY, 2008.

[195] A.F. Vakakis, L.I. Manevitch, Y.V. Mikhlin, V.N. Pilipchuk, and A.A. Zevin. *Normal Modes and Localization in Nonlinear Systems.* John Wiley & Sons, New-York, NY, 2008.

[196] B. Vaurigaud, L.I. Manevitch, and C.H. Lamarque. Passive control of aeroelastic instability in a long span bridge model prone to coupled flutter using targeted energy transfer. *Journal of Sound and Vibration*, 330(11):2580–2595, 2011.

[197] R. Viguié and G. Kerschen. Nonlinear vibration absorber coupled to a nonlinear primary system: A tuning methodology. *Journal of Sound and Vibration*, 326(3):780–793, 2009.

[198] R. Viguié and G. Kerschen. On the functional form of a nonlinear vibration absorber. *Journal of Sound and Vibration*, 329(25):5225–5232, 2010.

[199] L.N. Virgin. *Introduction to Experimental Nonlinear Dynamics: A Case Study in Mechanical Vibration.* Cambridge University Press, Cambridge, United Kingdom, 2000.

[200] G. von Groll and D.J. Ewins. The harmonic balance method with arc-length continuation in rotor/stator contact problems. *Journal of Sound and Vibration*, 241(2):223–233, 2001.

[201] K.C. Woo, A.A. Rodger, R.D. Neilson, and M. Wiercigroch. Application of the harmonic balance method to ground moling machines operating in periodic regimes. *Chaos, Solitons & Fractals*, 11(15):2515–2525, 2000.

[202] L. Xie. *Suivi Numérique des Bifurcations pour lAnalyse Paramétrique de la Dynamique Non-Linéeaire des Rotors.* PhD thesis, Université de Lyon, Lyon, France, 2016.

[203] L. Xie, S. Baguet, B. Prabel, and R. Dufour. Numerical tracking of limit points for direct parametric analysis in nonlinear rotordynamics. *Journal of Vibration and Acoustics*, 138(2):021007, 2016.

[204] J.L. Zapico-Valle, M. García-Diéguez, and R. Alonso-Camblor. Nonlinear modal identification of a steel frame. *Engineering Structures*, 56:246–259, 2013.

# List of Journal Publications

1. T. Detroux, L. Renson, L. Masset and G. Kerschen. The harmonic balance method for bifurcation analysis of large-scale nonlinear mechanical systems. *Computer Methods in Applied Mechanics and Engineering*, 296:18–38, 2015.
2. R.J. Kuether, L. Renson, T. Detroux, C. Grappasonni, G. Kerschen and M.S. Allen. Nonlinear normal modes, modal interactions and isolated resonance curves. *Journal of Sound and Vibration*, 351:299–310, 2015.
3. T. Detroux, G. Habib, L. Masset and G. Kerschen. Performance, robustness and sensitivity analysis of the nonlinear tuned vibration absorber. *Mechanical Systems and Signal Processing*, 60–61:799–809, 2015.
4. G. Habib, T. Detroux and G. Kerschen. Nonlinear generalization of Den Hartog's equal-peak method. *Mechanical Systems and Signal Processing*, 52–53:17–28, 2015.
5. T. Detroux, Y. Starosvetsky, G. Kerschen and A.F. Vakakis. Classification of periodic orbits of two-dimensional homogeneous granular crystals with no pre-compression. *Nonlinear Dynamics*, 76:673–696, 2014.

# List of Conference Publications

1. T. Detroux, J.P. Noël, G. Kerschen and L.N. Virgin. Experimental study of isolated response curves in a two-degree-of-freedom nonlinear system. In *Proceedings of the 34th International Modal Analysis Conference (IMAC)*, Orlando, FL, 2016.
2. E. Gourc, C. Grappasonni, J.P. Noël, T. Detroux and G. Kerschen. Obtaining nonlinear frequency responses from broadband testing. In *Proceedings of the 34th International Modal Analysis Conference (IMAC)*, Orlando, FL, 2016.
3. T. Detroux, L. Renson, L. Masset, J.P. Noël, and G. Kerschen. Bifurcation analysis of a spacecraft structure using the harmonic balance method. In *Proceedings of the ASME 2015 International Design Engineering Technical Conferences (IDETC)*, Boston, MA, 2015.
4. J.P. Noël, T. Detroux, G. Kerschen and L.N. Virgin. Isolated response curves in a base-excited, two-degree-of- freedom, nonlinear system. In *Proceedings of the ASME 2015 International Design Engineering Technical Conferences (IDETC)*, Boston, MA, 2015.
5. T. Detroux, J.P. Noël, L. Masset, G. Kerschen and L.N. Virgin. Numerical study of intrinsic features of isolas in a two-degree-of-freedom nonlinear system. In *Proceedings of the ICEDyn Conference*, Lagos, Portugal, 2015.
6. T. Detroux, L. Renson, L. Masset and G. Kerschen. Bifurcation analysis of large-scale dynamical systems using the harmonic balance method. In *Proceedings of the 12th Colloque National en Calcul des Structures (CSMA)*, Giens, France, 2015.
7. T. Detroux, L. Renson, L. Masset and G. Kerschen. The harmonic balance method for bifurcation analysis of nonlinear mechanical systems. In *Proceedings of the 33rd International Modal Analysis Conference (IMAC)*, Orlando, FL, 2015.
8. C. Grappasonni, G. Habib, T. Detroux and G. Kerschen. Experimental demonstration of a 3D-printed nonlinear tuned vibration absorber. In *Proceedings of the 33rd International Modal Analysis Conference (IMAC)*, Orlando, FL, 2015.
9. C. Grappasonni, G. Habib, T. Detroux, F. Wang, G. Kerschen and J.S. Jensen. Practical design of a nonlinear tuned vibration absorber. In *Proceedings of the ISMA Conference*, Leuven, Belgium, 2014.

10. T. Detroux, G. Habib, L. Masset and G. kerschen. The nonlinear tuned vibration absorber, part II: Robustness and sensitivity analysis. In *Proceedings of the 5th Conference on Nonlinear Vibrations, Localization and Energy Transfer*, Istanbul, Turkey, 2014.

11. G. Habib, T. Detroux and G. kerschen. The nonlinear tuned vibration absorber, part I: Design and performance analysis. In *Proceedings of the 5th Conference on Nonlinear Vibrations, Localization and Energy Transfer*, Istanbul, Turkey, 2014.

12. T. Detroux, L. Renson and G. Kerschen. The harmonic balance method for advanced analysis and design of nonlinear mechanical systems. In *Proceedings of the 32nd International Modal Analysis Conference (IMAC)*, Orlando, FL, 2014.

13. G. Habib, T. Detroux and G. kerschen. Generalization of Den Hartog's equal-peak method for nonlinear primary systems. In *Proceedings of the International Conference on Structural Nonlinear Dynamics and Diagnosis*, Agadir, Morocco, 2014.

14. T. Detroux, L. Masset and G. Kerschen. Performance and robustness of the nonlinear tuned vibration absorber. In *Proceedings of the GDR DYNOLIN 3437*, Lille, France, 2013.